Next generation electrochemical energy storage with nanocarbons and carbon nanohybrid materials

Dissertation
zur Erlangung des Grades
des Doktors der Naturwissenschaften
der Naturwissenschaftlich-Technischen Fakultät
der Universität des Saarlandes

von
Marco Zeiger

Saarbrücken
2017

Tag des Kolloquiums:	29.11.2017
Dekan:	Prof. Dr. G. Kickelbick
Vorsitzender:	Prof. Dr.-Ing. Mücklich
Berichterstatter:	Prof. Dr. V. Presser
	Priv.-Doz. Dr.-Ing. G. Falk
	Prof. Dr. Y. Gogotsi
Akad. Beisitzer:	Dr.-Ing. F. Aubertin

“Leonard, please don't take this the wrong way, but the day you win a Nobel Prize
is the day I begin my research on the drag co-efficient
of tassels on flying carpets.”

(Sheldon Lee Cooper)
The Big Bang Theory

TABLE OF CONTENT

ACKNOWLEDGEMENTS

This PhD thesis has been prepared in the Energy Materials Group at the INM - Leibniz Institute for New Materials in Saarbrücken under the supervision of Prof. Volker Presser. The work was funded by the German Federal Ministry for Research and Education (BMBF) in support of the nanoEES^{3D} project (award number 03EK3013) as part of the strategic funding initiative energy storage framework. Prof. Presser gave me the opportunity to continue my Master thesis work on a very fascinating and important topic in the field of energy storage materials. During this time he supported me exceptionally, helped me a lot in every life situation, and always had time to talk and to discuss my research. I owe him a lot and I am glad to be working together with him and to be part of his research group.

I want to thank PD Dr.-Ing. habil. Guido Falk for being my scientific supervisor from Saarland University, for our fruitful discussions, and that he reviews my thesis.

I have to thank Prof. Yury Gogotsi from Drexel University in Philadelphia very much for working as an external reviewer of my thesis.

Science and research are impossible without team work and good atmosphere in the lab. I was very lucky to be part of a very motivated and productive research team, which almost feels like a small family. I have to thank the whole Energy Materials Group, since they supported me not only during work, as colleagues, co-authors or students, but also were friends. I spent time with them during lunch, coffee breaks, or on the weekend and I always felt at home. Especially, the following people I would like to spend my deepest gratitude: Anna Schreiber, Simon Fleischmann, Nicolas Jäckel, Aura Tolosa, Benjamin Krüner, Pattarachai Srimuk, Dr. Daniel Weingarth, Dr. Soumyadip Choudhury, and Dr. Mesut Aslan. Thank you for the wonderful time!

I have been working at the INM since 2011, so that I have to thank several other people for their support: Prof. Eduard Arzt, Dr. Andreas Schneider, Prof. Tobias Kraus, Dr. Elmar Kroner, Prof. Roland Bennewitz, Dr. Jennifer Atchison, Dr. Marcus Koch, Robert Drumm, Rudolf Karos, Tobias Dörr, and all people from the workshop, the analytics department, the human resources department, and the administration department.

Some of this work would have been impossible without my collaborators around the world: I would like to thank Prof. Vadym Mochalin, Prof. Bastian Etzold, Dr. Simon Thiele and his group, and Nicolas J. Peter.

Apart from the great support during work at the INM, I was privileged to have the best family one can imagine. Thank you for everything, Mama, Papa, Janine und Ariane.

ZUSAMMENFASSUNG

Neuartige Energiespeicher sind aktuell im Fokus der Forschung, angetrieben durch die stetig steigende Nachfrage nach portablen Elektronikgeräten und die Implementierung erneuerbarer Energiequellen. Diese Speicher sollen idealerweise eine hohe Kapazität aufweisen und gleichzeitig schnell geladen werden können, was durch die Hybridisierung von redox-aktiven Materialien und Doppelschichtkondensatoren erreicht werden kann. In dieser Dissertation wurden verschiedene Strategien verfolgt: Nasschemische Beschichtungsprozesse für Übergangsmetalloxide, die Funktionalisierung mit redox-aktiven Oberflächengruppen und die Synthese von Kern-Schale-Partikeln. Dabei lag der besondere Fokus auf der Optimierung des Kohlenstoffsubstrates hinsichtlich Oberfläche, Porosität und Struktur. Es zeigte sich, dass nanoskalige Kohlenstoffe, wie Kohlenstoffnanozwiebeln, mit ausschließlich äußerer Oberfläche und hoher Leitfähigkeit ein ideales Substrat für Batterie- und Pseudokondensator-Hybride darstellen. Dies wurde für pseudokapazitives Manganoxid, eine redox-aktive Oberflächenfunktionalisierung mit Chinonen und Lithium-Schwefel-Batterien gezeigt. Die Beschichtung von nanoporösen Kohlenstoffen führt, im Vergleich zu Nanokohlenstoffen, zu einer signifikanten Reduktion der Porosität und der spezifischen Oberfläche, sodass diese eher bei einer Kern-Schale Materialarchitektur zum Einsatz kommen, wobei sich das redox-aktive Material im Kern befindet und der nanoporöse Kohlenstoff in der Schale.

ABSTRACT

Energy storage technologies are at the focal point of current research activities, propelled by the increasing demand on mobile storage for portable electronics and the rapidly growing implementation of renewable energy sources. To fulfill the requirements of an advanced energy storage device - high power and high energy - a hybridization of redox-active materials and electrical double-layer materials can be used. In this PhD thesis, several strategies and material architectures will be employed: Wet-chemical carbon coating procedures with transition metal oxides, carbon functionalization with redox-active surface groups, and the synthesis of core-shell particles. A special focus was on the optimization of the carbon substrate properties, such as porosity, surface area, and structure. It was shown that carbon nanomaterials, like carbon onions, with exclusively outer surface area and high conductivity are ideal substrates for battery and pseudocapacitor hybrids. This is exemplified for pseudocapacitive manganese oxide, a quinone-based surface functionalization, and lithium-sulfur batteries. Coating nanoporous carbons led to substantial pore blocking and thus a reduction of the specific surface area and the resulting capacity. To take advantage from the high double-layer capacitance, nanoporous carbons can be effectively used in core-shell particles, with the battery material in the core and the nanoporous carbon in the shell, which avoids the pore blocking issues.

1. INTRODUCTION

Planet earth presents optimal conditions for life and nature. These are mainly sustained by its relative position to the sun, the natural greenhouse effect, and the specific composition of its elements.[1] However, since the past few decades some of these circumstances are changing, which may threaten humanity and all living species in the future.[2] At the moment, it is not clear how fast and to what extend the earth's climate will change, but the first results and indications can already be seen and are represented by the increase of the world's mean temperature, changes in weather pattern, and the consequent rise of the sea level.[1]

The availability of electrical energy has enabled an extensive development of industrialization in the last centuries. For this reason, the demand for energy sources has rapidly increased and currently reaches its availability limits. Especially fossil fuels like coal, gas, and oil have been accelerating this technological development, but on the other hand they are responsible for the consequent climate change.[2, 3] Greenhouse gases, for example carbon dioxide (CO_2), are mostly produced by burning fossil fuels in industry or in the transportation sector. Owing to their long atmospheric lifetime, they have been accumulated and distributed over the whole planet. The resulting sealing of radiation avoids the transmission of outgoing radiation and ultimately warms the whole planet. As a consequence, air and water temperatures increase, which in turn leads to melting of the polar ice caps and rising sea levels.[1]

Figure 1 shows the development of the annual mean global temperature of 14 °C and the mean atmospheric CO_2 concentration of 334 ppm_v (parts per million by volume) over time. Since the start of the industrialization, the part of CO_2 in the earth's atmosphere has risen by 31 %. Even half of this increase was established after 1965 because of the progressive industrial development. Over the same time period from 1958 to 2004, the mean annual global temperature has increased by ~1 °C.[1] Considering the current emission regulations and the calculated impacts on the future, a further climate change must be expected. Of course, the impact can be slowed down but a complete stop in this century is quite unlikely.[1]

Since the burning of fossil fuels is the main reason for the continuous increase of CO_2 emissions and the resulting greenhouse effect, many developed countries have established regulations like emission constraints for cars, speed limits on highways, and low-traffic zones in cities, for instance. Moreover, it is essential to consequently replace fossil fuels in the near future by other energy sources, which have no or less impact on the environment. For this purpose, the generation and implementation of renewable energy sources are planned to be extended.[4]

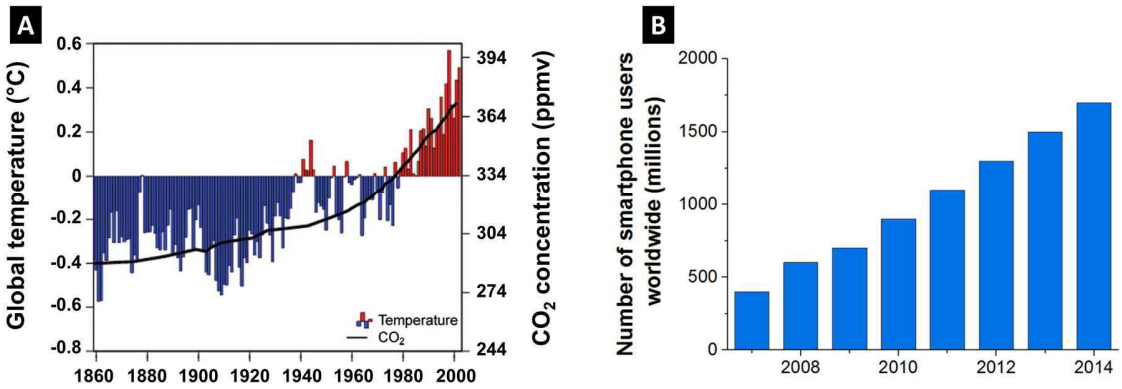

Figure 1: (**A**) Annual mean global temperature of 14.0°C (bars) and mean carbon dioxide concentration (solid curve), using data from ice cores and from Mauna Loa after 1958.[1] (**B**) Number of smartphone users from 2007 to 2014.[5]

The most practical renewable energy sources are wind and solar power, which potentially could meet the world's energy demand many fold. While green energy sources are inexhaustible, sustainable, and quickly renewable, their major disadvantage is the varying and unpredictable output, fluctuating over broad time scales from seconds to several hours and even days.[3] For example, the sun is not always shining and wind is typically stronger during the night. Furthermore, the energy demand of the population is changing too, which leads to a huge mismatch between energy demand and production.[4] To bridge this gap intermittent energy storage can be used, which stores excess energy and releases it when it is needed. Energy storage technologies are important drivers of the global energy revolution, which compensate the divergency between the costumer's energy consumption and the output fluctuations from renewables. Additionally, they are a main contributor to the global digitalization since they ensure the constant energy supply of portable and mobile electronics.

The development of portable electronics, such as mobile phones, laptops and tablets has been the key for the world-wide connection. Every day more people are using mobile applications, and the demand for portable energy storage devices is rapidly growing. In 2007, less than 400 million people world-wide were using a smartphone (**Figure 1B**). In 2014, the number of smartphone users is more than four times higher and is expected to further increase in the next years.[5] Additionally, the performance of every electronic application has to meet the increasing costumer's expectations, which is higher capacity, shorter charging times, and longer life times. For this purpose, new energy storage solutions must be developed which fulfill both, the requirements of high energy and high power. Especially electrochemical energy storage demonstrates a key technology owing to its high development potential and its broad application possibilities.

1.1 Electrochemical energy storage

There exists a variety of energy storage techniques, differing by its storage principle and categorized by their performance values, such as storage capacity and power.[4] The specific energy in Wh/kg is a value for the amount of energy, which can be stored per mass and the specific power is a value of the rate at which the system stores and releases energy in W/kg. Dependent on the application, the performance values normalized to their volume are more important, especially when limited space is given, for example in portable electronics. When both values are shown in one plot, it is called a Ragone plot, which is among the most important performance metrics in energy storage (**Figure 2A**).[6]

The choice of an energy storage technique depends on the application where specific amounts of energy must be stored and released in a defined time scale. With respect to the discharge time, different techniques can be separated into power management, bridging power and energy management. The first two present ramping services with short charge and discharge times, for example, for applications with high input fluctuations. The power management compensates short fluctuations from seconds to minutes and the bridging power section closes the gap between those with fluctuations in the order of minutes to hours. The energy management sector is responsible for moving large amounts of energy over several hours to days.[7] The latter part is mainly covered

by pumped hydro energy storage, which stores large amounts of water in high reservoirs. During the release, the water flows down the plateau and a generator is powered.[8, 9] Typical examples in the bridging power section are superconducting magnetic energy storage devices (SMES)[10] and batteries.[11, 12]

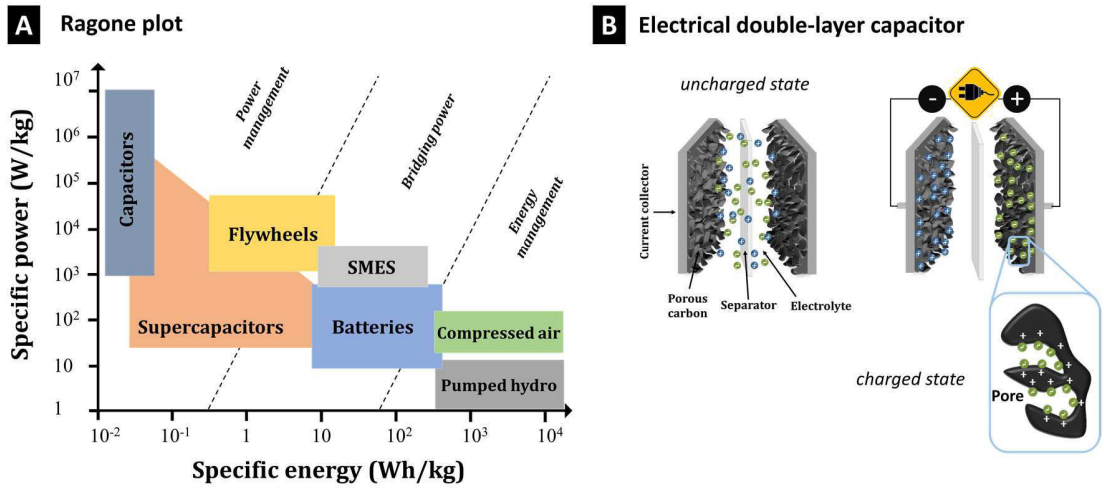

Figure 2: (**A**) Ragone plot presenting the specific energy and power values of different energy storage technologies.[4, 11, 13] (**B**) Set up of an electrical double-layer capacitor (EDLC) in charged and uncharged state.[14]

Capacitors are favorable for very high rates, belonging to the power management part, whereas supercapacitors work in the range of seconds to minutes and rather belong to both, power management and bridging power. Supercapacitors can be divided into EDLCs, pseudocapacitors, and hybrid devices. In case of EDLCs, the energy storing mechanism is purely physical, with a reversible electrosorption of ions at the interface between a porous carbon electrode and the electrolyte (**Figure 2B**). For comparison, Faradaic reactions, like intercalation or conversion reactions take place in batteries and pseudocapacitors, leading to much higher specific capacities, but lower power.[14]
Since most of the energy storage techniques present either high specific energy or high specific power, an optimized device achieving both properties is still missing. Yet, the combination of two complementary techniques, such as batteries and supercapacitors, can be a feasible way to develop hybrid electrochemical energy storage devices. For this, the properties of batteries (lithium-ion and lithium-sulfur batteries) and supercapacitors will be explained in the next chapters, to extract adequate hybridization strategies.

1.2 Lithium-ion batteries

Lithium-ion batteries (LIBs) are the most advanced and best commercialized electrochemical energy storage devices. Compared to EDLCs, LIBs are characterized by high specific energies of >100 Wh/kg, but with a rather low power performance of less than 1 kW/kg and a limited long-time stability in the order of a few hundred cycles.[11, 12] A commercial LIB is typically composed of graphite as anode and a lithium transition metal oxide (e.g., $LiCoO_2$ - LCO) as cathode with Li-containing organic, carbonate-based electrolyte. During charging, Li^+ ions move from the metal oxide and intercalate into the graphite anode. The discharging step involves deintercalation from the anode (graphite) and intercalation into the cathode ($LiCoO_2$). The respective reactions for the discharge step are shown in **Eq. 1-2**:

$$Li_yC_n \rightarrow C_n + yLi^+ + ye^- \quad (\mathbf{1})$$

$$Li_{1-y}MO_x + yLi^+ + ye^- \rightarrow LiMO_x \quad (\mathbf{2})$$

Eq. 1 presents the reaction at the graphite anode and **Eq. 2** for the metal oxide (MO) cathode. The transportation of ions between both electrodes, which can host lithium ions, is called the rocking chair.[15] Dependent on the electrode materials the working potential range of Li-ion batteries is between 2.5 V and 4.1-4.3 V vs. Li/Li^+.[15] Typical anode materials are graphite, lithium titanate (LTO) or Si with theoretical specific capacities ranging from 300 mAh/g (graphite: 372 mAh/g) to more than 4000 mAh/g (Si: 4200 mAh/g). The most common cathode material, $LiCoO_2$, has a theoretical specific capacity of 274 mAh/g, but it is quite expensive, presents a low thermal stability, and fast capacity decrease at high currents.[16] Therefore, several other types of cathode materials were developed in the past few decades. The main alternatives are $LiFePO_4$, $LiMn_2O_4$, and $LiNiMnCoO_2$.[17] Although Li-ion batteries are currently the dominant energy storage device for portable electronics, research is trying to identify alternatives, such as Na-, K-, Zn-, or Mg-batteries, because a shortage of Li is expected to happen in the near future.[18]

1.3 Lithium-sulfur batteries

Other possibilities to store energy via Faradaic reactions, besides the lithium ion intercalation into transition metal oxides in LIBs, are alloying and conversion reactions. These reactions occur between two materials forming a new compound with new material properties. An example is the formation of Li_2S using metallic lithium and elemental sulfur in lithium-sulfur batteries.[19] Since the energy storage capacity of LIBs is strongly limited by the specific capacity of the cathode (e.g., transition metal oxides) with values between 200-400 mAh/g (e.g. LCO: 274 mAh/g), there is a large need for new electrode materials. Recently, the attention came to elemental sulfur due to its high theoretical specific capacity of 1672 mAh/g, its low costs and high natural abundance.[19] The lithium sulfur battery is on lab-scale composed of elemental sulfur as active cathode material, often combined with a lithium metal anode to balance the high specific capacity of the sulfur (sulfur: 1672 mAh/g; lithium: 3861 mAh/g).[20] The latter is mixed or hybridized with a conductive additive (for example carbon black or porous carbons) due to the insulating properties of sulfur and Li_2S. The whole discharge process is known to happen in several steps. First, lithium ions form at the anode and are transferred to the sulfur cathode (**Eq. 3**).[20] Orthorhombic cyclic octasulfur (S_8) is reduced to polysulfides in multiple reactions from Li_2S_x ($6<x\leq8$) to Li_2S_x ($2<x\leq6$) resulting in Li_2S as the end product (**Eq. 4**). The charging process reconverts the Li_2S to elemental sulfur by multiple lithium polysulfide intermediates.[19, 21, 22] The occurring reactions for the discharge are shown in **Eq. 3**-**4**:

$$16Li \rightarrow 16Li^+ + 16e^- \quad (3)$$

$$S_8 + 16Li^+ + 16e^- \rightarrow 8Li_2S \quad (4)$$

However, a practical application of this system still requires resolving several challenges: The dendrite formation on the lithium metal anode may damage the separator, leading to short-circuiting, which makes the electrochemical system unpredictable and highly unstable. Also, the volume expansions during the Li_2S formation of ~80 % compromises structural integrity during long-time cycling operation.[19-22] In addition, the intermediately formed lithium polysulfides (Li_2S_x) are soluble in the electrolyte and

shuttle between anode and cathode. The latter is the main reason for the low charge efficiency and the rapid self-discharge.

The high resistance of sulfur with ~10^{-30} S/cm is a great challenge, so that carbon additives must be added, combined with advanced materials architecture, to provide high conductivity, high sulfur loading, and large interface to increase the sulfur accessibility.[19, 21, 22] For this purpose, porous carbons were used in recent literature due to their high conductivity, their chemical inertness and low density.[20] Dependent on the surface area, the pore size distribution and the electrode architecture high amounts of sulfur can be accommodated, the dissolved polysulfides can be prevented from shuttling, and sulfur leaching can be partially avoided.[20] For example, a high pore volume consisting of mainly mesopores enables high sulfur loadings and fast kinetics. On the other hand, a nanoconfinement of sulfur in micropores favors trapping of the polysulfides, leading to improved long-time stability.[20]

1.4 Supercapacitors

Supercapacitors belong to the large family of electrochemical energy storage devices.[14] In general, they can be divided into electrical double-layer capacitors (EDLCs),[23] pseudocapacitors (PCs),[24] and hybrid devices[25].

1.4.1 Electrical double-layer capacitors

EDLCs present very high charge and discharge rates due to their purely physical energy storage mechanism. Reversible electrosorption of charged electrolyte ions takes place at the interface between a porous carbon electrode and the electrolyte when a voltage is applied (**Figure 2B**). The absence of chemical reactions favors high power ratings, but also limits the energy storing capacity.[26] For example, EDLCs consisting of two activated carbon (AC) electrodes with a capacitance of 100 F/g per electrode (25 F/g cell capacitance) and an organic electrolyte with a stability window of 2.7 V would reach a full cell specific energy of ~25 Wh/kg. For comparison, batteries can reach more than 100 Wh/kg but suffer from their lower specific power of ~1 kW/kg, which is more than

ten times smaller than for EDLCs (>10 kW/kg).[11] The specific energy of a supercapacitor can be calculated according to **Eq. 5**:

$$E_{cell} = \frac{1}{2} C_{cell} U^2 \qquad [E] = \frac{Wh}{kg} \qquad (5)$$

U is the applied voltage and C_{cell} the specific capacitance of the cell. The capacitance can be derived from **Eq. 6**:

$$C_{cell} = \frac{1}{m} \cdot \frac{Q}{U} = \frac{1}{m} \cdot \frac{1}{U} \cdot \int_{t_1}^{t_2} I dt \qquad [C] = \frac{F}{g} \qquad (6)$$

where Q is the reversibly stored charge or discharge, I the current, U the applied cell voltage, t_1 and t_2 the start and end time of charging or discharging, and m the mass of both electrodes. Note that the specific capacitance of one electrode in a symmetrical set up can be calculated by multiplication of the cell capacitance with 4. The specific power is directly related to the specific energy divided by the discharge time $\Delta t = t_2 - t_1$.

$$P_{cell} = \frac{E_{cell}}{\Delta t} \qquad [P] = \frac{W}{kg} \qquad (7)$$

As defined by Zhang et al., a capacitive electrical response, that is, a sloping voltage profile and a rectangular cyclic voltammogram, is the main characteristic of a supercapacitor. It distinguishes supercapacitors from other energy storage techniques, such as batteries with distinct potential-dependent redox-reactions.[27] In the case of EDLCs, this mechanism is only related to pure ion electrosorption, whereas pseudocapacitors allow fast redox-reactions.[24]

The capacitance and the consequent specific energy of EDLCs scale somewhat with the accessible specific surface area (SSA) of the carbon electrode. For this, high surface area carbons are typically used in commercial devices.[28, 29] The most commonly employed material is activated carbon (AC), which can be derived from coconut shells, pyrolysed and activated to achieve a porous structure with high surface area in the order of 1500-3000 m^2/g with a capacitance of ~100 F/g per electrode (i.e., 25 F/g per device).[14, 30, 31] Higher capacitances can be achieved by increasing the SSA, for example, using activation procedures[32] and tuning the pore structure to a certain degree by using carbide-derived carbons, for instance[33].

However, there is an upper limit of the surface area, defined by a minimum required size of the pores allowing the electrolyte ions to penetrate and a minimum wall thickness to screen the adsorbed charges.[32] For example, in a study by Lozano-Castelló et al., the capacitance of microporous AC decreased for higher surface areas.[34] A study by Barbieri et al., comparing the gravimetric capacitances of several carbon blacks and activated carbons to their SSAs, came to the same conclusion: The capacitance linearly increases to ~90 F/g for a SSA of ~1500 m^2/g, but higher SSAs did not lead to further capacitance improvement.[32] This result is supported by the study of Stoller et al., investigating the capacitance of a single graphene sheet.[35] It was shown that the capacitance per surface area in contact decreased when the electrolyte was in contact with both sides of the graphene electrode.[35] Other studies using microporous AC show similar results and the same trend.[30, 31, 36, 37]

Although the increase in SSA does not necessarily induce a capacitance improvement, the design or the optimization of the pore size and its distribution can lead to higher capacitances. By tuning the micropores to a pore diameter exactly matching the ion size, the latter one is squeezed through the pore and its solvation shell becomes highly distorted and is even (partially) stripped off. As result, the closer packing of the ion to the carbon surface leads to a higher capacitance. This is often called “anomalous” pattern, since a maximum capacitance can be found for a specific pore size and not a constant dependency is measured.[33] Paradoxically, in several other studies, for example by Centeno and Stoeckli, contrary findings put the earlier results into question: A linear or regular behavior between capacitance and surface area/ pore size was measured.[38, 39] The controversy about capacitance dependency on pore size and surface area is still ongoing, but it has to be pointed out, that the precise determination of capacitance and surface area is a very crucial issue.[40] Capacitance values can be measured using several techniques, for example galvanostatic cycling and cyclic voltammetry using a variety of setup parameters. In addition, the electrode preparation is changing from study to study, ranging from pure powder electrodes and monoliths, to polymer bound electrodes with binder contents of up to more than 20 mass%. This complicates the normalization of the specific capacitance and changes the conductivity of the composite electrode, which ultimately results in a variety of different and incomparable capacitance values. It

becomes even more complex when different SSA measurement strategies are used (nitrogen, argon or carbon dioxide) in gas sorption analysis and calculation methods like BET (after Brunauer, Emmett, and Teller)[41] are compared to DFT (density functional theory)[42, 43] calculations.

In a detailed study by Jäckel et al., six different microporous carbons were tested in different organic electrolytes and ionic liquids. Compared to other studies, the electrochemical data were correlated with the pore size distribution (PSD) using the ion size and the influence of the solvation shell. As a general result, it can be summarized that both, the anomalous and the regular pattern, do not precisely simulate the capacitance-surface area dependency for a specific PSD. Dependent on the normalization, both patterns could be achieved.[40] Yet, when taking into account the electrochemical active surface area (surface area accessible for the ions) and not just using the volume-weighted average pore width (d_{50}), but instead the spread between d_{25} and d_{75} (pore width enfolding 25 and 75% of the total pore volume) a clear trend of increasing normalized capacitance for pores in the range of the ion size can be measured.[44]

Apart from that, it was shown by Gerischer et al. that the capacitance itself is rather dependent on the applied voltage and not an intrinsic material property per se.[45] Owing to the non-metallic conduction properties of carbon, the density of charge carriers increases when increasing the applied potential and more charges accumulate on its surface.[46] This so called electrochemical doping or butterfly-shape, named by the special shape of the cyclic voltammogram (CV), was shown for graphite,[45] nanodiamond-derived carbon onions,[47] templated carbons,[48] and carbon nanotubes[49]. For amorphous carbon, this effect has been measured to be much smaller than for more graphitic carbon, experimentally supported when using carbon onions with different degrees of carbon ordering.[47]

The usage of carbon materials for energy applications, especially in supercapacitors necessitates several properties, such as high SSA, precisely tuned PSD with ion matching pore sizes, high conductivity, and high chemical inertness. Dependent on the required performance, different carbon materials can be used and will be discussed in the next chapter.

1.4.2 Carbon materials in EDLCs

For a very long time, carbon has been known to exist in three main forms: diamond, graphite, and amorphous carbon. These carbon allotropes present the same chemical composition, but their properties strongly differ dependent on how the atoms are arranged and bonded.[50] The emergence of new carbon nanoforms, first with the discovery of the buckminsterfullerene C_{60}[51], and followed by the development of carbon nanotubes[52], has opened a new field in carbon research. Since a variety of microstructures (carbon ordering and crystallinity) and different dimensionalities, ranging from 0D to 3D (**Figure 3**), exist, the physico-chemical properties of the carbon material can be tuned to a large degree.[53]

Diamond is the hardest natural occurring material on earth with a sp^3 hybridization and a face-centered cubic crystal lattice. It presents a very high electrical resistivity compared to other carbons, such as amorphous carbon or graphite.[54] The latter one consists of covalently bonded, hexagonally oriented carbon atoms in sp^2 hybridization formed to layers which are arranged in an AB stacking order, causing soft mechanical properties and a high electrical conductivity.[50]

New carbon nanoforms, such as graphene, carbon nanotubes, or fullerenes opened the way for new applications in electronics, optics, and energy storage.[53] Graphene, often considered as the main building block of all carbon nanomaterials, is composed of one layer of hexagonally oriented carbon atoms. The rolling of this carbon layer to a tube-like morphology yields a single wall carbon nanotube (SWCNT) and the formation of a single-layer sphere presents a fullerene.[53]

For supercapacitors, and especially EDLCs, typically porous carbons with high SSA are used.[14] Dependent on the synthesis procedure and the precursor materials their structure is a combination of different carbon hybridizations and structural compositions. For example, activated carbon can be composed of amorphous carbon parts (sp^2 and sp^3 hybridization), nanocrystalline graphite, and graphene sheets.[55] Structurally, Stoeckli et al. described AC as a random arrangement of graphene layers, which are highly defective and terminated by surface functional groups.[56]

Typically, AC is produced via thermal decomposition/carbonization of carbon-rich precursors at high temperatures, for instance, naturally abundant materials, such as

coconut shells[57] or polymeric precursors with high carbon contents[58]. After carbonization, the existing micropores often present slit shapes and wormlike pore architectures with a very broad size distribution. A widening of these pores to increase the pore volume and surface area can be achieved by physical activation processes under oxidizing atmospheres, such as steam or CO_2.[59]

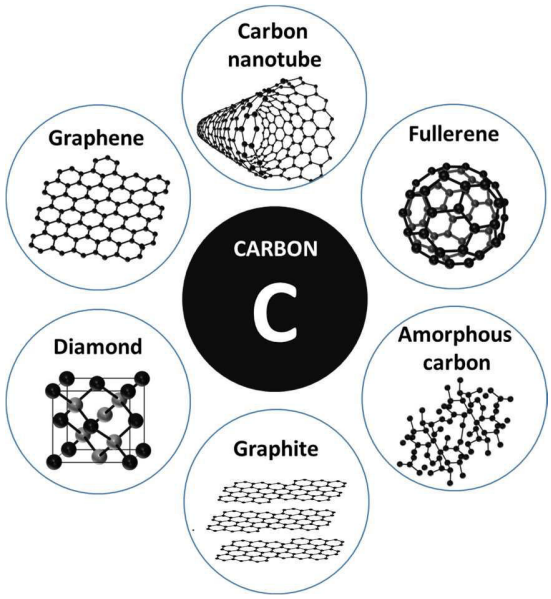

Figure 3: Overview of different carbon materials and carbon nanomaterials.

The structure, including surface area and pore size distribution, can be tuned by activation time, temperature, and type of atmosphere. Specific surface areas of up to 3000 m^2/g with a distinct microporous structure (pores <2 nm) can be synthesized.[60] According to IUPAC, pores can be divided into micropores (<2 nm), mesopores (2-50 nm), and macropores (>50 nm).[61] Longer activation times typically increase the pore diameter and the pore volume until the internal structure collapses.[60] Other possibilities to increase the surface area of carbons are chemical activation procedures, for example with agents like potassium hydroxide (KOH).

When using natural precursors such as coconut shells, the resulting particle morphology is very irregular with a size in the range of 1-50 µm (**Figure 4B**).[57] However, the use of polymeric precursors facilitates the tuning of size and morphology since the polymers can be shaped by emulsion reactions to beads[58] or using electrospinning to fabrics or fibers[62, 63]. To precisely tune and to achieve defined pore diameters, carbide-derived carbons (CDC)[64] or templated carbons[48] can be used (**Figure 4B**).

All these porous carbons with high SSA are called endohedral, since their SSA is predominantly located inside the carbon particles (**Figure 4A**). Exohedral carbons present exclusive outer surface area, like carbon nanomaterials.[65] An overview about different endo- and exohedral carbons is given in **Figure 4** with a rough estimation of their specific surface area.

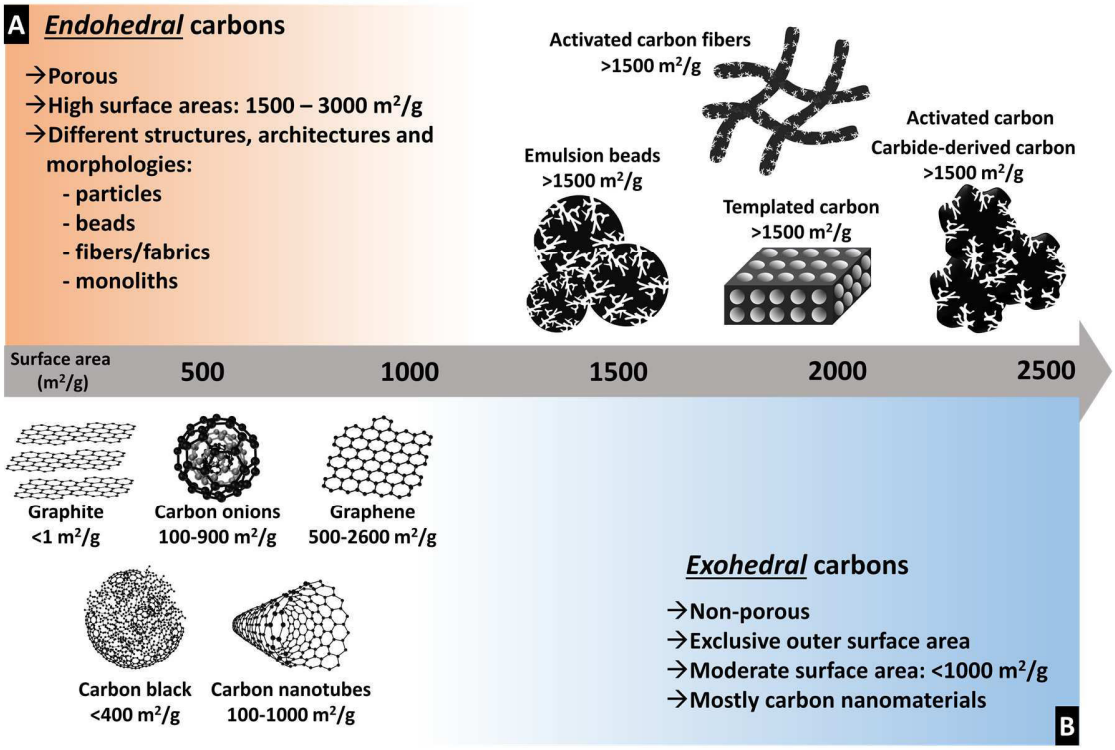

Figure 4: Overview about carbon materials and their surface areas. (**A**) Endohedral carbons with distinct porosity and (**B**) exohedral carbons with exclusive outer surface area such as for carbon nanomaterials. The surface area values are representative of typical ranges.

One well-known example for an exohedral carbon is carbon black (**Figure 4B**), which is typically synthesized by the combustion of carbonaceous gases (for example from petroleum). Its primary particle size ranges from 10-500 nm with a structure composed of curved and cracked graphene layers.[66] Due to its small size, high conductivity, but rather moderate SSA they are mainly used as conductive additives to decrease the interparticle contact resistances in batteries[67] or EDLCs[68, 69]. Carbon nanomaterials present a very small primary particle size, for example nanodiamond-derived carbon onions with a diameter <10 nm, and a resulting surface area of 300-600 m^2/g.[70]

Compared to porous carbons, the respective capacitance of <50 F/g is rather small, but their easy ion accessibility and high conductivity favor high power applications.[70] Since their surface area is exclusively located on the outside of the nanometer-sized particles, they present an ideal substrate for redox-active species.[70] These can be chemically active surface functional groups, like quinones, or typical battery materials like transition metal oxides. Thin coatings of metal oxides are deposited on the carbon substrate by retaining partial surface accessibility. Using this strategy, the issues of pore blocking (a notorious problem for porous carbons) can be effectively mitigated.[71]

As shown in the last chapter, the advantage of EDLCs is their very high power performance due to reversible ion electrosorption in porous carbons. Yet, due to several reasons (see chapter 1.4.1), their capacitance can only be increased to a certain degree by changing the properties of the carbon electrode materials. To further enhance the performance of EDLCs, alternative electrode materials or additives, such as pseudocapacitors with distinct redox activity, can be used and are discussed in the next chapter.

1.4.3 Pseudocapacitors

Pseudocapacitive materials show a capacitor-like, linear charge-voltage profile as known for EDLCs, but their energy storage mechanism is related to a Faradaic reaction. Compared to batteries, pseudocapacitors are not limited by solid-state ion-diffusion within the time-frame of the charge- and discharge-process, which favors high power applications.[24, 72] Typical materials are oxides, dichalcogenides, carbides, nitrides, carbonitrides (MXenes) of transition metals, as well as redox-active polymers.[73] They are able to achieve battery-like specific energies in combination with the high specific power and the long-time stability of EDLCs.[72] Dependent on the underlying pseudocapacitive reaction, they can be divided into intrinsic and extrinsic pseudocapacitors. Intrinsic reactions are due to the material itself, like for hydrous RuO_2 and MnO_2, whereas the extrinsic reaction is caused by the nanoscopic architecture, namely the phase, the space group, or the crystallite size.[24, 72] A more detailed analysis of pseudocapacitive mechanisms and their differentiation from batteries will be given in the next chapter.

1.4.4 Comparison of pseudocapacitors and batteries

Since Faradaic reactions in pseudocapacitors are difficult to differentiate from others and the nomenclature is not well defined, all electrode material-related energy storage mechanisms are compared in the following paragraph and in **Figure 5**. The mechanisms can be divided into double-layer formation (non-Faradaic; **Figure 5A**) and Faradaic reactions, including surface redox reactions, intercalation reactions, and alloying/conversion reactions (**Figure 5B-D**). Note that in this summary, only the reactions directly related to the electrode are presented. This does not include electrochemical reactions originating from redox electrolytes.[74]

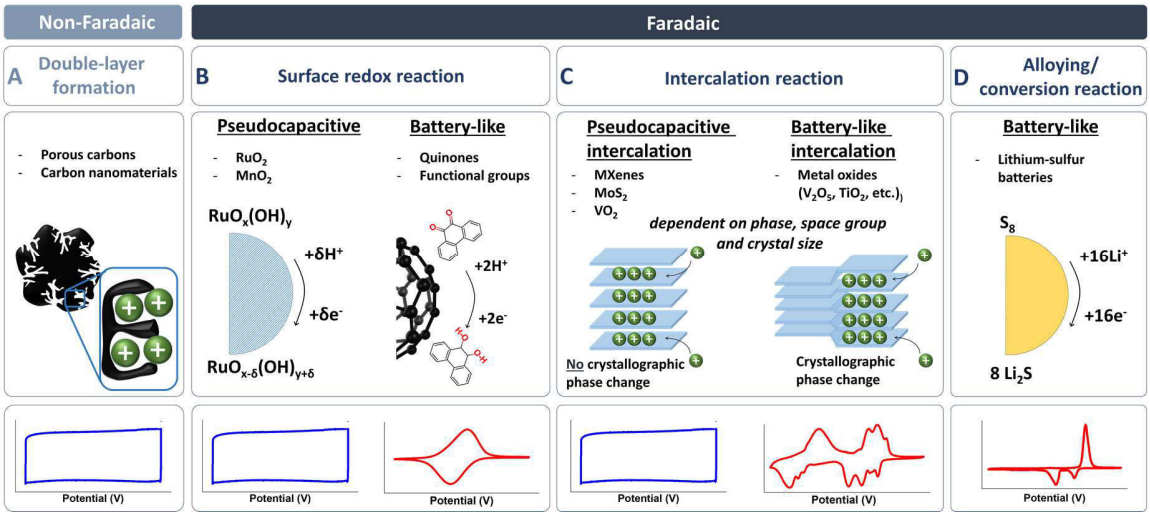

Figure 5: Different types and mechanisms of electrochemical reactions. (**A**) Non-Faradaic process in electrical double-layer capacitors (EDLCs). Faradaic process using (**B**) surface redox reactions, (**C**) intercalation reactions, and (**D**) alloying or conversion reactions. The electrochemical response can be either classified as pseudocapacitive or battery-like.

Surface redox reactions (**Figure 5B**) can present Faradaic responses which are pseudocapacitive or battery-like. For example, surface functional groups, such as quinones, contribute to the surface redox reaction by a reversible proton (hydrogen) transfer at a specific potential.[75, 76] In contrast, thin film hydrous RuO_2 reacts like a pseudocapacitor, although the same material as single crystalline bulk material showed distinct redox peaks.[24, 77] The latter pseudocapacitive behavior of metal oxides is especially pronounced for nanometer-sized materials (for crystals <10 nm) since the majority of their atoms are surface atoms.[72] Hydrous RuO_2 was the first

pseudocapacitive material studied in aqueous electrolytes.[77] Due to reversible surface redox reactions and its high electrical conductivity, this material presents ideal properties with values exceeding 700 F/g.[24] For hydrous RuO_2, the importance of structural water, which improves the fast proton transport, was demonstrated and clearly shows the impact of the interplay between electrode properties and electrolyte.[24] This so-called redox pseudocapacitance comes from the electrochemical adsorption of ions on or close to the surface of a material including a Faradaic charge-transfer.[24] However, due to the high price of RuO_2 the attention has been directed to cheaper and more environmentally friendly metal oxides like MnO_2, for instance[78].

In contrast to ideal surface redox reactions, intercalation reactions of electrolyte ions pertain to the bulk material (**Figure 5C**). Dependent on the electrochemical response, the redox-reaction is pseudocapacitive (i.e., capacitor-like) or battery-like. The latter is the general energy storage mechanism as found in batteries with a distinct potential dependent reaction. During this reaction a change of the crystallographic phase occurs which is responsible for the significant expansion of the material upon charging.[17] This battery-like intercalation can be converted to a pseudocapacitive reaction when the material exposes a nanoscale architecture[24] or the space group is changed[79]. This effect was measured for nanostructured Nb_2O_5,[80] nanocrystalline V_2O_5,[81, 82] and 2D layered materials such as MXenes[83]. These materials present a pseudocapacitive behavior accompanied with a Faradaic charge-transfer not being limited by solid-state diffusion.

Conversion and alloying reactions are characterized by the formation of a new compound with new material properties, such as the formation of Li_2S in lithium-sulfur batteries (**Figure 5D**). The purely Faradaic mechanism is represented by a distinct battery-like reaction with redox peaks in the CV. A detailed description of LSBs and the redox reactions is already given in chapter 1.3. All these materials, independent from whether they show battery-like or pseudocapacitive properties, are attractive for high capacity energy storage. Most of them, for example sulfur, MnO_2, and V_2O_5, are still suffering from their very low electrical conductivity and limited specific power.[82] Therefore, redox-active materials are mixed or coated with conductive additives (typically carbon) to decrease the interparticle contact resistances (**Figure 6A-B**).[84-86]

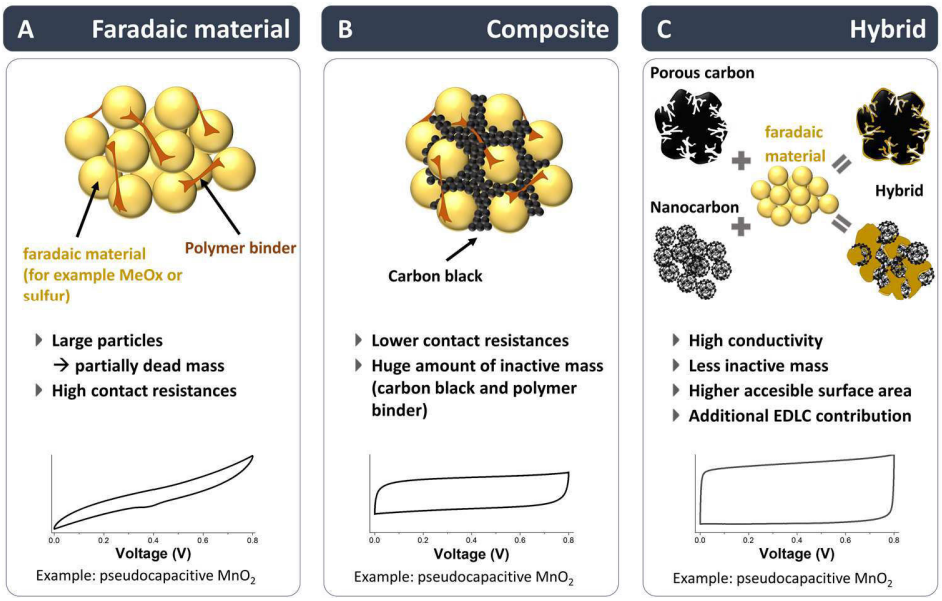

Figure 6: (**A**) Cathode material particles for batteries bound together using a polymeric binder. (**B**) Additional carbon conductive additive particles reduce the contact resistances. (**C**) Hybridization of carbon material with the Faradaic component to achieve an advanced materials architecture with high electrochemical performance.

The need of carbon supports is even more obvious for redox active surface functional groups like quinones, working as electron carrier and mechanical substrate. In these systems, the carbon substrate is not only responsible for the electron support but also serves as a binding substrate.[75]

Highly conductive carbon black particles with sizes between a few nanometers to a few micrometers are used dependent on the application and the manufacturing process (**Figure 6B**).[12, 17, 19, 24] In this case, a mixture of both, conductive additive and active material with a separation of the components on the nanoscale is commonly known as a composite, whereas the molecular chemical bonding on the nanometer-level is called hybrid.[87, 88] By adding the appropriate amount (up to 20 mass%) of conductive additive to the material, the capacity of the whole electrode drops significantly. When 10 mass% of a polymer binder are added, the specific capacity drops dramatically, for example, from 200 mAh/g to only 140 mAh/g, since 30 mass% of the electrode does not contribute significantly to the charge storage. This emphasizes the importance to carefully distinguish between capacity per mass of active electrode material and per mass of the entire electrode (including binder and additive, but not the electrolyte or casing).

For some of the mentioned Faradaic systems the charge storage mainly occurs on the surface of the material or the support (surface redox reactions). For these materials, an optimized large interface between the material surface and the electrolyte must be achieved (**Figure 6C**). The latter combined with short bulk diffusion pathways favors higher energy storage capacities and higher power ratings.[24, 72] For this purpose, Faradaic materials can be hybridized with high surface area and highly conductive carbon materials (**Figure 6C**). Dependent on the electrochemical response of the hybrids consisting of carbon double-layer material and Faradaic compounds, they are either called battery or pseudocapacitor hybrids.

1.5 Hybrid electrochemical energy storage

The hybridization of different materials is used to combine different energy storage mechanisms, typically EDLCs with pseudocapacitors or batter
es. To benefit from both, a hybridization on the nanometer-scale, as well as advanced electrode architectures are necessary. The most important properties and design criteria are the following:

- A high conductivity of the hybrid electrode is necessary for high power applications. This can be achieved using highly conductive nanocarbons as substrate for the Faradaic material, core-shell particles with the porous carbon material as shell, or free-standing carbon fiber substrates.
- Dependent on the carbon substrate, specific hybridization techniques must be used to avoid a strong decrease in surface area and pore blocking, to achieve a uniform distribution, and to generate a large interface with the electrolyte.
- Thin coatings or deposits of Faradaic material favor high power applications by providing short diffusion paths for the ions to the reactive sites.
- The ratio of carbon to the Faradaic compound must be precisely adjusted to achieve a compromise between high power and high energy. Typically, high loadings of redox-active material are favored for high energy storage capacities.

These design criteria are applicable for all kinds of Faradaic materials in combination with carbon, especially for typical LIB materials such as metal oxides, but also for elemental sulfur for LSBs. In the case of surface functional groups, such as quinones, the ratio of

carbon support/redox additive cannot be adjusted by thicker coatings since the deposition method is a functionalization of the carbon and its surface terminations. For this purpose, a higher loading can be achieved by further increasing the SSA and the porosity of the carbon material. However, in general, three different types of hybridization strategies can be used, summarized in **Figure 7**.

The redox-active material can be deposited onto the carbon material (**Figure 7B**) or it is synthesized inside a carbon shell (**Figure 7C**). Both strategies lead to particles with a core-shell architecture. Alternatively, nanoscopic fabrication methods can be used, which do not significantly change the shape and the porosity of the carbon particles by depositing thin layers or nanoparticles (**Figure 7D**).

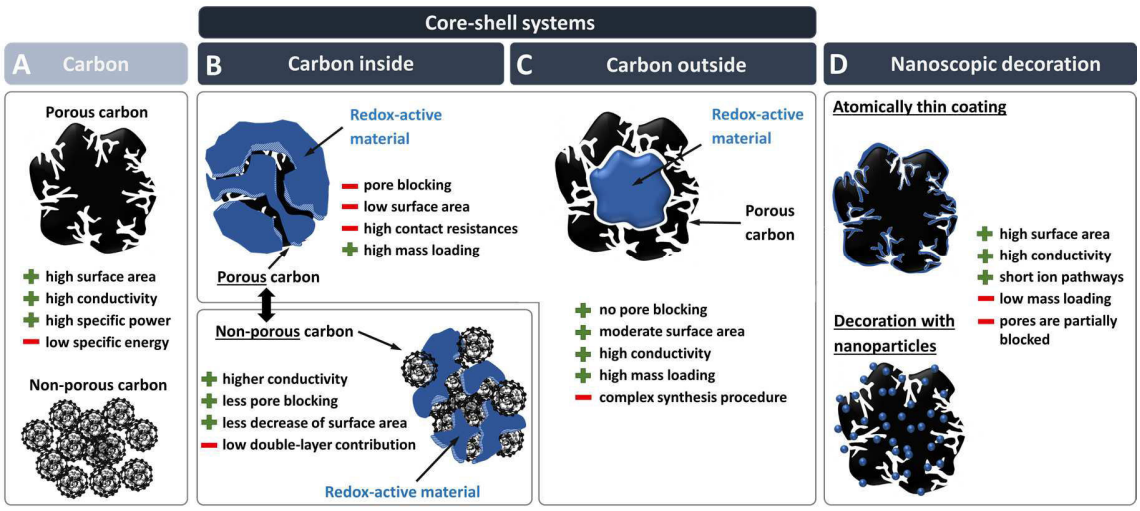

Figure 7: Hybridization strategies for carbon materials with redox-active compounds. (**A**) Ideal EDLC materials, such as porous activated carbons or carbon nanomaterials. (**B**) Coating procedures on endo- or exohedral carbons to achieve core-shell systems with carbon as core and the Faradaic material as shell. (**C**) Core-shell systems with porous carbon as shell and the Faradaic material as core. (**D**) Nanoscopic decoration of porous carbons using micro- and nanofabrication methods.

Wet chemical approaches or macroscopic methods with limited control over thickness and homogeneity can be used as easy and cheap deposition method to synthesize core-shell systems with a microporous carbon in the core (**Figure 7B**). With this, very high mass loadings of the redox-active material on carbon are possible, but this sacrifices the high SSA and high conductivity. Such coating procedures commonly cause pore clogging of the microporous carbon, which decreases the surface area and, in turn, the double-

layer contribution to a certain degree.[71] Furthermore, larger contact resistances are generated by non-conductive coatings. To overcome these severe disadvantages, advanced hybridization techniques with carbon as shell (**Figure 7C**), nanofabrication methods (**Figure 7D**), or different non-porous carbon supports can be used (**Figure 7B**). The latter is especially interesting because cheap and large-scale synthesis methods can be applied.

As shown in chapter 1.4.3, there exists a variety of carbon substrate materials. Since the surface area of porous or endohedral carbons can be significantly decreased by coating procedures, exohedral carbons with exclusive outer surface area might be more feasible (**Figure 7B**).[71, 89] In principle, all carbon nanomaterials can be used for this issue as they present no internal porosity, but a moderate external surface area combined with a very high conductivity[23, 55, 90]. Well-known examples are carbon nanotubes (CNTs)[91] and carbon onions[70] with SSAs up to 1000 m^2/g.

Although microporous carbons present much higher SSAs of more than 1500 m^2/g and their double-layer capacitance exceeds that of carbon nanomaterials by at least two-fold, the latter possibly demonstrates similar or even better properties as support for redox-active materials. The moderate SSA of carbon nanomaterials such as CNTs and carbon onions is generated by their morphology and their small size that results in a high surface-to-volume ratio. Any coating up to a certain thickness and loading follows the morphology of the carbon substrate without significantly reducing the SSA.[70, 71, 89, 92, 93]

Alternative coating procedures can partially prevent the pore blocking of porous carbon supports, for example microfabrication techniques like atomic layer deposition (ALD)[89, 94, 95] and nanoparticle deposition using sol-gel methods[96, 97] (**Figure 7D**). These deposition methods with high control and precision on the nanometer-scale can produce very thin coatings or nanoparticle deposits, even inside the pores to a certain degree. Even though the latter nanofabrication methods prevent pore blocking, the amount of loading is very limited. For this reason, core-shell systems, with the Faradaic material as core and the porous carbon as shell may overcome this issue (**Figure 7C**). Since the porous carbon covers the outside of the Faradaic material, the latter cannot block the carbon porosity. A highly conductive network is formed by the carbon shell which provides very high accessibility of the Faradaic core.[98]

2. Approach and Overview

As discussed in the previous chapter, there are several ways to hybridize carbon materials with redox-active compounds (**Figure 7**). Especially the choice of carbon material is crucial for the development of high performance hybrid electrochemical energy storage devices. The carbon interface controls the nucleation and phase formation of the deposited Faradaic material.[79] This directly influences the resulting surface area, the ion accessibility as well as the loading. Thus, carbon nanomaterials with exclusively outer surface area are very attractive supports for redox-active species, such as carbon nanotubes and carbon onions.[62, 71, 89]

In this PhD thesis, nanodiamond-derived carbon onions were investigated as support for pseudocapacitive materials as well as battery-materials (**Figure 7B**). An overview of the different topics is given in **Figure 8.** To achieve an optimum performance and an adequate interface, their synthesis and physico-chemical properties were studied, highlighted by two publications.[99, 100] In the first study the influence of the synthesis conditions such as annealing temperature and time on the resulting SSA and PSD were studied.[99] This was completed by a second study, in which the influence of the annealing atmosphere, vacuum or argon flow, on the resulting physical and electrochemical properties was investigated (**Figure 8**).[100]

Since carbon onions were already used in supercapacitors for several years, a comprehensive review has been published. The topics range from nomenclature, the differences between carbon onion types, to the physico-(electro)chemical properties of nanodiamond-derived carbon onions in detail. The latter is mainly used as support for a variety of pseudocapacitive materials such as transition metal oxides and battery-like surface functional groups, which were critically compared and discussed (**Figure 8**).[70] The most common pseudocapacitive material in literature is manganese oxide.[101, 102] There exist hundreds of publications about different manganese oxides, as thin films,[103] as coatings on carbon nanomaterials,[101] and as deposits on activated carbons[104]. So far, the influence of the carbon substrate was not systematically studied in terms of microstructural and morphological influences. In our publication, we have investigated the influence of the degree of carbon ordering, for example rather

amorphous compared to partially graphitic, and the difference between endohedral and exohedral carbons. For this, nanodiamond (ND)-derived carbon onions were chosen since they can be synthesized with varying degree of graphitization. They were coated with MnO_2 in a hydrothermal syntheses and compared to activated carbon substrates (**Figure 8**).[71]

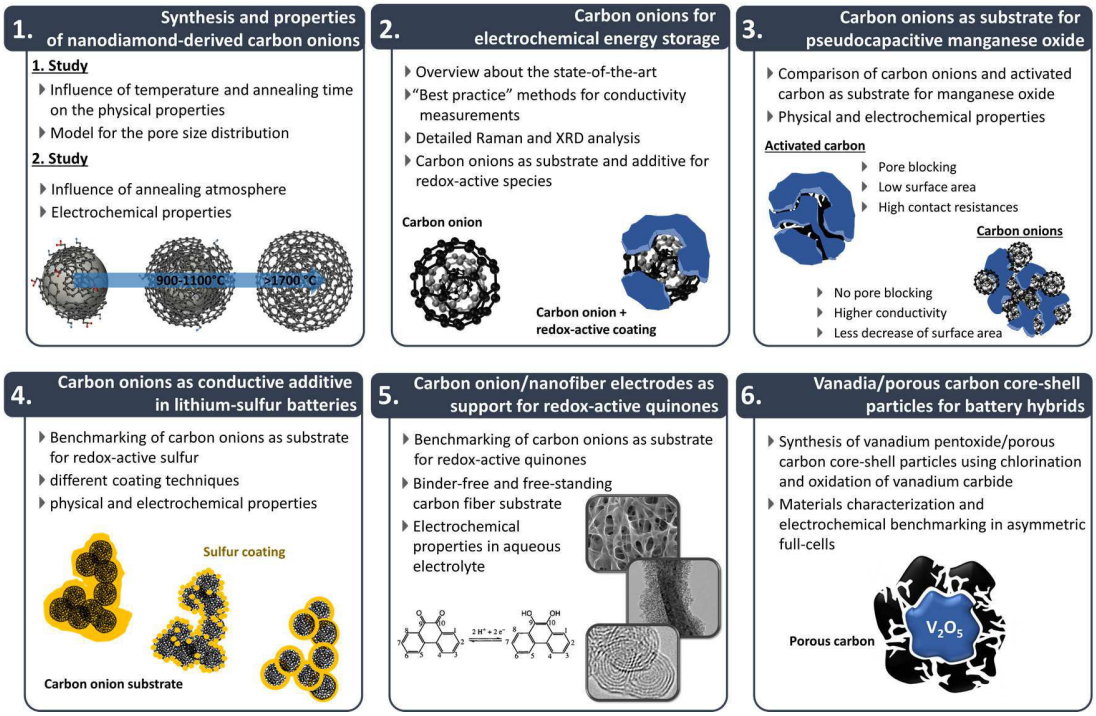

Figure 8: Overview about the different topics and chapters.

The use of carbon onions in battery-applications was exemplarily shown as sulfur support for lithium-sulfur batteries[93] and as substrate for quinone surface functional groups[62]. In the latter study carbon onions were additionally combined with a free-standing and highly conductive carbon fiber network (**Figure 8**).

However, dependent on the material architecture and the hybridization, also endohedral porous carbons can be used. For example using a core-shell manner with the Faradaic material in the core. This kind of hybridization was investigated using vanadium pentoxide as core and carbide-derived carbon as shell. The resulting battery-like electrochemical response of the vanadia was efficiently combined with the high surface area carbon (**Figure 8**).[98]

3. RESULTS AND DISCUSSION

3.1 Understanding structure and porosity of nanodiamond- derived carbon onions

Marco Zeiger,[1,2] Nicolas Jäckel,[1,2] Mesut Aslan,[1] Daniel Weingarth,[1] and Volker Presser[1,2]

[1] INM - Leibniz Institute for New Materials, Campus D2 2, 66123 Saarbrücken, Germany
[2] Saarland University, Campus D2 2, 66123 Saarbrücken, Germany

Citation:
Zeiger, M.; Jäckel, N.; Aslan, M.; Weingarth, D.; Presser, V., Understanding structure and porosity of nanodiamond-derived carbon onions. *Carbon* **2015,** 84, 584-598. (https://doi.org/10.1016/j.carbon.2014.12.050)

Own contribution: Design, planning, writing, synthesis, Raman spectroscopy, Scanning-, and Transmission electron microscopy, EDX analysis, Particle size measurements, zeta potential measurements, helium gas pycnometry.

Abstract

Carbon onions derived by thermal annealing of nanodiamonds are an intriguing material for various applications that capitalize the nanoscopic size, high electrical conductivity, or moderately high external surface area. Yet, the impact on synthesis conditions and possible post-synthesis treatment on the pore characteristics lacks a detailed parametric understanding. We present a comprehensive model describing the change of structure, morphology, specific surface area (SSA), and pore size distribution (PSD) of carbon onions derived via thermal annealing of nanodiamonds as a function of synthesis parameters and the effect of physical activation in air. Different heating rates, temperatures, holding times, as well as two different nanodiamond precursors were used. During thermal annealing the increase in SSA occurs along with a loss of surface functional groups and volatile impurities. The sp^3-to-sp^2 conversion results in a much lower density and an increase in SSA of up to ~160%. At high temperatures, a sintering and carbon redistribution process limits the increase in SSA and leading to the formation of micrometer-sized graphitic particles with a very low SSA. Oxidation in air is a facile way for the effective removal of predominately amorphous carbon between carbon onion particles and the removal of outer carbon shells.

CARBON 84 (2015) 584–598

Available at www.sciencedirect.com

ScienceDirect

journal homepage: www.elsevier.com/locate/carbon

Understanding structure and porosity of nanodiamond-derived carbon onions

Marco Zeiger [a,b], Nicolas Jäckel [a,b], Mesut Aslan [a], Daniel Weingarth [a], Volker Presser [a,b,*]

[a] INM – Leibniz Institute for New Materials, Campus D2 2, 66123 Saarbrücken, Germany
[b] Saarland University, Campus D2 2, 66123 Saarbrücken, Germany

ARTICLE INFO

Article history:
Received 10 August 2014
Accepted 16 December 2014
Available online 23 December 2014

ABSTRACT

Carbon onions derived by thermal annealing of nanodiamonds are an intriguing material for various applications that capitalize the nanoscopic size, high electrical conductivity, or moderately high external surface area. Yet, the impact on synthesis conditions and possible post-synthesis treatment on the pore characteristics lacks a detailed parametric understanding. We present a comprehensive model describing the change of structure, morphology, specific surface area (SSA), and pore size distribution (PSD) of carbon onions derived via thermal annealing of nanodiamonds as a function of synthesis parameters and the effect of physical activation in air. Different heating rates, temperatures, holding times, as well as two different nanodiamond precursors were used. During thermal annealing the increase in SSA occurs along with a loss of surface functional groups and volatile impurities. The sp^3-to-sp^2 conversion results in a much lower density and an increase in SSA of up to ~160%. At high temperatures, a sintering and carbon redistribution process limits the increase in SSA and leading to the formation of micrometer-sized graphitic particles with a very low SSA. Oxidation in air is a facile way for the effective removal of predominately amorphous carbon between carbon onion particles and the removal of outer carbon shells.

1. Introduction

Carbon onions, also known as onion-like carbon (OLC), are a relatively young addition to the family of carbon nanomaterials: they were first discovered by Iijima in 1980 [1] and described by Ugarte in 1992 [2]. OLCs are spherical carbon nanoparticles, but unlike fullerenes [3,4] they consist not of just one but of several concentric stacks of graphene-like carbon shells. Depending on the synthesis method and processing parameters, the size of carbon onions may range from around 2–50 nm [5,6]. So far, carbon onions have been synthesized by several techniques, such as arc discharge [7–9], electron beam irradiation [2,10], catalytic decomposition of carbon-containing precursors [11–14], heat treatment of nanodiamonds [15–17], mechanical milling [18], carbon ion beam implantation [19,20], and detonation reactions [21]. Due to their nanoscopic size and facile fabrication, carbon onions have attracted significant interest for various applications, such as a conductive additive [22], solid state lubricant [23], field emitters [24,25], in polymer composites for electromagnetic shielding [26], or as electrode material for supercapacitors with high power density [5,27].

Nanodiamonds [28] are an intriguing precursor for the gram-scale synthesis [29] of carbon onions with high level

* *Corresponding author at:* INM – Leibniz Institute for New Materials, Campus D2 2, 66123 Saarbrücken, Germany.
E-mail address: volker.presser@inm-gmbh.de (V. Presser).
http://dx.doi.org/10.1016/j.carbon.2014.12.050
0008-6223/

of control over the resulting structure and properties via thermal annealing [27]. The typical size of nanodiamonds used for OLC synthesis is around 5 nm [28] with dangling bonds on the surface that are typically stabilized by functional groups, mostly carboxyls [28,30], and locally terminated by a thin layer of sp^2-hybridized carbon [31–33]. These two surface features contribute to the notorious aggregation of individual nanodiamond particles forming clusters in the range of tens to hundreds of nanometer [34]: individual grains are engulfed by thin layers of graphitic carbon or covalently linked by bridging functional groups [28,34], leading to the formation of so-called tight agglomerates. In addition, a significant mass of each nanodiamond grain is not related to carbon but to nitrogen, oxygen, and hydrogen, and we often find metal impurities such as iron, silver, or copper [28].

Studies on the synthesis of carbon onions from nanodiamonds indicate that the sp^3-to-sp^2 transformation starts at around 600 °C by forming amorphous carbon [35]. At temperatures between 900 and 1100 °C, this amorphous layer progressively graphitizes and continuing sp^3-to-sp^2 transformation protrudes from the outside to the core of the particles [36]. Transmission electron microscopy (TEM) investigations have shown that smaller particles can be transformed to sp^2-hybridized carbon more readily resulting in a possible coexistence of small carbon onions with larger, partially transformed nanodiamonds [15,37,38]. In addition, the presence of surface functional groups significantly influences the onset temperature of the nanodiamond-to-OLC conversion [38].

The reconstructive phase transition from nanodiamond to OLC brings along a dramatic change in the crystal structure and the unique feature of radially bent lattice planes. As shown by X-ray diffraction (XRD) and Raman spectroscopy studies, the degree of graphitization increases with higher temperatures due to the higher ordering of the carbon shells into graphitic carbon [17,39–41]. On a single particle level, the transformation causes a significant increase in volume because of the much larger (002)-plane spacing of graphitic carbon (0.344 nm; extending radially from the center of the onions) compared to the initial C—C bonding distance of diamond (0.154 nm). This strain-buildup also results in the occurrence of d-spacings much smaller than 0.344 nm near the core of carbon onions [39]. The expansion depends on the sp^3-to-sp^2 ratio and an increase in diameter from around 5 nm up to 10 nm has been observed experimentally by TEM [39] and calculated with reactive force field modeling [37]. A broad overview about the mechanism of phase transition from nanodiamond to carbon onions, as well as the kinetics and the influence of the precursor, is given in Ref. [42].

The specific surface area (SSA) of nanodiamonds and carbon onions depends on the interplay between particle size and density, as typical for non-porous materials. Thus, along with the increase in particle diameter during the sp^3-to-sp^2 transition, there is also a severe decrease in density, and consequently the SSA increases significantly [15]. Yet, at high temperatures (>1800 °C), carbon onions start sintering which ultimately gives raise to the formation of tight agglomerates [39]. This process is promoted by the evolution of reactive gases originating from surface functional groups leading ultimately to the formation of large polyhedral crystals [43]. The final SSA depends on the synthesis conditions and ranges commonly between 200 and 600 m^2/g [5,27,44]. These SSA values are low compared to many porous carbons, such as activated carbon with typically 1200–1800 m^2/g [45].

Many applications, especially in the field of electrochemistry, are dependent on the pore size distribution (PSD) and ultimately limited by the surface area; hence, efforts have been made to increase the SSA of carbon onions. The main strategy to increase the SSA is related to chemical activation, for example per use of H_2SO_4/HNO_3 or KOH mixtures, yielding up to ~820 m^2/g SSA [46,47] and also physical activation using oxidation in air has been proposed [48]. Yet, albeit numerous studies on sp^3-to-sp^2 transition of nanodiamonds to carbon onions and different post-modification processes, we still have a very limited understanding of the quantitative correlation of density, SSA, and correlated PSD.

The purpose of this paper is to investigate the sp^3-to-sp^2 transition of two nanodiamond precursors with different initial surface area and particle size and the influence of oxidation in air from a morphological and pore structure point of view. A more detailed understanding is needed to specifically tune the properties of carbon onions to different applications, for example in the field of electrochemical energy storage. Therefore, this study investigates in detail the effect of the synthesis conditions and post-synthesis treatment on the properties which has not been done so far in the same extend. In detail, we investigate the influence of synthesis parameters such as annealing temperature, holding time, and heating rate in argon and the post-modification in air on the SSA and PSD. In addition to the sp^3-to-sp^2 transition, our focus remains with physical activation which, compared to chemical activation, has the benefit of being easier to scale and does not involve post-activation washing of the carbon material.

2. Experimental section

2.1. *Thermal annealing of nanodiamonds and physical activation of carbon onions*

To obtain carbon onions, nanodiamond powders were placed in graphite crucibles (30 mm × 20 mm) and thermally annealed in a water cooled high temperature furnace with tungsten heaters (Thermal Technology, USA) in argon (purity 4.6) with a flow rate of 1.3 L/min at 0.1 MPa. Before and after the thermal treatment, the mass of the samples was measured with a microbalance. Two heating rates, namely 5 and 20 °C/min, were used while the cooling rate for all procedures was 15 °C/min. The holding temperatures were 800, 900, 1100, 1300, or 1700 °C with holding times of 1, 3, or 10 h.

Two nanodiamond precursors were used, in the following named ND1 and ND2. ND1 (PlasmaChem, Germany) was supplied in a 5 mass% water dispersion which was freeze-dried in liquid nitrogen (Dieter Piatkowski Forschungsgeräte, Germany) prior to thermal treatment. The supplier used a post-synthesis treatment to produce a dispersion composed of so-called single-digit nanodiamonds fully dispersed and deagglomerated in water with an average aggregate size of 5–15 nm and a SSA of 350–390 m^2/g. ND2 (NaBond

Technologies, China) was supplied as a powder consisting of non-modified nanodiamonds with a SSA of 283 m^2/g and a mean primary particle size of 4–6 nm.

Carbon onions were oxidized in air (i.e., physical activation) to increase the surface area. The samples were placed in Al_2O_3 crucibles (30 mm × 60 mm) and heated under semi-isothermal conditions in a furnace (Nabertherm, Germany) in ambient air at 535 °C for 1 h. These conditions yielded as outlined in the experimental section an insignificant change in SSA and was used to precondition the sample material. After, the samples were semi-isothermally annealed at 575 °C for 15, 30, or 60 min. Semi-isothermal means that the holding temperature was reached before the sample was placed in the furnace. During sample insertion the temperature dropped by ~5% and reached the end temperature again after ~2 min.

The nomenclature of the samples includes the name of the nanodiamond precursor, the temperature, and the post-modification process. For example, "ND2-1300"or "ND2-1700" describe carbon onions derived from ND2 in argon at 1300 or 1700 °C, respectively, for 1 h and a heating rate of 20 °C/min. "ND2-1300-air60" denotes air oxidation at 575 °C for 60 min starting with ND2-1300 that was subject to pre-conditioning at 535 °C in air for 1 h as outlined before.

2.2. Chemical and structural characterization

2.2.1. Chemical composition of the precursors

The chemical composition of the nanodiamond powders was determined with CHNS element analysis, inductively-coupled plasma optical emission spectroscopy (ICP-OES), and energy-dispersive X-ray analysis (EDX). CHNS analysis was performed with a vario Micro Cube system (Elementar Analysensysteme GmbH, Germany) after sample combustion under oxygen at 1150 °C in a tin sample holder. Calibration of the CHNS analyzer was carried out with sulphanilic acid of different initial masses as provided by the system manufacturer (41.6 mass% C, 4.1 mass% H, 8.1 mass% N, 18.5 mass% S). ICP-OES measurements were done with an Ultima 2 system (Horiba Jobin–Yvon, France) with a Czerny–Turner type monochromator having a focal length of 1 m. High frequency power of 1 kW was supplied by a regulated generator at 40.68 MHz. Table S1 in the Supporting Information shows the parameters used for ICP-OES measurements. Prior to the separate analysis for each element, a screening was performed to analyze which impurities are present in the sample. Calibration was performed using aqueous standard solutions of 0, 1.0, and 2.0 mg/L yielding a calibration coefficient of 0.999. Approximately 50 mg of sample material was diluted to a total volume of 25 mL.

EDX spectra of nanodiamond powder samples were measured using a JSM-7500F (JEOL, Japan) scanning electron microscope equipped with an EDX system (Thermo Fisher Scientific, USA). Samples were placed on a conductive carbon tape and spectra were recorded at 5 different positions for each sample with 10 kV acceleration voltage.

2.2.2. Particle size and zeta potential analysis

The particle size was measured using centrifugal sedimentation analysis (LUMiSizer; LUM Corporation, USA). The powder was dispersed in water (5 mass%), sonicated at ~4 W for 1 h, and tested in a range from 1000 to 4000 rpm. Several dilutions were made to eliminate the influence of the starting transmission.

The zeta potentials were measured with a Malvern Zetasizer Nanosizer Nano-Z (Malvern, UK) in distilled water (10 ppm dispersion). The used zeta cuvettes were disposable capillary cells (DTS1070, Malvern, UK). Each measurement was repeated three times with an acquisition time of 30 s.

2.2.3. Electron microscopy

Scanning electron microscope (SEM) images were recorded with a FEI Versa 3D Dual Beam (FEI Company, USA) at 10 kV. Powder samples were mounted on steel sample holders with adhesive carbon tape. All measurements with a transmission electron microscope (TEM) were carried out on a 2100F microscope (JEOL, Japan) operating at 200 kV. Samples were prepared by dispersing powders in ethanol and drop casting them on a copper grid with a lacey carbon film (Gatan, USA). For that, sample powders were first tip sonicated in ethanol for 5 min to perform a homogenous drop casting.

2.2.4. Raman spectroscopy

Raman spectra were recorded with a Renishaw in via Raman Microscope using an Nd-YAG laser with an excitation wavelength of 532 nm, a grating with 2400 lines/mm, a 50× objective (numeric aperture: 0.9), and a spectral resolution of ~1.2 1/cm. The spot size on the sample was in the focal plane ~2 μm using an output power of 0.2 mW. The acquisition time was 10 s and 50 accumulations were used to eliminate cosmic rays and to improve the signal-to-noise ratio. Peak analysis and peak fitting was performed assuming one Lorentzian peak for each the D- and the G-mode to enable comparability with literature values. The background was subtracted using a linear baseline function. Only OLC was subject to Raman spectroscopy since nanodiamonds require UV laser radiation for a comprehensive characterization of sp^3-hybridized carbon nanodomains.

2.2.5. X-ray diffraction

X-ray diffractograms (XRD) were recorded using Cu-Kα radiation with a Bruker AXS D8 Advance diffractometer (Bruker AXS, Germany). The step size was 0.02° and the measurement time was 1 s/step. Prior to the measurements, the system was calibrated with a LaB_6 single crystal.

2.2.6. Helium gas pycnometry and gas sorption analysis

Pycnometric densities of the nanodiamond precursor and the carbon onion samples were determined with a AccuPyc 1330 gas pycnometer (Micromeritics, Germany) using helium gas (purity grade: 5.0). To decrease the influence of adsorbed water, all samples were dried in an oven at 120 °C and 1 kPa for 1 h. The sample holder had a maximum volume of 1 cm^3 and the pycnometer was programmed to perform 10 purges, followed by an analysis of 20 separate measurements. Both purge and analysis fill pressures were set at 134 Pa and an equilibration rate of 34 Pa/min was used.

Gas sorption analysis was carried out using an Autosorb iQ system (Quantachrome, USA). Prior to the measurements, the

powder samples were outgassed at 300 °C for 10 h under vacuum conditions (10^2 Pa). Nitrogen gas sorption was performed at −196 °C in the relative pressure range from $5 \cdot 10^{-7}$ to 1.0 in 68 steps. The pore size distribution (PSD) between 0.56 and 37.5 nm was derived using the quenched-solid density functional theory (QSDFT) [39,40] supplied by Quantachrome assuming a slit shape pore geometry. The latter has recently been shown to be the most appropriate model for carbon onions [49]. The SSA using the BET equation after Brunauer–Emmett–Teller [41] was calculated in the linear regime of the measured isotherms at a partial pressure range between 0.1 and 0.3 P/P_0.

Carbon dioxide gas sorption measurements were carried out at 0 °C in the relative pressure range from $1 \cdot 10^{-4}$ to $1 \cdot 10^{-2}$ in 40 steps. SSA and PSD were calculated for pore sizes between 0.3 and 1 nm with the ASiQwin software using non-local density functional theory (NLDFT) [50,51]. Values for the total ultramicropore volume (pore size <0.7 nm) correspond to $P/P_0 = 5 \cdot 10^{-3}$.

In general, the SSA of powders consisting of mono dispersed spherical particles with the density ρ, and the particle size d can be calculated by Eq. (1):

$$\mathrm{SSA} = \frac{6}{\rho \cdot d} \tag{1}$$

The ideal SSA of spherical carbon onions ($\mathrm{SSA_{OLC}}$) derived from nanodiamonds with a surface area of $\mathrm{SSA_{ND}}$ should rather be calculated using Eq. (2):

$$\mathrm{SSA_{OLC}} = \mathrm{SSA_{ND}} \left(\frac{\rho_{\mathrm{ND}}}{\rho_{\mathrm{OLC}}}\right)^{2/3} \tag{2}$$

Taking mass losses into account, the SSA of the OLC can be calculated using Eq. (3):

$$\mathrm{SSA_{OLC}} = \mathrm{SSA_{ND}} \left(\frac{\rho_{\mathrm{ND}}}{\rho_{\mathrm{OLC}}}\right)^{2/3} \left(\frac{m_{\mathrm{ND}}}{m_{\mathrm{OLC}}}\right)^{1/3} \tag{3}$$

with ρ as the density of nanodiamond (ND) or carbon onions (OLC) and m the mass, respectively.

2.2.7. *Thermogravimetric analysis coupled with mass spectrometry*

In order to detect the gases produced during the synthesis of OLCs, a thermogravimetric analysis coupled with mass spectrometry was performed with a Jupiter 449 C STA system and a quadrupole mass spectrometer QMS 403 C (Netzsch-Gerätebau, Germany). ND1 and ND2 samples were heated to 1500 °C in argon (purity grade 6.0) with a heating rate of 20 °C/min and then cooled down to room temperature at 15 °C/min. The mass loss and the released gas fragments were measured.

3. Results and discussion

3.1. *Structure, morphology, and chemical analysis of nanodiamond*

Both types of nanodiamonds used for this study show the typical diamond (1 1 1) related d-spacing of 0.26 nm in the center of the particles and disordered, amorphous carbon engulfing the sp^3-hybridized core (Fig. 1). TEM investigations show a somewhat smaller primary particle diameters for ND1 of around 4–6 nm compared to ND2 with 5–7 nm. This

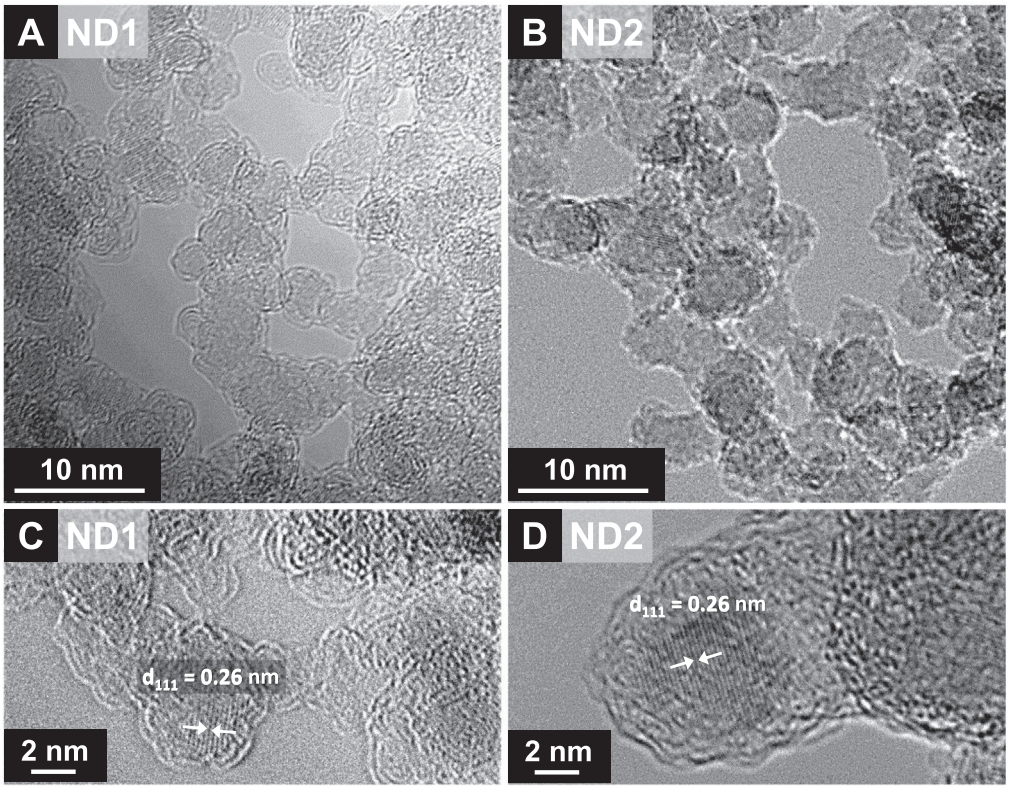

Fig. 1 – Transmission electron micrographs of nanodiamonds. (A, C) ND1 and (B, D) ND2.

Table 1 – Chemical composition of the nanodiamond precursors measured via CHNS, ICP-OES, and EDX analysis. N.A. denotes values below the detection limit.

Element	ND1 (mass%)	ND2 (mass%)	Method
Ag	N.A.	0.083	ICP-OES
Al	N.A.	0.2 ± 0.2	EDX
B	0.012	0.054	ICP-OES
C	76.97	89.92	CHNS
	77.7 ± 6.2	90.2 ± 2.9	EDX
Ca	0.014	0.013	ICP-OES
Cl	0.7 ± 0.5	0.8 ± 0.3	EDX
Fe	0.05	0.154	ICP-OES
H	1.286	1.434	CHNS
N	2.141	2.336	CHNS
	3.9 ± 1.2	5.6 ± 3.5	EDX
Na	0.315	1.024	ICP-OES
	N.A.	1.9 ± 1.3	EDX
O	19.4 ± 6.9	3.4 ± 1.9	EDX
S	N.A.	N.A.	CHNS

observation aligns well with the higher BET specific surface area of ND1 (353 m^2/g) compared to ND2 (279 m^2/g); yet, we will later adopt a more detailed discussion on the differences between ND1 and ND2 to fully understand why the SSA values differ so strongly (i.e., by 27%). In both cases, the isotherms of nanodiamond show a characteristic type II shape with a small H3 hysteresis loop (see Supporting Information, Fig. S1A) following the nomenclature in Ref. [52].

Besides the size difference, both nanodiamond powders also show a different density determined with helium gas pycnometry with 2.70 ± 0.01 g/cm^3 for ND1 and 3.31 ± 0.02 g/cm^3 for ND2. The much lower density of ND1 can be correlated with a higher amount of oxygen-containing surface functional groups as confirmed by elemental analysis (Table 1) and the carbon content of ND2 (89.92 mass%) is much higher than for ND1 (76.97 mass%). Yet, the content for metal impurities, nitrogen, and hydrogen are similar for both. Thus, using Eq. (1), we derive a SSA of 370–556 m^2/g for a particle size of 4–6 nm (ND1) and 259–363 m^2/g when assuming 5–7 nm (ND2). These values show qualitatively a comprehensive trend, but a more detailed analysis is needed on a quantitative level as outlined in the next paragraph.

The BET SSA is also influenced by the formation of tight agglomerates. As seen from TEM (Fig. 1), both types of nanodiamond form such agglomerates which are covered and connected by amorphous or graphene-like layers. These layers are highly defective and form aggregates ranging from ~20 nm to several micrometers [53]. After detonation synthesis usually all types of nanodiamonds form tight agglomerates. In the case of ND1 the supplier used a post-synthesis treatment to fully de-agglomerate the particles producing a stable dispersion in water. Using centrifugation sedimentation analysis, we found a monomodal particle size distribution for ND1 below 10 nm, whereas ND2 exhibits a broad distribution pattern ranging from 10 to 1000 nm (Fig. 2; see also Supporting Information Fig. S2). We see that although different in sign, both solutions should be stable due to the large zeta potential for ND1 of −52.4 ± 0.9 mV and for ND2 of +39.7 ± 0.5 mV at pH = 6.4. Thus, the smaller BET SSA of ND2 is a result of combined effects: slightly larger size, higher density, and stronger agglomeration compared to ND1.

3.2. *Structural characterization of carbon onions*

3.2.1. *Electron microscopy and X-ray diffraction*

Thermal annealing of nanodiamond yields the well-known formation of OLC as evidenced by X-ray diffraction (see Supporting Information, Fig. S3). TEM investigations show concentric stacks of (002)-planes of graphitic carbon as typical for carbon onions (Fig. 3). ND1-1700 (Fig. 3A) and ND2-1700 (Fig. 3B) exhibit similar structures but with the presence of a very sharp peak at 25.7 (2θ) indicating larger graphitic structures for ND1-1700 compared to ND2-1700 (see Supporting Information, Fig. S3). The carbon onions of either precursor consist of 2–8 shells with an interlayer spacing of 0.34 nm for the outer shells. The particle size for ND2-OLC is in the order of 5–10 nm whereas for ND1 smaller carbon onions of 4–8 nm are observed. At lower synthesis temperatures (Fig. 3C), we see a larger amount of amorphous carbon

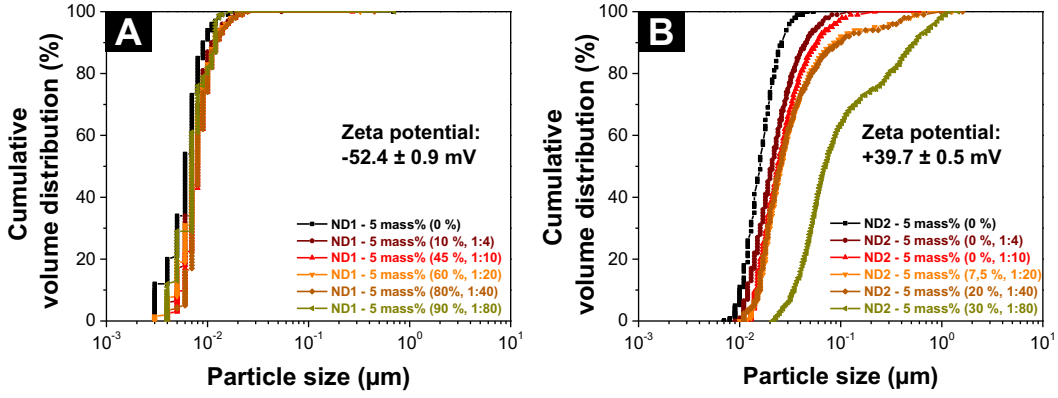

Fig. 2 – Cumulative particle size distribution measured with centrifugal sedimentation analysis in water. (A) ND1 and (B) ND2. The concentration was 5 mass% and different dilutions from 1:4 to 1:80 were measured resulting in different starting transmission between 0% and 90%. The displayed zeta potentials were determined in a 10 ppm water dispersion. (A color version of this figure can be viewed online.)

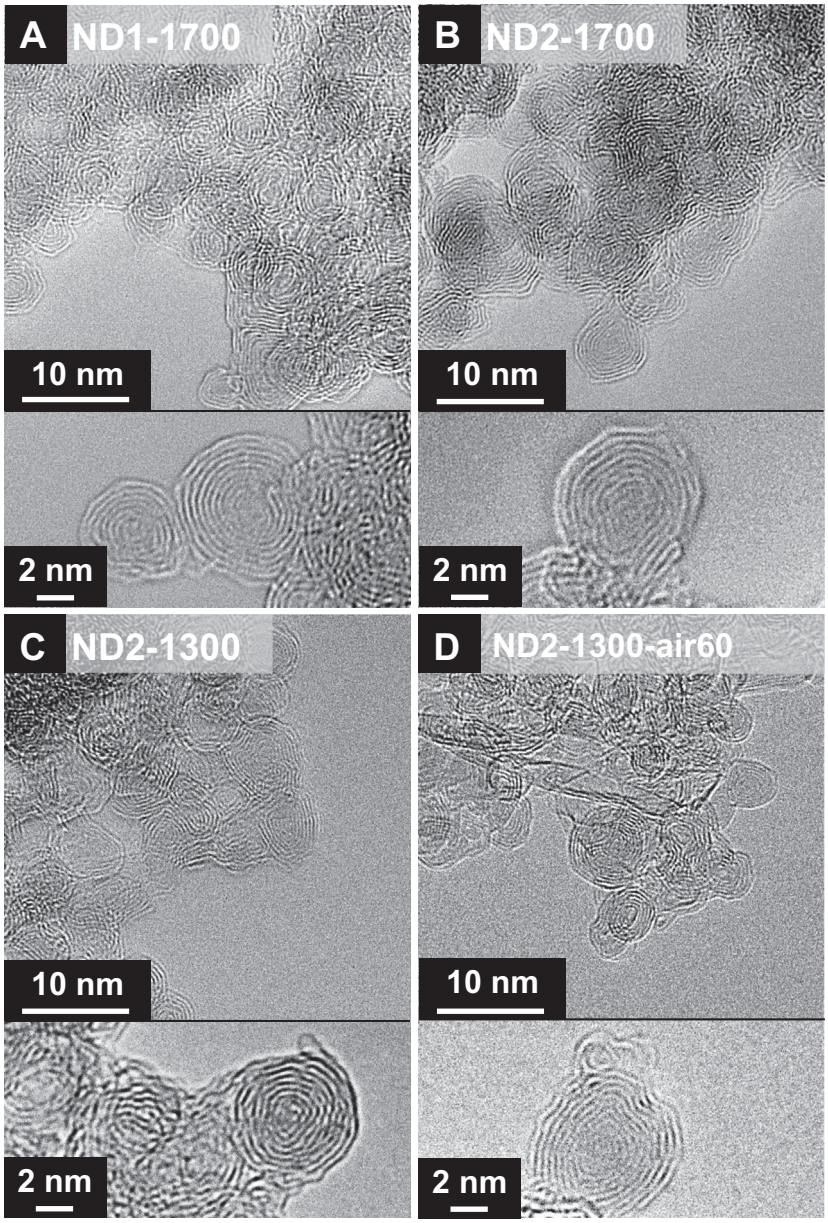

Fig. 3 – Transmission electron micrographs of (A) ND1-1700, (B) ND2-1700, (C) ND2-1300, and (D) ND2-1300-air 60.

especially at the necks between individual carbon onions; these interparticle bottlenecks are severely reduced at higher annealing temperatures (Fig. 3B) or when applying air oxidation on OLCs synthesized at only 1300 °C (Fig. 3D). Beyond the decreased level of necking, oxidation in air at 575 °C of up to 1 h seemingly leads to an effective removal of the outer shells and accordingly to a rearrangement of loose graphene-like sheath layers between the carbon onions (Fig. 3D).

For ND1 annealed at 1700 °C using a holding time of 1 h and a heating rate of 20 °C/min (ND1-1700), we also observed the emergence of large flake-like structures of around 1 μm (Fig. 4A). TEM shows that these samples are highly ordered with a typical lattice spacing of 0.344 nm along the *c*-direction of graphite crystals (Fig. 4B and C). The structures consist of stacks of parallel graphitic layers which are terminated in the basal plane by onion-like caps with a diameter of *ca.* 4 nm corresponding to 3–4 shells (Fig. 4B). Perpendicular, we only see continuing stacks of parallel graphite layers (Fig. 4C). Such features are known from carbon fibers annealed at temperatures in excess of 2000 °C and commonly referred to as herringbone structure [54]. The drastic change from nanoscopic to microscopic size and the complete loss of the spherically bent lattice planes must be the result of extensive sintering and carbon redistribution. In Section 3.2.4 we will establish that this transition is accompanied by a dramatic loss of surface area.

3.2.2. *Raman spectroscopy*

The Raman spectra of all OLCs samples show D- and G-modes characteristic of partially-graphitic carbon between 1200 and 1700 1/cm and a well-pronounced range of overtones and combinational modes between 2300 and 3400 1/cm (Fig. 5A).

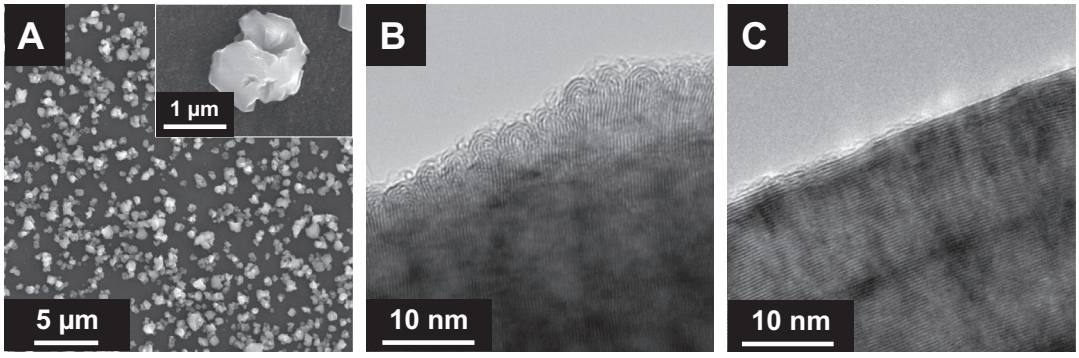

Fig. 4 – Scanning electron microscope image (A) and transmission electron micrographs (B and C) of graphite flakes derived from annealing of ND1 at 1700 °C (ND1-1700).

The G-mode at ~1585 1/cm is characteristic for sp^2-hybridized carbon and is a first-order peak with E_{2g}-symmetry [55]. The D-mode at ~1345 1/cm corresponds to defects and disorder induced phonon transitions [56] with its overtone, 2D, at ~2690 1/cm [57] activated via double-resonance of phonons at the K-point in the Brillouin zone [58]. Noticeably, the I_D/I_G ratio of OLC synthesized at low temperatures (800–900 °C) is rather low (1.5–1.6), increases at 1100 °C to 2.0–2.4, and decreases again for temperatures up to 1700 °C to around 1.2 (Fig. 5B). These trends are roughly identical for ND1- and ND2-derived carbon onions. The initial increase in I_D/I_G ratio can be explained by the model of Ferrari and Robertson [59] when we consider that we have at low temperatures first a thin layer of sp^2-hybridized carbon that, at higher temperatures, finally encompasses the entire nanodiamond particles. The Ferrari and Robertson model assumes two regions: below 2 nm, the I_D/I_G ratio increases with domain size approximately quadratic; only for values above 2 nm, the I_D/I_G ratio

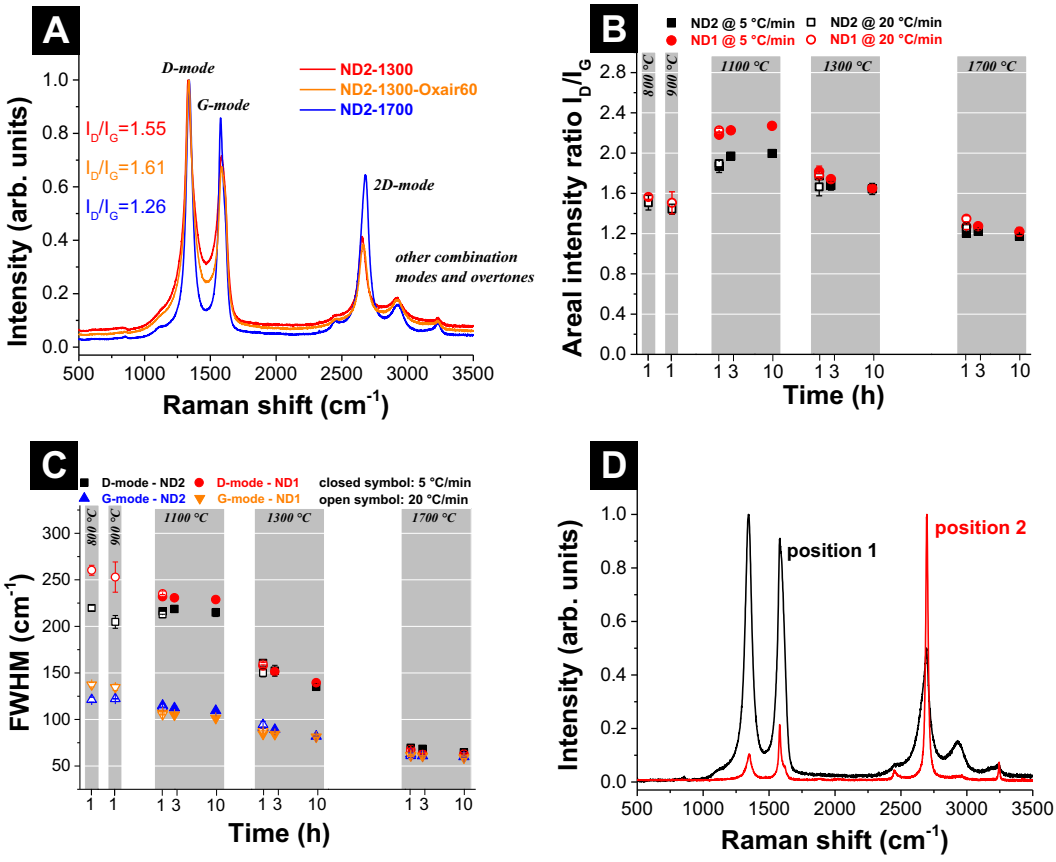

Fig. 5 – (A) Raman spectra of ND2-1300, ND2-1700, and ND2-1300-air60. (B) Areal intensity ratio of the D-peak and the G-peak derived from the Raman spectra of OLCs. (C) FWHM of the D-peak and the G-peak derived from the Raman spectra of OLCs. (D) Raman spectra on two different positions of ND1-1700. Position 1 belongs to the OLCs and position 2 to the large graphite flakes according to Fig. 4A. (A color version of this figure can be viewed online.)

of nanocrystalline graphite decreases with the reciprocal domain size according to the correlation first established by Tuinstra and Koenig [60]. The latter is also observed in the case of OLC: at temperatures of or above 1100 °C, the I_D/I_G ratio decreases constantly with annealing temperature [40,41,61–64]. These findings and conclusions are in agreement with the evolution of the full-width at half maximum (FWHM) of the D- and G-mode (Fig. 5C). There, we have a constant decrease in FWHM rather than an increase and subsequent decrease. This is consistent with the assumption that we have a constant enhancement in long-range ordering of graphitic carbon with higher annealing temperatures. We note that for the I_D/I_G ratio and FWHM, the annealing temperature is of higher importance than the actual annealing time.

Graphite flakes seen for ND1-1700 exhibit noticeable deviations from the typical Raman spectra for OLC discussed before (Fig. 5D). Spectra measured exactly on top of one graphite flake (position 2 in Fig. 5D) show a resonantly enhanced 2D-mode which has roughly 5-times the intensity of the G-mode with a very small I_D/I_G ratio of 0.98. These features are in agreement with Raman spectra of polyhedral graphite crystals [65]. The reason for the strong 2D-peak possibly comes from the arches (i.e., the specific layer-folded ends), that form coupled coherent states between the opposite carbon atoms which increases the double-resonant Raman effect [65,66]. In-between these graphite flakes carbon onions are found and the typical Raman spectrum of OLC particles is seen (position 1 in Fig. 5D).

Oxidation of carbon onions (ND2-1300-air60) does not yield dramatic changes in the Raman spectrum; however, we notice a smaller FWHM of both D- and G-mode of 86.0 and 75.1 1/cm after oxidation compared to 105.8 and 87.9 1/cm for ND2-1300. While the I_D/I_G ratio remains almost unchanged at around 1.6, the significant decrease in FWHM aligns well with the TEM observation of removed amorphous carbon at onion-onion necks (see Fig. 3D). In fact, if we would just decrease the size of carbon onions by removing layer by layer using physical activation, we would actually expect the FWHM to decrease [67].

3.2.3. *Skeletal density and mass change*

Raman spectroscopy of OLCs shows the proceeding graphitization by thermal annealing of ND. The conversion from ND to OLC results in a decrease in density investigated with helium gas pycnometry (Fig. 6A). As mentioned before, we derived a value of 2.70 g/cm^3 for ND1 and 3.31 g/cm^3 for ND2 with helium pycnometry. Thus, while the density of ND2 is very close to the theoretical density of diamond of 3.51 g/cm^3 [68], the density of ND1 is much lower. We have shown in Section 3.1 that this is related to the much larger amount of surface functional groups per the larger surface area of ND1. After annealing of up to 900 °C, the density of ND1-OLC barely increases compared to the nanodiamond material, whereas for ND2 we see a decrease by 18% to 2.73 g/cm^3. Since these temperatures are sufficient to remove oxygen surface groups and leave behind partially graphitic carbon, the resulting OLC nanoparticles are very comparable in structure (see Sections 3.2.1–3.2.2) and, thus, a very similar skeletal density can be rationalized. From 1100 to 1700 °C at 20 °C/min, the density continuously decreases to 1.95 g/cm^3 for ND1 and 1.77 g/cm^3 for ND2. No significant influence of the heating rate is observed. The mass loss upon inert gas treatment corresponds almost ideally with the measured amount of non-carbon atoms (Fig. 6B); hence, inert gas annealing achieves not only conversion of nanodiamond to carbon onions but also the effective removal of surface functional groups.

The slight increase in density after physical activation (stars in Fig. 6A) leads to important conclusions. In detail, we see a constant increase in ρ from ~2.1 g/cm^3 (ND2-1300) to ~2.6 g/cm^3 (ND2-1300-air60) as the oxidation progresses. The same trend can be seen for the activation of ND1-1300. First, if oxidation would merely remove carbon in a layer-by-layer fashion, hence making the particles effectively smaller, the density should increase, because the ratio of the outer graphitic carbon to the inner diamond core would decrease. The presence of diamond after annealing in argon at 1300 °C was shown using XRD (Fig. S3A). A smaller carbon onion might additionally reduce the density per expansion of the strained inner shells which is easier to accomplish with a lower number of carbon layers. The same increase in density would be measured if the outer amorphous carbon between onion-onion necks was removed after oxidation. Second, if the oxidation would create intraparticle pores, as suggested by Gao et al. (Ref. [47]), then the same would apply: the density should increase. However, the formation of intraparticle pores after oxidation is not supported by CO_2 gas sorption data (see Section 3.2.5). Yet, we see that the SSA dramatically increases during oxidation. This can only be explained by decreasing the particle size and the formation of interparticle pores, which means the removal of amorphous carbons at onion-onion necks (as seen in Fig. 3D) when we consider that the latter is typically characterized by a low density of 1.4–2.7 g/cm^3 [69]. The mass loss of oxidized OLC is not shown in Fig. 6B, because the values do not refer to the nanodiamond precursor but rather to ND2-1300. The mass loss for an oxidation at 535 °C for 1 h followed by an oxidation at 575 °C for 15 min was 8.3 ± 3.4 mass%, for 30 min 15.7 ± 2.5 mass%, and for 1 h 42.4 ± 5.1 mass% and is shown in Fig. S4B together with the BET SSA (Fig. S4A). The increase in SSA after activation of ND1-1300 follows the same trend as ND2-1300, but does not reach the same high values (Fig. S4A). The reason for the lower SSA after the same activation process is the smaller starting particle size of ND1-1300. This results in a larger mass loss (see Fig. S4B) due to a complete removal of the smaller particles and only partial activation of larger particles.

3.2.4. *Surface area and pore volume*

When transitioning from sp^3-to-sp^2-hybridization, we see an increase in total pore volume in the nitrogen sorption isotherms; yet, the latter still remain characteristic for non-porous nanoparticles with a type II shape and a slight H3 hysteresis loop (see Supporting Information, Fig. S1B). The SSA increases successively with annealing time and temperature up to 1300 °C and 10 h (Fig. 6C). In detail, the BET SSA further increases for 1300 °C up to 493 m^2/g for ND1 and 390 m^2/g for ND2. After these maximum values, we see that higher temperatures (1700 °C) lead to an enhanced decrease of surface area over annealing time which is stronger for ND1

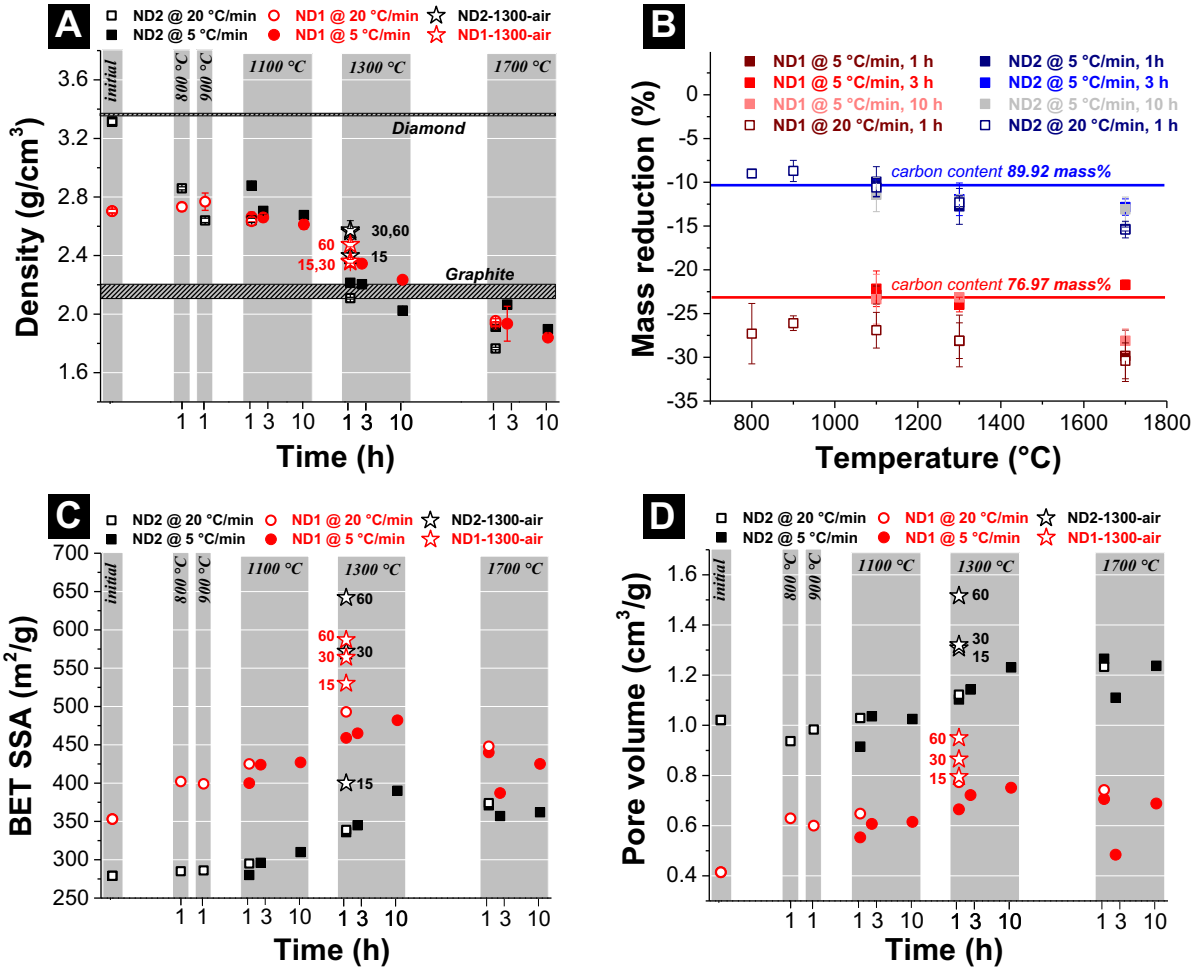

Fig. 6 – (A) Pycnometric densities of OLCs and nanodiamonds. (B) Mass losses of OLCs after the synthesis. (C) Measured BET SSAs from the nitrogen sorption isotherms for different OLCs derived from the nanodiamond precursors ND1, ND2, and after post-synthesis oxidation for different heating times. (D) Pore volumes of OLCs and nanodiamonds calculated using QSDFT and a slit-pore shape from the nitrogen sorption isotherms. The numbers for ND1-1300-air and ND2-1300-air indicate the oxidation times in minutes at 575 °C. (A color version of this figure can be viewed online.)

(380–450 m^2/g at 1700 °C) than for ND2 (350–380 m^2/g at 1700 °C). Noteworthy, all these trends are equally valid for the two heating rates 5 °C/min and 20 °C/min and the BET SSA of all OLC samples is higher than for the precursors ND1 and ND2 (see Supporting Information, Table S2). Similar trends are observed for the pore volume (Fig. 6D); here, however, the pore volume remains rather constant even for prolonged annealing at 1700 °C for both nanodiamond precursors. It is important to note that the pore volume cannot directly be derived from particle size and density as it depends on the particle–particle arrangement and pore geometry. This will be discussed in the next section related to the modeling of the pore size distribution.

After an initial mass loss because of the removal of impurities such as nitrogen or oxygen, the continuing change of SSA beyond 800 °C is related to the decrease in density. This can be seen when calculating the SSA as a parameter of density and initial surface area of ND1-800 and ND2-800 (Eq. (2)). It is important to note that for the calculation using Eq. (2) not the density and SSA of the nanodiamond is used. Both values have to be corrected for the amount of non-carbon surface groups and impurities. For that, we used OLC synthesized at 800 °C for 1 h. Once we have formed the first graphitic shell, one would not expect any further mass loss during the continuing isochemical sp^3-to-sp^2 transition. Systematically applying Eq. (2) to the measured data shows an excellent agreement between the actually measured SSA and the SSA which was calculated on the basis of the density and the initial surface area (all related to BET SSA; Fig. 7). Yet, two noticeable deviations from the parity line can be seen, corresponding to either sintering and carbon redistribution or etching and activation. Thus, we can postulate that as long as neither sintering nor activation occurs, we can assign the changes in surface area of carbon onions exclusively to the change in particle size and density. The parity plot in Fig. 7 is also calculated using the DFT SSA (Fig. S5A) and using Eq. (3) which takes into account the mass loss during heating. Both plots show the same qualitative result as demonstrated in Fig. 7 using Eq. (2) with the BET SSA and constant mass.

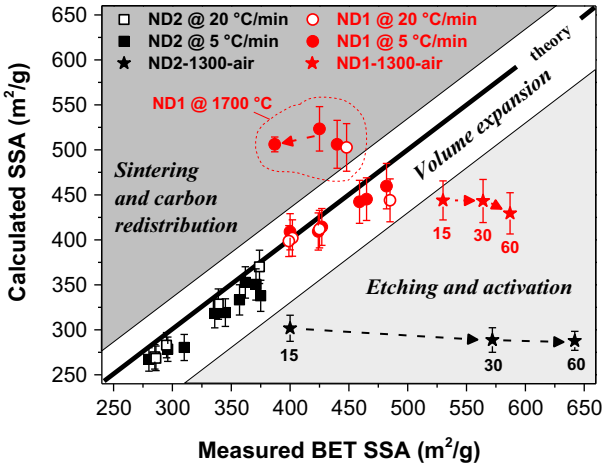

Fig. 7 – Parity plot showing the comparison between the measured BET SSAs of OLCs (*x*-axis) and the calculated SSAs using a volume expansion (*y*-axis). The numbers for ND1-1300-air and ND2-1300-air indicate the oxidation times in minutes at 575 °C. (A color version of this figure can be viewed online.)

A coherent group of data points deviating from the predicted line by showing a lower surface area belong to ND1 annealed at 1700 °C. In previous sections, we have established that this ND1-derived carbon onions exhibit unique graphite flakes; hence, a lower surface area aligns with the emergence of microscopic graphite structures which formation will be subject in Section 3.2.6. The other noticeable deviation occurs when the SSA of activated carbon onions using oxidation in air is underestimated by our prediction. The BET SSA and pore volume can be increased significantly by oxidation of ND2 at 575 °C for up to 1 h (Fig. 6C and D; see also Supporting Information Fig. S4). The longest oxidation treatment of ND2-1300 leads to a specific surface area of 642 m^2/g which is much higher than the highest SSA of any of the OLC annealing conditions with a maximum value of 390 m^2/g at 1300 °C. We also note that 642 m^2/g is much higher than the chemical activation by acid-treatment reported by Gu et al. (i.e., 578 m^2/g) [46] and, in percent of increase (i.e., +164%), is comparable to the KOH-activation reported by Gao et al. (i.e., ~440 $m^2/g \rightarrow$ 820 m^2/g =+186%) [47]. Additional surface area is created by removing outer shells and amorphous carbon preferably from the necks between single carbon onion particles; hence, the total surface area can increase without much structural change of the primary OLC particles.

3.2.5. *Pore size distribution*

Until now, we have limited our discussion to the structure and morphology of carbon onions and nanodiamonds, without accessing the actual pore size distribution. Yet, the latter is readily accessible via DFT deconvolution of the gas sorption data using CO_2 (for pores between *ca.* 0.3–1.0 nm) and N_2 (for pores between *ca.* 0.6 and 30 nm). In lack of a better model, we will assume slit-shaped pores that were recently shown by Weingarth et al. to be the best-fit model for carbon onions among currently available DFT models [49]. Spherical or cylindrical pore geometries are unsuitable to model the ogee-arch-like pores in-between carbon onion particles. As seen from the PSDs (Fig. 8) for ND2-derived OLC and activated carbon onions (ND2-1300-air60), pores are found that stretch from about 0.3 to 20 nm which represents the entire range that is accessible by this method. While the minimum in the NLDFT PSD data at around 0.7 nm for CO_2 sorption is related to a well-known mathematical artifact [70], we see two noticeable distribution maxima in the QSDFT data range from N_2 sorption experiments (Fig. 8B). These two ranges, one centered at around 1 nm and the other one ranging from 3 to 20 nm, were previously attributed to interparticle and intercluster pores, respectively [27,71]. Yet, this aspect deserves a more thorough investigation and quantitative substantiation.

For a better understanding of the pore size distribution we developed a series of geometric pore models (Fig. 9). The pore width depending on the particle size is calculated using primitive cubic, body-centered cubic (bcc), and face-centered cubic (fcc) packing densities for spherical particles as model systems. Pore type D represents the distance between two particles at the edges in a bcc lattice with a spacer particle on top. Pore types A and F correspond to the distance between two particles with a spacer particle in-between like in a primitive

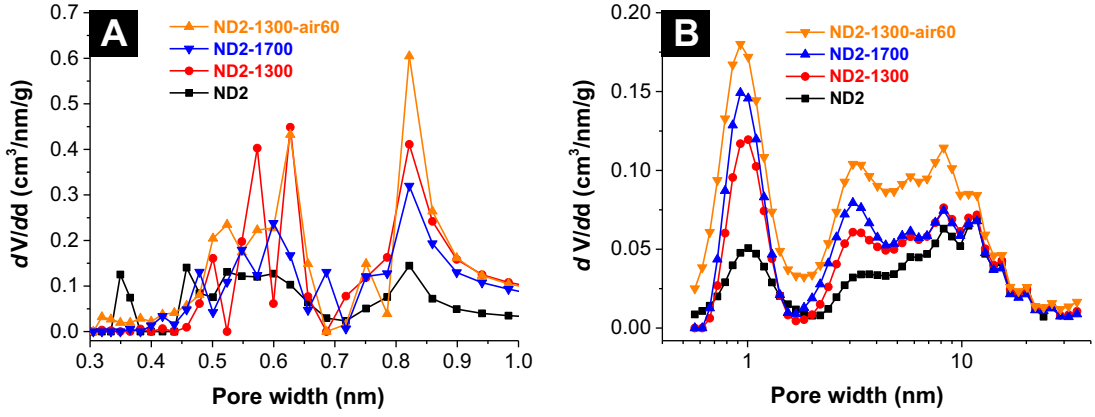

Fig. 8 – Pore size distributions for ND2, ND2-1300, ND2-1300-air60, and ND2-1700 calculated using NLDFT for carbon dioxide sorption isotherms (A) and using QSDFT (slit-pore shape) (B) for nitrogen sorption isotherms. (A color version of this figure can be viewed online.)

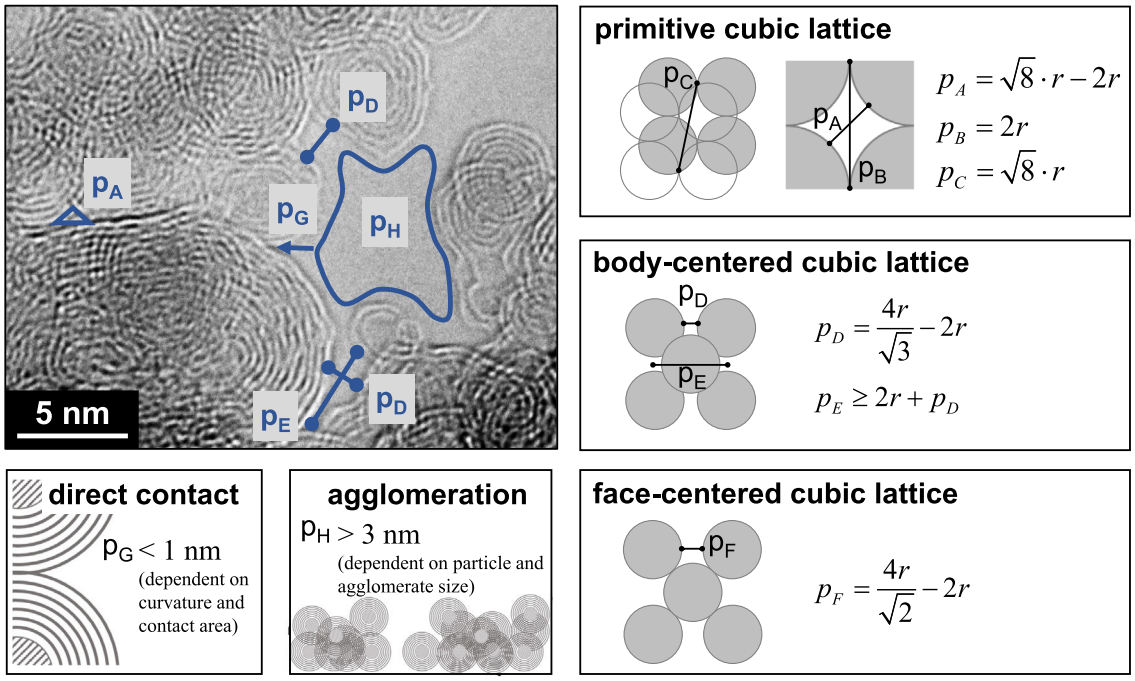

Fig. 9 – Transmission electron micrograph of ND2-1700 with different pore types. The pore types can be calculated assuming standard crystal lattices and basic geometrical equations dependent on the particle radius *r*. (A color version of this figure can be viewed online.)

cubic lattice or fcc lattice. The pore characteristic for a direct contact between two particles is represented by pore type G and is dependent on the curvature, the shape, and the direct contact area of the particles. As a first approximation this pore size can be set smaller than 1 nm. Finally, pore type H presents pores between agglomerates of OLC with a width of at least the minimum particle size (>3 nm). Looking at typical TEM images, we can see hat we find examples of all these theoretical pore geometries in our samples (see Fig. 9).

Assuming a Gaussian distribution for the particle size between 3 and 10 nm with a mean value of 6.5 nm (Supporting Information, Fig. S6), PSDs can be calculated for each type of pores and compared to the measured PSD (Fig. 10). This comparison was done for ND2-1700 as it exhibits a typical PSD for carbon onions. The range between 1.5 and 2.0 nm represents an important transition zone where none of pore models yields a significant contribution to the pore volume. Below that threshold, we see type D and G pores, while above the threshold type A, B, C, E, and H pores prevail. The calculated peaks align with the measured pattern and distribution maxima. For pores larger than 2 nm, a broad background is measured which possibly is related to the space between agglomerates (pore type H). The peaks below 0.8 nm, measured with CO_2 sorption, refer to the pores built in direct contact between two particles (pore type G).

While oxidation severely enhances the volume associated with mesopores and pores of around 1 nm, one would expect for a ~5 nm small particle the emergence of small ultramicropores (below 0.7 nm) if the material is activated (formation of intraparticle pores); hence, we need to closely investigate the NLDFT PSD data for CO_2 sorption in this regard. Yet, the similarity of the PSD before and after physical activation in air strongly indicates that no or only insignificant amounts of intraparticles pores have been formed. This confirms that the large increase in SSA must stem from removing interparticle connections and the decrease in particle size.

The mechanism of removing interparticle connections due to the oxidation has a similar effect concerning the change in PSD compared to the increase in particle size. The thermal annealing in inert gas increases the pore volume due to the expansion of particles whereas the oxidation etches the less bonded graphite blocking the pores between the particles.

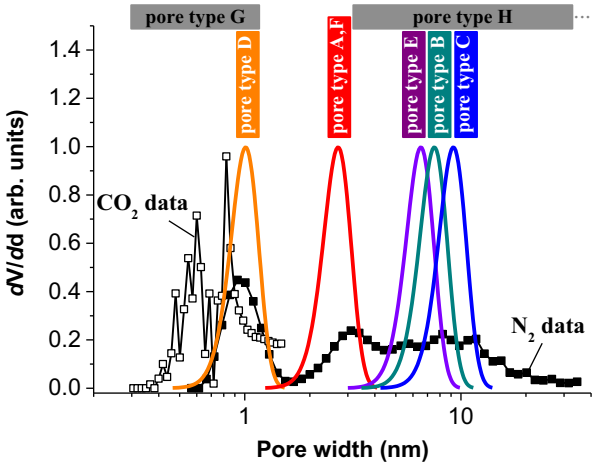

Fig. 10 – Measured PSD of ND2-1700 with the calculated PSD derived from the equations in Fig. 9. All calculated curves are normalized to 1. (A color version of this figure can be viewed online.)

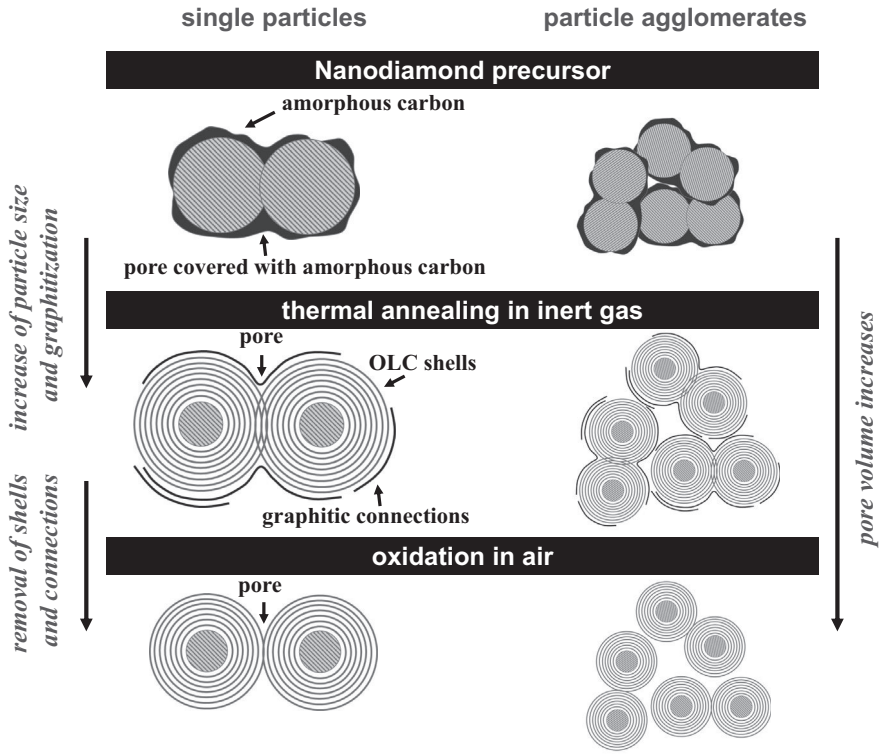

Fig. 11 – Schematic overview of the transformation of nanodiamond to OLC (OLC with diamond core) and the etching using air oxidation. The process is shown for two single particles and for particle agglomerates. During thermal annealing in argon the nanodiamond increases in size and graphitization occurs. During annealing in air OLC shells and interparticle connections are removed. The pore volume increases for both procedures.

Both mechanisms result in the increase of pore volume and are schematically illustrated in Fig. 11 for two OLCs as well as for an agglomerate.

3.2.6. *Carbon redistribution*

The presence of reactive gases during thermal annealing in argon was verified using thermogravimetric analysis coupled with mass spectrometry (Fig. 12). During heating functional groups containing oxygen are released resulting in an O^{2+} signal which disappears at higher temperatures (750 °C). During this release, oxygen can react with carbon to form CO and CO_2 [43]. According to Kuznetsov et al. [43], CO_2 can act as an etching agent which reacts with carbon and forms CO. After all CO_2 has been released, the corresponding ion current signal drops and etching as indicated by the emergence of a strong signal for CO starts. During further heating, the CO signal does not change significantly; yet, during cooling, this signal decreases as a result of carbon

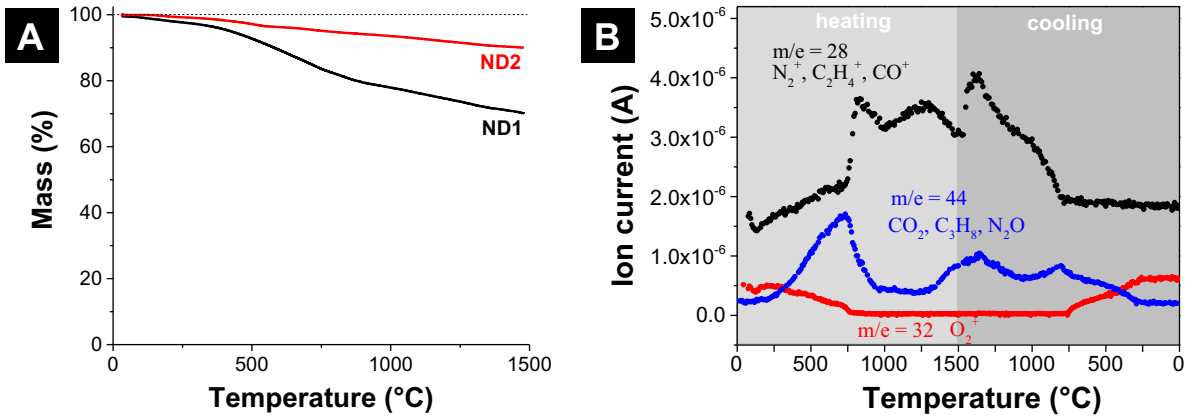

Fig. 12 – (A) Mass loss of ND1 and ND2 measured using thermogravimetric analysis in argon with a heating rate of 20 °C/min and an end temperature of 1500 °C. (B) Ion currents determined via mass spectrometry during the thermogravimetric analysis in (A) for ND1. The plot shows heating and cooling. (A color version of this figure can be viewed online.)

formation and larger graphitic ribbons are built via the Boudouard reaction Eq. (4). Cooling induces the increase in the CO_2 signal as well as the increase in oxygen indicating the end of the redistribution process.

$$CO_2 + C = 2CO \quad (4)$$

The formation of micrometer-sized graphitic structures can be explained by the presence of reactive gases which emerge from nanodiamond surfaces. The evolution of reactive gases is found to a much greater extent in ND1 compared to ND2 where no polyhedral crystals were identified. During thermal annealing, surface functional groups are removed between 800 and 1100 °C. After that, the presence of dangling bonds of the nanodiamonds increases the surface energy which induces graphitization, resulting in a significant drop of their total free energy [16,72]. The reaction of gases coming from the surface functional groups leads to an etching and a redistribution process during thermal annealing in argon. This assumption is supported since none of these effects has been reported so far for OLC derived via vacuum annealing of nanodiamond powder (vacuum removes emerging gases while in an inert gas these gases can remain near the surface). This also explains the observed mass reduction.

4. Conclusions

In this study a model was developed describing the change in SSA during the conversion from nanodiamond to OLC by thermal annealing in argon and the post synthesis activation using oxidation in air. The pore size distribution and the SSA were measured with nitrogen and carbon dioxide gas sorption. The increase in SSA starts with the release of surface functional groups until the onset of graphitization between 800 and 1100 °C. This results in a mass loss dependent on the amount of non-carbon content. The graphitization of nanodiamonds decreases the density and leads to an increase in volume. The SSA continuously increases until 1300 °C and stays constant or slightly decreases for higher temperatures forming larger graphitic structures or polyhedral crystals. This rearrangement of carbon atoms is strongly dependent on the chemical composition of the nanodiamond precursor.

Oxidation of carbon onions in air leads to removal of interparticle amorphous carbon and an etching of outer shells without significantly inducing intraparticle pores. Furthermore, a model was developed using standard crystal lattices to calculate different pore types dependent on the particle size. Our calculated results are in agreement with the measured data for the annealed nanodiamond in argon as well as oxidation of OLC in air.

Acknowledgements

The INM (www.inm-gmbh.de) is part of the Leibniz Research Alliance Energy Transition (LVE). We acknowledge funding from the German Federal Ministry for Research and Education (BMBF) in support of the nanoEES^{3D} project (award number 03EK3013) as part of the strategic funding initiative energy storage framework. We also acknowledge financial support via the INM FOCUS project ELECTRIC. The authors thank Rudolf Karos for the XRD measurements, Dr. Claudia Fink-Straube for the CHNS and ICP OES analysis, and Prof. Eduard Arzt for his continuing support (all at the INM). Robert Drumm (INM) is thanked for his kind support with thermal analysis.

Appendix A. Supplementary data

Supplementary data associated with this article can be found, in the online version, at http://dx.doi.org/10.1016/j.carbon.2014.12.050.

REFERENCES

[1] Iijima S. Direct observation of the tetrahedral bonding in graphitized carbon black by high resolution electron microscopy. J Cryst Growth 1980;50(3):675–83.
[2] Ugarte D. Curling and closure of graphitic networks under electron-beam irradiation. Nature 1992;359(6397):707–9.
[3] Kroto HW, Heath JR, O'Brien SC, Curl RF, Smalley RE. C 60: buckminsterfullerene. Nature 1985;318(6042):162–3.
[4] Suarez-Martinez I, Grobert N, Ewels CP. Nomenclature of sp^2 carbon nanoforms. Carbon 2012;50(3):741–7.
[5] Portet C, Yushin G, Gogotsi Y. Electrochemical performance of carbon onions, nanodiamonds, carbon black and multiwalled nanotubes in electrical double layer capacitors. Carbon 2007;45(13):2511–8.
[6] Zhao M, Song H, Chen X, Lian W. Large-scale synthesis of onion-like carbon nanoparticles by carbonization of phenolic resin. Acta Mater 2007;55(18):6144–50.
[7] Lange H, Sioda M, Huczko A, Zhu Y, Kroto H, Walton D. Nanocarbon production by arc discharge in water. Carbon 2003;41(8):1617–23.
[8] Ishigami M, Cumings J, Zettl A, Chen S. A simple method for the continuous production of carbon nanotubes. Chem Phys Lett 2000;319(5):457–9.
[9] Sano N, Wang H, Chhowalla M, Alexandrou I, Amaratunga G. Nanotechnology: synthesis of carbon 'onions' in water. Nature 2001;414(6863):506–7.
[10] Banhart F, Füller T, Redlich P, Ajayan P. The formation, annealing and self-compression of carbon onions under electron irradiation. Chem Phys Lett 1997;269(3):349–55.
[11] Maquin B, Derré A, Labrugère C, Trinquecoste M, Chadeyron P, Delhaès P. Submicronic powders containing carbon, boron and nitrogen: their preparation by chemical vapour deposition and their characterization. Carbon 2000;38(1):145–56.
[12] Serin V, Brydson R, Scott A, Kihn Y, Abidate O, Maquin B, et al. Evidence for the solubility of boron in graphite by electron energy loss spectroscopy. Carbon 2000;38(4):547–54.
[13] He C, Zhao N, Shi C, Du X, Li J. Carbon nanotubes and onions from methane decomposition using Ni/Al catalysts. Mater Chem Phys 2006;97(1):109–15.
[14] Tsai S, Lee C, Chao C, Shih H. A novel technique for the formation of carbon-encapsulated metal nanoparticles on silicon. Carbon 2000;38(5):781–5.
[15] Butenko YV, Kuznetsov VL, Chuvilin AL, Kolomiichuk VN, Stankus SV, Khairulin RA, et al. Kinetics of the graphitization of dispersed diamonds at "low" temperatures. J Appl Phys 2000;88(7):4380.
[16] Kuznetsov VL, Chuvilin AL, Butenko YV, Mal'kov IY, Titov VM. Onion-like carbon from ultra-disperse diamond. Chem Phys Lett 1994;222(4):343–8.

[17] Tomita S, Burian A, Dore JC, LeBolloch D, Fujii M, Hayashi S. Diamond nanoparticles to carbon onions transformation: X-ray diffraction studies. Carbon 2002;40(9):1469–74.
[18] Huang J, Yasuda H, Mori H. Highly curved carbon nanostructures produced by ball-milling. Chem Phys Lett 1999;303(1):130–4.
[19] Cabioc'h T, Jaouen M, Thune E, Guerin P, Fayoux C, Denanot M. Carbon onions formation by high-dose carbon ion implantation into copper and silver. Surf Coat Technol 2000;128:43–50.
[20] Thune E, Cabioc'h T, Guérin P, Denanot M-F, Jaouen M. Nucleation and growth of carbon onions synthesized by ion-implantation: a transmission electron microscopy study. Mater Lett 2002;54(2):222–8.
[21] Wu W, Zhu Z, Liu Z, Xie Y, Zhang J, Hu T. Preparation of carbon-encapsulated iron carbide nanoparticles by an explosion method. Carbon 2003;41(2):317–21.
[22] Jäckel N, Weingarth D, Zeiger M, Aslan M, Grobelsek I, Presser V. Comparison of carbon onions and carbon blacks as conductive additives for carbon supercapacitors in organic electrolytes. J Power Sources 2014;272(1):1122–33.
[23] Hirata A, Igarashi M, Kaito T. Study on solid lubricant properties of carbon onions produced by heat treatment of diamond clusters or particles. Tribol Int 2004;37(11–12):899–905.
[24] Gubarevich AV, Kitamura J, Usuba S, Yokoi H, Kakudate Y, Odawara O. Onion-like carbon deposition by plasma spraying of nanodiamonds. Carbon 2003;41(13):2601–6.
[25] Okotrub A, Bulusheva L, Gusel'nikov A, Kuznetsov V, Butenko YV. Field emission from products of nanodiamond annealing. Carbon 2004;42(5):1099–102.
[26] Kuzhir PP, Paddubskaya AG, Maksimenko SA, Kuznetsov VL, Moseenkov S, Romanenko AI, et al. Carbon onion composites for EMC applications. Electromagn Compat IEEE Trans 2012;54(1):6–16.
[27] McDonough JK, Frolov AI, Presser V, Niu J, Miller CH, Ubieto T, et al. Influence of the structure of carbon onions on their electrochemical performance in super capacitor electrodes. Carbon 2012;50(9):3298–309.
[28] Mochalin VN, Shenderova O, Ho D, Gogotsi Y. The properties and applications of nanodiamonds. Nat Nanotechnol 2012;7(1):11–23.
[29] Gogotsi Y, Presser V. Carbon nanomaterials. 2nd edition. CRC Press; 2014.
[30] Barnard A, Russo S, Snook I. Structural relaxation and relative stability of nanodiamond morphologies. Diam Relat Mater 2003;12(10):1867–72.
[31] Fang X, Mao J, Levin E, Schmidt-Rohr K. Nonaromatic core–shell structure of nanodiamond from solid-state NMR spectroscopy. J Am Chem Soc 2009;131(4):1426–35.
[32] Panich A, Shames A, Vieth H-M, Ōsawa E, Takahashi M, Vul AY. Nuclear magnetic resonance study of ultra nanocrystalline diamonds. Eur Phys J B 2006;52(3):397–402.
[33] Dubois M, Guérin K, Petit E, Batisse N, Hamwi A, Komatsu N, et al. Solid-state NMR study of nanodiamonds produced by the detonation technique. J Phys Chem C 2009;113(24):10371–8.
[34] Krüger A, Kataoka F, Maa Ozawa, Fujino T, Suzuki Y, Aleksenskii A, et al. Unusually tight aggregation in detonation nanodiamond: identification and disintegration. Carbon 2005;43(8):1722–30.
[35] Zou Q, Wang MZ, Li YG, Lv B, Zhao YC. HRTEM and Raman characterisation of the onion-like carbon synthesised by annealing detonation nanodiamond at lower temperature and vacuum. J Exp Nanosci 2010;5(6):473–87.
[36] Zou Q, Wang M, Li Y, Zhao Y, Zou L. Fabrication of onion-like carbon from nanodiamond by annealing. Sci China Ser E Technol Sci 2009;52(12):3683–9.
[37] Ganesh P, Kent P, Mochalin V. Formation, characterization, and dynamics of onion-like carbon structures for electrical energy storage from nanodiamonds using reactive force fields. J Appl Phys 2011;110(7):073506.
[38] Butenko YV, Kuznetsov VL, Paukshtis EA, Stadnichenko AI, Mazov IN, Moseenkov SI, et al. The thermal stability of nanodiamond surface groups and onset of nanodiamond graphitization. Fullerenes Nanotubes Carbon Nanostruct 2006;14(2–3):557–64.
[39] Zou Q, Li YG, Lv B, Wang MZ, Zou LH, Zhao YC. Transformation of onion-like carbon from nanodiamond by annealing. Inorg Mater 2010;46(2):127–31.
[40] Cebik J, McDonough JK, Peerally F, Medrano R, Neitzel I, Gogotsi Y, et al. Raman spectroscopy study of the nanodiamond-to-carbon onion transformation. Nanotechnology 2013;24(20):205703.
[41] Bogdanov K, Fedorov A, Osipov V, Enoki T, Takai K, Hayashi T, et al. Annealing-induced structural changes of carbon onions: high-resolution transmission electron microscopy and Raman studies. Carbon 2014;73:78–86.
[42] Kuznetsov VL, Butenko YV. Chapter 7 – diamond phase transitions at nanoscale. In: Gruen OASM, editor. Ultrananocrystalline diamond, 2nd ed. Oxford: William Andrew Publishing; 2012. p. 181–244.
[43] Kuznetsov V, Butenko YV, Zaikovskii V, Chuvilin A. Carbon redistribution processes in nanocarbons. Carbon 2004;42(5):1057–61.
[44] Pech D, Brunet M, Durou H, Huang P, Mochalin V, Gogotsi Y, et al. Ultrahigh-power micrometre-sized supercapacitors based on onion-like carbon. Nat Nanotechnol 2010;5(9):651–4.
[45] Gu W, Yushin G. Review of nanostructured carbon materials for electrochemical capacitor applications: advantages and limitations of activated carbon, carbide-derived carbon, zeolite-templated carbon, carbon aerogels, carbon nanotubes, onion-like carbon, and graphene. Wiley Interdiscip Rev: Energy Environ 2014;3(5):424–73.
[46] Gu W, Peters N, Yushin G. Functionalized carbon onions, detonation nanodiamond and mesoporous carbon as cathodes in Li-ion electrochemical energy storage devices. Carbon 2013;53:292–301.
[47] Gao Y, Zhou YS, Qian M, He XN, Redepenning J, Goodman P, et al. Chemical activation of carbon nano-onions for high-rate supercapacitor electrodes. Carbon 2013;51:52–8.
[48] Plonska-Brzezinska ME, Molina-Ontoria A, Echegoyen L. Post-modification by low-temperature annealing of carbon nano-onions in the presence of carbohydrates. Carbon 2014;67:304–17.
[49] Weingarth D, Zeiger M, Jäckel N, Aslan M, Feng G, Presser V. Graphitization as a universal tool to tailor the potential-dependent capacitance of carbon supercapacitors. Adv Energy Mater 2014;4(13):1400316.
[50] Vishnyakov A, Ravikovitch PI, Neimark AV. Molecular level models for CO_2 sorption in nanopores. Langmuir 1999;15(25):8736–42.
[51] Ravikovitch PI, Vishnyakov A, Neimark AV. Density functional theories and molecular simulations of adsorption and phase transitions in nanopores. Phys Rev E 2001;64(1):011602.
[52] Sing KS. Reporting physisorption data for gas/solid systems with special reference to the determination of surface area and porosity (Recommendations 1984). Pure Appl Chem 1985;57(4):603–19.
[53] Krüger A, Kataoka F, Ozawa M, Fujino T, Suzuki Y, Aleksenskii AE, et al. Unusually tight aggregation in detonation nanodiamond: identification and disintegration. Carbon 2005;43(8):1722–30.

[54] Kim T, Lim S, Kwon K, Hong S-H, Qiao W, Rhee CK, et al. Electrochemical capacitances of well-defined carbon surfaces. Langmuir 2006;22(22):9086–8.
[55] Pimenta MA, Dresselhaus G, Dresselhaus MS, Cancado LG, Jorio A, Saito R. Studying disorder in graphite-based systems by Raman spectroscopy. Phys Chem Chem Phys 2007;9(11):1276–91.
[56] Ferrari AC. Raman spectroscopy of graphene and graphite: disorder, electron–phonon coupling, doping and nonadiabatic effects. Solid State Commun 2007;143(1–2):47–57.
[57] Nemanich R, Solin S. First-and second-order Raman scattering from finite-size crystals of graphite. Phys Rev B 1979;20(2):392.
[58] Dresselhaus MS, Jorio A, Hofmann M, Dresselhaus G, Saito R. Perspectives on carbon nanotubes and graphene Raman spectroscopy. Nano Lett 2010;10(3):751–8.
[59] Ferrari A, Robertson J. Interpretation of Raman spectra of disordered and amorphous carbon. Phys Rev B 2000;61(20):14095.
[60] Tuinstra F. Raman spectrum of graphite. J Chem Phys 1970;53(3):1126.
[61] Wang X, Xu B, Liu X, Jia H, Hideki I. The Raman spectrum of nano-structured onion-like fullerenes. Phys B 2005;357(3–4):277–81.
[62] Roy D, Chhowalla M, Wang H, Sano N, Alexandrou I, Clyne TW, et al. Characterisation of carbon nano-onions using Raman spectroscopy. Chem Phys Lett 2003;373(1–2):52–6.
[63] Obraztsova ED, Fujii M, Hayashi S, Kuznetsov VL, Butenko YV, Chuvilin AL. Raman identification of onion-like carbon. Carbon 1998;36(5–6):821–6.
[64] Bokova-Sirosh SN, Pershina AV, Kuznetsov VL, Ishchenko AV, Moseenkov SI, Orekhov AS, et al. Raman spectra for characterization of onion-like carbon. J Nanoelectron Optoelectron 2013;8(1):106–9.
[65] Tan P, Dimovski S, Gogotsi Y. Raman scattering of non–planar graphite: arched edges, polyhedral crystals, whiskers and cones. Phil Trans R Soc Lond Ser A 1824;2004(362):2289–310.
[66] Gogotsi Y, Libera JA, Kalashnikov N, Yoshimura M. Graphite polyhedral crystals. Science 2000;290(5490):317–20.
[67] Zickler GA, Smarsly B, Gierlinger N, Peterlik H, Paris O. A reconsideration of the relationship between the crystallite size La of carbons determined by X-ray diffraction and Raman spectroscopy. Carbon 2006;44(15):3239–46.
[68] McSkimin H, Bond W. Elastic moduli of diamond. Phys Rev 1957;105(1):116.
[69] Robertson J. Amorphous carbon. Adv Phys 1986;35(4):317–74.
[70] Neimark AV, Lin Y, Ravikovitch PI, Thommes M. Quenched solid density functional theory and pore size analysis of micro-mesoporous carbons. Carbon 2009;47(7):1617–28.
[71] Hantel M, Presser V, McDonough J, Feng G, Cummings PT, Gogotsi Y, et al. In situ electrochemical dilatometry of onion-like carbon and carbon black. J Electrochem Soc 2012;159(11):A1897–903.
[72] Jiang Q, Chen Z. Thermodynamic phase stabilities of nanocarbon. Carbon 2006;44(1):79–83.

Supporting Information

Understanding structure and porosity of nanodiamond-derived carbon onions

Marco Zeiger,[1,2] Nicolas Jäckel,[1,2] Mesut Aslan,[1]

Daniel Weingarth,[1] and Volker Presser[1,2,]*

[1] *INM - Leibniz Institute for New Materials, Campus D2 2, 66123 Saarbrücken, Germany*

[2] *Saarland University, Campus D2 2, 66123 Saarbrücken, Germany*

Table S1: Instrument parameters for ICP OES measurements.

RF (W)	Flow rate plasma (L/min)	Nebulizer gas (L/min)	Nebulizer	Spray chamber	Injector tube diameter (mm)	Slit (µm)	Ana-lytical mode	Inte-gration time (s)	Used standard
1000	12	0.7	sea spray	cyclonic	3	20x15	Gauss	0.5	Fe

Table S2: Overview over SSA, pore volume, and density of the analyzed samples using N_2 gas sorption analysis. * denotes the oxidation time (in min) for the oxidized samples at 575 °C.

	Heating rate (°C/min)	Temperature (°C)	Time (h)	Density (g/cm³)	BET SSA (m²/g)	DFT SSA (m²/g)	Pore volume (cm³/g)
ND1 argon	0	0	0	2.70±0.01	353	280	0.414
	5	1100	1	2.66±0.03	400	376	0.553
	5	1100	3	2.66±0.03	424	385	0.607
	5	1100	10	2.61±0.03	427	398	0.615
	5	1300	1	2.37±0.01	459	433	0.665
	5	1300	3	2.34±0.02	465	444	0.722
	5	1300	10	2.23±0.01	482	455	0.751
	5	1700	1	1.93±0.01	440	424	0.706
	5	1700	3	1.93±0.12	387	362	0.484
	5	1700	10	1.84±0.01	425	411	0.688
	20	800	1	2.73±0.03	402	359	0.629
	20	900	1	2.77±0.06	399	349	0.600
	20	1100	1	2.63±0.03	425	375	0.648
	20	1300	1	2.35±0.01	493	436	0.773
	20	1700	1	1.95±0.01	448	413	0.742
ND2 argon	0	0	0	3.31±0.02	279	246	1.021
	5	1100	1	2.88±0.02	280	276	0.915
	5	1100	3	2.70±0.02	296	293	1.036
	5	1100	10	2.68±0.01	310	317	1.025
	5	1300	1	2.21±0.01	336	344	1.103
	5	1300	3	2.20±0.02	345	352	1.143
	5	1300	10	2.02±0.01	390	364	1.231
	5	1700	1	1.91±0.01	371	385	1.265
	5	1700	3	2.06±0.01	357	363	1.110
	5	1700	10	1.90±0.01	362	373	1.237
	20	800	1	2.86±0.01	285	251	0.937
	20	900	1	2.64±0.01	286	256	0.983
	20	1100	1	2.64±0.01	295	288	1.029
	20	1300	1	2.11±0.01	339	341	1.122
	20	1700	1	1.77±0.01	374	387	1.233
ND1-1300 air	15*	575	0.25	2.36±0.03	530	488	0.795
	30*	575	0.5	2.36±0.01	564	514	0.865
	60*	575	1	2.47±0.02	587	539	0.950
ND2-1300 air	15*	575	0.25	2.40±0.02	400	401	1.199
	30*	575	0.5	2.56±0.02	572	565	1.321
	60*	575	1	2.57±0.06	642	623	1.516

Table S3: Overview over peak position, FWHM and areal intensity ratio I_D/I_G of the analyzed samples. * denotes the oxidation time (in min) for the oxidized samples at 575 °C (first heated at 535 °C for 1 h followed by an oxidation at 575 °C).

	Heating rate (°C/min)	Temperature (°C)	Time (h)	D-mode position (1/cm)	G-mode position (1/cm)	D-mode FWHM (1/cm)	G-mode FWHM (1/cm)	I_D/I_G ratio (…)
ND1 argon	5	1100	1	1349	1576	232	107	2.18
	5	1100	3	1351	1577	231	105	2.23
	5	1100	10	1353	1579	229	101	2.27
	5	1300	1	1345	1586	158	85	1.82
	5	1300	3	1348	1590	151	84	1.74
	5	1300	10	1344	1586	139	81	1.65
	5	1700	1	1343	1591	68	62	1.27
	5	1700	3	1342	1589	63	61	1.27
	5	1700	10	1344	1590	63	59	1.22
	20	800	1	1359	1572	260	137	1.56
	20	900	1	1355	1573	253	135	1.51
	20	1100	1	1351	1577	235	105	2.23
	20	1300	1	1350	1589	160	87	1.78
	20	1700	1	1342	1590	67	61	1.35
ND2 argon	5	1100	1	1345	1573	216	115	1.87
	5	1100	3	1345	1572	219	112	1.97
	5	1100	10	1348	1574	215	109	2.00
	5	1300	1	1341	1584	161	92	1.77
	5	1300	3	1345	1583	152	89	1.68
	5	1300	10	1343	1585	135	82	1.64
	5	1700	1	1343	1586	70	63	1.20
	5	1700	3	1340	1583	68	61	1.22
	5	1700	10	1342	1585	65	60	1.17
	20	800	1	1360	1573	220	121	1.51
	20	900	1	1353	1570	205	122	1.44
	20	1100	1	1343	1573	213	113	1.90
	20	1300	1	1341	1584	150	94	1.66
	20	1700	1	1341	1584	68	61	1.26
ND1-1300 air	semi-isothermal	575	15*	1341	1583	159	87	1.86
		575	30*	1346	1593	155	81	1.98
		575	60*	1346	1589	179	85	2.16
ND2-1300 air	semi-isothermal	575	15*	1336	1587	81	80	1.50
		575	30*	1338	1588	80	78	1.49
		575	60*	1338	1589	86	75	1.61

Table S4: Overview over NLDFT SSA and pore volume of the CO_2 gas sorption data. The oxidized sample was first heated at 535 °C for 1 h followed by an oxidation at 575 °C for 1 h. For comparison, data for ND2 as received material without argon or other treatment have been added.

	Heating rate (°C/min)	**Temperature** (°C)	**Time** (h)	**NLDFT SSA** (m^2/g)	**Pore volume** (cm^3/g)
ND2 argon	as received	as received	as received	170	0.059
	20	1300	1	313	0.127
	20	1700	1	266	0.107
ND2-1300 air	semi-isothermal	575	1	370	0.141

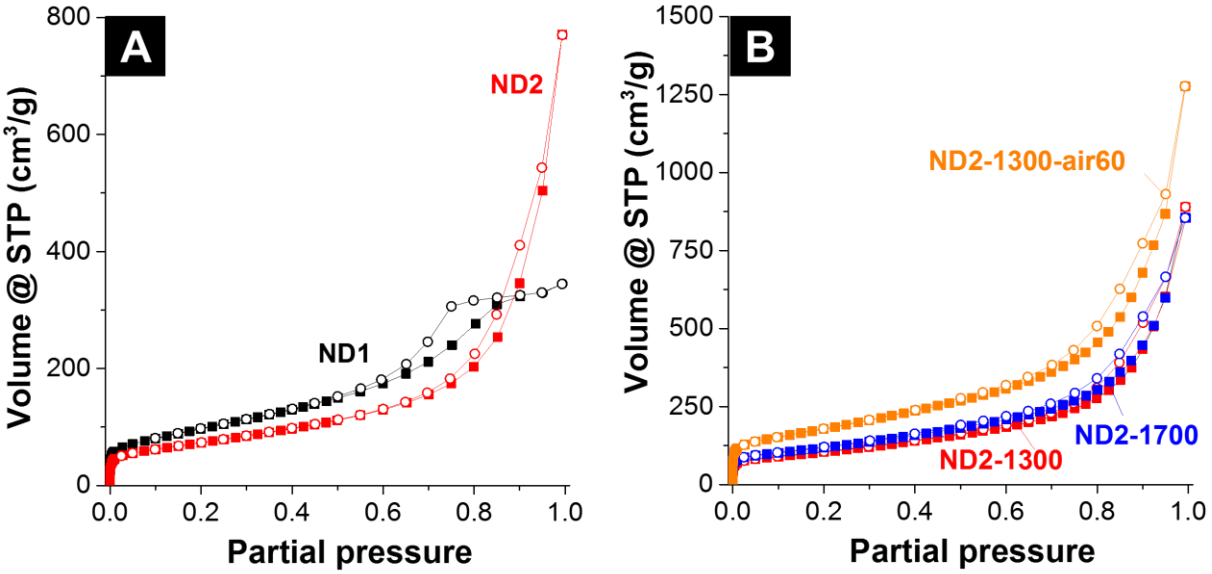

Figure S1. Nitrogen gas sorption isotherms of ND1 and ND2 at -196 °C (A) and different carbon onions (B).

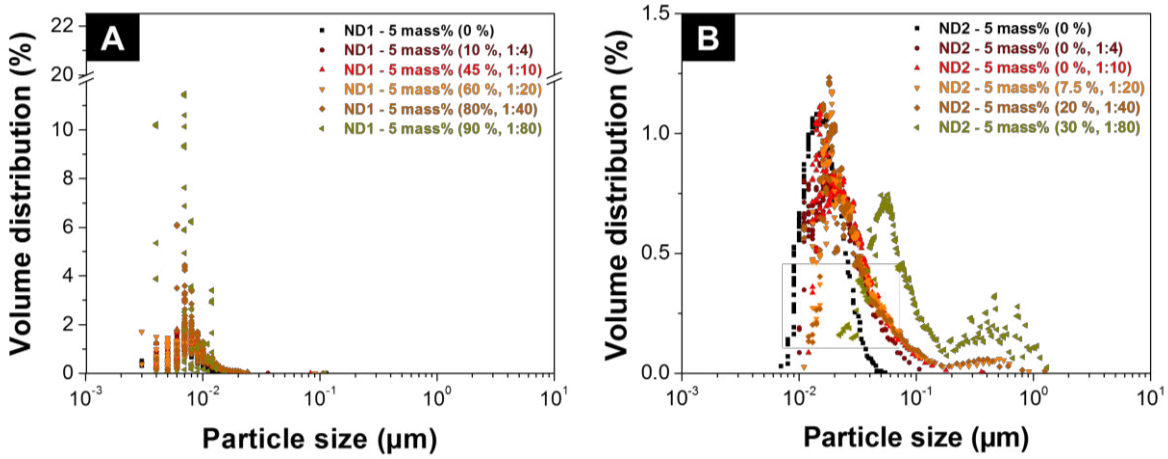

Figure S2. Volumetric particle size distribution measured with centrifugal sedimentation analysis in water. (A) ND1 and (B) ND2. The concentration was 5 mass% and different dilutions from 1:4 to 1:80 were measured resulting in different starting transmission between 0 and 90 %.

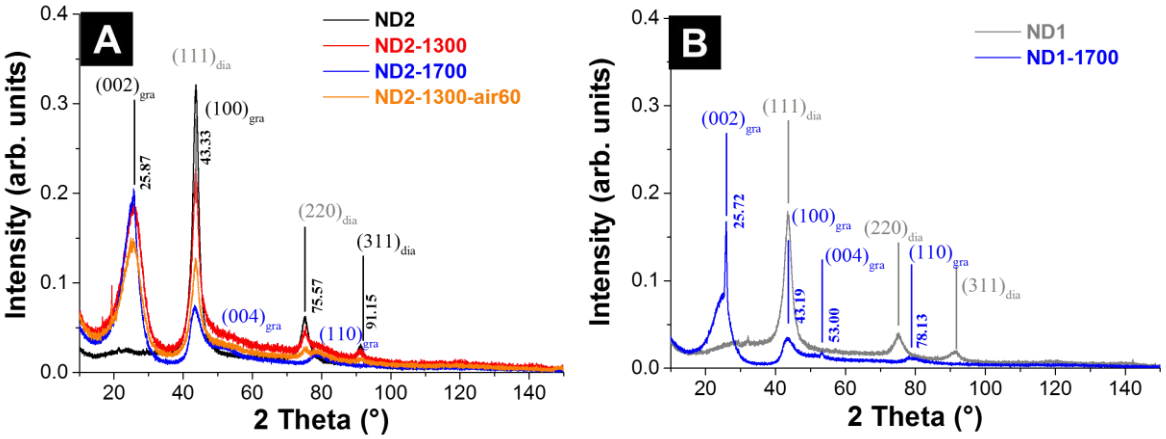

Figure S3. X-ray diffractogramms of (A) ND2, ND2-1300, ND2-1300-air60, ND2-1700, and (B) ND1, and ND1-1700. The index *dia* represents diamond and *gra* graphite. Using the powder diffraction database the PDF-number of diamond is 71-364 and of graphite 75-1621.

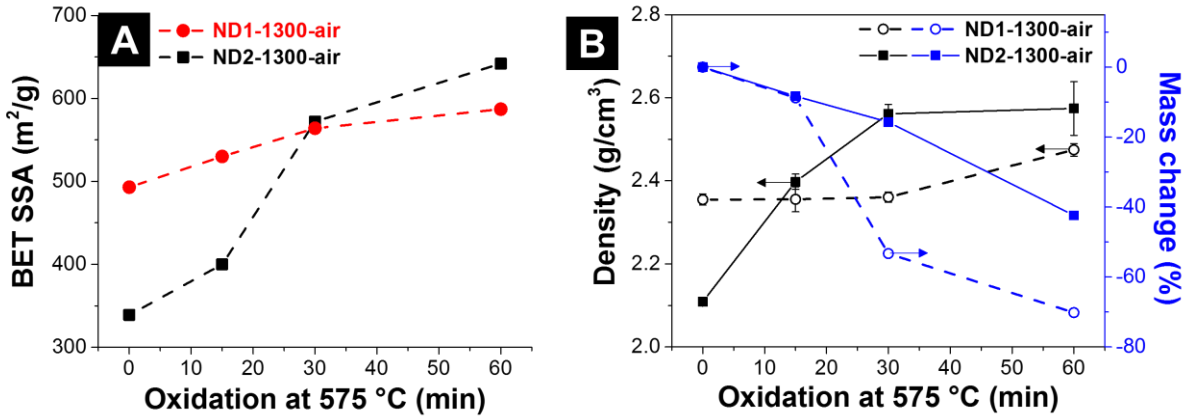

Figure S4. Influence of air oxidation on BET SSA (A) and skeletal density (B) of OLC derived from ND1, and ND2 via thermal annealing at 1300 °C and oxidized in air 535 °C for 1 h followed by additional oxidation in air at 575 °C for 15, 30, and 60 min. The first data point (0 min) belongs to ND1-1300 and ND2-1300.

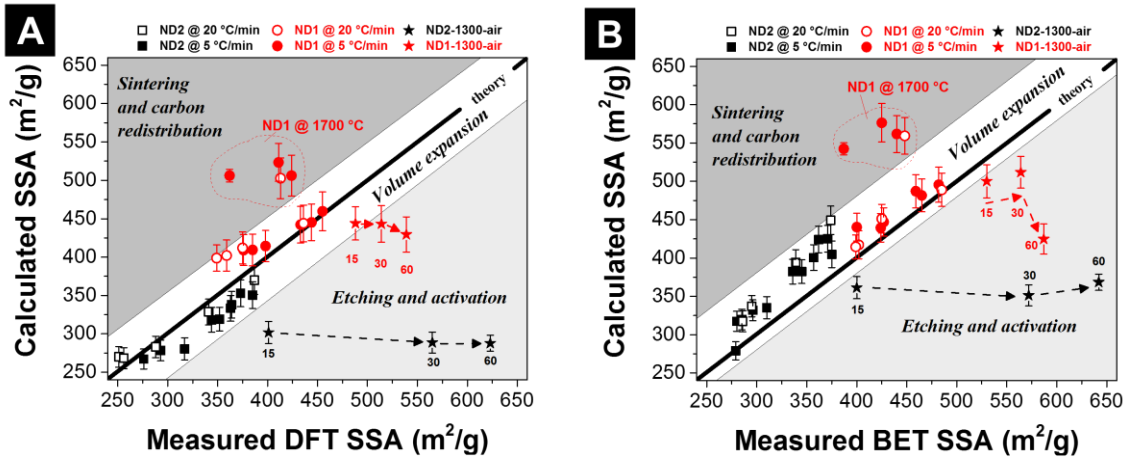

Figure S5. (A) Parity plot showing the comparison between the measured DFT SSAs (NLDFT for ND1-1300-air and ND2-1300-air and QSDFT for the other samples) of OLCs (*x*-axis) and the calculated SSAs using a volume expansion (*y*-axis). (B) Parity plot showing the comparison between the measured BET SSAs of OLCs in due consideration of the mass loss during heating shown in **Figure 6B** and normalized to the nanodiamond precursor. The numbers for the ND1-1300-air and ND2-1300-air data points denote the oxidation time in minutes at 575 °C.

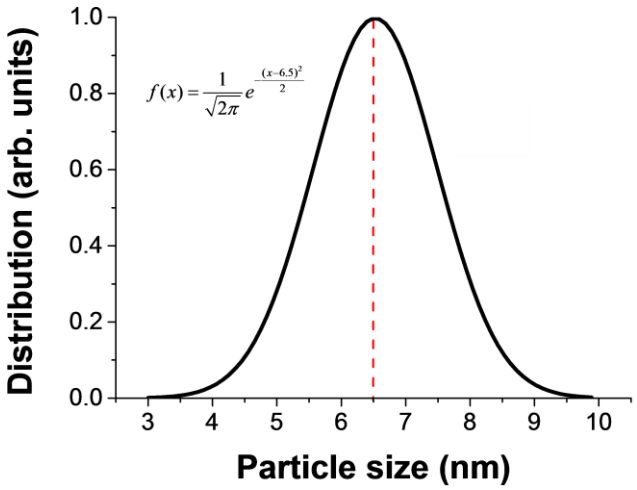

Figure S6.Gaussian function showing the particle size distribution of OLC derived from nanodiamond. The distribution assumes a particle size between 3 nm and 10 nm maximum range.

3.2 Vacuum or flowing argon: What is the best synthesis atmosphere for nanodiamond-derived carbon onions for supercapacitor electrodes?

Marco Zeiger,[1,2] Nicolas Jäckel,[1,2] Daniel Weingarth,[1] and Volker Presser[1,2]

[1] INM - Leibniz Institute for New Materials, Campus D2 2, 66123 Saarbrücken, Germany
[2] Saarland University, Campus D2 2, 66123 Saarbrücken, Germany

Citation:
Zeiger, M.; Jäckel, N.; Weingarth, D.; Presser, V., Vacuum or flowing argon: What is the best synthesis atmosphere for nanodiamond-derived carbon onions for supercapacitor electrodes? *Carbon* **2015,** 94, 507-517. (https://doi.org/10.1016/j.carbon.2015.07.028)

Own contribution: Design, planning, writing, Raman spectroscopy, Scanning-,and Transmission electron microscopy, EDX analysis, Particle size measurements, conductivity measurements, helium gas pycnometry, electrochemistry.

Abstract

We present a comprehensive study on the influence of the synthesis atmosphere on the structure and properties of nanodiamond-derived carbon onions. Carbon onions were synthesized at 1300 and 1700 °C in high vacuum or argon flow, using rapid dynamic heating and cooling. High vacuum annealing yielded carbon onions with nearly perfect spherical shape. An increase in surface area was caused by a decrease in particle density when transitioning from sp^3 to sp^2 hybridization and negligible amounts of disordered carbon were produced. In contrast, carbon onions from annealing nanodiamonds in flowing argon are highly interconnected by few-layer graphene nanoribbons. The presence of the latter improves the electrical conductivity, which is reflected by an enhanced power handling ability of supercapacitor electrodes operated in an organic electrolyte (1M tetraethylammonium tetrafluoroborate in acetonitrile). Carbon onions synthesized in argon flow at 1700 °C show a specific capacitance of 20 F/g at 20 A/g current density and 2.7 V cell voltage which is an improvement of more than 40% compared to vacuum annealing. The same effect was measured for a synthesis temperature of 1300 °C, with a 140% higher capacitance at 20 A/g for argon flow compared to vacuum annealing.

CARBON 94 (2015) 507–517

Contents lists available at ScienceDirect

CARBON

journal homepage: www.elsevier.com/locate/carbon

Vacuum or flowing argon: What is the best synthesis atmosphere for nanodiamond-derived carbon onions for supercapacitor electrodes?

Marco Zeiger [a,b], Nicolas Jäckel [a,b], Daniel Weingarth [a], Volker Presser [a,b,*]

[a] INM – Leibniz Institute for New Materials, Campus D2 2, 66123 Saarbrücken, Germany
[b] Saarland University, Campus D2 2, 66123 Saarbrücken, Germany

ARTICLE INFO

Article history:
Received 7 May 2015
Accepted 7 July 2015
Available online 7 July 2015

ABSTRACT

We present a comprehensive study on the influence of the synthesis atmosphere on the structure and properties of nanodiamond-derived carbon onions. Carbon onions were synthesized at 1300 and 1700 °C in high vacuum or argon flow, using rapid dynamic heating and cooling. High vacuum annealing yielded carbon onions with nearly perfect spherical shape. An increase in surface area was caused by a decrease in particle density when transitioning from sp^3 to sp^2 hybridization and negligible amounts of disordered carbon were produced. In contrast, carbon onions from annealing nanodiamonds in flowing argon are highly interconnected by few-layer graphene nanoribbons. The presence of the latter improves the electrical conductivity, which is reflected by an enhanced power handling ability of supercapacitor electrodes operated in an organic electrolyte (1 M tetraethylammonium tetrafluoroborate in acetonitrile). Carbon onions synthesized in argon flow at 1700 °C show a specific capacitance of 20 F/g at 20 A/g current density and 2.7 V cell voltage which is an improvement of more than 40% compared to vacuum annealing. The same effect was measured for a synthesis temperature of 1300 °C, with a 140% higher capacitance at 20 A/g for argon flow compared to vacuum annealing.

1. Introduction

Carbon has always been an element of central technological use, be it as primary energy source (coal), refractories (graphite), or abrasive medium (diamond). Especially the emergence of novel carbon nanoforms with intriguing properties has propelled carbon research over the last decades [1,2]. Carbon onions are a relatively new member of the vast carbon family, first discovered in 1980 by Iijima and described in 1992 by Ugarte [3,4]. They are spherical or polyhedral carbon nanoparticles and consist of several fullerene-like shells which are highly defective and disordered [5]. Typically, the size of carbon onions ranges between 2 and 50 nm, dependent on the synthesis method and parameters [6–8]. Several methods exist for their synthesis, like underwater arc discharge between graphite electrodes [9–11], electron beam irradiation of carbon containing materials [3,12], decomposition of carbon-containing precursors [13–16], mechanical milling [17], detonation reactions [18,19], or plasma spraying of nanodiamonds (ND) [20]. Thermal annealing of ND [7,21–26] has emerged as the most practical synthesis method, considering the very high yield of high purity carbon onions with a small size distribution between 5 and 10 nm and a large-scale material production with high reproducibility [2,7]. As precursor material, detonation NDs with a size of typically 5 nm are commonly used, which are engulfed by thin amorphous and disordered carbon layers [27–30]. The latter is also causing particle agglomeration forming entities of up to more than 100 nm [31]. Chemically, detonation ND consist out of 80–90 mass% of carbon, a few mass% of oxygen, hydrogen, nitrogen partially located in the core and coming from particle stabilizing functional groups, and possibly minor metal impurities [7,30,32].

Several experimental and theoretical studies have investigated the thermal transformation of ND to carbon onions. In a first stage, the decomposition of surface functionalities on NDs starts with the condensation of oxygen-containing surface functional groups, and their desorption together with water molecules [33,34] below temperatures of 200 °C. At higher temperatures, acidic groups like carboxyl, anhydride, and lactone groups decompose evolving CO and CO_2 gases [7,33]. Thus, functional groups decompose which initially had stabilized the ND surface. The thermal stability of ND surface functional groups has been investigated in several studies [7,34–37]. To minimize

* Corresponding author at: INM – Leibniz Institute for New Materials, Campus D2 2, 66123 Saarbrücken, Germany.
E-mail address: volker.presser@leibniz-inm.de (V. Presser).

http://dx.doi.org/10.1016/j.carbon.2015.07.028
0008-6223/

the surface energy of newly formed dangling bonds, the surface reconstructs and this onsets a gradual transformation from ND to carbon onions. The reconstructive phase transformation from sp^3- to sp^2-hybridization has an onset between 700 and 1100 °C and we first see a phase transformation from diamond to disordered carbon from the outside of the particle to the inside [7,21,37,38]. At elevated temperatures, typically starting between 1100 and 1300 °C, the sp^2-carbon continuously graphitizes and builds highly graphitic carbon shells, resulting in a complete transformation from ND to carbon onion at temperatures between 1800 and 2000 °C [23,39]. More details on the mechanism of ND graphitization is described, for example, in Ref. [40].

The thermal transformation of ND to carbon onions has been investigated so far in vacuum [21–25,37,41], argon [7,42–47], nitrogen [48], and hydrogen [49]. The onset temperature for graphitization is typically in the range between 700 and 1100 °C, but varies as a function of used atmospheres, heating rates, and type of ND material. Different synthesis atmospheres may also differ in the amount of gases containing reactive oxygen from the atmosphere or desorbing from the precursor. The catalytic effect of oxygen decreases the onset of graphitization and increases the graphitization rate, which may lead to different carbon nanostructures [50–52].

In a recent publication, we have shown a gradual volume increase during the transformation from nanodiamond to carbon onions in argon due to the lower density of graphitic carbon compared to nanodiamond [7]. Therefore, the specific surface area (SSA) increases with temperature and reaches a maximum at ~1300 °C dependent on the heating rate, holding temperature, and the precursor type [7]. In other studies, the maximum SSA was observed at 1500 °C [53] or 1800 °C [6], depending on the kind of ND. After reaching a maximum SSA, the increase in surface area saturates or the SSA may even decrease, especially for slow heating rates and long holding times [7]. Desorbing surface functional groups containing oxygen may partially etch the carbon onions and yield a redistribution process leading to large graphitic or polyhedral structures with high conductivity but low surface area [7,54]. Yet, no such structures were found after vacuum annealing, as described in other studies [21–25,37,41]. A decrease in surface area is disadvantageous for many electrochemical applications; ideally, a high surface area should be combined with a high electrical conductivity to enable a high energy and high power performance for supercapacitors [45,53]. Yet, it remains a challenge to find an optimum synthesis condition to maximize conductivity (1700–2000 °C) and surface area (typically at lower temperatures) [6,7,53].

Our study compares the benefits and limitations of carbon onion synthesis using either vacuum (minimum carbon redistribution) or argon (attractive for large scale synthesis). For this, we used rapid heating to and cooling from the annealing temperature (1300 or 1700 °C) within 2 min. This way, the ND powder is heated up to accomplish near-complete transformation to carbon onions without giving raise to extensive particle sintering. Local carbon redistribution may still facilitate nanocarbon formation between the carbon onions and impact on electrical conductivity (positively) and surface area (negatively). All synthesized materials were characterized comprehensively by 4-point probe, chemical analysis, transmission electron microscopy, Raman spectroscopy, nitrogen and carbon dioxide gas sorption, and X-ray diffraction (XRD) to determine the differences in carbon structure and ordering. The electrochemical properties were analyzed in organic electrolyte and 2-electrode configuration using cyclic voltammetry and galvanostatic cycling with potential limitation.

2. Experimental section

2.1. Synthesis of carbon onions

ND powders were thermally annealed in graphite crucibles ($30 \times 20\ mm^2$) using a custom-built dynamic furnace system (Xerion Advanced Heating Ofentechnik, Germany). To avoid structural changes during prolonged heating and cooling, we heated to and cooled from 1300 to 1700 °C within 2 min to have a nearly isothermal process. The holding time for all samples was 1 h and the temperature was measured directly at the sample. For each holding temperature, the ND powder was annealed either in argon flow (flow rate: 1 L/min) or in a high vacuum of 10^{-2} Pa (during the annealing the vacuum changed to ca. 1 Pa for several seconds due to desorption of functional groups). The samples were named in reflectance of the treatment conditions; for example 1300-VAC for 1300 °C annealing temperature and the use of vacuum.

2.2. Chemical and structural characterization

2.2.1. Electron microscopy and chemical analysis

Transmission electron microscopy (TEM) was carried out with a 2100F microscope (JEOL, Japan) operating at 200 kV. Samples were dispersed in ethanol and drop casted on a copper grid with a lacey carbon film (Gatan, USA). The chemical composition of ND powder and carbon onion samples was analyzed using energy-dispersive X-ray spectroscopy (EDX), CHNS elemental analysis, and inductively-coupled optical emission spectroscopy (ICP-OES). EDX analysis was performed using a JSM-7500F (JEOL, Japan) scanning electron microscope equipped with an EDX system (Oxford Instruments, UK). The samples were fixed on a conductive carbon tape and 5 spectra were recorded at 5 different positions with 10 kV acceleration voltage. CHNS elemental analysis was conducted with a Vario Micro Cube system (Elementar Analysensysteme GmbH, Germany) after combustion of the sample under oxygen at 1150 °C in a tin holder. The CHNS analyzer was calibrated with sulphanilic acid using different masses (41.6 mass% C, 4.1 mass% H, 8.1 mass% N, 18.5 mass% S). For ICP-OES analysis, an Ultima 2 system (Horiba Jobin-Yvon, France) was used with a Czerny–Turner type monochromator with a focal length of 1 m and high frequency power of 1 kW was supplied by a regulated generator at 40.68 MHz. Prior to the analysis of each element, a screening was performed to survey all included elements. Calibration was performed using aqueous standard solutions of 0, 1.0, and 2.0 mg/L yielding a calibration coefficient of 0.999. For every sample analysis, ca. 50 mg of material was diluted to a total volume of 25 mL.

2.2.2. Raman spectroscopy

Raman spectra were recorded using a Renishaw inVia Raman microscope equipped with an Nd-YAG laser with an excitation wavelength of 532 nm, a grating with 2400 lines/mm, a 50× objective (numeric aperture: 0.9), and a spectral resolution of ~1.2 cm^{-1}. The spot size on the sample in the focal plane was approximately 2 μm using an output power of 0.2 mW. The acquisition time was 30 s and 10 accumulations were used to eliminate cosmic rays and to improve the signal-to-noise ratio. Peak analysis and peak fitting were performed assuming several Voigt profiles dependent on the phase composition. Voigt profiles were used to fit broad Raman signals of amorphous carbon as well as sharp Raman modes for graphitic carbon. The background was subtracted using a linear baseline function. Only carbon onions were subject to Raman spectroscopy since NDs require UV laser radiation for a comprehensive characterization of sp^3-hybridized carbon nanodomains.

2.2.3. X-ray diffraction and helium gas pycnometry

X-ray diffractogramms (XRD) were measured using Cu-Kα radiation with a Bruker AXS D8 Advance diffractometer (Bruker AXS, Germany). The step size was 0.02° and the measurement time was 1 s/step. Prior to the measurements, the system was calibrated with a LaB_6 single crystal. Pycnometric densities were measured with an AccuPyc 1330 gas pycnometer (Micromeritics, Germany) using helium gas (purity grade: 5.0). Adsorbed water was removed by drying the samples in an oven at 120 °C and 1 kPa for 1 h prior to the measurement. The sample holder had a maximum volume of 1 cm^3 and the pycnometer was programmed to perform 10 purges, followed by an analysis of 20 separate measurements. Both purge and analysis fill pressures were set at 134 Pa and an equilibration rate of 34 Pa/min was used. The theoretical SSA of spherical carbon onions (SSA_{OLC}; OLC: onion-like carbon) derived from NDs with a surface area of SSA_{ND} was calculated using the pycnometric density assuming a volume expansion and constant mass according to Ref. [7] (Eq. 1):

$$SSA_{OLC} = SSA_{ND} \cdot \left(\frac{\rho_{ND}}{\rho_{OLC}}\right)^{\frac{2}{3}} \quad (1)$$

2.2.4. Gas sorption analysis

Gas sorption analysis was carried out using an Autosorb iQ system (Quantachrome, USA). First, powder samples were outgassed at 300 °C for 10 h under vacuum conditions (10^2 Pa). Nitrogen gas sorption was performed at −196 °C in the relative pressure range from 5×10^{-7} to 1.0 in 68 steps. The pore size distribution (PSD) between 0.56 and 37.5 nm was derived using the quenched-solid density functional theory (QSDFT) [55,56] supplied by Quantachrome assuming a slit-shape pore geometry. The latter has recently been shown to be the most appropriate model for carbon onions [45]. The SSA using the BET equation after Brunauer–Emmett–Teller [57] was calculated in the linear regime of the measured isotherms at a partial pressure range between 0.1 and 0.3 P/P_0. Carbon dioxide gas sorption measurements were carried out at 0 °C in the relative pressure range from 1×10^{-4} to 1×10^{-2} in 40 steps. SSA and PSD values were calculated from CO_2 sorption data for pore sizes between 0.3 and 1 nm with the ASiQwin software using non-local density functional theory (NLDFT) [56,58].

2.2.5. Dynamic light scattering and electrical conductivity measurements

Volumetric particle size distributions were measured using dynamic light scattering method with a Nanotrac Ultra (Microtrac Europe GmbH, Germany). For all samples a 0.1 mass% water dispersion was used and 3 independent measurements were performed with an acquisition time of 30 s.

The electrode conductivity was measured with a custom built 4-point probe (tip diameter: 1.5 mm; tip distance 1.75 mm). The areal resistance was measured 10-times on different positions of the electrode material (3×3 cm^2) and Eq. (2) was used to calculate the electrode conductivity normalized to the thickness.

$$\sigma = \frac{\ln(2)}{\pi} \frac{I}{U \cdot d} \quad (2)$$

In this equation, I is the current, U the voltage, and d the thickness of the electrode measured with a micrometer screw.

2.2.6. Electrochemical characterization

To prepare polymer-bound carbon electrodes, carbon onion powder was dispersed in ethanol, sonicated for 10 min, and then heated to 90 °C to remove some solvent. The viscous slurry was put into a mortar and 10 mass% of polytetrafluoroethylene (PTFE, 60 mass% solution in water from Sigma Aldrich, USA) were added. The dough-like carbon paste was rolled with a rolling machine (MTI HR01, MTI Corp., USA) to 200 µm thick free standing electrodes and dried at 120 °C at 2 kPa for at least 24 h.

For all measurements, 1 M tetraethylammonium tetrafluoroborate (TEA-BF_4) in acetonitrile (ACN) from BASF (Germany) was used in a 2-electrode setup. The electrode discs (12 mm in diameter) were separated by a glass-fiber separator with a diameter of 13 mm (type GF/D, GE Healthcare, USA). The electrode/separator/-electrode arrangement was placed between two carbon-coated aluminum foils (diameter 12 mm, type Zflo 2653, Coveris Advanced Coatings, USA) and compressed with spring-loaded titanium pistons. The cells were dried at 120 °C and a vacuum of 2 kPa for 12 h before they were put in an argon-filled glove box (MBraun, Germany; Labmaster 130; O_2, H_2O < 1 ppm), where they were vacuum filled with a syringe containing 1 M TEA-BF_4 in ACN.

All electrochemical measurements were carried out using a VSP300 or VMP300 potentiostat/galvanostat from Bio-Logic (France) in cyclic voltammetry (CV) and galvanostatic mode (GCPL). Cyclic voltammograms at different scan rates from 1 mV/s to 2 V/s from 0 to 2.7 V were conducted. Each voltage was applied for 3-times and the capacitance at 2.7 V for every scan rate was calculated using Eq. (3).

$$C = \frac{\int_{t_0}^{t_{end}} I(t)\mathrm{d}t}{U} \quad (3)$$

with the capacitance C, the time t (t_0: start of discharge, t_{end}: end of discharge), and the electrical potential U. The specific capacitance was determined with Eq. (4):

$$C_{sp} = 4 \cdot \frac{C}{m} \quad (4)$$

with the active mass m of both electrodes and the device capacitance C. Using GCPL mode the current was varied to apply different current densities from 0.1 to 20 A/g with 10 s resting time between charging/discharging and a potential limitation of 2.7 V. The specific current relates in this case to the active mass of both electrodes and the resulting capacitance was calculated from the current and the time for discharge with respect to the IR drop of the cell (Eq. 3).

The electrochemical stability was measured using long-time voltage floating tests between 0 and 2.7 V with a constant current of 0.5 A/g and a holding time of 10 h. After three full galvanostatic cycles, the voltage was held for 10 h at 2.7 V and the procedure was repeated to an overall holding time of 100 h.

3. Results and discussion

3.1. Chemical and structural characterization

3.1.1. Chemical composition

Chemical analysis was carried out using EDX, CHNS analysis, and ICP-OES (Table 1). The ND precursor is composed of 89.92 ± 0.91 mass% carbon, 2.34 ± 0.64 mass% nitrogen, and 1.43 ± 0.73 mass% hydrogen, according to CHNS analysis. Spectral analysis with EDX reveals the presence of small amounts of chlorine (0.8 mass%). Additional ICP-OES analysis shows minor amounts of Ag, Al, B, Ca, Fe, and Na (cumulatively less than 2 mass%). In comparison to EDX, CHNS and ICP-OES analyses are more adequate for quantitative chemical analysis; therefore, an oxygen content of 4.77 mass% was determined using the total mass of materials minus the detected elements of the CHNS and ICP-OES analysis. These values are in good agreement with the recent literature [31,32,59–63]. It is expected that the detected oxygen and hydrogen atoms mostly belong to surface functionalities like

Table 1
Chemical composition of the ND and the OLC samples measured using EDX and CHNS elemental analysis. All values are given in mass%. Oxygen contents from CHNS analysis are derived from the difference of the total amount and the other detected elements using CHNS analysis and ICP-OES.

	Method	Al	B	Ca	Ag	Fe	Na
ND	ICP-OES	0.212	0.054	0.013	0.083	0.154	1.024
	Method	C	O	N	H	Cl	
ND	CHNS	89.92 ± 0.91	4.77	2.34 ± 0.64	1.43 ± 0.73	–	
	EDX	90.20 ± 2.90	3.4 ± 1.9	5.6 ± 3.5	–	0.8 ± 0.3	
1300-AR	CHNS	96.62 ± 1.66	3.38	–	–	–	
	EDX	98.91 ± 0.22	1.09 ± 0.22	–	–	–	
1300-VAC	CHNS	97.18 ± 0.69	2.82	–	–	–	
	EDX	98.44 ± 0.38	1.56 ± 0.38	–	–	–	
1700-AR	CHNS	98.94 ± 0.28	1.06	–	–	–	
	EDX	98.76 ± 0.10	1.24 ± 0.10	–	–	–	
1700-VAC	CHNS	98.73 ± 0.53	1.27	–	–	–	
	EDX	99.26 ± 0.21	0.74 ± 0.21	–	–	–	

carboxylic, ketonic, or hydroxylic groups [40]. Nitrogen found for ND commonly stems from surface functional groups like amide [35] or nitro groups [64,65], but can also be structurally bound in the diamond core [37]. Carbon onions synthesized at 1300 °C show around 3 mass% of oxygen when using argon flow (3.4 mass%) or vacuum annealing (2.8 mass%). For comparison, thermal annealing at 1700 °C yields only 1.1 mass% (1700-AR) and 1.3 mass% (1700-VAC) oxygen. It has been shown that oxygen containing surface functional groups desorb when heating to 1000 °C [7,33], but may partially re-adsorb during cooling or when re-exposed to ambient atmosphere. A higher degree of carbon ordering after annealing at 1700 °C may result in a lower number of dangling bonds on the surface, causing a decreased affinity for surface functional groups. This correlation can explain the higher oxygen content found for carbon onions synthesized at 1300 °C. Applying a high vacuum during the synthesis leads to the removal of desorbing functional groups. The lower content of molecules in the atmosphere inhibits the adsorption during cooling and induces lower oxygen contents for 1300-VAC than for 1300-AR.

3.1.2. Carbon onion structure

Transmission electron microscopy demonstrates the structure and the morphology of carbon onions (Fig. 1). The samples show a characteristic particle size of 5–10 nm, spherical shape, several defective fullerene-like shells, and localized particle sintering to form agglomerates of several hundreds of nanometers. The only visible difference between samples synthesized at 1300 or 1700 °C is a more pronounced tendency to express a polyhedral shape at higher annealing temperatures (Fig. 1F), as has been reported in the literature [40]. Samples obtained in vacuum at 1300 °C show locally fused spherical carbon onions (Fig. 1C, D). When using argon at the same temperature, additional defective few-layer graphene nanoribbons (2–5 layers) can be found (Fig. 1A, B). The same is seen when comparing samples synthesized at 1700 °C and almost perfect carbon onions without a distinct amount of few-layer graphene nanoribbons or other carbon phases are obtained by vacuum synthesis. In contrast, 1700-AR is composed of carbon onions interconnected by a multitude of few-layer graphene nanoribbons (Fig. 1E). These layers are highly defective, partially curved, directly connected to carbon onions, and consist of 2–5 graphene layers (Fig. 1F). Compared to 1300 °C, the few-layer graphene nanoribbons seen after annealing ND at 1700 °C are more ordered and locally polygonised. The used term few-layer graphene nanoribbons is in accordance with the proposed nomenclature in Ref. [66].

Fig. 2A presents the Raman spectra of the four types of carbon onions in the range between 500 and 3500 cm^{-1} and the fitting results can be found in Table 2. The spectra exhibit the characteristic G-mode between 1580 and 1590 cm^{-1} indicative of sp^2-hybridized carbon. More precisely, this mode represents the bond stretching of sp^2-hybridized carbon atoms in rings and chains coming from the zone center E_{2g} mode [67]. Between 1330 and 1342 cm^{-1}, the so-called D-mode can be seen. This peak represents the breathing mode of the sixfold rings, but is only Raman active because of the presence of "defects" in the widest possible meaning. Defects can be vacancies, additional atoms, curvature, and edges. Therefore, the D-mode is a double resonant Raman process, due to the scattering of the electron with the phonon as well as a defect [68]. Perfect graphite single crystals would be void of the D-mode [67].

1300-VAC samples show a Raman spectrum characteristic for carbon onions synthesized at rather lower temperatures with very broad D- and G-mode [7]. In comparison to the material after vacuum annealing at 1300 °C, the Raman spectrum of 1300-AR is significantly different although the annealing temperature and time were the same (Fig. 2A, B). The spectrum presents a much sharper D-mode, the G-mode shows a small shoulder at 1610 cm^{-1}, and the transition between D- and G-mode is less distinct than for 1300-VAC. The Raman spectrum of 1300-AR is not characteristic for just *one* specific carbon material rather for the combination of *different* carbons. As seen from Fig. 2B, the D-mode shows a broad shape at the base, but a very sharp peak near the maximum. The same can be seen for the G-mode, where a doublet structure is caused by the emergence of a pronounced shoulder at higher frequencies. These features can be explained when assuming the presence of disordered nanocrystalline carbon onion similar to 1300-VAC with a broad D- and G-mode and *additionally* a second carbon phase with a higher degree of structural ordering responsible for the sharp part of the D-mode and the doublet structure of the G-mode. This assumption aligns very well with the TEM images shown in Fig. 1.

The same trend is seen for carbon onions synthesized at 1700 °C (Fig. 2A, B). 1700-VAC material shows very sharp D- and G-modes. The higher degree of carbon ordering at elevated synthesis temperatures comes from the rearrangement of carbon atoms, especially concerning the distortion of carbon rings, bond length variation, and interstitial atoms. For 1700-AR, the Raman spectrum is quite similar to 1700-VAC, but with the additional emergence of a shoulder at 1610 cm^{-1} (similar to 1300-AR). For both synthesis temperatures, 1300 and 1700 °C, the second order Raman spectrum presents more pronounced peaks for carbon onions synthesized in Argon, reflecting the higher degree of carbon ordering.

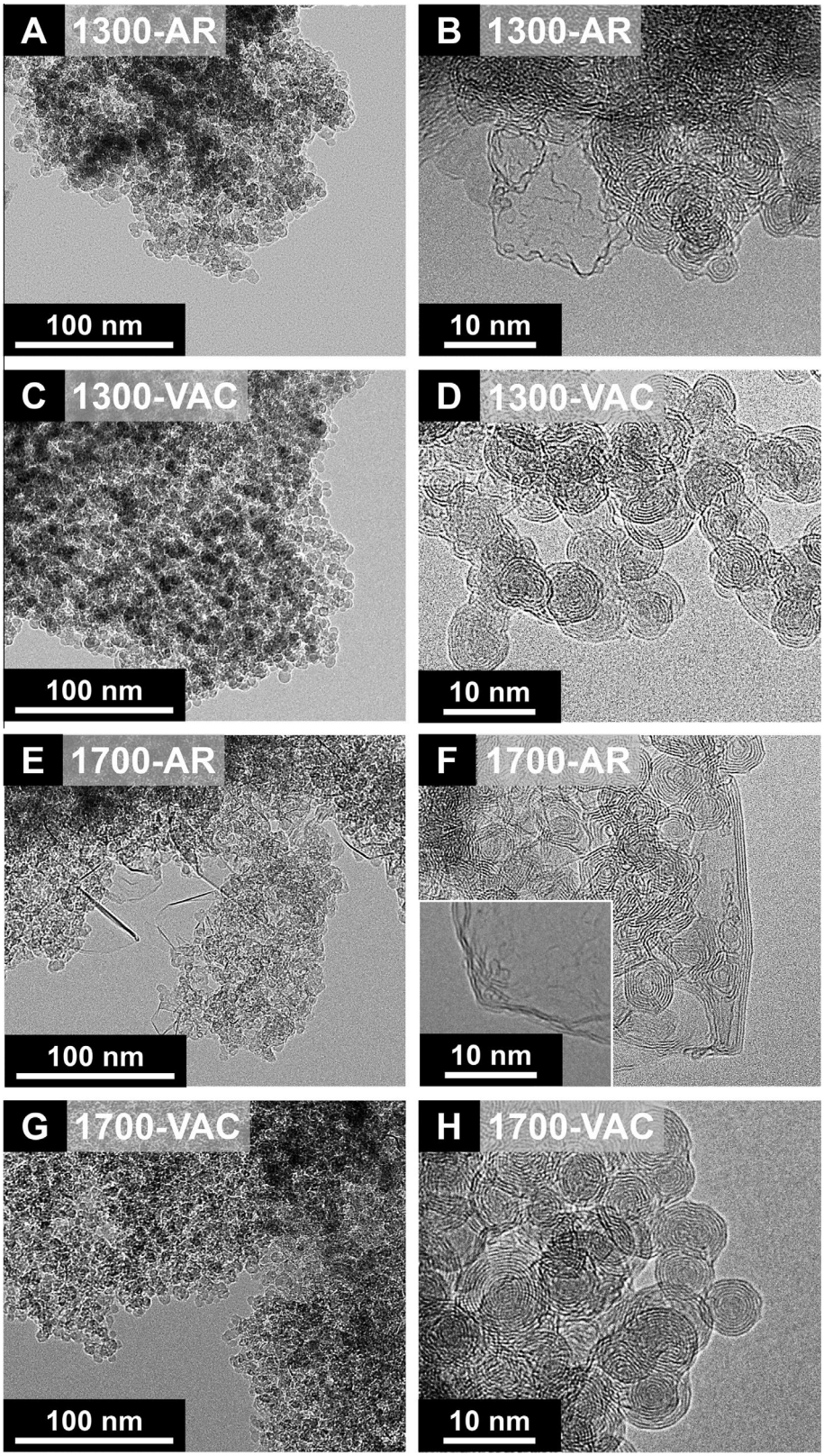

Fig. 1. Transmission electron micrographs of 1300-AR (A, B), 1300-VAC (C, D), 1700-AR (E, F), and 1700-VAC (G, H).

To exemplify the impact of two separate carbon phases on the resulting Raman spectrum when using argon annealing, 1300-VAC carbon onions were mixed with graphite flakes and the resulting spectrum is shown in Fig. 2C. The graphite flakes show a Raman spectrum resembling few-layer graphene nanoribbons. When admixing graphite flakes to 1300-VAC, we see the superimposition of two carbon phases with different degrees of structural ordering. The resulting spectrum shows the same

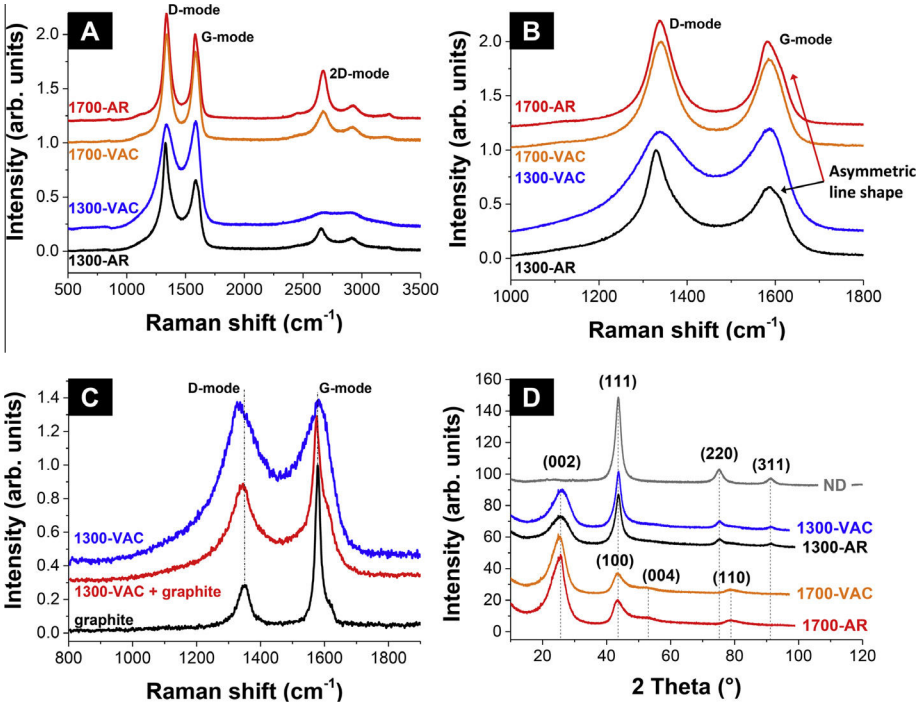

Fig. 2. Raman spectra of the carbon onion samples (A and B), Raman spectra of the combination of carbon onions and graphite flakes (C), and X-ray diffractogramms (D) of carbon onion samples.

Table 2
Properties of the deconvoluted Raman peaks.

		Pos. D (cm^{-1})	Pos. G	Area D	Area G	I_D/I_G (...)	FWHM D (cm^{-1})	FWHM G
1300-AR	Carbon onion	1343	1610	44	29	1.52	135	96
	Few-layer graphene	1331	1585	40	21	1.90	47	64
1300-VAC	Carbon onion	1341	1592	106	63	1.68	139	87
1700-AR	Carbon onion	1345	1593	62	42	1.40	69	69
	Few-layer graphene	1332	1584	20	11	2.10	45	33
1700-VAC	Carbon onion	1340	1588	90	56	1.61	74	71

characteristics than 1300-AR with an "unexpectedly" sharp D-mode, a less distinct transition between D- and G-mode, and a doublet structure of the G-mode. The existence of two different carbon species resulting in one Raman spectrum with doublet structure had also been shown for nanographite ribbons on HOPG [69].

To further understand the presence of different carbon phases, we performed peak deconvolution of the Raman spectra (Fig. 3). As both synthesis temperatures do not induce a complete transformation from diamond to graphite, especially for 1300 °C, a remaining nanodiamond core is expected. Given the use of visible light laser radiation (532 nm), this contribution will not show up in the Raman spectra. It was shown that nanodiamond first transforms into amorphous carbon before graphitization from the outside to the inside starts. Additionally, particle–particle connections are established and an amorphous carbon phase at the interface between graphitic shells and diamond core exists [70]. Therefore, besides a non-Raman visible diamond core and the actual carbon onion material, we have to consider amorphous carbon when fitting the spectra. Bogdanov et al. used one peak to describe amorphous carbon at ~1530 cm^{-1} [39]. Yet, to adequately represent the Raman signal of amorphous carbon with very broad peaks, we fitted three peaks: one for transpolyacetylene (TPA) at ~1130 cm^{-1} and two for the broad D- and G-mode of amorphous carbon coming from interstitial atoms with sp^3 connections in the planes of sixfold rings, or the presence of five- or sevenfold rings. The TPA-peak may also come from carbon chains in a transpolyacetylene-like ordering at the zigzag edges of the defective carbon shells on the particles [39]. The D-mode of amorphous carbon is seen as a small low-frequency shoulder of the G-peak [71]. Once accommodating for the presence of amorphous carbon, there are two more carbon phases to consider: The actual carbon onions and, in case of argon-annealed samples, few-layer graphene nanoribbons between the particles. For the latter two phases, each one pair of corresponding D- and G-modes were used to deconvolute the spectra (Table 2).

Material after vacuum annealing at 1300 °C shows a Raman spectrum related to carbon onions with a D-mode at 1341 cm^{-1} and a G-mode at 1592 cm^{-1} with relatively broad peaks indicated by a FWHM of 139 and 87 cm^{-1}, respectively (Fig. 3A). According to the model by Ferrari and Robertson [72], a broad G-mode is indicative of a high degree of distortion of the sp^2-hybridized carbon rings as well as their bond length variation leading to an incompletely graphitized material. This is supported by the G-mode position at 1592 cm^{-1}, which is larger than for ideal graphite at 1580 cm^{-1}. For comparison: the G-mode position of

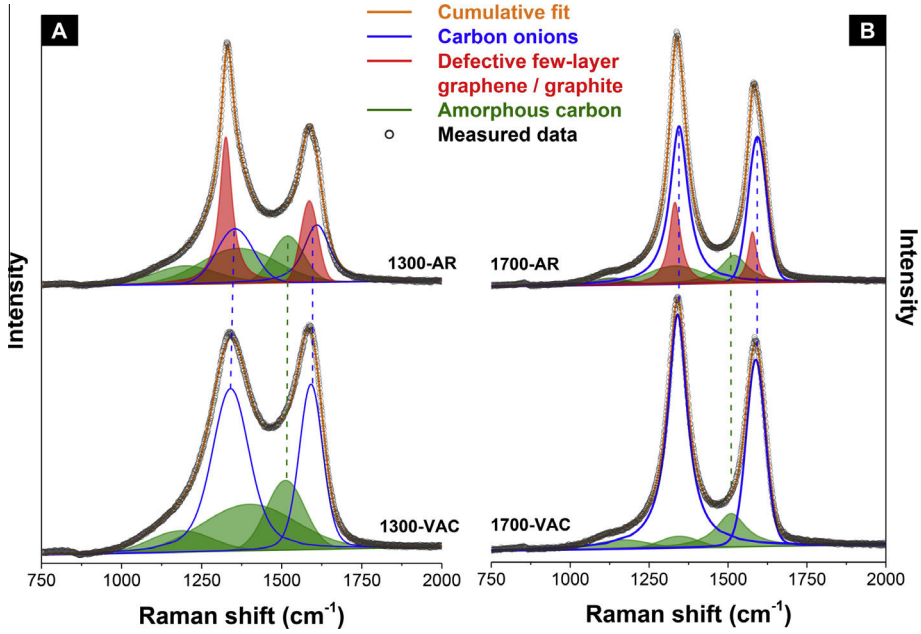

Fig. 3. Raman spectra of (A) 1300-AR and 1300-VAC and (B) 1700-AR and 1700-VAC. Peak fitting was applied using Voigt line shapes.

Table 3
Surface area and pore volume values derived from gas sorption isotherms using nitrogen gas sorption (QSDFT) as well as carbon dioxide gas sorption (NLDFT), and the calculated SSA using the model from [7] derived from the pycnometric density.

N_2 sorption	BET SSA (m^2/g)	QSDFT SSA (m^2/g)	Pore volume (cm^3/g)	Skeletal density (g/cm^3)	Calculated SSA (m^2/g)
1300-AR	356	323	1.109	2.42 ± 0.03	300 ± 14
1300-VAC	314	291	1.109	2.36 ± 0.01	305 ± 16
1700-AR	430	404	1.230	1.91 ± 0.01	351 ± 18
1700-VAC	364	340	1.304	1.97 ± 0.01	344 ± 17

CO_2 sorption	Ultramicropore volume (cm^3/g)
1300-AR	0.052
1300-VAC	0.038
1700-AR	0.068
1700-VAC	0.051

nanocrystalline graphite should be at ca. 1600 cm^{-1} [72]. This is larger than what we see for 1300-VAC due to the combination of different types of defects, a confinement due to the nanoscopic size, and defected sixfold rings. Considering the nanocrystalline (nc) and defective character of carbon onions, the Raman spectrum can be best discussed in view of the three stage model for carbon transition by Ferrari and Robertson [72]. This model assumes that ideal graphite is first transformed to nanocrystalline graphite due to a decrease in mean grain size and then the nanocrystalline graphite transforms to sp^2-hybridized amorphous carbon with bond length variation and distorted carbon six-rings [72]. This means that the G-mode position is effectively a combination of the first two stages in the amorphization trajectory from Ferrari and Robertson leading to smaller G-mode position than for nc graphite but still larger than in ideal graphite. For 1300-AR, the FWHMs of D- and G-mode are similar to those of 1300-VAC indicating the same kind of incompletely graphitized material. This is supported by a similar I_D/I_G ratio and the similarity of the carbon onion phase from argon and vacuum annealing demonstrates that the carbon onions themselves are not directly affected by the synthesis atmosphere (Table 2).

When annealing in argon, the Raman spectrum can only be adequately deconvoluted when assuming besides some amounts of amorphous carbon and carbon onions also few-layer graphene nanoribbons as a third carbon phase. As exemplified for 1300-AR, this additional nanocarbon phase is composed of defective few-layer graphene nanoribbons, presenting very sharp peaks with a FWHM of 47 and 64 cm^{-1} for the D- and the G-mode (Table 2). Such sharp Raman modes indicate a much more graphitic character compared to the carbon onions. The G-mode is located at 1585 cm^{-1}, which is slightly larger than for perfect graphite and a large I_D/I_G demonstrates the nanocrystalline nature [72]. The same phase analysis was used for the samples synthesized at 1700 °C (Fig. 3B). Compared to 1300 °C, the Raman signal for amorphous carbon found in the material after annealing at 1700 °C is smaller and the signal for carbon onions is larger. Yet, an adequate fit can only be obtained when assuming the presence of some amounts of amorphous carbon. It is indicated that the remaining amorphous carbon at 1300 °C is transformed to a more graphitic material. This is supported by the decrease in FWHM of the D- and G-mode for both synthesis atmospheres. For 1700-AR, also a second phase consisting of graphitic nanoribbons is present similar to 1300-AR.

X-ray diffractogramms of the samples, including the ND material, are shown in Fig. 2D. With increasing synthesis temperature, the signal intensity of the (002)-graphite reflection (26° 2θ for 1300-VAC) increases, whereas the (111)-diamond signal (43.8° 2θ for 1300-VAC) decreases and vanishes at 1700 °C completely with the emergence of the (100)-graphite signal [23]. Yet, all samples obtained after annealing at 1300 °C show still the presence of a small amount of the diamond phase. This aligns with the literature, where it was shown that a small diamond core may remain at 1300 °C, especially for NDs with a larger diameter of up to 10 nm [7,23]. The diffraction pattern of 1300-VAC and 1300-AR are virtually indistinguishable. Finally, thermal annealing at 1700 °C yields a nearly complete transformation from ND to carbon onion with a large (002)-graphite reflection and a vanishing (111)-diamond reflection. 1700-AR shows an asymmetric (002)-graphite reflection with a sharp maximum at 25.7° 2θ.

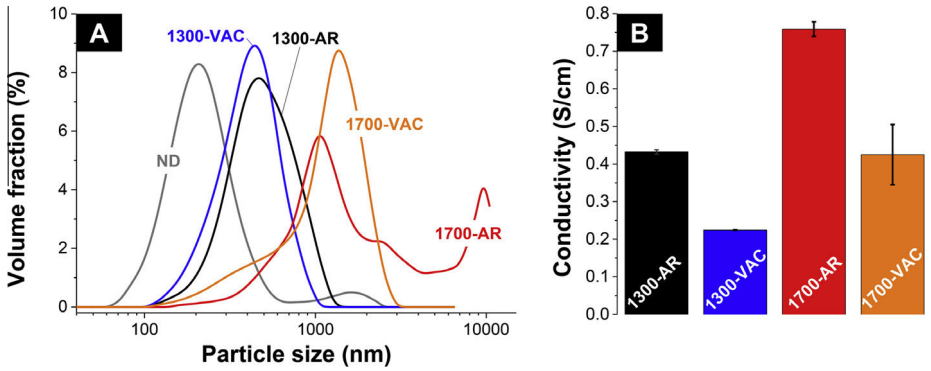

Fig. 4. Particle- and agglomerate size distributions measured using DLS (A) and electrical conductivity of film electrodes (10 mass% PTFE) using 4-point probe (B).

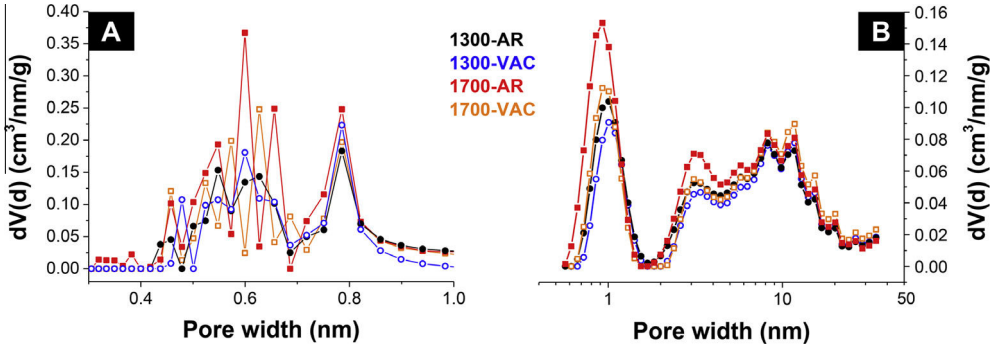

Fig. 5. Pore size distributions derived from the gas sorption isotherms using carbon dioxide with NLDFT deconvolution (A) and nitrogen gas sorption with QSDFT deconvolution (B).

These characteristics align again well with the presence of two different carbon structures (i.e., carbon onions and graphitic nanoribbons).

XRD measurements are in good agreement with the skeletal densities measured by pycnometry (Table 3). Carbon onion samples synthesized using the same annealing temperature show an almost identical density: 2.42 ± 0.03 and 2.36 ± 0.01 g/cm^3 for 1300-AR and 1300-VAC, respectively, and 1.91 ± 0.01 and 1.98 ± 0.01 g/cm^3 for 1700-AR and 1700-VAC, respectively (Table 3). Using a reducing-sphere-model [21], this computes to a diamond mass fraction in the range of ~50% for 1300 °C and less than 10% for 1700 °C in agreement with the literature [73,74].

3.1.3. Particle agglomeration and electrode conductivity

The pronounced tendency of ND powders to form agglomerates of several hundreds of nanometers is well known from earlier studies [7,30,31]. The ND powder used in our study showed as a dispersion in water a bimodal size distribution with a large peak at ~200 nm and a second much smaller maximum at 1.5 µm (Fig. 4A). After thermal annealing, we see an increase in the primary particle size due to a volume expansion from pycnometric measurements and TEM micrographs; this is accompanied by an increase in agglomerate size due to additional sintering and redistribution of carbon [7,21]. This effect is much more pronounced after annealing at 1700 °C than for 1300 °C, in agreement with Ref. [7].

Carbon onions synthesized in flowing argon show consistently larger agglomerate sizes compared to vacuum annealing for both studied synthesis temperatures (Fig. 4A). While this difference is expressed rather in a general shift of the monomodal particle size distribution for samples annealed at 1300 °C, we see a multimodal particle size distribution for 1700-AR. This strong agglomeration behavior is not the result of additional surface functional groups because no significant change in chemical composition was detected (Table 1). In agreement with Raman spectroscopy, XRD, and TEM, 1300-AR and 1700-AR built larger few-layer graphene nanoribbons which interconnect the carbon onions to form larger agglomerates.

The nanoscopic formation of graphitic ribbons and particle–particle-sintering also impacts on the electrical conductivity. Film electrodes with ~200 µm thickness (10 mass% of PTFE) were used to more accurately reflect the effectively usable conductivity and measurement inconsistencies when investigating non-compacted powders. As shown in Fig. 4B, the presence of graphitic ribbons between carbon onions lead to a higher electrode conductivity when comparing 1300-AR and 1700-AR with 1300-VAC and 1700-VAC. As a result, the electrical conductivity of 1300-AR (0.43 S/cm) is as high as 1700-AR (0.42 S/cm) although the annealing temperature has been much lower. When comparing only carbon onions annealed either in flowing argon or vacuum, we see an increase in electrical conductivity with higher synthesis temperature, in agreement with the literature [6,53].

3.1.4. Porosity analysis

The pore size distribution pattern derived from CO_2 and N_2 gas sorption are shown in Fig. 5A and B, respectively. Correspondingly, the calculated pore characteristics are provided in Table 3. Using CO_2 sorption for micropores smaller than ca. 1 nm, no significant difference between carbon onions synthesized in different atmospheres can be seen. The distribution patterns are characterized by pores between 0.4 and 0.9 nm and belong to interparticle pores because carbon onions must be considered as intrinsically non-porous carbon nanoparticles [7]. At higher synthesis temperature, the total pore volume increases and higher distribution peaks

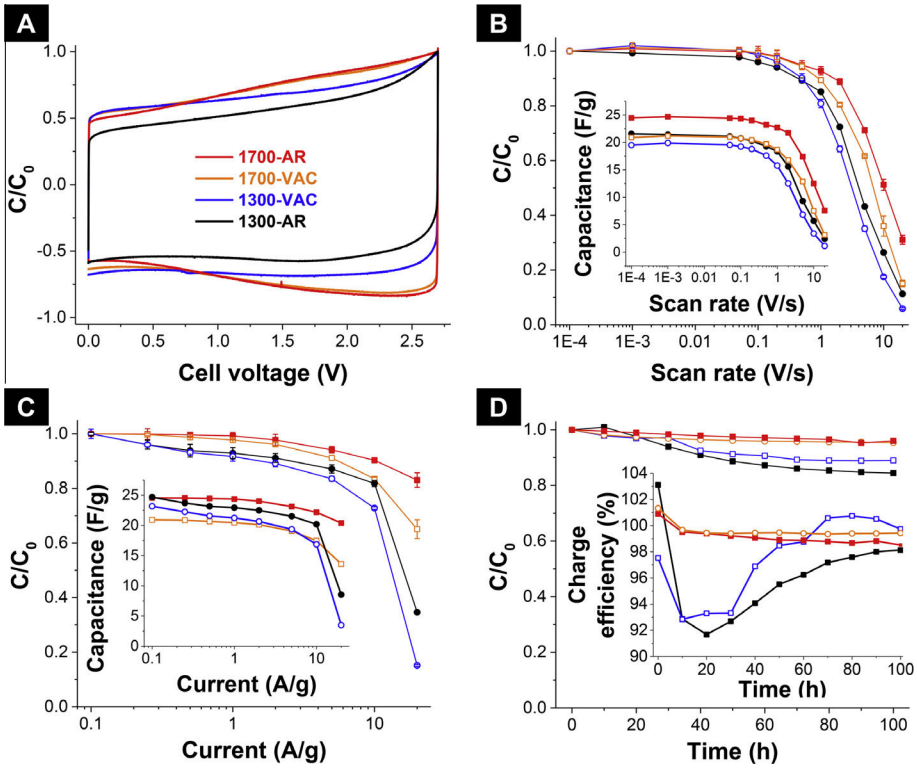

Fig. 6. Cyclic voltammograms (A), capacitance dependent on the scan rate and capacitance retention for different scan rates (B), galvanostatic cycling using different current densities (C), and long-time voltage floating test with the charge efficiency (charge/discharge capacitance) at a rate of 0.5 A/g (D). All measurements were performed in 1 M TEA-BF_4 in ACN using a 2-electrode configuration and a cell voltage of 2.7 V. The color-coding for all panels is the same (as provided in panel A). (For interpretation of the references to colour in this figure legend, the reader is referred to the web version of this article.)

can be seen for carbon dioxide and nitrogen sorption data. This pore volume increase stems from the volume expansion of the particles and the decrease in density. In ND powder, the individual particles stick strongly together. During annealing the particles expand and free volume is generated between the particles.

The PSDs derived from nitrogen gas sorption can be differentiated into pores related to particles in direct contact (for pores <1 nm), particles separated by spacer particles (at 1 nm pore size and between 2 and 20 nm), and pores between particle agglomerates [7,75]. We see an enhanced porosity for carbon onions annealed in flowing argon particularly in the range between 0.6 and 1.5 nm and a shift of the PSDs to smaller pore sizes (Fig. 5B). The increased pore volume for 1300-AR and 1700-AR can be explained by a smaller particle size and few-layer graphene nanoribbons between the particles. Additionally, there is necking of carbon onion particles and we also have to consider partially amorphous carbon between the particles. By etching the outer shells and the removal of amorphous carbon, the particle–particle connections are primarily removed and additional pore volume is created. This is supported by the redistribution of carbon to few-layer graphene nanoribbons between the particles leading to additional surface area. The smaller size of the particles alone cannot explain the shift to smaller pores because local particle sintering prevents the dynamic response of the carbon onions by a particle rearrangement when the size is reduced. Therefore, the removal of particle–particle connections is the main reason for the increase in pore volume. In addition, the formation of few-layer graphene nanoribbons between the particles effectively decreases the pore size between the particles.

It can be seen from the data in Table 3 that the surface area for carbon onions synthesized in argon is always larger, with a BET SSA of 356 and 430 m^2/g for 1300-AR and 1700-AR, respectively, compared to 314 and 364 m^2/g for 1300-VAC and 1700-VAC, respectively. Using the geometric pore model from Ref. [7], it is possible to calculate the SSA based on the measured particle density and assuming a spherical shape. As seen from Table 3, the calculated values agree very well with the measured SSA data for vacuum annealed samples. The values for carbon onions obtained from annealing in argon are always slightly larger indicating the existence of additional surface area not coming from the particles themselves. This additional surface area is related to the redistribution of carbon atoms and the formation of few-layer graphene nanoribbons between the particles, in agreement with XRD, Raman spectroscopy, and TEM measurements.

3.2. Electrochemical performance

Electrochemical characterization in organic electrolyte was performed on PTFE-bound carbon onion electrodes using cyclic voltammetry and galvanostatic cycling. Cyclic voltammograms were measured from 0 to 2.7 V which is the maximum electrochemical voltage window for acetonitrile based electrolytes (Fig. 5A) [76]. The cyclic voltammograms were normalized to the capacitance at 2.7 V. The CVs present a fast response with rectangular shapes indicative of near-ideal capacitive behavior. Carbon onions synthesized at 1300 °C show a rapid increase in current at 2.5 V, indicating the onset of electrolyte degradation due to high oxygen contents. In contrast, the more graphitic and less oxygen rich carbon onions after annealing at 1700 °C show no electrolyte degradation. This is in line with a recent study that showed improved electrochemical stability and enhanced Coulombic efficiency of carbide-derived carbons after post-synthesis treatment via high temperature vacuum annealing [77]. Electrolyte degradation will be further discussed using long-time voltage floating test

in Fig. 5D. Carbon onions obtained by annealing at 1700 °C also show a very distinct capacitance increase in the CV with increased cell voltage. The resulting CV shape is commonly referred to as butterfly-shape and is characteristic of a material with a high degree of carbon ordering [45].

To investigate in more detail the power handling, we plotted in Fig. 5B the capacitance versus the applied scan rate (derived from cyclic voltammograms) and in Fig. 5C versus the current density in a potential window from 0 to 2.7 V (derived from galvanostatic cycling). The measured capacitance from GCPL testing at 1 A/g varies between 24 and 20 F/g for 1700-AR and 1700-VAC, respectively, and 22 and 21 F/g for 1300-AR and 1300-VAC, respectively. Such values are typical for carbon onion supercapacitors with a surface area between 300 and 450 m^2/g [45,53]. The capacitance values differ only slightly from sample to sample because of the minor differences in SSA; still, 1700-AR shows the highest capacitance value as it has the largest SSA. Fig. 5B, C demonstrates the rate handling behavior using cycling voltammetry and galvanostatic cycling and show the same trend. 1700-AR demonstrates a superior rate handling capability with still more than 50% of the initial capacitance at 10 V/s scan rate and more than 90% at 10 A/g current density. Using the same synthesis temperature but applying vacuum (1700-VAC), the rate handling is severely lowered with only 36% of the initial capacitance at 10 V/s and 84% at 10 A/g. Carbon onions synthesized at 1300 °C demonstrate a lower rate handling due to the lower degree of carbon ordering and the lower conductivity, in agreement with literature [6,45,53].

Due to the electrolyte decomposition above 2.5 V (Fig. 5A), we see an enhanced degradation for samples synthesized at 1300 °C during long-time voltage floating at 2.7 V (Fig. 5D) with 85% and 90% initial capacitance for 1300-AR and 1300-VAC. It can be expected that higher contents of oxygen might lead to electrolyte degradation for the low temperature carbon onions (see Table 1). This is supported by the charge efficiency (relative change of charge/discharge) shown in Fig. 6A. For the carbon onions obtained at 1700 °C, no significant change in charge efficiency is observed demonstrating the high electrochemical stability. In comparison, the low temperature carbon onions present a lower charge efficiency of ~92% until 50 h floating time. This indicates a chemical reaction of the functional groups with the electrolyte leading to the mentioned degradation. After 50 h floating time, (practically) all functional groups have reacted and the charge efficiency approaches 100%. The degradation of the electrolyte leads to the blocking of pores and accordingly to the decrease in capacitance (Fig. 5D).

4. Conclusions

This study presents the influence of the synthesis atmosphere on nanodiamond-derived carbon onions. We used high vacuum and flowing argon atmosphere with ultrafast heating/cooling and two synthesis temperatures, 1300 and 1700 °C. It was shown that high-dynamic synthesis in vacuum leads to nearly perfect carbon onions with spherical shape and low amounts of interparticle carbon. In comparison, when only using flowing argon as synthesis atmosphere, oxygen containing desorbing gases were not removed and start partially etching the carbon, leading in the formation of few-layer graphene nanoribbons between the particles. This composition leads to higher surface area, higher conductivity, and better rate handling behavior as a supercapacitor electrode material in organic electrolyte for both synthesis atmospheres. Higher synthesis temperatures also yielded carbons lower in carbon heteroatom concentration and a higher electrochemical stability.

Acknowledgements

We acknowledge funding from the German Federal Ministry for Research and Education (BMBF) in support of the nanoEES^{3D} project (award number 03EK3013) as part of the strategic funding initiative energy storage framework. The authors thank Prof. Eduard Arzt for his continuing support, Rudolf Karos for XRD measurements, and Dr. Claudia Fink-Straube for the CHNS and ICP-OES analysis (all at the INM).

References

[1] A. Hirsch, The era of carbon allotropes, Nat. Mater. 9 (11) (2010) 868–871.
[2] Y. Gogotsi, V. Presser, Carbon Nanomaterials, CRC Press, 2013.
[3] D. Ugarte, Curling and closure of graphitic networks under electron-beam irradiation, Nature 359 (6397) (1992) 707–709.
[4] S. Iijima, Direct observation of the tetrahedral bonding in graphitized carbon black by high resolution electron microscopy, J. Cryst. Growth 50 (3) (1980) 675–683.
[5] I. Suarez-Martinez, N. Grobert, C.P. Ewels, Nomenclature of sp 2 carbon nanoforms, Carbon 50 (3) (2012) 741–747.
[6] C. Portet, G. Yushin, Y. Gogotsi, Electrochemical performance of carbon onions, nanodiamonds, carbon black and multiwalled nanotubes in electrical double layer capacitors, Carbon 45 (13) (2007) 2511–2518.
[7] M. Zeiger, N. Jäckel, M. Aslan, D. Weingarth, V. Presser, Understanding structure and porosity of nanodiamond-derived carbon onions, Carbon 84 (2015) 584–598.
[8] M. Zhao, H. Song, X. Chen, W. Lian, Large-scale synthesis of onion-like carbon nanoparticles by carbonization of phenolic resin, Acta Mater. 55 (18) (2007) 6144–6150.
[9] H. Lange, M. Sioda, A. Huczko, Y. Zhu, H. Kroto, D. Walton, Nanocarbon production by arc discharge in water, Carbon 41 (8) (2003) 1617–1623.
[10] M. Ishigami, J. Cumings, A. Zettl, S. Chen, A simple method for the continuous production of carbon nanotubes, Chem. Phys. Lett. 319 (5) (2000) 457–459.
[11] N. Sano, H. Wang, M. Chhowalla, I. Alexandrou, G. Amaratunga, Nanotechnology: synthesis of carbon 'onions' in water, Nature 414 (6863) (2001) 506–507.
[12] F. Banhart, T. Füller, P. Redlich, P. Ajayan, The formation, annealing and self-compression of carbon onions under electron irradiation, Chem. Phys. Lett. 269 (3) (1997) 349–355.
[13] B. Maquin, A. Derré, C. Labrugère, M. Trinquecoste, P. Chadeyron, P. Delhaès, Submicronic powders containing carbon, boron and nitrogen: their preparation by chemical vapour deposition and their characterization, Carbon 38 (1) (2000) 145–156.
[14] V. Serin, R. Brydson, A. Scott, Y. Kihn, O. Abidate, B. Maquin, et al., Evidence for the solubility of boron in graphite by electron energy loss spectroscopy, Carbon 38 (4) (2000) 547–554.
[15] C. He, N. Zhao, C. Shi, X. Du, J. Li, Carbon nanotubes and onions from methane decomposition using Ni/Al catalysts, Mater. Chem. Phys. 97 (1) (2006) 109–115.
[16] S. Tsai, C. Lee, C. Chao, H. Shih, A novel technique for the formation of carbon-encapsulated metal nanoparticles on silicon, Carbon 38 (5) (2000) 781–785.
[17] J. Huang, H. Yasuda, H. Mori, Highly curved carbon nanostructures produced by ball-milling, Chem. Phys. Lett. 303 (1) (1999) 130–134.
[18] T. Cabioc'h, M. Jaouen, E. Thune, P. Guerin, C. Fayoux, M. Denanot, Carbon onions formation by high-dose carbon ion implantation into copper and silver, Surf. Coat. Technol. 128 (2000) 43–50.
[19] E. Thune, T. Cabioc'h, P. Guérin, M.-F. Denanot, M. Jaouen, Nucleation and growth of carbon onions synthesized by ion-implantation: a transmission electron microscopy study, Mater. Lett. 54 (2) (2002) 222–228.
[20] A.V. Gubarevich, J. Kitamura, S. Usuba, H. Yokoi, Y. Kakudate, O. Odawara, Onion-like carbon deposition by plasma spraying of nanodiamonds, Carbon 41 (13) (2003) 2601–2606.
[21] Y.V. Butenko, V.L. Kuznetsov, A.L. Chuvilin, V.N. Kolomiichuk, S.V. Stankus, R.A. Khairulin, et al., Kinetics of the graphitization of dispersed diamonds at "low" temperatures, J. Appl. Phys. 88 (7) (2000) 4380.
[22] V.L. Kuznetsov, A.L. Chuvilin, Y.V. Butenko, I.Y. Mal'kov, V.M. Titov, Onion-like carbon from ultra-disperse diamond, Chem. Phys. Lett. 222 (4) (1994) 343–348.
[23] S. Tomita, A. Burian, J.C. Dore, D. LeBolloch, M. Fujii, S. Hayashi, Diamond nanoparticles to carbon onions transformation: X-ray diffraction studies, Carbon 40 (9) (2002) 1469–1474.
[24] Q. Zou, Y.G. Li, B. Lv, M.Z. Wang, L.H. Zou, Y.C. Zhao, Transformation of onion-like carbon from nanodiamond by annealing, Inorg. Mater. 46 (2) (2010) 127–131.
[25] O.O. Mykhaylyk, Y.M. Solonin, D.N. Batchelder, R. Brydson, Transformation of nanodiamond into carbon onions: A comparative study by high-resolution transmission electron microscopy, electron energy-loss spectroscopy, X-ray diffraction, small-angle X-ray scattering, and ultraviolet Raman spectroscopy, J. Appl. Phys. 97 (7) (2005).

[26] V. Kuznetsov, Y.V. Butenko, Nanodiamond graphitization and properties of onion-like carbon, in: Synthesis, Properties and Applications of Ultra nanocrystalline Diamond, Springer, 2005, pp. 199–216.
[27] X. Fang, J. Mao, E. Levin, K. Schmidt-Rohr, Nonaromatic core–shell structure of nanodiamond from solid-state NMR spectroscopy, J. Am. Chem. Soc. 131 (4) (2009) 1426–1435.
[28] A. Panich, A. Shames, H.-M. Vieth, E. Ōsawa, M. Takahashi, A.Y. Vul, Nuclear magnetic resonance study of ultrananocrystalline diamonds, Eur. Phys. J. B 52 (3) (2006) 397–402.
[29] M. Dubois, K. Guérin, E. Petit, N. Batisse, A. Hamwi, N. Komatsu, et al., Solid-state NMR study of nanodiamonds produced by the detonation technique, J. Phys. Chem. C 113 (24) (2009) 10371–10378.
[30] V.N. Mochalin, O. Shenderova, D. Ho, Y. Gogotsi, The properties and applications of nanodiamonds, Nat. Nanotechnol. 7 (1) (2012) 11–23.
[31] A. Krüger, F. Kataoka, Ozawa Maa, T. Fujino, Y. Suzuki, A. Aleksenskii, et al., Unusually tight aggregation in detonation nanodiamond: identification and disintegration, Carbon 43 (8) (2005) 1722–1730.
[32] D.P. Mitev, A.T. Townsend, B. Paull, P.N. Nesterenko, Direct sector field ICP-MS determination of metal impurities in detonation nanodiamond, Carbon 60 (2013) 326–334.
[33] V. Kuznetsov, Y.V. Butenko, Synthesis and properties of nanostructured carbon materials: nanodiamond, onion-like carbon and carbon nanotubes, in: Nanostructured Materials and Coatings for Biomedical and Sensor Applications, Springer, 2003, pp. 187–202.
[34] F. Cataldo, A.P. Koscheev, A study on the action of ozone and on the thermal stability of nanodiamond, Fullerenes, Nanotubes, Carbon Nanostruct. 11 (3) (2003) 201–218.
[35] T. Jiang, K. Xu, FTIR study of ultradispersed diamond powder synthesized by explosive detonation, Carbon 33 (12) (1995) 1663–1671.
[36] B. Spitsyn, M. Gradoboev, T. Galushko, T. Karpukhina, N. Serebryakova, I. Kulakova, et al., Purification and functionalization of nanodiamond, in: Synthesis, Properties and Applications of Ultrananocrystalline Diamond, Springer, 2005, pp. 241–252.
[37] Y.V. Butenko, V.L. Kuznetsov, E.A. Paukshtis, A.I. Stadnichenko, I.N. Mazov, S.I. Moseenkov, et al., The thermal stability of nanodiamond surface groups and onset of nanodiamond graphitization, Fullerenes, Nanotubes, Carbon Nanostruct. 14 (2–3) (2006) 557–564.
[38] Q. Zou, M.Z. Wang, Y.G. Li, Onion-like carbon synthesis by annealing nanodiamond at lower temperature and vacuum, J. Exp. Nanosci. 5 (5) (2010) 375–382.
[39] K. Bogdanov, A. Fedorov, V. Osipov, T. Enoki, K. Takai, T. Hayashi, et al., Annealing-induced structural changes of carbon onions: high-resolution transmission electron microscopy and Raman studies, Carbon 73 (2014) 78–86.
[40] V.L. Kuznetsov, Y.V. Butenko, Chapter 7 – diamond phase transitions at nanoscale, in: O.A.S.M. Gruen (Ed.), Ultrananocrystalline Diamond, second ed., William Andrew Publishing, Oxford, 2012, pp. 181–244.
[41] S. Tomita, T. Sakurai, H. Ohta, M. Fujii, S. Hayashi, Structure and electronic properties of carbon onions, J. Chem. Phys. 114 (17) (2001) 7477.
[42] N. Xu, J. Chen, S. Deng, Effect of heat treatment on the properties of nano-diamond under oxygen and argon ambient, Diam. Relat. Mater. 11 (2) (2002) 249–256.
[43] A. Aleksenskii, M. Baidakova, A.Y. Vul, V.Y. Davydov, Y.A. Pevtsova, Diamond-graphite phase transition in ultradisperse-diamond clusters, Phys. Solid State 39 (6) (1997) 1007–1015.
[44] M. Baidakova, V. Siklitsky, A.Y. Vul, Ultradisperse-diamond nanoclusters. Fractal structure and diamond–graphite phase transition, Chaos, Solitons Fractals 10 (12) (1999) 2153–2163.
[45] D. Weingarth, M. Zeiger, N. Jäckel, M. Aslan, G. Feng, V. Presser, Graphitization as a universal tool to tailor the potential-dependent capacitance of carbon supercapacitors, Adv. Energy Mater. (2014).
[46] O.E. Andersson, B. Prasad, H. Sato, T. Enoki, Y. Hishiyama, Y. Kaburagi, et al., Structure and electronic properties of graphite nanoparticles, Phys. Rev. B 58 (24) (1998) 16387.
[47] J. Chen, S. Deng, J. Chen, Z. Yu, N. Xu, Graphitization of nanodiamond powder annealed in argon ambient, Appl. Phys. Lett. 74 (24) (1999) 3651–3653.
[48] F.Y. Xie, W.G. Xie, L. Gong, W.H. Zhang, S.H. Chen, Q.Z. Zhang, et al., Surface characterization on graphitization of nanodiamond powder annealed in nitrogen ambient, Surf. Interface Anal. 42 (9) (2010) 1514–1518.
[49] A. Aleksenskii, M. Baidakova, A.Y. Vul, A. Dideikin, V. Siklitskii, Effect of hydrogen on the structure of ultradisperse diamond, Phys. Solid State 42 (8) (2000) 1575–1578.
[50] T. Evans, Changes produced by high temperature treatment of diamond, in: The Properties of Diamond, 1979, pp. 403–424.
[51] B. Palosz, E. Grzanka, C. Pantea, T. Zerda, Y. Wang, J. Gubicza, et al., Microstructure of nanocrystalline diamond powders studied by powder diffractometry, J. Appl. Phys. 97 (6) (2005) 064316.
[52] J. Qian, C. Pantea, G. Voronin, T. Zerda, Partial graphitization of diamond crystals under high-pressure and high-temperature conditions, J. Appl. Phys. 90 (3) (2001) 1632–1637.
[53] J.K. McDonough, A.I. Frolov, V. Presser, J. Niu, C.H. Miller, T. Ubieto, et al., Influence of the structure of carbon onions on their electrochemical performance in supercapacitor electrodes, Carbon 50 (9) (2012) 3298–3309.
[54] V. Kuznetsov, Y.V. Butenko, V. Zaikovskii, A. Chuvilin, Carbon redistribution processes in nanocarbons, Carbon 42 (5) (2004) 1057–1061.
[55] G.Y. Gor, M. Thommes, K.A. Cychosz, A.V. Neimark, Quenched solid density functional theory method for characterization of mesoporous carbons by nitrogen adsorption, Carbon 50 (4) (2012) 1583–1590.
[56] P.I. Ravikovitch, A. Vishnyakov, A.V. Neimark, Density functional theories and molecular simulations of adsorption and phase transitions in nanopores, Phys. Rev. E 64 (1) (2001) 011602.
[57] S. Brunauer, P.H. Emmett, E. Teller, Adsorption of gases in multimolecular layers, J. Am. Chem. Soc. 60 (2) (1938) 309–319.
[58] A. Vishnyakov, P.I. Ravikovitch, A.V. Neimark, Molecular level models for CO_2 sorption in nanopores, Langmuir 15 (25) (1999) 8736–8742.
[59] O. Shenderova, V. Zhirnov, D. Brenner, Carbon nanostructures, Crit. Rev. Solid State Mater. Sci. 27 (3–4) (2002) 227–356.
[60] V. Danilenko, Synthesis and Sintering of Diamond by Detonation, Energoatomizdat, Moscow, 2003. 271.
[61] V. Loktev, V. Makal'skii, I. Stoyanova, A. Kalinkin, V. Likholobov, V. Mit'kin, Surface modification of ultradispersed diamonds, Carbon 29 (7) (1991) 817–819.
[62] T. Jiang, K. Xu, S. Ji, FTIR studies on the spectral changes of the surface functional groups of ultradispersed diamond powder synthesized by explosive detonation after treatment in hydrogen, nitrogen, methane and air at different temperatures, J. Chem. Soc., Faraday Trans. 92 (18) (1996) 3401–3406.
[63] E. Mironov, E. Petrov, A. Koretz, Chemical aspect of ultradispersed diamond formation, Diam. Relat. Mater. 12 (9) (2003) 1472–1476.
[64] V. Kuznetsov, M. Aleksandrov, I. Zagoruiko, A. Chuvilin, E. Moroz, V. Kolomiichuk, et al., Study of ultradispersed diamond powders obtained using explosion energy, Carbon 29 (4) (1991) 665–668.
[65] E. Mironov, A. Koretz, E. Petrov, Detonation synthesis ultradispersed diamond structural properties investigation by infrared absorption, Diam. Relat. Mater. 11 (3) (2002) 872–876.
[66] A. Bianco, H.-M. Cheng, T. Enoki, Y. Gogotsi, R.H. Hurt, N. Koratkar, et al., All in the graphene family – a recommended nomenclature for two-dimensional carbon materials, Carbon 65 (2013) 1–6.
[67] F. Tuinstra, Raman spectrum of graphite, J. Chem. Phys. 53 (3) (1970) 1126.
[68] C. Thomsen, S. Reich, Double resonant Raman scattering in graphite, Phys. Rev. Lett. 85 (24) (2000) 5214.
[69] L. Cançado, M. Pimenta, B. Neves, G. Medeiros-Ribeiro, T. Enoki, Y. Kobayashi, et al., Anisotropy of the Raman spectra of nanographite ribbons, Phys. Rev. Lett. 93 (4) (2004) 047403.
[70] Q. Zou, M.Z. Wang, Y.G. Li, B. Lv, Y.C. Zhao, HRTEM and Raman characterisation of the onion-like carbon synthesised by annealing detonation nanodiamond at lower temperature and vacuum, J. Exp. Nanosci. 5 (6) (2010) 473–487.
[71] A. Ferrari, J. Robertson, Interpretation of Raman spectra of disordered and amorphous carbon, Phys. Rev. B 61 (20) (2000) 14095.
[72] A.C. Ferrari, J. Robertson, Raman spectroscopy of amorphous, nanostructured, diamond-like carbon, and nanodiamond, Philos. Trans. A Math. Phys. Eng. Sci. 2004 (362) (1824) 2477–2512.
[73] A. Ferrari, A. Libassi, B. Tanner, V. Stolojan, J. Yuan, L. Brown, et al., Density, sp 3 fraction, and cross-sectional structure of amorphous carbon films determined by X-ray reflectivity and electron energy-loss spectroscopy, Phys. Rev. B 62 (16) (2000) 11089.
[74] V.L. Kuznetsov, I.L. Zilberberg, Y.V. Butenko, A.L. Chuvilin, B. Segall, Theoretical study of the formation of closed curved graphite-like structures during annealing of diamond surface, J. Appl. Phys. 86 (2) (1999) 863.
[75] M. Hantel, V. Presser, J. McDonough, G. Feng, P.T. Cummings, Y. Gogotsi, et al., In situ electrochemical dilatometry of onion-like carbon and carbon black, J. Electrochem. Soc. 159 (11) (2012) A1897–A1903.
[76] M. Lu, F. Beguin, E. Frackowiak, Supercapacitors: Materials, Systems and Applications, John Wiley & Sons, 2013.
[77] B. Dyatkin, Y. Gogotsi, Effects of structural disorder and surface chemistry on electric conductivity and capacitance of porous carbon electrodes, Faraday Discuss. 172 (2014) 139–162.

3.3 Review: carbon onions for electrochemical energy storage

Marco Zeiger,[1,2] Nicolas Jäckel,[1,2] Vadym Mochalin,[3] and Volker Presser[1,2]

1 *INM - Leibniz Institute for New Materials, 66123 Saarbrücken, Germany*
2 *Department of Materials Science and Engineering, Saarland University, 66123 Saarbrücken, Germany*
3 *Missouri University of Science & Technology, Rolla, MO 65409, United States of America*

Citation:
Zeiger, M.; Jäckel, N.; Mochalin, V. N.; Presser, V., Review: carbon onions for electrochemical energy storage. *J. Mater. Chem. A* **2016,** 4, 3172-3196. (DOI: 10.1039/C5TA08295A)

Own contribution: Design, planning, writing, synthesis, Raman spectroscopy, transmission electron microscopy, electrode preparation, conductivity measurements.

Abstract:
Carbon onions are a relatively new member of the carbon nanomaterials family. They consist of multiple concentric fullerene-like carbon shells which are highly defective and disordered. Due to their small size of typically below 10 nm, the large external surface area, and high conductivity they are used for supercapacitor applications. As electrode materials, carbon onions provide fast charge/discharge rates resulting in high specific power but present comparatively low specific energy. They improve the performance of activated carbon electrodes as conductive additives and show suitable properties as substrates for redox-active materials. This review provides a critical discussion of the electrochemical properties of different types of carbon onions as electrode materials. It also compares the general advantages and disadvantages of different carbon onion synthesis methods. The physical and chemical properties of carbon onions, in particular nanodiamond-derived carbon onions, are described with emphasis on those parameters especially important for electrochemical energy storage systems, including the structure, conductivity, and porosity. Although the primary focus of current research is on electrode materials for supercapacitors, the use of carbon onions as conductive additives and for redox-active species is also discussed.

Showcasing the review on electrochemical energy storage with carbon onions by the INM – Leibniz Institute for New Materials (Prof. Presser, M. Zeiger, N. Jäckel), Germany, and Prof. Mochalin (Missouri University of Science and Technology), USA.

Title: Review: carbon onions for electrochemical energy storage

Carbon onions are nanoscopic carbon spheres with tunable structure. The combination of highly accessible outer surface, high interparticle pore volume and high electrical conductivity has made carbon onions highly attractive for electrochemical applications. In particular, ultrafast supercapacitors, high performance pseudocapacitors, improved conductive additives for batteries and supercapacitors, and redox hybrids are being reviewed.

As featured in:

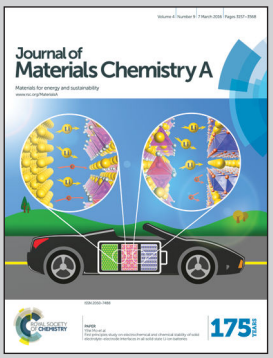

See Vadym N. Mochalin, Volker Presser *et al.*, *J. Mater. Chem. A*, 2016, **4**, 3172.

ROYAL SOCIETY OF CHEMISTRY

www.rsc.org/MaterialsA

Registered charity number: 207890

Journal of Materials Chemistry A

REVIEW

View Article Online
View Journal | View Issue

Cite this: J. Mater. Chem. A, 2016, 4, 3172

Review: carbon onions for electrochemical energy storage

Marco Zeiger,[ab] Nicolas Jäckel,[ab] Vadym N. Mochalin*[c] and Volker Presser*[ab]

Carbon onions are a relatively new member of the carbon nanomaterials family. They consist of multiple concentric fullerene-like carbon shells which are highly defective and disordered. Due to their small size of typically below 10 nm, the large external surface area, and high conductivity they are used for supercapacitor applications. As electrode materials, carbon onions provide fast charge/discharge rates resulting in high specific power but present comparatively low specific energy. They improve the performance of activated carbon electrodes as conductive additives and show suitable properties as substrates for redox-active materials. This review provides a critical discussion of the electrochemical properties of different types of carbon onions as electrode materials. It also compares the general advantages and disadvantages of different carbon onion synthesis methods. The physical and chemical properties of carbon onions, in particular nanodiamond-derived carbon onions, are described with emphasis on those parameters especially important for electrochemical energy storage systems, including the structure, conductivity, and porosity. Although the primary focus of current research is on electrode materials for supercapacitors, the use of carbon onions as conductive additives and for redox-active species is also discussed.

Received 15th October 2015
Accepted 7th December 2015

DOI: 10.1039/c5ta08295a

www.rsc.org/MaterialsA

1. Introduction

1.1 Electrochemical energy storage with nanocarbons

Carbon materials have always been at the focal point of energy applications, ranging from the ongoing use of coal as the primary energy source to the utilization as the standard anode material for lithium ion batteries. The emergence of new carbon nanoforms, foremost carbon nanotubes and graphene, has

[a]INM – Leibniz Institute for New Materials, 66123 Saarbrücken, Germany. E-mail: volker.presser@leibniz-inm.de
[b]Department of Materials Science and Engineering, Saarland University, 66123 Saarbrücken, Germany
[c]Missouri University of Science & Technology, Rolla, MO 65409, USA. E-mail: mochalinv@mst.edu

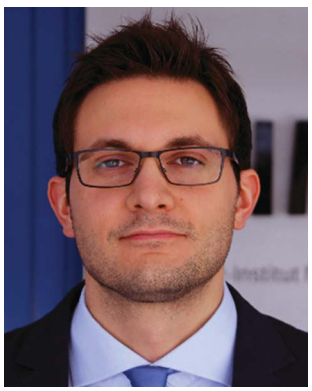

Marco Zeiger studied Microfabrication and Nanostructures in the Department of Physics and Mechatronics at Saarland University, Germany. Between 2011 and 2013 he worked in the Metallic Microstructures Group of the INM – Leibniz Institute for New Material on the antibacterial properties of copper and its application in touch surfaces. In 2013 he joined the INM Energy Materials Group working on the synthesis and characterization of nanodiamonds and carbon onions with the focus on electrochemical energy storage. Receiving his M.Sc., he began his PhD studies in 2014 on the development of carbon/metal oxide hybrid materials for redox-enabled energy storage devices.

Nicolas Jäckel studied Microfabrication and Nanostructures in the Department of Physics and Mechatronics at Saarland University, Germany. In 2012 he completed his Bachelors thesis on gas sensors at Drägerwerk AG & Co. KGaA, Lübeck. In 2013, he joined the INM Energy Materials Group working on atomic layer deposition and advanced supercapacitors. In 2015 he received his M.Sc. and started his PhD studies. In collaboration with the Group of Prof. Doron Aurbach, Bar-Ilan University, Israel, he is working on the in situ electrochemical methodology for tracking of charging and related mechanical processes in batteries and supercapacitors.

propelled research related to electrochemical energy storage and conversion, leading to what has been coined the "carbon new age".[1] Among all carbon nanoforms and allotropes, carbon onions are one of the most interesting. Carbon onions, also called onion-like carbon or carbon nano-onions, are nanoscopic carbon particles, with a nearly spherical shape made of multiple enclosed fullerene-like carbon shells. The unique combination of high electrical conductivity (comparable to carbon black), large external surface area, and nanoscopic size (commonly below 10 nm), alongside the possibility for large-scale synthesis and chemical modification,[2] has made this material very attractive for applications, ranging from lubrication and catalysis[3] to electrochemical energy storage (EES),[4] biomedical imaging,[2] and water treatment.[5] Carbon onions have been explored intensively for EES applications as electrode materials for ultrafast charge/discharge devices[6] or as a potent conductive additive to enhance the power handling ability of activated carbon.[7] With the increasing number of carbon onion studies for advanced electrochemical applications,[8,9] this review summarizes the state-of-the-art and provides a comprehensive overview of relevant topics of the structure as well as electrochemical and relevant properties of carbon onions.

Efficient and adaptable energy storage has emerged as a key enabling technology for the large scale utilization of renewable energy from sustainable ("green") sources, such as solar or wind power.[10,11] Carbon nanomaterials and hybrids have been at the focal point of many electrochemical energy storage technologies,[12,13] as exemplified by supercapacitors[14] or batteries.[15,16] The electrochemical energy storage mechanisms range from ion electrosorption and interfacial redox-reactions of the electrode material or bulk faradaic reactions of the electrolyte to ion intercalation into the anode or cathode.[12,17,18] The most prominent group of supercapacitors, the electrical double-layer capacitors (EDLCs), capitalizes on fast ion electrosorption to enable very high power handling.[14] Energy is stored at the electrode/electrolyte interface where electric charges are accumulated on the electrode surfaces and ions of opposite charge are arranged on the electrolyte side of both electrodes. A high electrosorption rate and the absence of (electro)chemical reactions (faradaic reactions) enable very high specific power of EDLCs at the cost of a rather low specific energy compared to batteries.[19] An approximate storage capacity for pure ion electrosorption is $\sim$0.1 F m^{-2} = 0.03 mA h m^{-2} at 1 V, when normalized to the surface area of a nanoporous carbon electrode.[20]

Considering the limitations of ion electrosorption in stored energy, it is intriguing to utilize faradaic reactions to enhance the energy storage capacity.[21] This can be achieved by adding redox-active materials, such as electroactive polymers, surface functional groups, transition metal oxides, or by using a redox-active electrolyte, such as the iodine/iodide redox couple.[17] Depending on the electrochemical response, the resulting behavior may be classified as capacitor-like (pseudocapacitor) or battery-like (sometimes referred to as the supercabattery).[18,22] Operation of such hybrid cells, in contrast to EDLCs, involves the charge transfer between the electrode and electrolyte where, for example, ruthenium changes its oxidation state from Ru(III) to Ru(VI).[23–26] Carbon onions, featuring a fully available outer surface, are a highly attractive material for hybrid designs because of the facile access to the surface and the ease of functionalization with, for example, metal oxides or surface groups, to enable enhanced energy storage capacity.[27] For a more substantial review of the energy storage technologies, such as supercapacitors, batteries, and hybrid devices, the reader is referred to recent comprehensive articles on these topics.[14,18,28]

1.2 What is a carbon onion?

Carbon onions can be defined by virtue of their structure as spherical or polyhedral carbon nanoparticles, often smaller

Vadym N. Mochalin received his PhD in Physical Chemistry from L. M. Litvinenko Institute of Physical Organic and Coal Chemistry, National Academy of Sciences of Ukraine, and M.S. in Biochemistry from Donetsk National University, Ukraine. In 2005–2015 he worked with Prof. Yury Gogotsi at Drexel University, leading the research on nanodiamonds. He is now Associate Professor in Chemistry at Missouri University of Science and Technology. His current research interests include synthesis, characterization, purification, chemical modification, computational modeling, and applications of nanodiamonds, MXene, nanoonions, nanocarbons, and other materials for composites, energy storage, biomedical applications, and extreme environments.

Volker Presser obtained his PhD in Applied Mineralogy in 2006 from the Eberhard Karls University in Tübingen, Germany. As a Humboldt Research Fellow and Research Assistant Professor, he worked between 2010 and 2012 at the A.J. Drexel Nanotechnology Institute in the team of Yury Gogotsi at Drexel University, Philadelphia, USA. As Chair for Energy Materials, he is Full Professor at the Department of Materials Science and Engineering at Saarland University and Group Leader at the INM – Leibniz Institute for New Materials in Saarbrücken, Germany. His research activities include nanocarbon and hybrid nanomaterials for electrochemical energy storage, harvesting, and water desalination.

than 10 nm, consisting of several fullerene-like carbon shells enclosed in a "Russian doll" manner which are defective and disordered to a certain degree.[29] This distinct multi-layer architecture is also the name-giving feature for carbon onions. First discovered by Iijima in 1980 and described by Ugarte in 1992,[30,31] carbon onions are a rather novel addition to the carbon materials family. Depending on their synthesis method and the synthesis parameters, the resulting carbon onions differ in size, chemical composition, phase, and morphology. The most commonly used synthesis method for carbon onions is graphitization of nanodiamonds at high temperatures (>1700 °C) in an inert gas or vacuum. The resulting carbon onions are typically smaller than 10 nm and present a high degree of carbon ordering. The amount of non-carbon material is very small (typically in the range of 1–2 mass%) and surface areas can reach up to 600 $m^2 g^{-1}$. Key structural characteristics of a carbon onion are summarized in Fig. 1, with more details about the synthesis methods given in the next section.[32]

1.3 Nomenclature

So far, there is no consistent nomenclature for carbon onions in the literature. Consistent nomenclature is a notorious issue throughout the entire field of nanocarbons, especially when it comes to rather new carbon structures.[33] Most reports, often interchangeably, use either "carbon onions", "carbon nano-onions", or "onion-like carbon". All three are not in agreement with the nomenclature for sp^2-hybridized carbon nanoforms by Suarez-Martinez, Grobert, and Ewels.[29] They suggest consistently calling carbons with an "onion" structure "multi-wall fullerene". This unifying nomenclature employs purely geometrical classification, independent of the state of carbon ordering (defects), particle size and shape, or synthesis method. When considering very large structures referred to as carbon onions with size more than 100 nm and a high defect density, the conceptual description as "fullerene", normally applied to molecules, may be arguable. On the other hand, onion-like carbon, which is an umbrella term for any onion-type structure is just as vague as other terms, like diamond-like carbon. Also, compared to carbon nanotubes, the differentiation between single-, double-, few-, and multi-wall architectures is not practical for carbon onions: almost all carbon onions qualify as multi-wall structures. Subtler differentiation in the name based on the shape ranging from spherical to polyhedral is also neither practical nor easily quantifiable. Based on considerations similar to those used in the nomenclature of carbon nanotubes, we suggest application of the term "carbon onions" only to those carbon particles that have at least 4 shells (like multi-wall carbon nanotubes), a size smaller than 100 nm, spherical or polyhedral shape, and a partially defective structure (amorphous domains, or islands of sp^3-hybridized carbon). The distinct structural characteristic defining carbon onions should be the clearly visible multi-shell character. This nomenclature also includes hollow carbon onions (hollow core), and carbon onions with a core (*e.g.*, metal clusters or residual nanodiamonds remaining inside the carbon onion due to incomplete transformation).

As with any other material, the issues related to nomenclature for carbon onions are much more difficult to address than in the nomenclature of molecules. The key reason for this, as the authors believe, is the undefined variable composition of a material, whereas the composition of molecules, by definition, is always fixed. Taking into consideration chemical modifications of materials, any attempts to use nomenclature in the sense it is applied to molecules, become meaningless. This necessitates alternative approaches to distinguish materials. A more practical differentiation is based on the type of precursor and/or the synthesis method. For example, clearly stating "nanodiamond-derived carbon onions" *versus* "arc-discharge carbon onions" unambiguously refers to a specific group of carbons.

Finally, the community may consider to adopt a size-dependent differentiation between carbon onions (in general) and carbon nano-onions, with the latter referring to carbon onions smaller than 10 nm. This suggestion is motivated by the differentiation between nanodiamonds and single-digit nanodiamonds, with the latter covering the range below 10 nm.[34] Yet, it is beyond the scope of this review to establish a clear nomenclature recommendation. Thus, in the absence of definite nomenclature, thorough and complete description of the

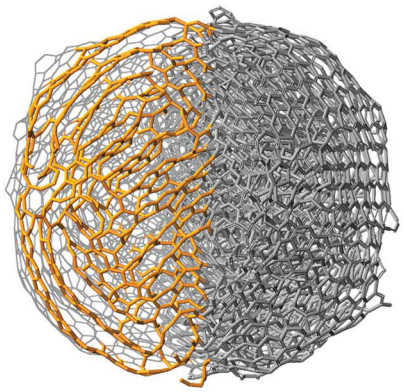

Fig. 1 Typical features of carbon onions.

experimental procedure and the obtained carbon onion structures becomes even more important to enable a scientifically useful basis for comparison.

2. Synthesis of carbon onions

2.1 Overview of synthesis methods

Different methods can be used for the synthesis of carbon onions, such as decomposition of carbon-containing precursors including combustion and detonation methods,[35–45] mechanical milling,[46,47] carbon ion implantation,[48,49] underwater arc discharge between graphite electrodes,[50–52] annealing of acetylene black in the presence of an iron catalyst,[53] or heating of a carbon filament in liquid alcohol.[54] Alternatively, carbon onions can also be derived *via* phase transformation of nanodiamonds by annealing in vacuum,[55–61] argon,[32,62–67] nitrogen,[68] hydrogen,[69] or helium,[27,70–75] plasma spraying of nanodiamonds,[76] laser irradiation of nanodiamonds in liquid alcohol,[77] electron beam irradiation of carbon materials,[30,78,79] or direct plasma treatment of coal.[80] The type of precursor and the synthesis conditions have a strong impact on the structure, as seen from transmission electron micrographs of different types of carbon onions given in Fig. 2, but all carbon onions share the multi-shell fullerene-like architecture.

In 1992, Daniel Ugarte observed the formation of carbon onions during electron beam irradiation of amorphous carbon particles in a transmission electron microscope (TEM).[30] Due to irradiation-stimulated graphitization, amorphous carbon can be transformed to nanometer-sized carbon onions with clearly visible nucleation centers (Fig. 2I). While scientifically intriguing, this method is limited in terms of the yield of synthesized carbon onions.[30]

The production of carbon onions *via* decomposition of carbon-containing precursors like CH_4 in the presence of Ni/Al composite catalysts (Fig. 2D) can be accomplished at rather moderate temperatures of 600 °C in hydrogen.[37] The resulting carbon onions showed a hollow structure with several carbon shells and a diameter larger than 30 nm. The catalytic decomposition enabled the formation of carbon onions with a metallic core. Hou *et al.* used a counterflow diffusion flame method (Fig. 2A) to obtain carbon onions on a nickel catalyst.[39] By mixing ethylene, methane, nitrogen, and oxygen, it was possible to control the yield as well as the size of carbon onions.[39] These synthesis methods, together with boron-doped carbon onions from chemical vapor deposition (Fig. 2P),[36] the carbonization of phenolic resin with ferric nitrate (Fig. 2F),[42] and carbon ion implantation in copper and silver (Fig. 2N),[48] present facile ways for the production of carbon onions, but may be disadvantageous due to a high amount of hetero-atoms in the product.

In a study by Choucair *et al.* (Fig. 2B), high purity carbon onions with more than 90 mass% carbon and no metal impurities were produced by a catalyst-free flash pyrolysis of naphthalene.[40] The particles of *ca.* 50 nm diameter were composed of highly defective carbon shells, as shown by Raman spectroscopy and TEM. Gao *et al.* (Fig. 2C) used laser-assisted combustion of C_2H_4 in air.[81] The resulting high purity carbon onions with a diameter of *ca.* 5 nm exhibited a high degree of sintering and the KOH activated materials showed a promising supercapacitor performance with a capacitance of up to 126 F g^{-1} in 2 M KNO_3 and a relatively high surface area of up to 804 m^2 g^{-1} (see Section 4.1 for further discussion).[81]

Underwater arc-discharge-derived carbon onions (Fig. 2M)[52] and nanodiamond-derived carbon onions (Fig. 2E) have been evaluated as electrodes for supercapacitors.[4,82–85] The advantages of these two synthesis methods are the high yield, the high purity, and the good controllability and reproducibility. Yet, not all synthesis routes reported in the context of carbon onion synthesis actually yielded carbon onions as defined above. For example, Fan *et al.* synthesized carbon particles by heating carbon in liquid alcohol; these particles had a nanoscopic size of ~50 nm, but without a multi-shell structure.[54] Structurally, such carbon nanoparticles are virtually indistinguishable from carbon black. Bystrzejewski *et al.* used the thermolysis of a NaN_3–C_6Cl_6 mixture to produce different types of carbon onions (Fig. 2G).[43] In some of their experiments, the multi-shell structure was clearly produced, but large amounts of carbon by-products were generated, too.[43] The same was observed by using ball milling of graphite published by Chen *et al.* (Fig. 2O).[47]

2.2 Nanodiamond-derived carbon onions

Thermal annealing of detonation nanodiamond powders has emerged as the most practical method for producing carbon onions.[8,61] Key benefits are the high purity, the small particle size between 5 nm and 10 nm, large-scale material production with high material homogeneity and a relatively low price of the precursor (currently ~2 € per gram). Further cost reductions are expected as worldwide synthesis capacities for carbon onions are increasing. Furthermore, the facile synthesis of nanodiamond-derived carbon onions is attractive because the material can be obtained by simple thermal treatment in an inert atmosphere (*i.e.*, dry powder processing).[87]

By now, various nanodiamond precursors, heating rates, annealing temperatures, and durations have been investigated. Considering the use of different synthesis atmospheres like vacuum,[55–61] argon,[32,62–67] nitrogen,[68] hydrogen,[69] or helium,[27,70,73–75] it is difficult to adequately compare the structure and properties of the resulting carbon onions. Typically, detonation nanodiamonds with a mean particle size of *ca.* 5 nm are used as precursors for carbon onion synthesis. Chemically, nanodiamonds consist of 80–90 mass% of carbon, a few mass% of oxygen, hydrogen, nitrogen, and minor amounts of other impurities.[32,88,89] Oxygen and hydrogen are associated with surface functional groups, whereas nitrogen can also be located in the nanodiamond core.[88] The detonation synthesis of nanodiamonds yields particles engulfed by a thin layer of amorphous and disordered carbon.[88,90–92] It also leads to particle agglomeration and sintering with agglomerates of several hundreds of nanometers.[93]

The thermal transformation of nanodiamonds to carbon onions is a multistep process. In general it starts with desorption of water and detachment of oxygen-containing surface functional groups from sp^3-hybridized carbon when heating up to around 200 °C.[94–96] Further increasing the temperature will

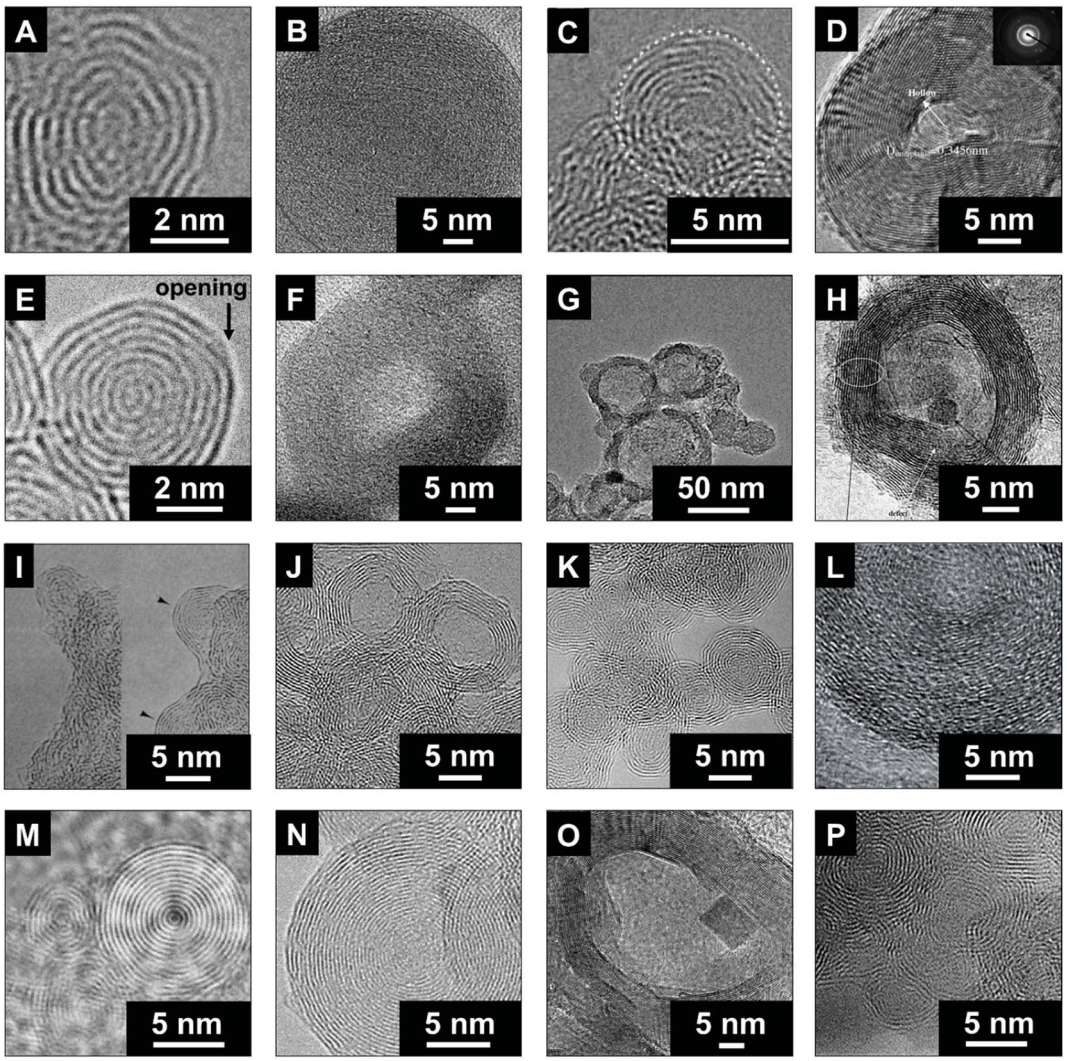

Fig. 2 Transmission electron micrographs of carbon onions synthesized using different methods. (A) Hou *et al.*, counterflow diffusion flame method (with permission from Elsevier);[39] (B) Choucair and Stride, flash pyrolysis of naphthalene (with permission from Elsevier);[40] (C) Gao *et al.*, laser-assisted combustion process using C_2H_4 and O_2 (with permission from IOP Publishing);[41,81] (D) He *et al.*, catalytic decomposition of C_2H_4 on Ni/Al (with permission from Elsevier);[37] (E) this work, annealing of nanodiamonds; (F) Zhao *et al.*, carbonization of phenolic resin in the presence of ferric nitrate (with permission from Elsevier);[42] (G) Bystrzejewski *et al.*, thermolysis of a NaN_3–C_6Cl_6 system under argon or air atmosphere (with permission from Elsevier);[43] (H) Lian *et al.*, annealing of acetylene black in the presence of ferric nitrate (with permission from Elsevier);[53] (I) Ugarte, electron-beam irradiation of amorphous carbon (with permission from Macmillan Publishers);[30] (J) Du *et al.*, radio frequency plasma treatment of coal (with permission from Elsevier);[80] (K) Xiao *et al.*, laser irradiation of nanodiamonds in liquid alcohol (with permission from American Chemical Society);[77] (L) Azhagan *et al.*, burning ghee (with permission from The Royal Society of Chemistry);[86] (M) Sano *et al.*, arc discharge between graphite rods in water (with permission from Macmillan Publishers);[52] (N) Cabioc'h *et al.*, carbon ion implantation in copper and silver (with permission from Elsevier);[48] (O) Chen *et al.*, ball milling of graphite (with permission from Elsevier);[47] (P) Serin *et al.*, chemical vapor deposition using BCl_3, C_2H_2, and H_2 (with permission from Elsevier).[36]

effectively remove functional groups like carboxyl, anhydride, and lactone groups, leading to the emergence of CO and CO_2 gases.[32,94,96] Detachment of functional groups causes the formation of dangling bonds on carbon atoms which can reconstruct and combine to form π-bonds, indicating the onset of graphitization when approaching 800–900 °C. The reconstructive phase transformation forms sp^2-hybridized carbon shells on the outside of the nanodiamonds, followed by continuous graphitization to the inside of the particle when increasing the temperature.[32,59,95,97–100] Structural defects of the nanodiamond surface, stemming from the synthesis or from the detachment of surface functional groups, increase the reactivity of surface carbon atoms which greatly facilitates the phase transformation process.[100] At temperatures between 1100 °C and 1300 °C, the initially highly disordered carbon shells become increasingly more graphitic with a lower defect density yielding a fully transformed highly ordered carbon onion at 1800–2000 °C.[55,101] During the phase transformation, if the nanodiamond particles are in direct contact, the dangling bonds of two adjacent particles may combine, forming a common π-bond; thus local particle sintering may occur, facilitated by carbon etching and redistribution at higher

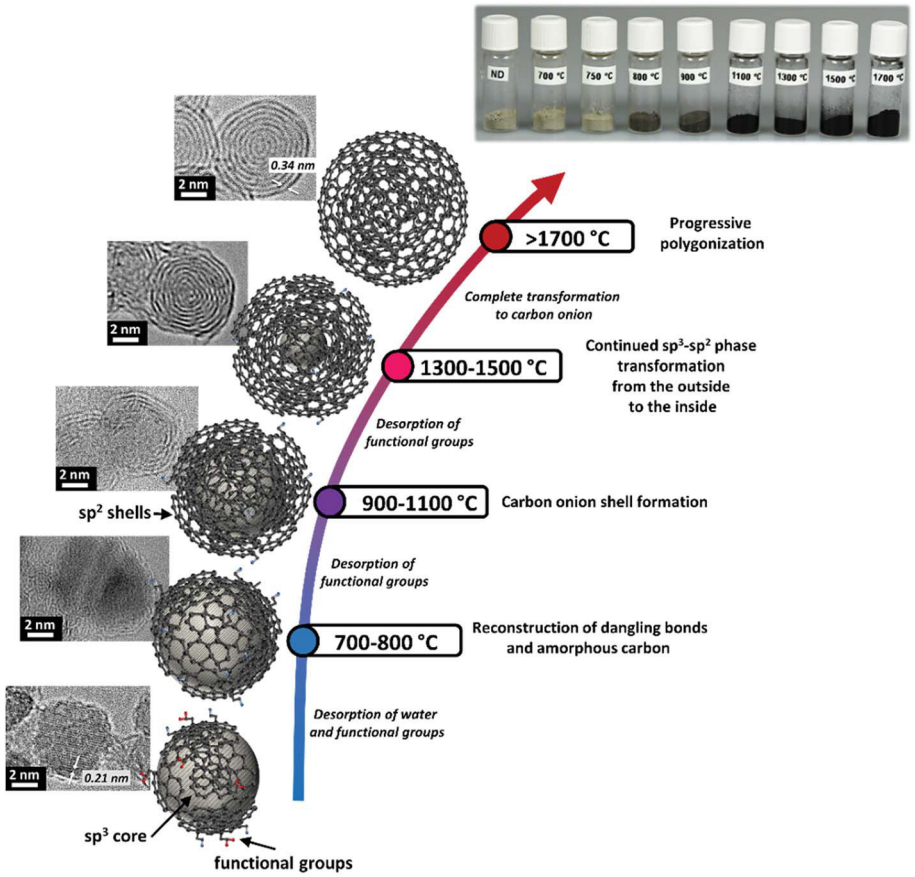

Fig. 3 Transformation from nanodiamonds to carbon onions by annealing shown using transmission electron micrographs, optical images, schematic illustrations of intermediate steps, and the assignment of physical effects depending on the annealing temperature (slight variations occur depending on the annealing atmosphere, especially when comparing vacuum with an inert gas atmosphere).

temperatures. Examples for the different stages of the nanodiamond to carbon onion transformation are given in Fig. 3.

3. Physical and chemical properties of nanodiamond-derived carbon onions

3.1 Properties of nanodiamond-derived carbon onions: overview

A summary of selected physical and chemical properties of nanodiamond-derived carbon onions is given in Fig. 4 in dependence on synthesis temperature. The next sections will address in more detail the structural aspects of the nanodiamond to carbon onion transition and specifically aspects of electrical conductivity and porosity. For electrochemical energy storage, carbon onions synthesized at temperatures of at least 1700 °C present the most attractive set of properties. Due to the high temperature, the nanodiamond transforms completely to carbon onion resulting in a low content of surface functionalities (mostly oxygen-containing functionalities), a low density leading to a relatively high surface area, and a high carbon ordering which is responsible for the high conductivity.

Kuznetsov *et al.* investigated the graphitization mechanism and formulated a model for the gradual phase transition.[61] The exfoliation to graphite sheets preferentially occurs on the (111) diamond facets and involves shrinkage along the graphitic network.[61,104] The decrease in density from nanodiamonds (~3.3 g cm^{-3}) to graphitic carbon (1.9–2.2 g cm^{-3}) induces an increase in particle volume.[32,56,61] Therefore, the number of diamond surface atoms was not sufficient to form a closed shell on the outside of the particle. The missing carbon atoms come from the edges or inner diamond layers leading to the complete closure of carbon onion shells. The transition from nanodiamond to carbon onion might be characterized by intermediate steps, for example spiral-like carbon shells or semi-spherical shells, which are yet to be reliably confirmed in experiments.[61,105,106]

In a theoretical study by Ganesh *et al.*, Reax force field was used to model the transformation from nanodiamonds to carbon onions.[97] In agreement with experimental studies, a step-wise transformation takes place, successively from the outside to the inside when increasing the annealing temperature. A full conversion, for example for a 2 nm nanodiamond, was only reached at 1800 °C. For temperatures below 627 °C, no conversion occurred, in agreement with experimental studies on larger nanodiamond particles.[32,84] It is expected that larger nanodiamonds would show a lower degree of transformation for the same temperature. The simulations yielded highly

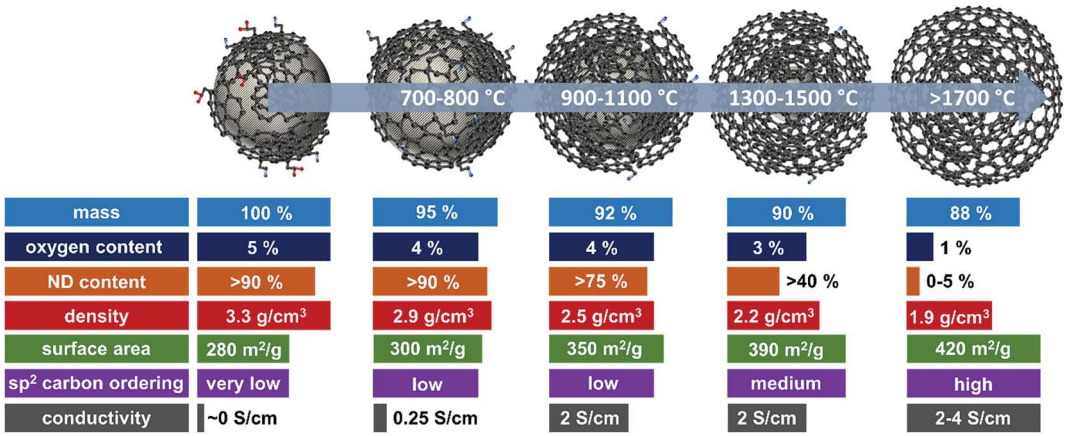

Fig. 4 Properties of nanodiamond-derived carbon onions dependent on the synthesis temperature. The values are approximations shown to demonstrate the trend in selected physical and chemical properties for carbon onions annealed at different temperatures. For more precise values, we recommend the following literature: mass loss and oxygen content,[32,87] ND content,[56,102] skeletal density,[32,56,87] specific surface area (see Fig. 6, Section 3.3), sp^2 carbon ordering,[32,65,83,101,103] and electrode conductivity (see Fig. 7, Section 3.4).

defective shells and an interlayer spacing of 0.34 nm, slightly smaller than 0.35 nm in graphite. This interlayer spacing makes the intercalation of small ions, for example, lithium, into carbon onions possible. Moreover, some of the simulations reported in this work yielded very interesting structures in which the carbon onion resembled a snail shell with one spiral channel going from the surface all the way down to the center of a carbon onion. This structure is in striking contrast to the closed multishell structure thought to be typical for carbon onions before and may change our perception of ionic and other species intercalation into the carbon onions.[97] Large spiraling channels, which would also allow the uptake of larger ions, are sometimes observed in experimental studies (Fig. 2E).[97,107,108]

3.2 Nanodiamond to carbon onion transformation

The physical and chemical properties of nanodiamond-derived carbon onions strongly depend on the precursor, the synthesis conditions, and the post-synthesis treatment. Both annealing of nanodiamonds in vacuum and inert gas lead to the transformation to carbon onions.[55,87,109] X-ray diffraction (XRD) shows for vacuum and inert gas annealing the emergence of the (002)-graphite peak for temperatures higher than 900 °C, whose intensity increases during annealing, while the intensity of the (111) diamond peak decreases (Fig. 5A). The phase transformation progresses at a faster rate at higher temperatures and is nearly completed for temperatures higher than 1700 °C, as is indicated by the small (111)-diamond peak (Fig. 5A).[55,87,109]

During the transformation, not only the carbon onion/diamond ratio increases, but also the degree of sp^2 carbon ordering. A high degree of sp^2 carbon ordering is desirable to enhance the electrical conductivity and can be accomplished by using high synthesis temperatures (above 1500 °C). With higher annealing temperature, carbon onions become more graphitic, leading to an increase of the density states of conductive electrons and furthermore to a higher intrinsic conductivity.[111] For spherical carbon onions, consisting of small poorly connected domains of graphitic sp^2-hybridized carbon, dangling bonds due to structural defects were detected using electron spin resonance (ESR). The π-electrons localized in the small graphitic domains might not provide sufficient conductivity. Gan and Banhart showed that spherical carbon onions are highly stable up to temperatures of more than 1200 °C.[112] For comparison, in polyhedral carbon onions, formed at temperatures higher than 1800–1900 °C,[57,83] dangling bonds were reduced and delocalization of π-electrons increased the intrinsic conductivity.[57]

Raman spectroscopy is a powerful tool to characterize the structure of carbon onions.[101,103,113–115] Carbon onion Raman spectra exhibit a G-mode coming from the vibration of carbon atoms in sp^2-hybridized carbon networks and a disordered D-mode related to the breathing of hexagonal carbon rings with defects (Fig. 5B). The G-mode, usually at 1582 cm^{-1} for planar graphite,[116] is commonly downshifted for carbon onions.[113,114] At lower synthesis temperature, such as 750 °C, the Raman spectrum of the material resembles amorphous carbon covering the surface of the particles, similar to the nanodiamond precursor (Fig. 5B).[117] Due to the limited ability to study nanodiamonds with visible light excitation, UV-Raman is often preferred. The UV-Raman spectrum of nanodiamonds is additionally presented in Fig. 5B. For a synthesis temperature of 800 °C, the graphitic G-mode and the disordered D-mode emerge from the nanodiamond starting material, presenting the onset of the transformation to carbon onions (Fig. 5B). The G-mode shows a relatively broad shape due to the large bond length variation in the material. Together with a broad background coming from amorphous carbon at ~1520 cm^{-1} and the emergence of the D-mode at ~1340 cm^{-1}, it can be concluded that the sp^3-hybridized carbon starts to transform into sp^2-hybridized carbon. Higher annealing temperature results in sharper D- and G-modes and lowers the secondary amorphous carbon signal.[87,101]

In general, Raman spectra of carbon onions can often be reasonably well explained assuming at least two different

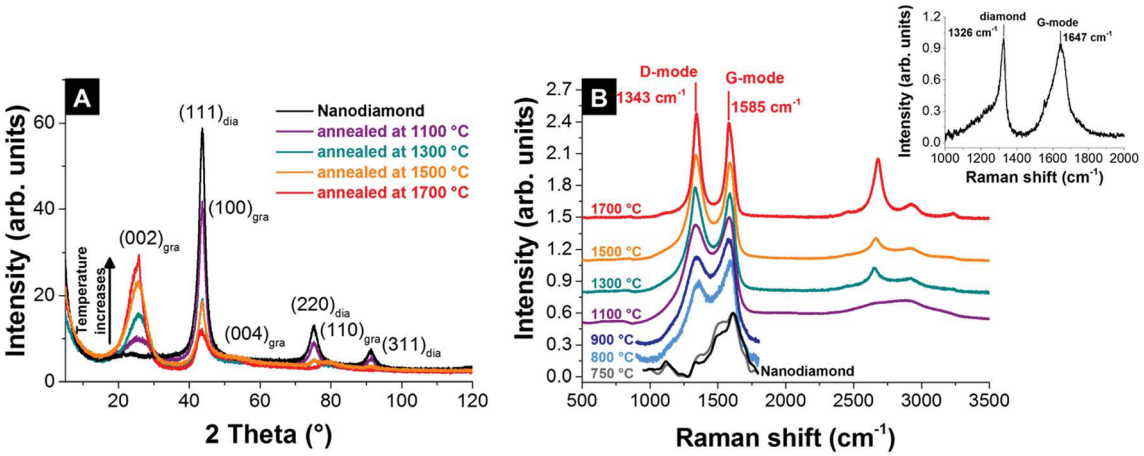

Fig. 5 (A) X-ray diffractograms of nanodiamond and carbon onions synthesized at different temperatures in an argon atmosphere.[32] (B) Raman spectra of nanodiamond-derived carbon onions synthesized in argon measured with a 532 nm laser (recorded using 0.2 mW, 30 accumulations, and 10 s acquisition time; for pristine nanodiamonds and nanodiamonds annealed at 750–900 °C the spectra were only recorded using 1 accumulation to avoid laser-induced heating and were baseline-corrected).[32] The inset shows the Raman spectrum of nanodiamonds measured with a 325 nm UV-laser.[110]

carbon phases present, namely the disordered carbon onion structure rather than a specific spectrum of spherical shells[113] and amorphous carbon.[87] Typically, additional low-intensity Raman modes are observed for wavenumbers below 1000 cm^{-1}. Roy *et al.* discussed these peaks using the 2D phonon density of states (PDOS) and the dispersion curves of graphite.[114]

In addition to XRD and Raman spectroscopy, TEM is a facile tool to image and analyze the nanodiamond to carbon onion transformation (see also Fig. 2).[55,58,61,77,83,101,103,109,118–121] The conversion can be directly performed using electron irradiation of nanodiamond powder in a TEM.[118] The shells form from the outside inward. According to electron energy loss spectroscopy (EELS), sp^2-hybridized carbon forms in this process, but some sp^3-hybridized carbon may remain. Various types of defects in the carbon onion structure were proposed such as holey shells, spiral-like structures, y-junctions, and protuberance, but the experimental investigation of the structure and defects of the shells is difficult.[118]

A key difference between vacuum and inert gas atmosphere annealing is related to the role of surface functional groups. A high oxygen content in nanodiamonds leads to an increased amount of decomposing functional groups, which form gaseous carbon oxides in the reaction zone.[32,122] If the nanodiamond annealing process is carried out in vacuum, the partial pressure of these carbon oxides remains near zero. However, if the process is carried out in an inert gas atmosphere, the partial pressure may stay high enough to cause local carbon etching and effective redistribution of carbon. The extreme case is the formation of micrometer-sized graphitic particles instead of nanometer-sized carbon onions leading to a total loss of the carbon onion structure.[32] Even in less extreme cases, carbon onions from annealing nanodiamonds in an inert gas atmosphere show other characteristic features related to carbon redistribution. As seen from XRD and Raman (Fig. 5A and B), the material after annealing in an inert gas atmosphere consists of two phases: nanometer-sized carbon onions and few-layer graphene nanoribbons (Fig. 6A and B). In contrast, a second carbon phase (*i.e.*, nanoribbons) is absent in carbon onions from vacuum annealing (Fig. 6C and D).[87]

3.3 Porosity characteristics of nanodiamond-derived carbon onions

Unlike many other carbon materials for electrochemical energy storage (*e.g.*, activated carbons), a relatively large surface area of nanodiamond-derived carbon onions is commonly believed to be entirely associated with their external surface. The typical

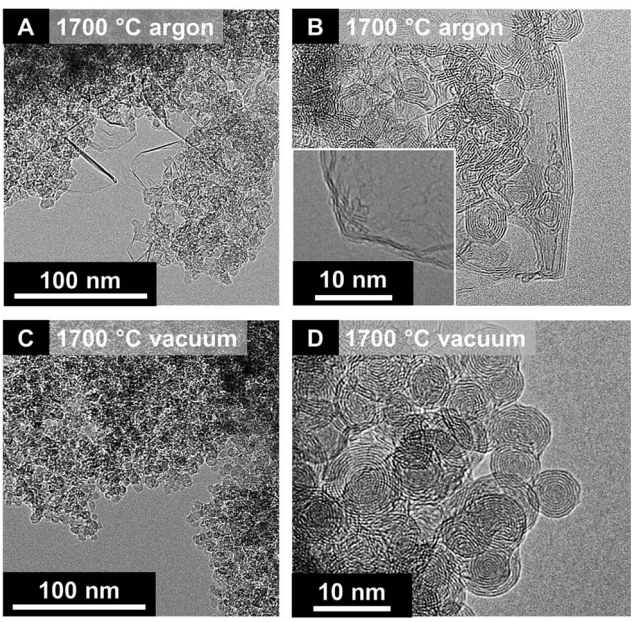

Fig. 6 Transmission electron micrographs of nanodiamond-derived carbon onions synthesized at 1700 °C in argon (A and B) and vacuum (C and D). Reproduced with permission from Elsevier from ref. 87.

values of specific surface area are 300–600 $m^2 g^{-1}$ (Fig. 7A) with more than 1 $cm^3 g^{-1}$ interparticle pore volume.[87] For comparison, activated carbons present usually more than 1500 $m^2 g^{-1}$ specific surface area, with a pore volume also around 1 $cm^3 g^{-1}$.[7] The fully accessible external surface area of carbon onions greatly facilitates ion transport during charge and discharge in electrochemical energy storage devices. This is in contrast to nanopores within micrometer-sized particles (*e.g.*, of activated carbon), as will be shown in Section 4.1. Typically, the pore size distribution (*i.e.*, interparticle pores) of carbon onion powders is relatively broad: from <1 nm up to 40 nm.[32] The surface area of nanodiamond-derived carbon onions strongly depends on the synthesis parameters with maximum values just below 650 $m^2 g^{-1}$ (Fig. 7A). For carbon onions synthesized by certain methods, such as arc discharge of graphite, even higher values can be reached (up to 984 $m^2 g^{-1}$).

To understand the dependency of the surface area on the synthesis conditions, we have to consider that the nanodiamond to carbon onion phase transformation not only brings along a structural change, but also significantly decreases the density.[32,56,97] The density of nanodiamonds (3.3 g cm^{-3}) is much higher than that of carbon onions (*e.g.*, ~1.9 g cm^{-3} for carbon onions produced at 1700 °C).[32] As a result of the large decrease in density, a volume expansion occurs during the formation of sp^2-hybridized carbon shells from the outside to the inside of the particles.[32,56] This expansion has been predicted by modeling and verified experimentally by the increase in surface area (nitrogen gas sorption analysis) and the continuous decrease in density (helium gas pycnometry).[32] The higher lattice spacing of graphite compared to diamond leads to a decrease in density, a volume expansion, and to an increase in specific surface area (Fig. 7B). By normalizing the surface areas of different nanodiamond-derived carbon onions to the surface area of the precursor nanodiamonds, one can determine a constant increase in surface area up to around 70% when annealing at 1500 °C. For temperatures higher than 1500 °C, the surface area does not increase and may even decrease, whereas the density keeps decreasing.[32] Locally occurring particle–particle sintering, as well as carbon etching and redistribution to larger structures, is an important factor for the decrease in surface area. At the end of this process, even consolidated structures in the form of micrometer-sized graphitic particles may occur when using an inert gas atmosphere for the synthesis.[32,122]

To increase the surface area of carbon onions beyond the values of ~600 $m^2 g^{-1}$, chemical or physical activation can be used, such as oxidation in air or acid treatment. So far, the highest value for activated nanodiamond-derived carbon onions was ~650 $m^2 g^{-1}$ using oxidation in air (corresponding to an increase of the surface area by 100% compared to the surface area of the nanodiamond precursor).[32] The increase in the surface area is accomplished by the removal of interparticle pore-blocking amorphous carbon and a partial decrease in the carbon onion diameter.[32] Higher values of the specific surface area above 800 $m^2 g^{-1}$ were achieved by KOH activation of carbon onions produced by laser-assisted combustion of methane.[81] Compared to oxidation in air, KOH etching does not remove carbon shells and amorphous carbon; rather this procedure etches new pores into the carbon onions.[81] The largest surface area reported so far is 984 $m^2 g^{-1}$ by using an arc-discharge method with graphite as the precursor and this high value was explained by the emergence of intraparticle pores due to surface roughening.[123] In the latter study, TEM images showed particles with a diameter of 4–36 nm which is up to 4-times larger than for nanodiamond-derived carbon onions. The rather low density of 1.64 g cm^{-3} may also indicate the presence of other carbon nanoforms in the sample (which is common for this type of synthesis method). Thus, it is difficult to tell to what extent this large specific surface area of the products can be assigned just to carbon onions.

Until now, the discussion was limited to surface area and pore volume, but ion accessibility to a certain pore can only be

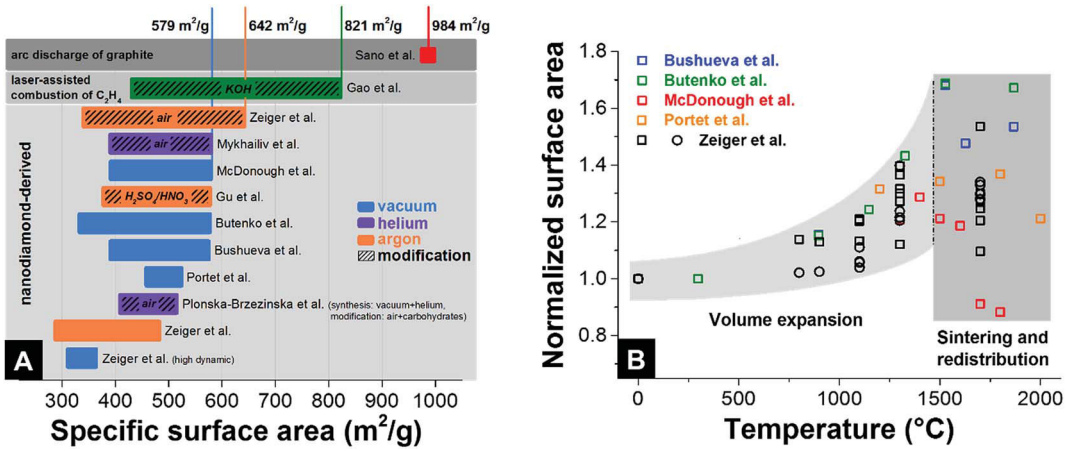

Fig. 7 (A) Surface areas of different types of carbon onions. The colored bars give the range in surface area with minimal and maximum values. See the legend for synthesis atmosphere and post-synthesis modification. Bushueva *et al.*,[84] Butenko *et al.*,[56] McDonough *et al.*,[83] Portet *et al.*,[4] Zeiger *et al.* (circle and square symbolize 2 different nanodiamond precursors),[32,87] Sano *et al.*,[123] Gao *et al.*,[81] Mykhailiv *et al.*,[70] Gu *et al.*,[124] Plonska-Brzezinska *et al.*[75] (B) Relative change of surface area during annealing of nanodiamond in an inert gas or vacuum.

understood when we consider the actual pore size distribution (PSD). The PSD can be derived from gas sorption isotherms using, for example, CO_2 at 0 °C (for pores between *ca.* 0.3 and 1.0 nm) and N_2 at −196 °C (for pores between *ca.* 0.6 nm and 30 nm). A slit-shaped pore model is typically assumed as the best-fit model for carbon onions among the available density functional theory (DFT) models.[65] Assuming a series of pores, the PSD of carbon onions can be defined as pores between particles in direct contact (<1 nm), pores between several particles (1–10 nm), and pores between agglomerates (larger than 2 nm).[32] The large number of mesopores with the size 2–50 nm facilitate ion transport which makes carbon onions a very attractive high-power material for supercapacitor electrodes.

3.4 Electrical conductivity of nanodiamond-derived carbon onion electrodes

The electrical conductivity of carbon onion electrodes is influenced by the intrinsic electrical conductivity of the material, the degree of particle sintering, the particle arrangement and compaction, as well as the electrode preparation (*e.g.*, use of binder *vs.* binder-free electrodes). The intrinsic conductivity of carbon onions can be tuned by adjusting the annealing temperatures. High temperatures (>1700 °C) result in a higher degree of carbon ordering. The resulting carbon onions are more graphitic and more electrically conductive (see also Section 3.2 and Fig. 4).[111] The particle sintering is typically caused by agglomeration of nanodiamonds, and partially provoked by high annealing temperatures.[32,125] In a recent study it was shown that annealing in argon instead of vacuum produces few-layer graphene flakes between the carbon onions, which enhance the electrode conductivity.[87]

The electrical conductivity of nanodiamond-derived carbon onion electrodes may reach *ca.* 4 S cm^{-1} measured with a four-point probe on pellets or polymer-bound electrodes.[4] However, the spread of reported values is very large, ranging from below 0.5 S cm^{-1} to above 4 S cm^{-1} (Fig. 8A). The maximum conductivity of ~4 S cm^{-1} (2.5–3 S cm^{-1} for polymer-bound electrodes) is comparable to that of carbon black (*ca.* 1–2 S cm^{-1}) and an order of magnitude higher than activated carbon (<0.5 S cm^{-1}).[4] A comprehensive and fair comparison of experimental data is complicated by the use of different synthesis temperatures, atmospheres, and different electrode preparation methods in the literature. For example, polytetrafluoroethylene (PTFE)-bound film electrodes and compressed pellets show significant differences in conductivity. However, we can assume an increased electrical conductivity for carbon onions synthesized

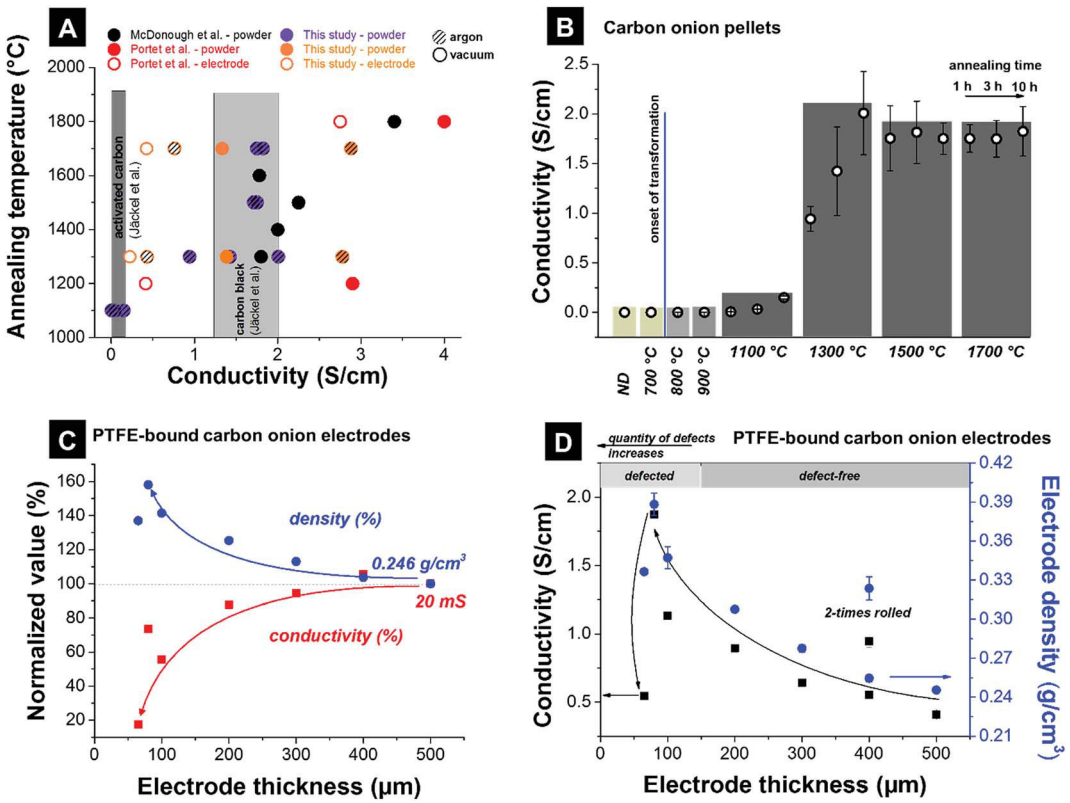

Fig. 8 Conductivities measured using a 4-point probe. (A) Literature values. McDonough *et al.*: powder compressed with 8 MPa;[83] Portet *et al.*: Teflon cylinder filled with powder, copper electrodes of 22 mm in diameter as probes, electrodes with 15 mass% PTFE (mass density 15 mg cm^{-2}) were painted on a current collector covered with conductive paint;[4] this study: ~200 mg powder compressed with 0.25 MPa, electrode with 10 mass% PTFE and a thickness of 200 μm; Jäckel *et al.*: electrodes with 5 mass% PTFE for activated carbon and 10 mass% PTFE for carbon black and a thickness of 200 μm (ref. 7). (B) Carbon onion pellet conductivities: powder of ~200 mg compressed with 0.25 MPa. (C and D) Electrode densities, and electrode conductivities of carbon onions synthesized at 1700 °C in argon for different electrode thicknesses (10 mass% PTFE, 60–500 μm thickness).

at higher temperatures as a result of enhanced carbon ordering, as confirmed by the literature. The large spread of literature values shown in Fig. 8A reflects the large influence of the measurement procedure.

To make a comparison within a cohesive data set, we show in Fig. 8B data for the electrical conductivity of compressed pellets. Nanodiamonds were annealed at different temperatures yielding carbon onions above *ca.* 1000 °C. Using a four-point probe, we measured an increase from the negligible electrical conductivity of nanodiamonds around the onset of carbon onion formation (*i.e.*, at around 800–1000 °C). By varying the annealing time (exemplified for 1100 °C and 1300 °C), we see a continuous increase of the electrical conductivity. This corresponds to a continuous transformation of nanodiamond powder to carbon onions. A residual diamond core and less perfect graphitic shells result in lower electrical conductivity. Finally, constant values are seen for synthesis temperatures exceeding 1500 °C where it is assumed that nearly full transformation to carbon onions has occurred within less than 1 h of annealing.

We show in Fig. 8C and D the influence of the electrode thickness with 10 mass% PTFE as the binder and packing density on the electrical conductivity measured by a four-point probe. For electrode thicknesses between 200 and 500 μm, the sheet conductivity (not normalized to the electrode thickness) varies only within ±10%, mirroring a moderate increase in electrode density by *ca.* 25%. Thus, for the electrode thickness values in the range 200–500 μm the sheet conductivity is not significantly influenced by electrode density and thickness. However, for thinner electrodes, the sheet conductivity drops, for example by more than 80% for 60 μm thickness (compared to 500 μm). Fig. 8D presents the conductivity values normalized to the thickness as common in the literature. By decreasing the electrode thickness the normalized conductivity continuously increases. Thin electrodes are commonly obtained by repeated rolling, which leads to a higher degree of particle compaction (*i.e.*, larger contact area) and a possible increase in electrical conductivity. In Fig. 8D, this is exemplified for a 400 μm thick electrode which was rolled two times. In the second rolling step, additional electrode material is used and rolled to a more compact electrode. A higher density is achieved and a higher conductivity can be reached. The nanoscopic size of carbon onions makes it quite difficult to prepare PTFE-bound electrodes with a thickness smaller than 200 μm. Consequently, very thin PTFE-bound electrodes suffer from cracking and similar issues may arise when using other polymer binders and non-freestanding, sprayed electrodes instead of (hot-)rolling. Therefore, in addition to normalizing the electrical conductivity to the electrode thickness (as commonly done in the literature), careful assessment of the electrode density is required when comparing experimental data.

4. Electrochemical properties of carbon onion electrodes

4.1 Carbon onions for electrical-double layer capacitors

The electrochemical performance of carbon onions reflects their physical and chemical properties, as well as the accessible surface area. Nanodiamond-derived carbon onions commonly show capacitance values of up to 52 F g^{-1} in aqueous 1 M H_2SO_4 (ref. 84) and *ca.* 40 F g^{-1} in 1.5 M TEA-BF_4 in acetonitrile (ACN) (Fig. 9).[4] Chemical and physical activation can be used to improve the relatively small capacitance (for comparison, activated carbon has >100 F g^{-1}) by increasing the surface area. Using a laser resonant excitation of ethylene molecules, carbon onions with a size between 5 nm and 50 nm were produced. For KOH activated carbon onions mentioned before, with surface areas in excess of 800 m^2 g^{-1} an enhanced capacitance of 115 F g^{-1} was achieved in 2 M KNO_3.[81] Carbon onions from the arc-discharge of graphite electrodes have shown a very low capacitance of *ca.* 5 F g^{-1} probably due to the low surface area of particles with a diameter of 25–35 nm.[82] The overall moderate surface area of carbon onions results in a rather low energy storage capacity compared to nanoporous carbons, such as activated carbon or carbide-derived carbon with typical values of 100–200 F g^{-1} (and surface areas above 1500 m^2 g^{-1}).[14] However, the facile ion access to the external surface of carbon

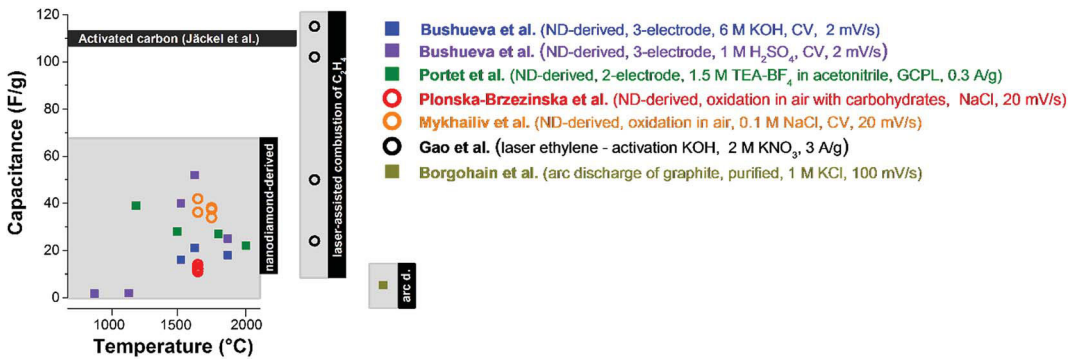

Fig. 9 Capacitance values of different types of carbon onions. Bushueva *et al.*,[84] Portet *et al.*,[4] Plonska-Brzezinska *et al.*,[75] Mykhailiv *et al.*,[70] Gao *et al.*,[81] Borgohain *et al.*[82] The synthesis methods and the settings for electrochemical characterization are presented in the figure. The panel on the left encloses capacitance values of nanodiamond-derived carbon onions, the one in the middle of carbon onions from the combustion of C_2H_4, and on the right of arc discharge carbon onions. Carbon onions without modification are shown by squares and with modification by circles. For comparison, the capacitance of PTFE-bound activated carbon is shown using 1 M TEA-BF_4 in ACN.[7]

onions makes them excel in power handling, as will be discussed in more detail later.

The combination of high intrinsic electrical conductivity (see Section 3.4) and facile ion accessibility *via* an external surface area (see Section 3.3) makes carbon onions very attractive for high power applications that require fast charge and discharge rates (*e.g.*, pulsed operation in hybrid electric cars or power stabilization for grid scale applications).[6] The high intrinsic electrical conductivity of nanodiamond-derived carbon onions is achieved by using high annealing temperatures as discussed in Section 3.4.[4,83,87] The higher degree of carbon ordering not only increases the conductivity and power handling but also leads to higher differential capacitances (*i.e.*, potential-dependent capacitance). In a recent study the influence of carbon ordering on the capacitance of carbon supercapacitors was systematically studied using carbon onions as the model material.[65] Carbon onions with similar porosities, but differing in carbon ordering, were synthesized at 1300 °C, 1500 °C, and 1750 °C in vacuum. Using PTFE-bound electrodes and different organic electrolytes and ionic liquids, the influence of carbon ordering on the electrochemical properties was investigated. Cyclic voltammograms showed a characteristic butterfly shape for all carbon onions, but it was much more pronounced for carbon onions synthesized at high temperatures with a higher degree of carbon ordering (Fig. 10A). The butterfly shape represents an increasing differential capacitance for higher potentials, because the electron density of states changes as a function of applied potential.[65,126] This so-called electrochemical doping[127] strongly depends on the degree of carbon ordering[128] and is enhanced for more ordered carbon onions with higher electrical conductivity. The change in electrical resistance measured with an *in situ* resistance cell is shown in Fig. 10B. At high electrode potentials, the normalized resistance of the electrodes reduces constantly by increasing the annealing temperature.[65]

The nanoscale size of carbon onions necessitates adding more binder during electrode manufacturing, typically 10 mass% PTFE for PTFE-bound electrodes.[7] For activated carbons, usually 5 mass% PTFE is sufficient to prepare free-standing, mechanically stable electrodes.[14] Polymer binders add electrochemically dead mass and may partially block pores leading to lower capacitance.[7] Microcavity electrodes present a facile tool to qualitatively compare different electrode materials without the influence of binders.[4] In a study by McDonough *et al.*, carbon onions synthesized at different temperatures were electrochemically tested using microcavity electrodes in 1 M H_2SO_4.[83] At scan rates up to 15 V s^{-1}, the relative capacitance for carbon onions synthesized at 1800 °C decreased by less than 30% compared to the low-rate value, while carbon onions synthesized at 1300 °C showed a reduction by 45% at 15 V s^{-1} (Fig. 10C). Compared to carbon onions, other carbon materials like activated carbon suffer from a lower degree of carbon ordering and lower ion mobility resulting in a decrease in capacitance of more than 70% under comparable testing conditions. The enhanced power handling ability of carbon onions synthesized at higher temperatures (*e.g.*, 1700 °C *vs.* 1300 °C) was also demonstrated for full cells with 200 μm thick electrodes in galvanostatic measurements.[87] Carbon onions in this study were derived from nanodiamonds *via* vacuum or argon annealing and higher synthesis temperatures led to higher capacitance retention when increasing the specific current.[87] By lowering the electrode thickness to 100 μm an even higher power performance and almost no loss in capacitance at 20 A g^{-1} compared to the low-rate value were reported (Fig. 10D). This again shows the high influence of the electrode design on the resulting electrochemical performance in addition to the intrinsic material properties.

As mentioned in Section 3.2, argon annealing leads to etching and redistribution of carbon onion outer shells and amorphous carbon.[32,87] Oxygen containing gaseous species, formed by the decomposition of functional groups, accumulate in the atmosphere around the sample etching the carbon and redistributing it to form few-layer graphene flakes between the particles (Fig. 6).[65,87,122] This effect was only observed by using ultrafast heating and cooling;[87] lower heating rates resulted in larger graphitic particles.[32] Due to the interconnection of the particles by few-layer graphene, a more open network with higher electrical conductivity was produced with an enhanced capacitance retention of 85% at 20 A g^{-1} (Fig. 10D) for PTFE-bound electrodes (10 mass% PTFE, 200 μm thick).[87]

Taking advantage of the high rate handling capability, carbon onions have been demonstrated as electrode materials for ultrahigh-power micro-supercapacitors.[6] Using an electrophoretic deposition technique, nanodiamond-derived carbon onions produced at 1800 °C were directly deposited onto patterned gold current collectors from an ethanol–water suspension. The electrodes showed ultrafast rate handling behavior in 1 M TEA-BF_4 in propylene carbonate (PC) up to 200 V s^{-1} scan rate.[6] This superior rate handling is partially due to the ultrathin electrode thickness of just a few micrometers; as demonstrated in ref. 6, the rate handling of conventional activated carbon is also severely enhanced for micro-supercapacitors as compared to conventional supercapacitors with much thicker electrodes (150–250 μm). The high rate handling ability of carbon onions was also shown for carbon onion/carbon fiber composite electrodes with a thickness below 50 μm.[129] Using 1 M TEA-BF_4 in ACN, a decrease of 37% of the initial low-rate capacitance was found at 100 A g^{-1} using a full-cell setup (two-electrode geometry) for the composite electrode; for comparison, PTFE-bound electrodes of carbon onions without the highly conductive network of carbon fibers showed a 75% decrease in capacitance already at 50 A g^{-1}.[129]

Electrochemical performance stability is another important parameter for energy storage devices; however, so far, only a few studies provided data in this regard for carbon onions. For example, using micro-supercapacitors with high temperature carbon onions (1800 °C, high vacuum), a capacitance retention of ~100% was maintained after 10 000 cycles at 10 V s^{-1} in an organic electrolyte.[6] Yet, micro-supercapacitor data are not directly transferable to estimate the performance stability of full cells. Two-electrode (full cell) data were provided by another study for the comparison of nanodiamond-derived carbon synthesized at 1300 °C and 1700 °C in argon or high vacuum.[87] While no significant difference in the performance stability was

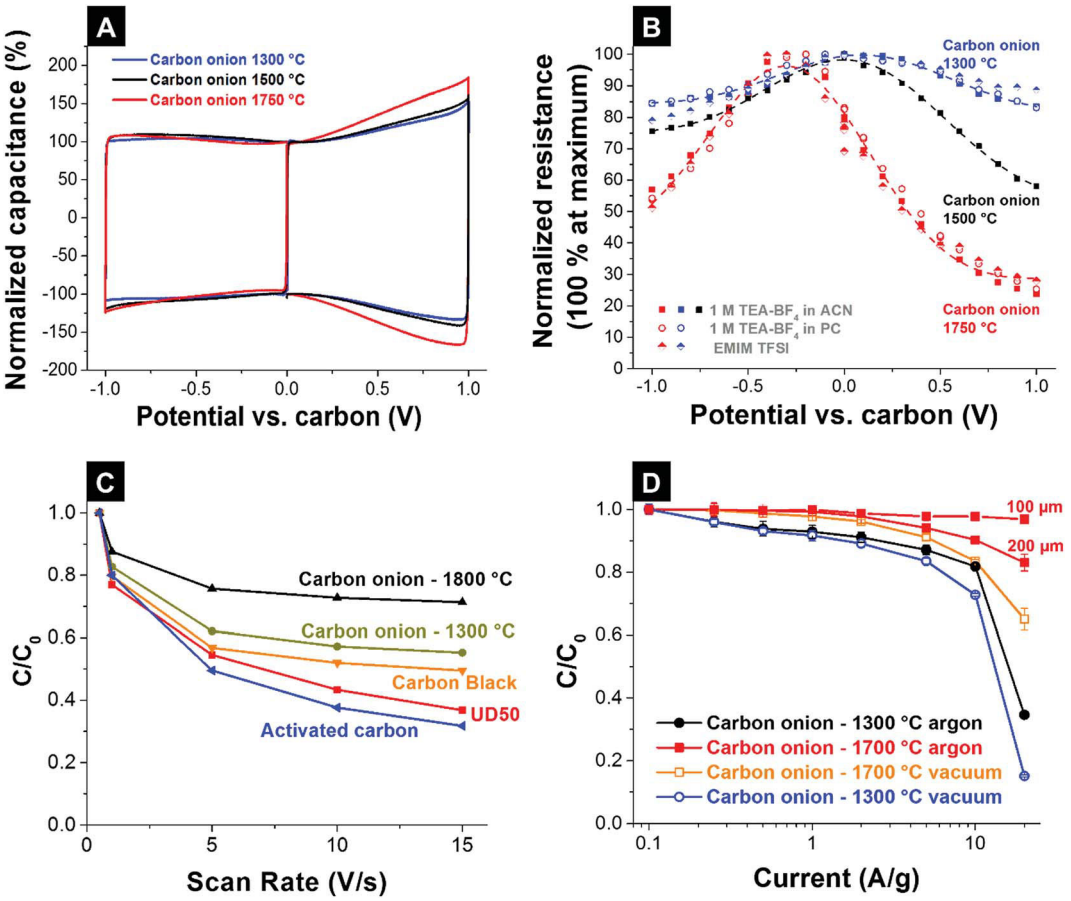

Fig. 10 (A) Cyclic voltammogram of PTFE-bound electrodes, made of nanodiamond-derived carbon onions synthesized at 1300 °C and 1750 °C in 1 M TEA-BF_4 in ACN at 10 mV s^{-1}.[65] (B) Resistance of the carbon onion electrodes after charging to a specific potential using an *in situ* resistivity measurement cell for different electrolytes.[65] (C) Rate handling behavior of the carbon onion powders compared with activated carbon, carbon black, and the nanodiamond precursor (UD50-detonation soot) measured in 1 M H_2SO_4.[83] (D) Rate handling behavior of film electrodes (200 µm, unless stated otherwise) of carbon onions synthesized from nanodiamonds at 1300 °C and 1700 °C in flowing argon or vacuum. All data from ref. 87 were measured in 1 M TEA-BF_4 in ACN using a full cell set-up with a cell voltage of 2.7 V.

caused by using different synthesis atmospheres (vacuum *vs.* argon), a significant difference was identified when comparing the different synthesis temperatures (1300 °C *vs.* 1700 °C). Using voltage floating at 2.7 V in TEA-BF_4 in ACN, high temperature carbon onions still showed nearly 100% capacitance retention after 100 h, while the capacitance of low temperature carbon onions decreased to ~90% after 20 h. These data correlate with the measured charge efficiency, which remains virtually unchanged at around 100% for high temperature carbon onions. The charge efficiency for low temperature carbon onions first decreases to around 92% after 20 h, but then recovers over time to ~98% after 100 h. This effect can be explained by the irreversible reactions of surface functional groups associated with the higher oxygen content after the low temperature synthesis (~3 mass%) compared to the high temperature synthesis (~1 mass%).[87]

In summary, the electrochemical properties of carbon onions depend on the synthesis conditions, as it is typical for carbon materials. Due to the lack of comprehensive electrochemical characterization data for non-nanodiamond-derived carbon onions, the following statements mainly concern carbon onions produced by thermal annealing of nanodiamonds.

- Carbon onions synthesized at higher temperatures (>1500 °C) show a higher degree of carbon ordering, higher differential capacitance for higher potentials, higher conductivity, higher electrochemical stability, and better rate handling capability.

- Typically, low temperature carbon onions (<1500 °C) present higher surface area and higher capacitance due to negligible sintering and carbon redistribution.

- By using rapid heating and cooling rates, sintering can be minimized and high conductivity high surface area carbon onions can be obtained for high annealing temperatures (1700 °C). Improved electrical conductivity, rate handling, and electrochemical stability can be obtained when using an inert gas like argon instead of vacuum for the annealing of carbon onions.

- Activation (*e.g.*, by using KOH) can lead to a roughening of outer shells, development of internal porosity, larger surface area, and accordingly higher capacitance.

- The thickness and packing density of the electrodes strongly influences the rate handling behavior, not only for

carbon onions, but also for other materials and should be taken into account when comparing data.

4.2 Carbon onions as conductive additives for electrical double-layer capacitors

The use of carbon onions as the primary electrode material for electrical double-layer capacitors is limited due to the low energy storage capacity resulting from a low specific surface area (<600 m^2 g^{-1}) when compared to commercial activated carbon.[7] However, their electrical conductivity superior to activated carbon makes them a promising conductive additive, effective in small amounts (typically 5–10 mass%). The very small carbon onions (below 10 nm) as well as their soft agglomerates (typically 100–200 nm) fit into very tight interparticle spaces. This results in a better (more homogeneous) distribution between the micrometer-sized activated carbon particles.[7] As such, carbon onions (1) fill effectively the gaps between larger carbon particles; (2) increase the overall particle–particle contact area between larger nanoporous carbon particles; and (3) decrease the particle–particle resistance since carbon onions are much more conductive than, for example, activated carbon.[7,130,131] Compared to conventional carbon black and graphite nanoparticles, carbon onions consistently lead to a better gravimetric and volumetric performance.[7]

So far, the use of carbon onions as a conductive aid to enhance power handling of carbon supercapacitor electrodes has been documented when admixing to activated carbon,[7,131] mesoporous carbon,[130] electrochemically active polymers,[132] and inserting between graphene oxide sheets.[133] Depending on the added amount of carbon onions, the activated carbon electrode sheet resistance drops by 30–80%.[7] The addition of 10 mass% carbon onions to flexible polyester electrodes leads to a 60% decrease in electrical series resistance.[130] Also, the performance of polymer electrodes based on polyaniline was enhanced by adding carbon onions, yielding an improved cycle stability and better rate handling ability.[132]

4.3 Carbon onions as a substrate for redox-enabled hybrid energy storage

Electrical double-layer capacitors show a high specific power due to fast ion electrosorption on high surface area carbons, but suffer from comparatively low specific energy (commonly around 5 W h kg^{-1} on a device-level).[134] A particularly attractive approach to enhance the energy storage capacity is the implementation of redox-active materials. Carbon onions are highly suited for this task as they are believed to only present an easily accessible external surface, which can be decorated with redox-active species, like surface functional groups, molecular species (*e.g.*, quinones), metal oxides (*e.g.*, manganese oxide), or conductive polymers (*e.g.*, polyaniline, PANI). This is in contrast to highly porous substrates, such as activated carbon, where adding redox-active materials brings along the issue of pore blocking in addition to the poor electrical conductivity of the substrate (especially activated carbon, see Section 3.4). Several types of redox-active species and/or pseudocapacitive materials were used in combination with carbon onions, including manganese oxide,[86,135–137] ruthenium oxide,[26] nickel hydroxide and oxide,[27] PANI,[74,132] poly(3,4-ethylenedioxythiophene):poly(styrenesulfonate) (PEDOT:PSS),[73] polypyrrole,[138] and quinones.[129,139] Among these materials, manganese oxide in combination with carbon onions shows the highest energy storage values with 575 F g^{-1} at 0.5 A g^{-1} in 0.5 M H_2SO_4.[86] A collection of SEM and TEM images of such hybrid materials is given in Fig. 11 and an overview of the capacitance values for redox-enabled carbon onions is presented in Fig. 12.

The vast majority of electrochemical applications of carbon onions relates to their use for supercapacitor electrodes as an active material, conductive additive, or substrate for redox-hybrid systems. In contrast, only a few studies have investigated their use as anode materials for battery systems, such as lithium ion batteries. In a study by Han *et al.*, carbon onions were chemically synthesized at 600 °C by a reaction between copper dichloride hydrate ($CuCl_2 \cdot 2H_2O$) and calcium carbide (CaC_2). The material was tested as an anode material for lithium-ion batteries. In a mixture of 1 M $LiPF_6$ in ethylene carbonate and dimethyl carbonate (EC/DMC, 1 : 1 by volume), carbon onions showed a capacity of 391 mA h g^{-1} at a rate of C/10 after 60 cycles which is slightly larger than the theoretical value of graphite with 372 mA h g^{-1}.[141] This may be explained by a shorter pathway for the ions and the carbon onion structure which exhibits an enhanced number of active sites for Li ion storage.[141] Wang *et al.* hydrothermally coated carbon onions with manganese oxide using $KMnO_4$ at 150 °C for use as lithium-ion battery anodes with a two-electrode configuration, lithium foil as the counter electrode, and 1 M $LiPF_6$ in EC/DMC (1 : 1 by volume) as the electrolyte.[142] The capacity of the manganese oxide composite was increased at 50 mA g^{-1} to ~630 mA h g^{-1} compared to ~260 mA h g^{-1} without carbon onions. The increased rate capability and an improved cycling stability were attributed to the structure of carbon onions leading to fast ion and electron transport.[142] In another publication by Wang *et al.* even 853 mA h g^{-1} was reached with a coulombic efficiency of 98% after pre-lithiation using MoS_2/onion-like carbon composites measured at a specific current of 50 mA g^{-1} in 1 M $LiPF_6$ in EC/DMC (1 : 1 by volume).[143]

4.3.1 Carbon onions decorated with manganese oxide. In a study by Azhagan *et al.*, carbon onions were synthesized by flame burning clarified butter (ghee) and the collected carbon black was annealed at 800 °C in an inert gas to produce graphitic multi-shell carbon onions in the size range of 40–45 nm (Fig. 11A).[86] A microwave assisted hydrothermal reaction with $KMnO_4$ as the precursor was used to coat the carbon onions with manganese oxide. The as-synthesized manganese oxide nanoparticles had a diameter of ~10 nm with the lattice constant of λ-MnO_2 (0.239 nm) measured using TEM. Carbon onion electrodes without metal oxides showed a surface area of 486 m^2 g^{-1} and a capacitance of 171 F g^{-1} at 0.5 A g^{-1} in 0.5 M H_2SO_4,[86] which is 5–10 times higher than that for neat nanodiamond-derived carbon onions from McDonough *et al.*[83] With regard to the presence of a redox peak between −1 V and +1 V, carbon onion surface functional groups may contribute to the enhanced capacitance even in the absence of additional

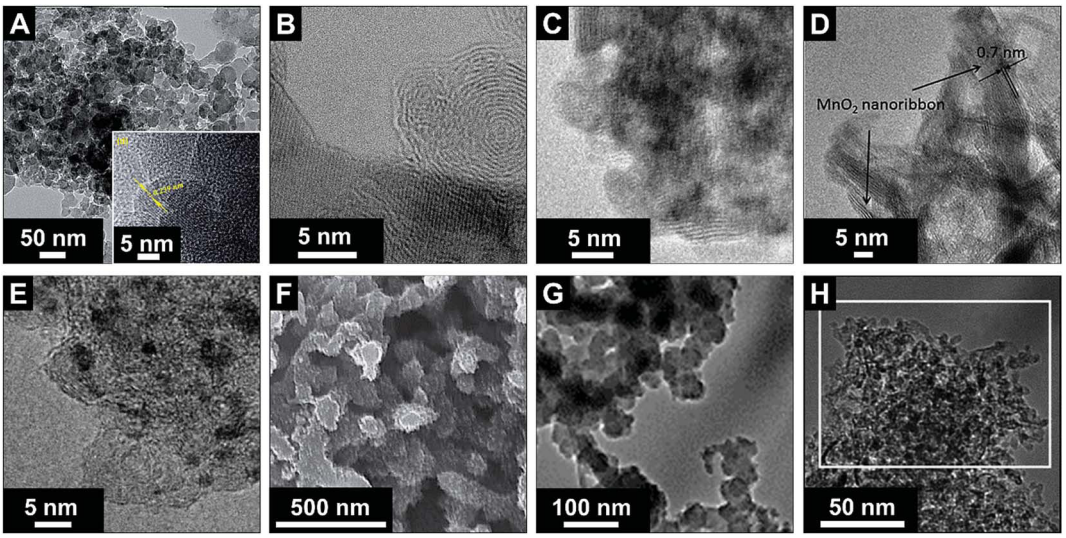

Fig. 11 Transmission and scanning electron micrographs of carbon onions loaded with different types of redox active species. (A–D) Carbon onions decorated with manganese oxide: Azhagan *et al.* (with permission from Royal Society of Chemistry),[86] Makgopa *et al.* (with permission from Royal Society of Chemistry),[135] Borgohain *et al.* (with permission from Royal Society of Chemistry),[136] and Wang *et al.* (with permission from Royal Society of Chemistry);[137] (E) loading with ruthenium oxide: Borgohain *et al.* (with permission from the American Chemical Society);[26] (F) coating with PANI: Kovalenko *et al.* (with permission from John Wiley & Sons Inc.);[132] (G) coating with polypyrrole (PPy): Mykhailiv *et al.* (with permission from John Wiley & Sons Inc.);[138] (H) loading with nickel hydroxide: Plonska-Brzezinska *et al.* (with permission from Royal Society of Chemistry)[27]

decoration with redox-active species (such as quinones or metal oxides). After coating with manganese oxide, the specific capacitance increased to 575 F g^{-1} at 0.5 A g^{-1}, measured in a two-electrode configuration, with a capacitance retention of 18% at 10 A g^{-1}. The relatively low capacitance retention for higher specific current might not only be the result of the low conductivity of the metal oxide coating, but also come from the carbon onion surface functionalities, undergoing irreversible electrochemical transformations at high currents. As shown in ref. 87, high purity carbon onions with a high degree of carbon ordering exhibit superior rate handling with more than 80% capacitance retention even at 20 A g^{-1}. Therefore, the low capacitance retention of the carbon onions before and after their combination with manganese oxide might be the result of large amounts of surface functionalities or the dissolution of manganese oxide in sulfuric acid. Still, the cycle stability after 2000 cycles was more than 90%.[86]

In a study by Borgohain *et al.*, nanodiamond-derived carbon onions were oxidized in sulfuric and nitric acids, and hybrid electrodes of oxidized carbon onions, polydiallyldimethylammonium chloride (PDDA), and delaminated manganese oxide were synthesized by a sequential chemical deposition technique (Fig. 11C).[136] Using a two-electrode configuration and 1 M Na_2SO_4, the highest capacitance of 219 F g^{-1} was reached for the loading with 55 mass% manganese oxide. For comparison, less than 50 F g^{-1} was measured for neat carbon onions.[136] The hybrid electrodes presented a capacitance retention of roughly 80% after 1000 cycles, which is smaller than for the material reported by Azhagan *et al.* with more than 95% after 2000 cycles.[86,136] Borgohain *et al.* used chemical oxidation of carbon onions before they were combined with manganese oxide.[136] Due to the oxidation induced formation of surface functional groups, the stability might be negatively influenced as shown for the as-synthesized carbon onions with a reduction of the capacitance by *ca.* 15% after 1000 cycles. Yet, the decrease was not monotonic: for the first 600 cycles, the capacitance anomalously increased due to faradaic reactions of the surface functional groups and only after their depletion, the capacitance decreased again.[136] A similar effect was found in a study with carbon onions showing reduced stability in an organic electrolyte due to higher contents of oxygen-containing functional groups.[87] The manganese oxide/carbon onion hybrids showed a decrease by *ca.* 15% at 20 mV s^{-1} of the initial low-rate capacitance.[136]

Wang *et al.* used phenolic resin-derived carbon onions hydrothermally coated with manganese oxide in $KMnO_4$ in aqueous solution.[137] In contrast to Borgohain *et al.*, the capacitance did not increase with the manganese oxide loading but rather showed a maximum value of 190 F g^{-1} (galvanostatic mode in 1 M Na_2SO_4) for 80 mass% manganese oxide with a flower-like morphology (Fig. 11D). Up to 2 A g^{-1} in galvanostatic cycling, the electrodes demonstrated good rate handling behavior with more than 93% capacitance retention and almost 100% performance stability over 1000 charge/discharge cycles.[137] For comparison, materials reported by Borgohain *et al.* (219 F g^{-1})[136] and Azhagan *et al.* (575 F g^{-1})[86] had a much lower rate handling ability. These data are in line with a recent study by Makgopa *et al.* using nanodiamond-derived carbon onions and a hydrothermal treatment with $KMnO_4$ producing birnessite-type manganese oxide with a loading of 47 mass% (Fig. 11B).[135] While the as-synthesized carbon onions only showed a capacitance around 30 F g^{-1}, the hybrid electrodes

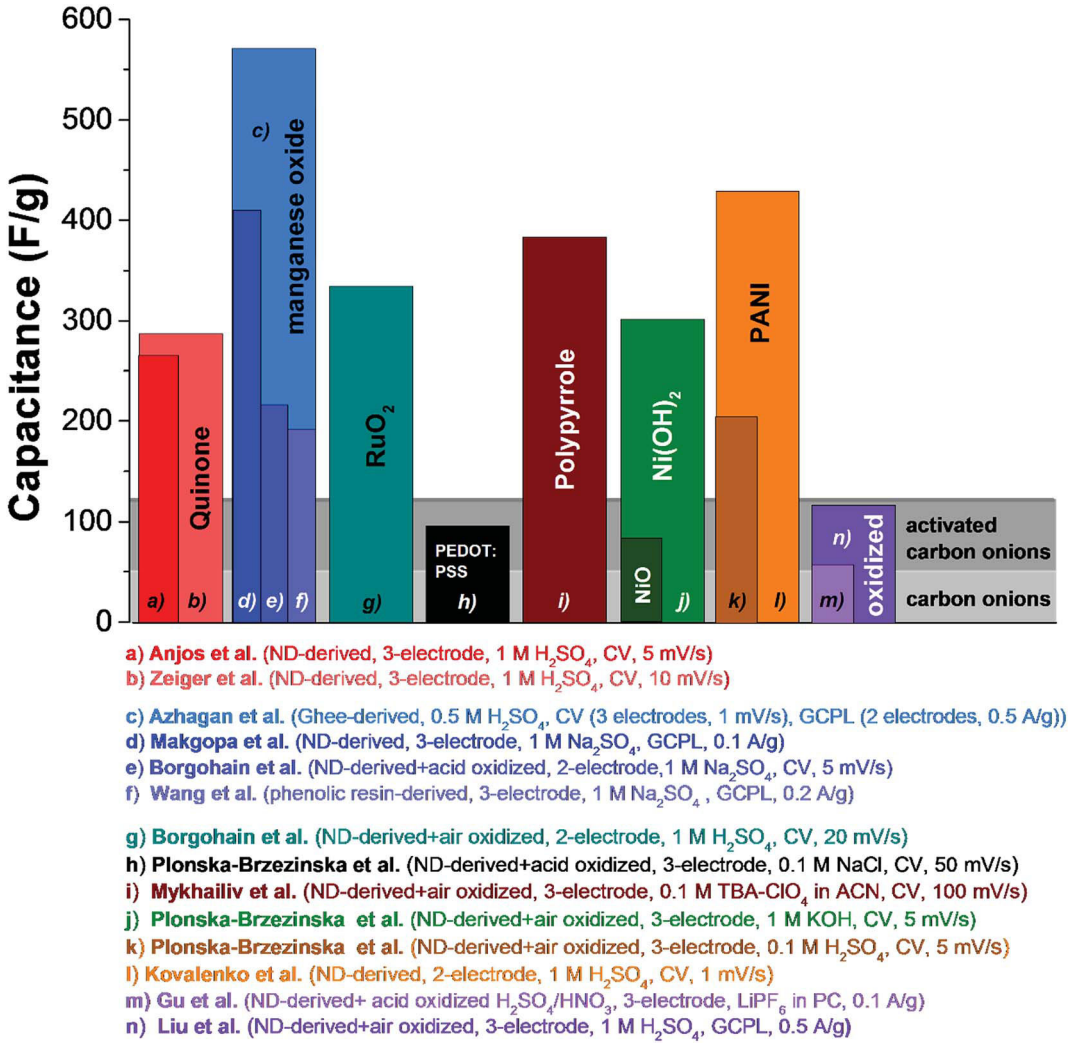

Fig. 12 Comparison of capacitance values of carbon onions decorated with surface functional groups, metal oxides, or conductive polymers. Experimental details are given in the figure. Anjos *et al.*,[139] Zeiger *et al.*,[129] Azhagan *et al.*,[86] Makgopa *et al.*,[135] Borgohain *et al.* (MnO_2),[136] Wang *et al.*,[137] Borgohain *et al.* (RuO_2),[26] Plonska-Brzezinska *et al.* (PEDOT:PSS),[73] Mykhailiv *et al.*,[138] Plonska-Brzezinska *et al.* ($Ni(OH)_2$, the capacitance value in the publication was 1225 F g^{-1}, which is normalized to the carbon content. We adjusted the value by normalization to the electrode mass to compare with other literature values),[27] Plonska-Brzezinska *et al.* (PANI),[74] Kovalenko *et al.*,[132] Gu *et al.*,[28] Liu *et al.*[140]

yielded more than 400 F g^{-1} in 1 M Na_2SO_4 at 0.1 A g^{-1} in a three-electrode setup (Fig. 13A). At higher rates up to 5 A g^{-1}, the material still presents *ca.* 250 F g^{-1} (*i.e.*, 37% decrease).

The rate handling data of several studies of carbon onion/manganese oxide hybrids are shown in Fig. 13B. The plot also shows values for conventional activated carbon and all data are in absolute values so that a direct comparison is possible. Still, a direct quantitative comparison of the rate handling data is difficult due to the different preparation methods and testing setups. For example, Makgopa *et al.*[135] and Wang *et al.*[137] used polyvinylidenefluoride PVDF (5 mass% Makgopa *et al.*, 10 mass% Wang *et al.*) as a binder, with 10 mass% (Wang *et al.*) or 15 mass% (Makgopa *et al.*) carbon black as a conductive additive. The improved charge transport in the presence of a conductive additive (carbon black) complicates a direct comparison of the rate handling data. Moreover, the use of highly graphitic carbon onions with high intrinsic conductivity in the studies by Makgopa *et al.* and Wang *et al.* makes a comparison difficult with other carbon onions, like ghee-derived carbon onions.[86] Also, by the use of carbon onions with a lower electrical conductivity and the absence of an additional conductive additive, the rate handling of the materials reported by Azhagan *et al.* is moderate.[86] While the power handling is limited, the capacitance is very high (575 F g^{-1}), probably due to additional surface functionalities on the carbon onions and the usage of sulfuric acid (oxidizer) as the electrolyte leading to higher values compared to chemically inert electrolytes.[144]

4.3.2 Carbon onions decorated with ruthenium oxide. Ruthenium oxide was also explored as a redox-active coating for carbon onions. Borgohain *et al.* used 5–7 nm nanodiamond-derived carbon onions synthesized at 1650 °C functionalized with polar carboxylic groups.[26] The carbon material was coated with non-agglomerated ruthenium oxide in a hydrothermal reaction using $RuCl_3$ as the precursor (Fig. 11E). Upon loading

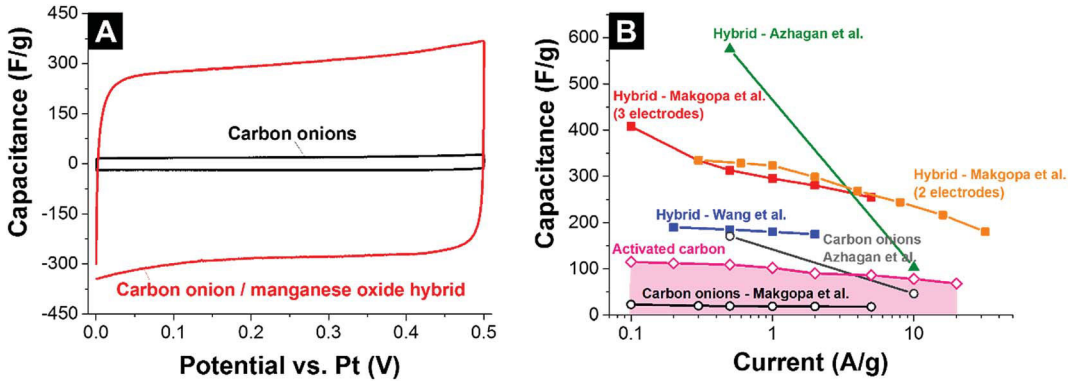

Fig. 13 (A) Cyclic voltammogram of carbon onions and carbon onion/manganese oxide nanohybrids in 1 M Na_2SO_4.[135] (B) Rate handling plot of different types of carbon onions and carbon onion/manganese oxide composites. Makgopa *et al.*: nanodiamond-derived carbon onions coated in a hydrothermal reaction with manganese oxide; 1 M Na_2SO_4 electrolyte.[135] Azhagan *et al.*: burning ghee-derived carbon onions coated using a microwave assisted hydrothermal reaction; 0.5 M H_2SO_4 electrolyte.[86] Borgohain *et al.*: nanodiamond-derived carbon onions were combined with polydiallyldimethylammonium chloride (PDDA), and delaminated-manganese oxide by a sequential chemical deposition technique; 1 M Na_2SO_4 electrolyte.[136] Wang *et al.*: phenolic resin-derived carbon onions were hydrothermally coated with manganese oxide; 1 M Na_2SO_4 electrolyte.[137] Activated carbon electrodes were prepared using 5% PTFE as a binder and measured in 1 M Na_2SO_4 using a full cell set up.

of ruthenium oxide, the surface area decreased from 369 $m^2\ g^{-1}$ for functionalized carbon onions to 126 $m^2\ g^{-1}$ for carbon onions with 68 mass% ruthenium oxide. Accordingly, the capacitance increased up to 334 F g^{-1} for the highest loading of ruthenium oxide measured in 1 M H_2SO_4 by cyclic voltammetry using a full cell setup and a scan rate of 20 mV s^{-1}. The material exhibited excellent power handling when increasing the scan rate from 50 mV s^{-1} to 8 V s^{-1} with nearly ideal capacitance retention.[26] The combination of high electrical conductivity and enhanced surface area (carbon onions) with redox active species (high faradaic charge storage capacity) benefitted improved accessibility of the redox material and allows taking full advantage of the high ion mobility provided by carbon onions. De-agglomerated RuO_2 nanoparticles in the size range of 2–3 nm have a very high surface-to-volume ratio leading to a large ratio of accessible surface to mass per particle. Facile accessibility of the metal oxide nanoparticles to the electrolyte, combined with the good electrical connection to the conductive carbon substrate, enabled a high rate handling behavior. This is paralleled by high performance stability (almost 100% capacity retention after 3000 charge/discharge cycles).[26] In contrast, acid-oxidized carbon onions in the same study without metal oxide decoration underwent irreversible redox reactions due to the surface functional groups and only show ~85% capacitance retention after 3000 cycles.[26]

4.3.3 Carbon onions decorated with nickel oxide. Plonska-Brzezinska *et al.* have explored nickel oxide (hydroxide)/carbon onion hybrids.[27] In one of their studies, nanodiamond-derived carbon onions synthesized at 1650 °C were further oxidized in air to remove amorphous carbon. The resulting carbon onions were loaded with nickel hydroxide nanoparticles (mass ratio *ca.* 4 : 1) in the presence of different modifiers, polyvinylpyrrolidone (PVP), (4-dimethylamino)pyridine (4-DMAP), and pyridinium *p*-toluenesulfonate (PPST). Through further annealing, the composite was transformed to carbon onion and nickel oxide (mass ratio *ca.* 4 : 1). Maximum capacitance values measured in a three-electrode configuration in 1 M KOH at 5 mV s^{-1} scan rate were 306 F g^{-1} for $Ni(OH)_2$ and 73 F g^{-1} for NiO hybrid electrodes with carbon onions. These values were normalized to the total electrode mass to enable a direct comparison with the literature; in the original paper, the reported values of 1225 F g^{-1} and 291 F g^{-1} were normalized only to the carbon content which accounts for ~25 mass% of the total electrode mass. The adjusted values align with values reported for other redox-active hybrid systems, such as a high mass loading of ruthenium oxide (334 F g^{-1})[26] and manganese oxide composites (190 F g^{-1} (ref. 137) to 575 F g^{-1} (ref. 86)). Rate handling was determined by cyclic voltammetry for the hybrid electrodes of carbon onions and $Ni(OH)_2$ or NiO carbon onion composites from 5 mV s^{-1} to 30 mV s^{-1} with a drop in capacitance of ~40% when using $Ni(OH)_2$ and ~6% for NiO. The latter presented promising power handling but suffers from a low 73 F g^{-1} initial capacitance. In contrast, $Ni(OH)_2$ was characterized by a much higher initial capacitance (300% higher) but has relatively poor power handling.

4.3.4 Carbon onions decorated with quinones and functional groups. Redox-active surface species like quinones can significantly enhance the energy storage capacity (preferably in acidic electrolytes).[145] Such systems often do not qualify as pseudocapacitors because their charge-*versus*-voltage is not linear (*i.e.*, non-capacitive), so the use of Farad as a unit has been questioned recently to characterize the capacity of such redox-active energy storage materials.[17,22] However, in order to be able to compare the literature data, we still report in this review values in F g^{-1}.

In a study by Anjos *et al.*, nanodiamond-derived carbon onions were decorated with different types of quinones and tested in 1 M H_2SO_4 in a three-electrode setup.[139] According to the quasielastic neutron scattering experiments by Chathoth *et al.*, quinones arrange parallel to the carbon onion surface due to π interactions between the aromatic rings of the quinones and the carbon planes.[146,147] By scanning from 0.1 V to 0.8 V

versus standard hydrogen, a redox peak was seen between 0.4 and 0.5 V due to a proton coupled electron transfer reaction.[148] The highest capacitance of 264 F g^{-1} was reached in cyclic voltammetry at 5 mV s^{-1} when using 9,10-phenanthrenequinones.[139] The rate handling behavior of these electrodes is rather moderate with only 75 F g^{-1} (*i.e.*, −72%) at 1 V s^{-1} but, in absolute numbers, still better than for activated carbon (*ca.* 20 F g^{-1} at that rate).[129,139] In addition, the performance stability was demonstrated to be high, with the capacitance retention more than 90% after 10 000 charge/discharge cycles.[139] Using nanodiamond-derived carbon onions embedded in a continuous network of conductive carbon nanofibers and 9,10-phenanthrenequinones, the reported capacitance reached values of 288 F g^{-1} at low scan rates and an enhanced power handling could be utilized (135 F g^{-1} at 1 V s^{-1} = −53%).[129]

The cyclic voltammograms of the carbon fiber/carbon onion composite electrodes decorated with different amounts of quinones are shown in Fig. 14A. The redox peak at *ca.* −0.2 V *vs.* Pt increased in area when quinone loading is increased, reaching 288 F g^{-1} capacitance.[129] For a better comparability, Fig. 14B provides an overview of the rate handling ability for different quinone-decorated carbon onion systems (data from cyclic voltammetry). As can be seen, the capacitance retention for carbon onion/carbon fiber composites nears 100% at high scan rates (2 V s^{-1}) and even though the absolute value is rather moderate (34 F g^{-1}) it is still higher than what can be achieved at this scan rate for conventional activated carbon (3 F g^{-1}) using the same set-up and electrolyte system. Loading with quinones increased the capacitance at low scan rates to a maximum value of 288 F g^{-1} at 1 mV s^{-1},[129] which is more than 2 times higher than 115 F g^{-1} for activated carbon at the same rate. For a higher scan rate of 1 V s^{-1}, the capacitance values were still 135 F g^{-1} (ref. 129) and 75 F g^{-1}.[139] Testing over 10 000 cycles demonstrated sufficient stability for quinone-decorated carbon onions and quinone-decorated carbon onion/carbon fiber composites with *ca.* 95% (ref. 139) and *ca.* 90% (ref. 129) capacitance retention, respectively (Fig. 14C).

Apart from loading carbon onions with redox-active or pseudocapacitive materials, an *in situ* electrochemical oxidation of carbon onions in an acidic electrolyte can lead to enhanced capacitive behavior. Liu *et al.* used nanodiamond-derived carbon onions and oxidized them in 1 M H_2SO_4 at a potential from 1.0 to 2.0 V *vs.* Ag/AgCl.[140] The cyclic voltammograms are shown in Fig. 14D. After the first oxidation cycle, the current increases with a maximum at ∼0.3 V and further develops until a capacitance of 99 F g^{-1} (120 F g^{-1} for galvanostatic cycling at 0.5 A g^{-1}) was reached.[140] Due to the insignificant change in specific surface area after electrochemical oxidation, the redox peak is seemingly related to redox-active oxygen functionalities (most probably the quinone–hydroquinone redox couple), which is generated at exfoliated graphene segments of the carbon onions.[140] This assumption is supported by the higher oxygen contents for electrochemically oxidized carbon onions measured with X-ray photoelectron emission spectroscopy (XPS).[140] However, with the higher content of functional groups, the capacitance at higher scan rates decreased to 75 F g^{-1}, which is comparable to what was found for quinone-decorated carbon onions (Fig. 14B).[139] The electrochemical stability was tested for 1000 cycles with nearly 100% capacitance retention in this range. After treating nanodiamond-derived carbon onions in a H_2SO_4/HNO_3 3 : 1 mixture to prepare surface oxidized carbon onions the surface area increased from 384 m^2 g^{-1} to 578 m^2 g^{-1}. Carbon onion shells were etched, interparticle amorphous carbon was removed, and the oxygen content increased from 0.5 at% to 18.3 at%.[124] Electrochemical characterization was performed in a two-electrode coin cell using 1 M lithium hexafluorophosphate ($LiPF_6$) in a 1 : 1 : 1 mixture of dimethyl carbonate (DMC), diethyl carbonate (DEC) and ethylene carbonate (EC), or 1 M $LiPF_6$ in PC.[124] The capacitance values for oxidized carbon onions measured in 1 M $LiPF_6$ in PC are shown in Fig. 14B. The capacitance more than doubled after oxidation compared to untreated carbon onions for all electrolytes. Even when the values were normalized to the enhanced surface area after oxidation, oxidative treatment still increased the normalized capacitance due to redox contributions.[124] However, compared to carbon onions with other surface functionalizations (Fig. 14B) or activated carbon, these values are rather small. The reason might be the lower amount of redox-active sites or the necessity for acidic/protic electrolytes.

4.3.5 Carbon onions decorated with electroactive polymers. Electroactive polymers present another attractive group of materials to impart carbon onion electrodes with additional redox-activity. Polyaniline (PANI) is one of the most popular electrochemically active conductive polymers with a high specific capacitance of maximum 430 F g^{-1} in combination with carbon onions.[132] Conductive polymers, including PANI, commonly suffer from slow charge and discharge compared to carbon materials and poor long-term stability due to volume changes leading to mechanical damage and disrupting conductivity.[132] Therefore, a conductive aid is needed, to enhance the conductivity of the composite. In a study by Kovalenko *et al.*, nanodiamond-derived carbon onions were coated with PANI using a wet chemical approach (Fig. 12F).[132] Pure PANI electrodes demonstrated a capacitance of 470 F g^{-1} in 1 M H_2SO_4 using a symmetric two-electrode configuration (Fig. 15A). The long-term stability after 10 000 cycles was rather low with less than 150 F g^{-1} (*i.e.*, −68%).[132] Electrodes composed of PANI and carbon onions (14 mass% carbon onions) present a more ideal capacitive behavior (Fig. 15B) with slightly smaller capacitance (*ca.* 430 F g^{-1}), but with a much better performance stability (*ca.* −3% capacitance after 10 000 cycles).[132] By increasing the carbon onion amount from 3 to 14 mass%, the capacitance of the composite increased but then decreased when using 28 mass%; thus, there seems to be an optimum load with regard to the electrochemically active surface area.[132] The filling of PANI with nanoparticles lead to a toughening of the polymer and a less distinct volume change during cycling. Interestingly, purified non-conductive nanodiamonds (3 mass%) also significantly enhance the electrode performance. This may sound surprising as purified nanodiamonds have a very low electrical conductivity (≪1 S cm^{-1}) and points to nanodiamond-mediated mechanical toughening and surface roughening of the polymer as the dominant

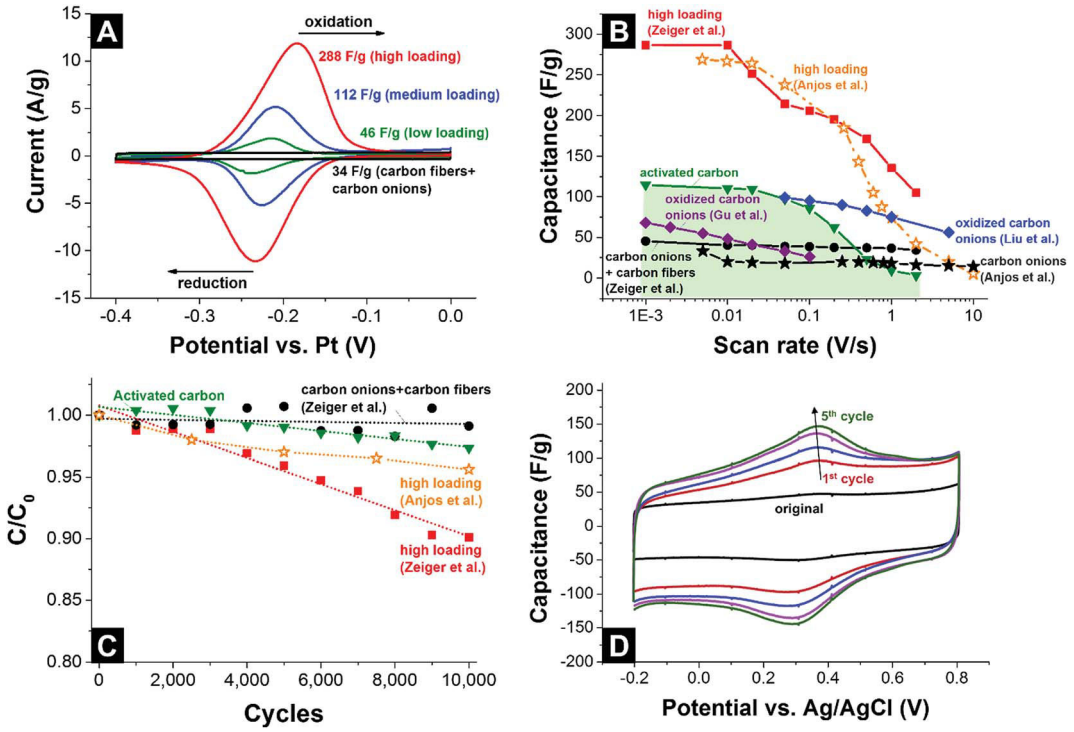

Fig. 14 (A) Cyclic voltammograms of carbon onion/carbon fiber composites loaded with different amounts of 9,10-phenanthrenequinones at 10 mV s^{-1} scan rate.[129] (B) Rate handling data of different types of carbon onions, activated carbon, and carbon onions loaded with quinones or other functional groups. (C) Stability test using 10 000 cycles (CV) with activated carbon, carbon onion/carbon fiber composites, carbon onions and carbon onion/carbon fiber composites loaded with 9,10-phenanthrenequinones. (D) Cyclic voltammograms of carbon onions during electrochemical oxidation. All measurements were performed in 1 M H_2SO_4.[140] Zeiger *et al.*: nanodiamond-derived carbon onion/carbon fiber composites (1700 °C synthesis temperature) loaded with 9,10-phenanthrenequinones, three-electrode set-up, free-standing mats.[87] Anjos *et al.*: nanodiamond-derived carbon onions (1800 °C synthesis temperature), three-electrode set-up, dropcast on glassy carbon.[139] Gu *et al.*: nanodiamond-derived carbon onions (1800 °C synthesis temperature) oxidized with H_2SO_4/HNO_3, two-electrode set-up, 1 M $LiPF_6$ in PC, PTFE-bound electrodes (10 mass%).[124] Liu *et al.*: nanodiamond-derived carbon onions (1650 °C synthesis temperature with further oxidation in air at 400 °C) electrochemically oxidized in 1 M H_2SO_4, three-electrode set-up, dropcast on glassy carbon.[140]

mechanisms responsible for the enhanced electrochemical performance of the PANI-nanodiamond composite (at least at low scan rates). A larger surface area in contact with the electrolyte is a direct result of the nanoscopic size of carbon onions, nanodiamonds, and nanodiamond soot particles and the change in the surface morphology of the PANI (increased roughness) that can be seen with electron microscopy (Fig. 11F). The best enhancement was found when using nanodiamond-containing raw detonation soot. Apparently, this material, which is a mixture of carbon onions, nanodiamonds, amorphous carbon, and other carbon nanoforms, provides an optimal combination of mechanical strength (nanodiamonds),

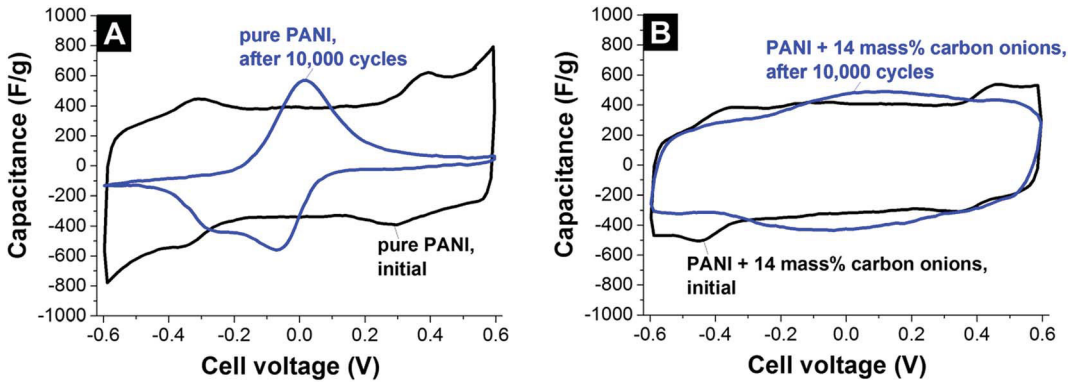

Fig. 15 Cyclic voltammograms of nanodiamond-derived carbon onions (1800 °C synthesis temperature) coated with PANI. Electrodes are PTFE-bound (3 mass%) and measured in a two-electrode configuration using 1 M H_2SO_4 recorded at a scan rate of 1 mV s^{-1}. (A) Pure PANI electrodes. (B) Carbon onion/PANI composite with 14 mass% carbon onions. Data adapted from ref. 132.

conductivity (carbon onions, graphitic carbon), and surface roughness (all together).[132]

Plonska-Brzezinska *et al.* used an *in situ* polymerization technique by first functionalizing nanodiamond-derived carbon onions with *p*-phenylenediamine or 4-aminobenzoic acid and subsequent growth of PANI on the surface groups using the synthesis method from ref. 149 and 150. The functionalized carbon onions were soluble in polar solvents and an increased hydrophilicity and wettability was achieved in aqueous electrolytes.[74] The capacitance measured in 0.1 M H_2SO_4 at 5 mV s^{-1} was 353 F g^{-1} for pure PANI, 207 F g^{-1} for the carbon onion/PANI hybrid with 4-amino-benzoic acid (4-ABAc) and carbon onions, and 155 F g^{-1} for the hybrid with poly-*p*-PDA and carbon onions. These values were slightly smaller than those reported in ref. 132, maybe due to the lower molarity of the electrolyte.

Another well-known inexpensive electroactive polymer is polypyrrole (Ppy) with comparable high conductivity and high stability in aqueous electrolytes. In the study by Mykhailiv *et al.*, carbon onion/polypyrrole hybrids were prepared by chemical polymerization of pyrrole.[138] Carbon onions and sodium dodecyl sulfate (SDS) functionalized carbon onions were coated by Ppy using $FeCl_3$ and pyrrole (Fig. 12G). Negatively charged surface functional groups of carbon onions interact with the pyrrole monomers leading to nucleation centers for the polymerization of pyrrole.[138] The largest capacitance was 805 F g^{-1} in 0.1 M TBA-ClO_4 in ACN at 5 mV s^{-1} scan rate with cyclic voltammetry and smaller values were obtained at higher rates (384 F g^{-1} at 100 mV s^{-1}, *i.e.*, −52%). The capacitance value of 384 F g^{-1} is derived from integration of the cyclic voltammogram and therefore more representative than the values derived from the current at a specific potential in the CV (in this case: 805 F g^{-1} at 0.1 V *versus* Ag/AgCl). The strong decrease in capacitance with increasing scan rate can be attributed to the inaccessibility of parts of the electrode at higher rates or degradation phenomena. Degradation of the electrode is supported by the low stability after 500 cycles at 100 mV s^{-1} of ∼20% and ∼35% depending on the potential window of −1 V to +0.3 V and −2 V to +0.6 V, respectively.[138]

Like for PANI and PPy, carbon onions can also be used as conductive substrates for poly(3,4-ethylenedioxythiophene):poly(styrenesulfonate) (PEDOT:PSS). Plonska-Brzezinska *et al.* used nanodiamond-derived carbon onions as well as their acid-oxidized form for coating with PEDOT:PSS layers.[73] By increasing the amount of PEDOT:PSS in the composite a maximum capacitance of 95 F g^{-1} was reached (1 : 1 mass ratio) for the composite with neat carbon onions and 47 F g^{-1} for the composite with oxidized carbon onions.[73]

5. Conclusions

This work provides an overview of electrochemical applications of carbon onions, and especially of nanodiamond-derived carbon onions. Several synthesis methods exist, but a standard method, with a high yield, reproducibility, and full control of structure, is the annealing of detonation nanodiamond powders. According to the synthesis conditions several properties, such as surface area and conductivity, can be tuned. Carbon onions as supercapacitor electrode materials present a superior rate handling behavior but suffer from a comparatively low specific energy. To overcome this issue, composites with metal oxides, conducting polymers, other redox species, as well as creation of surface functional groups can be used to induce the redox activity of carbon onions.

Carbon onions present a nearly ideal substrate for coating with redox-active substances due to their external and fully accessible surface area, combined with a high degree of sp^2-hybridized carbon ordering. In addition, carbon onions can be used as a potent conductive additive which enhances the power handling ability of supercapacitor carbon electrodes more than conventional carbon black or graphite nanoparticles. Further research aimed at enhancing the surface area of carbon onions and improving the rate handling for advanced redox-active hybrid electrodes will help to further promote the use of this unique carbon nanomaterial for electrochemical applications.

Acknowledgements

The authors thank Prof. Eduard Arzt (INM) for his continuing support. We acknowledge funding from the German Federal Ministry for Research and Education (BMBF) in support of the nanoEES^{3D} project (award number 03EK3013) as part of the strategic funding initiative energy storage framework. This work was supported by the CREATe-Network Project, Horizon 2020 of the European Commission (RISE Project No. 644013). The authors thank Prof. Gleb Yushin (Georgia Tech) for supporting us with experimental data and useful discussions.

References

1 A. H. C. Neto, The carbon new age, *Mater. Today*, 2010, **13**(3), 12–17.
2 J. Bartelmess and S. Giordani, Carbon nano-onions (multilayer fullerenes): chemistry and applications, *Beilstein J. Nanotechnol.*, 2014, **5**(1), 1980–1998.
3 M. G. Crestani, I. Puente-Lee, L. Rendón-Vazquez, P. Santiago, F. del Rio, D. Morales-Morales, *et al.*, The catalytic reduction of carbon dioxide to carbon onion particles by platinum catalysts, *Carbon*, 2005, **43**(12), 2621–2624.
4 C. Portet, G. Yushin and Y. Gogotsi, Electrochemical performance of carbon onions, nanodiamonds, carbon black and multiwalled nanotubes in electrical double layer capacitors, *Carbon*, 2007, **45**(13), 2511–2518.
5 S. Porada, L. Borchardt, M. Oschatz, M. Bryjak, J. Atchison, K. Keesman, *et al.*, Direct prediction of the desalination performance of porous carbon electrodes for capacitive deionization, *Energy Environ. Sci.*, 2013, **6**(12), 3700–3712.
6 D. Pech, M. Brunet, H. Durou, P. Huang, V. Mochalin, Y. Gogotsi, *et al.*, Ultrahigh-power micrometre-sized supercapacitors based on onion-like carbon, *Nat. Nanotechnol.*, 2010, **5**(9), 651–654.
7 N. Jäckel, D. Weingarth, M. Zeiger, M. Aslan, I. Grobelsek and V. Presser, Comparison of carbon onions and carbon

blacks as conductive additives for carbon supercapacitors in organic electrolytes, *J. Power Sources*, 2014, **272**, 1122–1133.

8 J. K. McDonough and Y. Gogotsi, Carbon onions: synthesis and electrochemical applications, *Electrochem. Soc. Interface*, 2013, **22**(3), 61–65.

9 M. E. Plonska-Brzezinska and L. Echegoyen, Carbon nano-onions for supercapacitor electrodes: recent developments and applications, *J. Mater. Chem. A*, 2013, **1**(44), 13703–13714.

10 Z. Yang, J. Zhang, M. C. Kintner-Meyer, X. Lu, D. Choi, J. P. Lemmon, *et al.*, Electrochemical energy storage for green grid, *Chem. Rev.*, 2011, **111**(5), 3577–3613.

11 J. R. Miller, Valuing reversible energy storage, *Science*, 2012, **335**(6074), 1312–1313.

12 D. Dubal, O. Ayyad, V. Ruiz and P. Gómez-Romero, Hybrid energy storage: the merging of battery and supercapacitor chemistries, *Chem. Soc. Rev.*, 2015, **44**(7), 1777–1790.

13 F. X. Index, *Nanocarbons for Advanced Energy Storage*, Wiley-VCH Verlag GmbH & Co. KGaA, 2015, p. 455–464.

14 F. Béguin, V. Presser, A. Balducci and E. Frackowiak, Carbons and Electrolytes for Advanced Supercapacitors, *Adv. Mater.*, 2014, **26**(14), 2219–2251.

15 A. Manthiram, S. H. Chung and C. Zu, Lithium–Sulfur Batteries: Progress and Prospects, *Adv. Mater.*, 2015, **27**(12), 1980–2006.

16 S. Goriparti, E. Miele, F. de Angelis, E. Di Fabrizio, R. P. Zaccaria and C. Capiglia, Review on recent progress of nanostructured anode materials for Li-ion batteries, *J. Power Sources*, 2014, **257**, 421–443.

17 A. Laheäär, P. Przygocki, Q. Abbas and F. Béguin, Appropriate methods for evaluating the efficiency and capacitive behavior of different types of supercapacitors, *Electrochem. Commun.*, 2015, **60**, 21–25.

18 P. Simon, Y. Gogotsi and B. Dunn, Where Do Batteries End and Supercapacitors Begin?, *Science*, 2014, **343**, 1210–1211.

19 J. R. Miller and A. F. Burke, Electrochemical capacitors: challenges and opportunities for real-world applications, *Electrochem. Soc. Interface*, 2008, **17**(1), 53.

20 T. A. Centeno, O. Sereda and F. Stoeckli, Capacitance in carbon pores of 0.7 to 15 nm: a regular pattern, *Phys. Chem. Chem. Phys.*, 2011, **13**(27), 12403–12406.

21 P. Bandaru, H. Yamada, R. Narayanan and M. Hoefer, Charge transfer and storage in nanostructures, *Mater. Sci. Eng., R*, 2015, **96**, 1–69.

22 B. Akinwolemiwa, C. Peng and G. Z. Chen, Redox electrolytes in supercapacitors, *J. Electrochem. Soc.*, 2015, **162**(5), A5140–A5147.

23 I. Hadjipaschalis, A. Poullikkas and V. Efthimiou, Overview of current and future energy storage technologies for electric power applications, *Renewable Sustainable Energy Rev.*, 2009, **13**(6–7), 1513–1522.

24 Y. Zhang, H. Feng, X. B. Wu, L. Z. Wang, A. Q. Zhang, T. C. Xia, *et al.*, Progress of electrochemical capacitor electrode materials: a review, *Int. J. Hydrogen Energy*, 2009, **34**(11), 4889–4899.

25 M. Vangari, T. Pryor and L. Jiang, Supercapacitors: Review of Materials and Fabrication Methods, *J. Energy Eng.*, 2013, **139**(2), 72–79.

26 R. Borgohain, J. Li, J. P. Selegue and Y.-T. Cheng, Electrochemical study of functionalized carbon nano-onions for high-performance supercapacitor electrodes, *J. Phys. Chem. C*, 2012, **116**(28), 15068–15075.

27 M. E. Plonska-Brzezinska, D. M. Brus, A. Molina-Ontoria and L. Echegoyen, Synthesis of carbon nano-onion and nickel hydroxide/oxide composites as supercapacitor electrodes, *RSC Adv.*, 2013, **3**(48), 25891–25901.

28 W. Gu and G. Yushin, Review of nanostructured carbon materials for electrochemical capacitor applications: advantages and limitations of activated carbon, carbide-derived carbon, zeolite-templated carbon, carbon aerogels, carbon nanotubes, onion-like carbon, and graphene, *Wiley Interdiscip. Rev.: Energy Environ.*, 2014, **3**(5), 424–473.

29 I. Suarez-Martinez, N. Grobert and C. P. Ewels, Nomenclature of sp^2 carbon nanoforms, *Carbon*, 2012, **50**(3), 741–747.

30 D. Ugarte, Curling and closure of graphitic networks under electron-beam irradiation, *Nature*, 1992, **359**(6397), 707–709.

31 S. Iijima, Direct observation of the tetrahedral bonding in graphitized carbon black by high resolution electron microscopy, *J. Cryst. Growth*, 1980, **50**(3), 675–683.

32 M. Zeiger, N. Jäckel, M. Aslan, D. Weingarth and V. Presser, Understanding structure and porosity of nanodiamond-derived carbon onions, *Carbon*, 2015, **84**, 584–598.

33 A. Bianco, H.-M. Cheng, T. Enoki, Y. Gogotsi, R. H. Hurt, N. Koratkar, *et al.*, All in the graphene family – a recommended nomenclature for two-dimensional carbon materials, *Carbon*, 2013, **65**, 1–6.

34 O. A. Shenderova and D. M. Gruen, *Ultrananocrystalline diamond: synthesis, properties and applications*, William Andrew, 2012.

35 B. Maquin, A. Derré, C. Labrugère, M. Trinquecoste, P. Chadeyron and P. Delhaès, Submicronic powders containing carbon, boron and nitrogen: their preparation by chemical vapour deposition and their characterization, *Carbon*, 2000, **38**(1), 145–156.

36 V. Serin, R. Brydson, A. Scott, Y. Kihn, O. Abidate, B. Maquin, *et al.*, Evidence for the solubility of boron in graphite by electron energy loss spectroscopy, *Carbon*, 2000, **38**(4), 547–554.

37 C. He, N. Zhao, C. Shi, X. Du and J. Li, Carbon nanotubes and onions from methane decomposition using Ni/Al catalysts, *Mater. Chem. Phys.*, 2006, **97**(1), 109–115.

38 S. Tsai, C. Lee, C. Chao and H. Shih, A novel technique for the formation of carbon-encapsulated metal nanoparticles on silicon, *Carbon*, 2000, **38**(5), 781–785.

39 S.-S. Hou, D.-H. Chung and T.-H. Lin, High-yield synthesis of carbon nano-onions in counterflow diffusion flames, *Carbon*, 2009, **47**(4), 938–947.

40 M. Choucair and J. A. Stride, The gram-scale synthesis of carbon onions, *Carbon*, 2012, **50**(3), 1109–1115.

41 Y. Gao, Y. Zhou, J. Park, H. Wang, X. N. He, H. Luo, *et al.*, Resonant excitation of precursor molecules in improving the particle crystallinity, growth rate and optical limiting performance of carbon nano-onions, *Nanotechnology*, 2011, **22**(16), 165604.
42 M. Zhao, H. Song, X. Chen and W. Lian, Large-scale synthesis of onion-like carbon nanoparticles by carbonization of phenolic resin, *Acta Mater.*, 2007, **55**(18), 6144–6150.
43 M. Bystrzejewski, M. H. Rummeli, T. Gemming, H. Lange and A. Huczko, Catalyst-free synthesis of onion-like carbon nanoparticles, *New Carbon Mater.*, 2010, **25**(1), 1–8.
44 D.-H. Chung, T.-H. Lin and S.-S. Hou, Flame synthesis of carbon nano-onions enhanced by acoustic modulation, *Nanotechnology*, 2010, **21**(43), 435604.
45 M. Choi, I. S. Altman, Y. J. Kim, P. V. Pikhitsa, S. Lee, G. S. Park, *et al.*, Formation of Shell-Shaped Carbon Nanoparticles Above a Critical Laser Power in Irradiated Acetylene, *Adv. Mater.*, 2004, **16**(19), 1721–1725.
46 J. Huang, H. Yasuda and H. Mori, Highly curved carbon nanostructures produced by ball-milling, *Chem. Phys. Lett.*, 1999, **303**(1), 130–134.
47 X. H. Chen, H. S. Yang, G. T. Wu, M. Wang, F. M. Deng, X. B. Zhang, *et al.*, Generation of curved or closed-shell carbon nanostructures by ball-milling of graphite, *J. Cryst. Growth*, 2000, **218**(1), 57–61.
48 T. Cabioc'h, M. Jaouen, E. Thune, P. Guerin, C. Fayoux and M. Denanot, Carbon onions formation by high-dose carbon ion implantation into copper and silver, *Surf. Coat. Technol.*, 2000, **128**, 43–50.
49 E. Thune, T. Cabioc'h, P. Guérin, M.-F. Denanot and M. Jaouen, Nucleation and growth of carbon onions synthesized by ion-implantation: a transmission electron microscopy study, *Mater. Lett.*, 2002, **54**(2), 222–228.
50 H. Lange, M. Sioda, A. Huczko, Y. Zhu, H. Kroto and D. Walton, Nanocarbon production by arc discharge in water, *Carbon*, 2003, **41**(8), 1617–1623.
51 M. Ishigami, J. Cumings, A. Zettl and S. Chen, A simple method for the continuous production of carbon nanotubes, *Chem. Phys. Lett.*, 2000, **319**(5), 457–459.
52 N. Sano, H. Wang, M. Chhowalla, I. Alexandrou and G. Amaratunga, Nanotechnology: synthesis of carbon 'onions' in water, *Nature*, 2001, **414**(6863), 506–507.
53 W. Lian, H. Song, X. Chen, L. Li, J. Huo, M. Zhao, *et al.*, The transformation of acetylene black into onion-like hollow carbon nanoparticles at 1000 °C using an iron catalyst, *Carbon*, 2008, **46**(3), 525–530.
54 J.-C. Fan, H.-H. Sung, C.-R. Lin and M.-H. Lai, The production of onion-like carbon nanoparticles by heating carbon in a liquid alcohol, *J. Mater. Chem.*, 2012, **22**(19), 9794.
55 S. Tomita, A. Burian, J. C. Dore, D. LeBolloch, M. Fujii and S. Hayashi, Diamond nanoparticles to carbon onions transformation: X-ray diffraction studies, *Carbon*, 2002, **40**(9), 1469–1474.
56 Y. V. Butenko, V. L. Kuznetsov, A. L. Chuvilin, V. N. Kolomiichuk, S. V. Stankus, R. A. Khairulin, *et al.*, Kinetics of the graphitization of dispersed diamonds at "low" temperatures, *J. Appl. Phys.*, 2000, **88**(7), 4380.
57 S. Tomita, T. Sakurai, H. Ohta, M. Fujii and S. Hayashi, Structure and electronic properties of carbon onions, *J. Chem. Phys.*, 2001, **114**(17), 7477.
58 O. O. Mykhaylyk, Y. M. Solonin, D. N. Batchelder and R. Brydson, Transformation of nanodiamond into carbon onions: a comparative study by high-resolution transmission electron microscopy, electron energy-loss spectroscopy, X-ray diffraction, small-angle X-ray scattering, and ultraviolet Raman spectroscopy, *J. Appl. Phys.*, 2005, **97**(7), 074302–074316.
59 Y. V. Butenko, V. L. Kuznetsov, E. A. Paukshtis, A. I. Stadnichenko, I. N. Mazov, S. I. Moseenkov, *et al.*, The Thermal Stability of Nanodiamond Surface Groups and Onset of Nanodiamond Graphitization, *Fullerenes, Nanotubes, Carbon Nanostruct.*, 2006, **14**(2–3), 557–564.
60 Q. Zou, Y. G. Li, B. Lv, M. Z. Wang, L. H. Zou and Y. C. Zhao, Transformation of onion-like carbon from nanodiamond by annealing, *Inorg. Mater.*, 2010, **46**(2), 127–131.
61 V. L. Kuznetsov, A. L. Chuvilin, Y. V. Butenko, I. Y. Mal'kov and V. M. Titov, Onion-like carbon from ultra-disperse diamond, *Chem. Phys. Lett.*, 1994, **222**(4), 343–348.
62 N. Xu, J. Chen and S. Deng, Effect of heat treatment on the properties of nano-diamond under oxygen and argon ambient, *Diamond Relat. Mater.*, 2002, **11**(2), 249–256.
63 A. Aleksenskii, M. Baidakova, A. Y. Vul, V. Y. Davydov and Y. A. Pevtsova, Diamond–graphite phase transition in ultradisperse-diamond clusters, *Phys. Solid State*, 1997, **39**(6), 1007–1015.
64 M. Baidakova, V. Siklitsky and A. Y. Vul, Ultradisperse-diamond nanoclusters. Fractal structure and diamond–graphite phase transition, *Chaos, Solitons Fractals*, 1999, **10**(12), 2153–2163.
65 D. Weingarth, M. Zeiger, N. Jäckel, M. Aslan, G. Feng and V. Presser, Graphitization as a universal tool to tailor the potential-dependent capacitance of carbon supercapacitors, *Adv. Energy Mater.*, 2014, **4**, 1400316.
66 O. E. Andersson, B. Prasad, H. Sato, T. Enoki, Y. Hishiyama, Y. Kaburagi, *et al.*, Structure and electronic properties of graphite nanoparticles, *Phys. Rev. B: Condens. Matter Mater. Phys.*, 1998, **58**(24), 16387.
67 J. Chen, S. Deng, J. Chen, Z. Yu and N. Xu, Graphitization of nanodiamond powder annealed in argon ambient, *Appl. Phys. Lett.*, 1999, **74**(24), 3651–3653.
68 F. Y. Xie, W. G. Xie, L. Gong, W. H. Zhang, S. H. Chen, Q. Z. Zhang, *et al.*, Surface characterization on graphitization of nanodiamond powder annealed in nitrogen ambient, *Surf. Interface Anal.*, 2010, **42**(9), 1514–1518.
69 A. Aleksenskii, M. Baidakova, A. Y. Vul, A. Dideikin and V. Siklitskii, Effect of hydrogen on the structure of ultradisperse diamond, *Phys. Solid State*, 2000, **42**(8), 1575–1578.
70 O. Mykhailiv, A. Lapinski, A. Molina-Ontoria, E. Regulska, L. Echegoyen, A. T. Dubis, *et al.*, Influence of the Synthetic Conditions on the Structural and

Electrochemical Properties of Carbon Nano-Onions, *ChemPhysChem*, 2015, **16**(10), 2182–2191.

71 M. E. Plonska-Brzezinska, A. T. Dubis, A. Lapinski, A. Villalta-Cerdas and L. Echegoyen, Electrochemical propertiesof oxidized carbon nano-onions: DRIFTS-FTIR and Raman spectroscopic analyses, *ChemPhysChem*, 2011, **12**(14), 2659–2668.

72 M. E. Plonska-Brzezinska, A. Lapinski, A. Z. Wilczewska, A. T. Dubis, A. Villalta-Cerdas, K. Winkler, *et al.*, The synthesis and characterization of carbon nano-onions produced by solution ozonolysis, *Carbon*, 2011, **49**(15), 5079–5089.

73 M. E. Plonska-Brzezinska, M. Lewandowski, M. Błaszyk, A. Molina-Ontoria, T. Luciński and L. Echegoyen, Preparation and Characterization of Carbon Nano-Onion/PEDOT: PSS Composites, *ChemPhysChem*, 2012, **13**(18), 4134–4141.

74 M. E. Plonska-Brzezinska, J. Mazurczyk, B. Palys, J. Breczko, A. Lapinski, A. T. Dubis, *et al.*, Preparation and Characterization of Composites that Contain Small Carbon Nano-Onions and Conducting Polyaniline, *Chem.–Eur. J.*, 2012, **18**(9), 2600–2608.

75 M. E. Plonska-Brzezinska, A. Molina-Ontoria and L. Echegoyen, Post-modification by low-temperature annealing of carbon nano-onions in the presence of carbohydrates, *Carbon*, 2014, **67**, 304–317.

76 A. V. Gubarevich, J. Kitamura, S. Usuba, H. Yokoi, Y. Kakudate and O. Odawara, Onion-like carbon deposition by plasma spraying of nanodiamonds, *Carbon*, 2003, **41**(13), 2601–2606.

77 J. Xiao, G. Ouyang, P. Liu, C. Wang and G. Yang, Reversible nanodiamond-carbon onion phase transformations, *Nano Lett.*, 2014, **14**(6), 3645–3652.

78 F. Banhart, T. Füller, P. Redlich and P. Ajayan, The formation, annealing and self-compression of carbon onions under electron irradiation, *Chem. Phys. Lett.*, 1997, **269**(3), 349–355.

79 D. Ugarte, Morphology and structure of graphitic soot particles generated in arc-discharge C_{60} production, *Chem. Phys. Lett.*, 1992, **198**(6), 596–602.

80 A. B. Du, X. G. Liu, D. J. Fu, P. D. Han and B. S. Xu, Onion-like fullerenes synthesis from coal, *Fuel*, 2007, **86**(1–2), 294–298.

81 Y. Gao, Y. S. Zhou, M. Qian, X. N. He, J. Redepenning, P. Goodman, *et al.*, Chemical activation of carbon nano-onions for high-rate supercapacitor electrodes, *Carbon*, 2013, **51**, 52–58.

82 R. Borgohain, J. Yang, J. P. Selegue and D. Y. Kim, Controlled synthesis, efficient purification, and electrochemical characterization of arc-discharge carbon nano-onions, *Carbon*, 2014, **66**, 272–284.

83 J. K. McDonough, A. I. Frolov, V. Presser, J. Niu, C. H. Miller, T. Ubieto, *et al.*, Influence of the structure of carbon onions on their electrochemical performance in supercapacitor electrodes, *Carbon*, 2012, **50**(9), 3298–3309.

84 E. G. Bushueva, P. S. Galkin, A. V. Okotrub, L. G. Bulusheva, N. N. Gavrilov, V. L. Kuznetsov, *et al.*, Double layer supercapacitor properties of onion-like carbon materials, *Phys. Status Solidi B*, 2008, **245**(10), 2296–2299.

85 M. E. Plonska-Brzezinska, A. Palkar, K. Winkler and L. Echegoyen, Electrochemical properties of small carbon nano-onion films, *Electrochem. Solid-State Lett.*, 2010, **13**(4), K35–K8.

86 M. V. K. Azhagan, M. V. Vaishampayan and M. V. Shelke, Synthesis and electrochemistry of pseudocapacitive multilayer fullerenes and MnO_2 nanocomposites, *J. Mater. Chem. A*, 2014, **2**(7), 2152–2159.

87 M. Zeiger, N. Jäckel, D. Weingarth and V. Presser, Vacuum or flowing argon: What is the best synthesis atmosphere for nanodiamond-derived carbon onions for supercapacitor electrodes?, *Carbon*, 2015, **94**, 507–517.

88 V. N. Mochalin, O. Shenderova, D. Ho and Y. Gogotsi, The properties and applications of nanodiamonds, *Nat. Nanotechnol.*, 2012, **7**(1), 11–23.

89 D. P. Mitev, A. T. Townsend, B. Paull and P. N. Nesterenko, Direct sector field ICP-MS determination of metal impurities in detonation nanodiamond, *Carbon*, 2013, **60**, 326–334.

90 X. Fang, J. Mao, E. Levin and K. Schmidt-Rohr, Nonaromatic Core–Shell Structure of Nanodiamond from Solid-State NMR Spectroscopy, *J. Am. Chem. Soc.*, 2009, **131**(4), 1426–1435.

91 A. Panich, A. Shames, H.-M. Vieth, E. Ōsawa, M. Takahashi and A. Y. Vul, Nuclear magnetic resonance study of ultrananocrystalline diamonds, *Eur. Phys. J. B*, 2006, **52**(3), 397–402.

92 M. Dubois, K. Guérin, E. Petit, N. Batisse, A. Hamwi, N. Komatsu, *et al.*, Solid-state NMR study of nanodiamonds produced by the detonation technique, *J. Phys. Chem. C*, 2009, **113**(24), 10371–10378.

93 A. Krüger, F. Kataoka, M. Ozawa, T. Fujino, Y. Suzuki, A. Aleksenskii, *et al.*, Unusually tight aggregation in detonation nanodiamond: identification and disintegration, *Carbon*, 2005, **43**(8), 1722–1730.

94 V. Kuznetsov and Y. V. Butenko, Synthesis and properties of nanostructured carbon materials: nanodiamond, onion-like carbon and carbon nanotubes, *Nanostructured Materials and Coatings for Biomedical and Sensor Applications*, Springer, 2003, pp. 187–202.

95 F. Cataldo and A. P. Koscheev, A study on the action of ozone and on the thermal stability of nanodiamond, *Fullerenes, Nanotubes, Carbon Nanostruct.*, 2003, **11**(3), 201–218.

96 B. J. M. Etzold, I. Neitzel, M. Kett, F. Strobl, V. N. Mochalin and Y. Gogotsi, Layer-by-Layer Oxidation for Decreasing the Size of Detonation Nanodiamond, *Chem. Mater.*, 2014, **26**(11), 3479–3484.

97 P. Ganesh, P. Kent and V. Mochalin, Formation, characterization, and dynamics of onion-like carbon structures for electrical energy storage from nanodiamonds using reactive force fields, *J. Appl. Phys.*, 2011, **110**(7), 073506.

98 T. Jiang and K. Xu, FTIR study of ultradispersed diamond powder synthesized by explosive detonation, *Carbon*, 1995, **33**(12), 1663–1671.

99 B. Spitsyn, M. Gradoboev, T. Galushko, T. Karpukhina, N. Serebryakova and I. Kulakova, *et al.*, Purification and functionalization of nanodiamond, *Synthesis, properties and applications of ultrananocrystalline diamond*, Springer, 2005, pp. 241–52.

100 T. Petit, J.-C. Arnault, H. A. Girard, M. Sennour and P. Bergonzo, Early stages of surface graphitization on nanodiamond probed by X-ray photoelectron spectroscopy, *Phys. Rev. B: Condens. Matter Mater. Phys.*, 2011, **84**(23), 233407.

101 K. Bogdanov, A. Fedorov, V. Osipov, T. Enoki, K. Takai, T. Hayashi, *et al.*, Annealing-induced structural changes of carbon onions: high-resolution transmission electron microscopy and Raman studies, *Carbon*, 2014, **73**, 78–86.

102 A. Ferrari, A. Libassi, B. Tanner, V. Stolojan, J. Yuan, L. Brown, *et al.*, Density, sp^3 fraction, and cross-sectional structure of amorphous carbon films determined by X-ray reflectivity and electron energy-loss spectroscopy, *Phys. Rev. B: Condens. Matter Mater. Phys.*, 2000, **62**(16), 11089.

103 J. Cebik, J. K. McDonough, F. Peerally, R. Medrano, I. Neitzel, Y. Gogotsi, *et al.*, Raman spectroscopy study of the nanodiamond-to-carbon onion transformation, *Nanotechnology*, 2013, **24**(20), 205703.

104 V. L. Kuznetsov, I. L. Zilberberg, Y. V. Butenko, A. L. Chuvilin and B. Segall, Theoretical study of the formation of closed curved graphite-like structures during annealing of diamond surface, *J. Appl. Phys.*, 1999, **86**(2), 863.

105 A. Siklitskaya, S. Yastrebov and R. Smith, Variable step radial ordering in carbon onions, *Diamond Relat. Mater.*, 2013, **32**, 32–35.

106 A. Siklitskaya, S. Yastrebov and R. Smith, Structure-induced negatively skewed X-ray diffraction pattern of carbon onions, *J. Appl. Phys.*, 2013, **114**(13), 134305.

107 M. Ozawa, H. Goto, M. Kusunoki and E. Ōsawa, Continuously Growing Spiral Carbon Nanoparticles as the Intermediates in the Formation of Fullerenes and Nanoonions, *J. Phys. Chem. B*, 2002, **106**(29), 7135–7138.

108 E. Akatyeva, J. Huang and T. Dumitrică, Edge-mediated dislocation processes in multishell carbon nano-onions?, *Phys. Rev. Lett.*, 2010, **105**(10), 106102.

109 Z. Qiao, J. Li, N. Zhao, C. Shi and P. Nash, Graphitization and microstructure transformation of nanodiamond to onion-like carbon, *Scr. Mater.*, 2006, **54**(2), 225–229.

110 L. Reinert, M. Zeiger, S. Suarez, V. Presser and F. Mücklich, Dispersion analysis of carbon nanotubes, carbon onions, and nanodiamonds for their application as reinforcement phase in nickel metal matrix composites, *RSC Adv.*, 2015, **5**, 95149–95159.

111 V. Kuznetsov, S. Moseenkov, A. Ischenko, A. Romanenko, T. Buryakov, O. Anikeeva, *et al.*, Controllable electromagnetic response of onion-like carbon based materials, *Phys. Status Solidi B*, 2008, **245**(10), 2051–2054.

112 Y. Gan and F. Banhart, The mobility of carbon atoms in graphitic nanoparticles studied by the relaxation of strain in carbon onions, *Adv. Mater.*, 2008, **20**(24), 4751–4754.

113 E. D. Obraztsova, M. Fujii, S. Hayashi, V. L. Kuznetsov, Y. V. Butenko and A. L. Chuvilin, Raman identification of onion-like carbon, *Carbon*, 1998, **36**(5–6), 821–826.

114 D. Roy, M. Chhowalla, H. Wang, N. Sano, I. Alexandrou, T. W. Clyne, *et al.*, Characterisation of carbon nano-onions using Raman spectroscopy, *Chem. Phys. Lett.*, 2003, **373**(1–2), 52–56.

115 S. N. Bokova-Sirosh, A. V. Pershina, V. L. Kuznetsov, A. V. Ishchenko, S. I. Moseenkov, A. S. Orekhov, *et al.*, Raman Spectra for Characterization of Onion-Like Carbon, *J. Nanoelectron. Optoelectron.*, 2013, **8**(1), 106–109.

116 F. Tuinstra, Raman Spectrum of Graphite, *J. Chem. Phys.*, 1970, **53**(3), 1126.

117 A. Ferrari and J. Robertson, Resonant Raman spectroscopy of disordered, amorphous, and diamondlike carbon, *Phys. Rev. B: Condens. Matter Mater. Phys.*, 2001, **64**(7), 075414.

118 V. V. Roddatis, V. L. Kuznetsov, Y. V. Butenko, D. S. Su and R. Schlögl, Transformation of diamond nanoparticles into carbon onions under electron irradiation, *Phys. Chem. Chem. Phys.*, 2002, **4**(10), 1964–1967.

119 L. Joly-Pottuz, N. Matsumoto, H. Kinoshita, B. Vacher, M. Belin, G. Montagnac, *et al.*, Diamond-derived carbon onions as lubricant additives, *Tribol. Int.*, 2008, **41**(2), 69–78.

120 V. Kuznetsov, Y. V. Butenko, A. Chuvilin, A. Romanenko and A. Okotrub, Electrical resistivity of graphitized ultra-disperse diamond and onion-like carbon, *Chem. Phys. Lett.*, 2001, **336**(5), 397–404.

121 Q. Zou, M. Wang, Y. Li, Y. Zhao and L. Zou, Fabrication of onion-like carbon from nanodiamond by annealing, *Sci. China, Ser. E: Technol. Sci.*, 2009, **52**(12), 3683–3689.

122 V. Kuznetsov, Y. V. Butenko, V. Zaikovskii and A. Chuvilin, Carbon redistribution processes in nanocarbons, *Carbon*, 2004, **42**(5), 1057–1061.

123 N. Sano, H. Wang, I. Alexandrou, M. Chhowalla, K. B. K. Teo, G. A. J. Amaratunga, *et al.*, Properties of carbon onions produced by an arc discharge in water, *J. Appl. Phys.*, 2002, **92**(5), 2783.

124 W. Gu, N. Peters and G. Yushin, Functionalized carbon onions, detonation nanodiamond and mesoporous carbon as cathodes in Li-ion electrochemical energy storage devices, *Carbon*, 2013, **53**, 292–301.

125 A. Krüger, F. Kataoka, M. Ozawa, T. Fujino, Y. Suzuki, A. E. Aleksenskii, *et al.*, Unusually tight aggregation in detonation nanodiamond: identification and disintegration, *Carbon*, 2005, **43**(8), 1722–1730.

126 A. Kornyshev, N. Luque and W. Schmickler, Differential capacitance of ionic liquid interface with graphite: the story of two double layers, *J. Solid State Electrochem.*, 2014, **18**(5), 1345–1349.

127 P. Ruch, R. Kötz and A. Wokaun, Electrochemical characterization of single-walled carbon nanotubes for electrochemical double layer capacitors using non-aqueous electrolyte, *Electrochim. Acta*, 2009, **54**(19), 4451–4458.

128 H. Gerischer, R. McIntyre, D. Scherson and W. Storck, Density of the electronic states of graphite: derivation

from differential capacitance measurements, *J. Phys. Chem.*, 1987, **91**(7), 1930–1935.

129 M. Zeiger, D. Weingarth and V. Presser, Quinone-Decorated Onion-Like Carbon/Carbon Fiber Hybrid Electrodes for High-Rate Supercapacitor Applications, *ChemElectroChem*, 2015, **2**(8), 1117–1127.

130 K. Jost, C. R. Perez, J. K. McDonough, V. Presser, M. Heon, G. Dion, *et al.*, Carbon coated textiles for flexible energy storage, *Energy Environ. Sci.*, 2011, **4**(12), 5060–5067.

131 P. F. Fulvio, R. T. Mayes, X. Wang, S. M. Mahurin, J. C. Bauer, V. Presser, *et al.*, "Brick-and-Mortar" Self-Assembly Approach to Graphitic Mesoporous Carbon Nanocomposites, *Adv. Funct. Mater.*, 2011, **21**(12), 2208–2215.

132 I. Kovalenko, D. G. Bucknall and G. Yushin, Detonation Nanodiamond and Onion-Like-Carbon-Embedded Polyaniline for Supercapacitors, *Adv. Funct. Mater.*, 2010, **20**(22), 3979–3986.

133 Y. Sun, Q. Wu, Y. Xu, H. Bai, C. Li and G. Shi, Highly conductive and flexible mesoporous graphitic films prepared by graphitizing the composites of graphene oxide and nanodiamond, *J. Mater. Chem.*, 2011, **21**(20), 7154.

134 J. M. Miller, *Ultracapacitor applications*, The Institution of Engineering and Technology, 2011.

135 K. Makgopa, P. M. Ejikeme, C. J. Jafta, K. Raju, M. Zeiger, V. Presser, *et al.*, A high-rate aqueous symmetric pseudocapacitor based on highly graphitized onion-like carbon/birnessite-type manganese oxide nanohybrids, *J. Mater. Chem. A*, 2015, **3**(7), 3480–3490.

136 R. Borgohain, J. P. Selegue and Y.-T. Cheng, Ternary composites of delaminated-MnO_2/PDDA/functionalized-CNOs for high-capacity supercapacitor electrodes, *J. Mater. Chem. A*, 2014, **2**(47), 20367–20373.

137 Y. Wang, S. F. Yu, C. Y. Sun, T. J. Zhu and H. Y. Yang, MnO_2/onion-like carbon nanocomposites for pseudocapacitors, *J. Mater. Chem.*, 2012, **22**(34), 17584–17588.

138 O. Mykhailiv, M. Imierska, M. Petelczyc, L. Echegoyen and M. E. Plonska-Brzezinska, Chemical *versus* Electrochemical Synthesis of Carbon Nano-onion/Polypyrrole Composites for Supercapacitor Electrodes, *Chem.–Eur. J.*, 2015, **21**(15), 5783–5793.

139 D. M. Anjos, J. K. McDonough, E. Perre, G. M. Brown, S. H. Overbury, Y. Gogotsi, *et al.*, Pseudocapacitance and performance stability of quinone-coated carbon onions, *Nano Energy*, 2013, **2**(5), 702–712.

140 Y. Liu and D. Y. Kim, Enhancement of Capacitance by Electrochemical Oxidation of Nanodiamond Derived Carbon Nano-Onions, *Electrochim. Acta*, 2014, **139**, 82–87.

141 F.-D. Han, B. Yao and Y.-J. Bai, Preparation of Carbon Nano-Onions and Their Application as Anode Materials for Rechargeable Lithium-Ion Batteries, *J. Phys. Chem. C*, 2011, **115**(18), 8923–8927.

142 Y. Wang, Z. J. Han, S. F. Yu, R. R. Song, H. H. Song, K. K. Ostrikov, *et al.*, Core-leaf onion-like carbon/MnO_2 hybrid nano-urchins for rechargeable lithium-ion batteries, *Carbon*, 2013, **64**, 230–236.

143 Y. Wang, G. Xing, Z. J. Han, Y. Shi, J. I. Wong, Z. X. Huang, *et al.*, Pre-lithiation of onion-like carbon/MoS_2 nano-urchin anodes for high-performance rechargeable lithium ion batteries, *Nanoscale*, 2014, **6**(15), 8884–8890.

144 E. Raymundo-Pinero, K. Kierzek, J. Machnikowski and F. Béguin, Relationship between the nanoporous texture of activated carbons and their capacitance properties in different electrolytes, *Carbon*, 2006, **44**(12), 2498–2507.

145 S. Roldán, C. Blanco, M. Granda, R. Menéndez and R. Santamaría, Towards a Further Generation of High-Energy Carbon-Based Capacitors by Using Redox-Active Electrolytes, *Angew. Chem., Int. Ed.*, 2011, **50**(7), 1699–1701.

146 S. M. Chathoth, D. M. Anjos, E. Mamontov, G. M. Brown and S. H. Overbury, Dynamics of phenanthrenequinone on carbon nano-onion surfaces probed by quasielastic neutron scattering, *J. Phys. Chem. B*, 2012, **116**(24), 7291–7295.

147 A. le Comte, D. Chhin, A. Gagnon, R. Retoux, T. Brousse and D. Belanger, Spontaneous grafting of 9,10-phenanthrenequinone on porous carbon as active electrode material in electrochemical capacitor in alkaline electrolyte, *J. Mater. Chem. A*, 2015, **3**(11), 6146–6156.

148 F. A. Armstrong, R. Camba, H. A. Heering, J. Hirst, L. J. Jeuken, A. K. Jones, *et al.*, Fast voltammetric studies of the kinetics and energetics of coupled electron-transfer reactions in proteins, *Faraday Discuss.*, 2000, **116**, 191–203.

149 F. Yılmaz and Z. Küçükyavuz, Conducting polymer composites of multiwalled carbon nanotube filled doped polyaniline, *J. Appl. Polym. Sci.*, 2009, **111**(2), 680–684.

150 H. Zengin, W. Zhou, J. Jin, R. Czerw, D. W. Smith, L. Echegoyen, *et al.*, Carbon nanotube doped polyaniline, *Adv. Mater.*, 2002, **14**(20), 1480–1483.

3.4 Influence of carbon substrate on the electrochemical performance of carbon/manganese oxide hybrids in aqueous and organic electrolytes

Marco Zeiger,[1,2] Simon Fleischmann,[1,2] Benjamin Krüner,[1,2] Aura Tolosa,[1,2] Stephan Bechtel,[1,2] Mathias Baltes,[2] Anna Schreiber,[1] Riko Moroni,[3] Severin Vierrath,[3] Simon Thiele,[3,4] and Volker Presser[1,2,*]

[1] *INM - Leibniz Institute for New Materials, Campus D2 2, 66123 Saarbrücken, Germany*
[2] *Department of Materials Science and Engineering, Saarland University, Campus D2 2, 66123 Saarbrücken, Germany*
[3] *IMTEK Department of Microsystems Engineering, University of Freiburg, Georges-Koehler-Allee 103, 79110 Freiburg, Germany*
[4] *FIT, University of Freiburg, Georges-Koehler-Allee 103, 79110, 79104 Freiburg, Germany*

Citation:
Zeiger, M.; Fleischmann, S.; Krüner, B.; Tolosa, A.; Bechtel, S.; Baltes, M.; Schreiber, A.; Moroni, R.; Vierrath, S.; Thiele, S.; Presser V., Influence of carbon substrate on the electrochemical performance of carbon/manganese oxide hybrids in aqueous and organic electrolytes. *RSC Adv.* **2016,** 6, 107163-107179. (DOI: 10.1039/C6RA24181F)

Own contribution: Design, planning, writing, synthesis, Raman spectroscopy, transmission electron microscopy, conductivity measurements, helium gas pycnometry, thermogravimetric analysis, electrochemistry.

Abstract:
Manganese oxide presents very promising electrochemical properties as an electrode material in supercapacitors, but there remain important open questions to guide further development of the complex manganese oxide/carbon/electrolyte system. Our work addresses specifically the influence of carbon ordering and the difference between outer and inner porosity of carbon particles for the application in aqueous 1 M Na_2SO_4 and 1 M $LiClO_4$ in acetonitrile. Birnessite-type manganese oxide was hydrothermally hybridized on two kinds of carbon onions with only outer surface area and different electrical conductivity, and conventional activated carbon with a high inner porosity. Carbon onions with a high degree of carbon ordering, high conductivity, and high outer surface area were identified as the most promising material, yielding 179 F g^{-1}. Pore blocking in activated carbon yields unfavorable electrochemical performances. The highest specific energy of 16.4 W h kg^{-1} was measured for a symmetric full-cell arrangement of manganese oxide coated high temperature carbon onions in the organic electrolyte. High stability during 10 000 cycles was achieved for asymmetric full-cells, which proved as a facile way to enhance the electrochemical performance stability.

RSC Advances

PAPER

View Article Online
View Journal | View Issue

Cite this: *RSC Adv.*, 2016, **6**, 107163

Influence of carbon substrate on the electrochemical performance of carbon/manganese oxide hybrids in aqueous and organic electrolytes†

Marco Zeiger,[ab] Simon Fleischmann,[ab] Benjamin Krüner,[ab] Aura Tolosa,[ab] Stephan Bechtel,[ab] Mathias Baltes,[b] Anna Schreiber,[a] Riko Moroni,[c] Severin Vierrath,[c] Simon Thiele[cd] and Volker Presser*[ab]

Manganese oxide presents very promising electrochemical properties as an electrode material in supercapacitors, but there remain important open questions to guide further development of the complex manganese oxide/carbon/electrolyte system. Our work addresses specifically the influence of carbon ordering and the difference between outer and inner porosity of carbon particles for the application in aqueous 1 M Na_2SO_4 and 1 M $LiClO_4$ in acetonitrile. Birnessite-type manganese oxide was hydrothermally hybridized on two kinds of carbon onions with only outer surface area and different electrical conductivity, and conventional activated carbon with a high inner porosity. Carbon onions with a high degree of carbon ordering, high conductivity, and high outer surface area were identified as the most promising material, yielding 179 F g^{-1}. Pore blocking in activated carbon yields unfavorable electrochemical performances. The highest specific energy of 16.4 W h kg^{-1} was measured for a symmetric full-cell arrangement of manganese oxide coated high temperature carbon onions in the organic electrolyte. High stability during 10 000 cycles was achieved for asymmetric full-cells, which proved as a facile way to enhance the electrochemical performance stability.

Received 28th September 2016
Accepted 25th October 2016

DOI: 10.1039/c6ra24181f

www.rsc.org/advances

1. Introduction

Supercapacitors are fast and efficient electrochemical energy storage devices.[1–4] Typically, they are classified in electrical double-layer capacitors (EDLCs), pseudocapacitors, and hybrid devices. EDLCs store energy *via* electrosorption of electrolyte ions at the charged surface of high surface area carbons, which is a capacitive, non-faradaic process. The physical nature of ion electrosorption in EDLCs enables faster and more efficient charge storage compared to chemically-driven redox reactions. Therefore, EDLCs are promising for high power applications utilizing rapid charge and discharge rates, moreover present high efficiency, and long lifetimes. Current EDLC devices suffer from low specific energies, compared to conventional batteries.[1,2,5–7] To overcome this issue, the energy storage capacity can be increased by improving the properties of the electrode material, the electrolyte, and the cell preparation/design. General requirements for suitable electrode materials are a high specific surface area (SSA) with well-developed pore size distribution, good conductivity, and high electrochemical stability.[8,9] A variety of carbon materials has been studied so far, including activated carbon (AC),[10,11] carbide-derived carbons,[12–14] templated carbons,[15] onion-like carbon (OLC),[16,17] graphene,[18,19] carbon nanotubes (CNTs),[20,21] carbon nanofibers,[22–24] and carbon aerogels.[25] AC is currently the most commonly used electrode material; typically, ACs present surface areas in the range of 1500–2000 m^2 g^{-1} resulting in capacitances of 100–200 F g^{-1} and specific energies between 2 W h kg^{-1} and 20 W h kg^{-1} (depending on the electrolyte and operation parameters).[1]

The ability to improve the specific energy of EDLCs by further increasing the porosity/surface area and optimizing the pore structure is limited by the minimum pore size accessible to ions, among others, and leads to a saturation of capacitance *versus* surface area.[26] An alternative approach to further increase the specific energy is the implementation of redox active materials. Common redox active materials used in combination with carbon are transition metal oxides, such as manganese

[a]*INM - Leibniz Institute for New Materials, Campus D2 2, 66123 Saarbrücken, Germany. E-mail: volker.presser@leibniz-inm.de*

[b]*Department of Materials Science and Engineering, Saarland University, Campus D2 2, 66123 Saarbrücken, Germany*

[c]*IMTEK Department of Microsystems Engineering, University of Freiburg, Georges-Koehler-Allee 105, 79110 Freiburg, Germany*

[d]*FIT, University of Freiburg, Georges-Koehler-Allee 103, 79110, 79104 Freiburg, Germany*

† Electronic supplementary information (ESI) available: Transmission electron micrographs of the carbon materials are shown. See DOI: 10.1039/c6ra24181f

oxide,[27] ruthenium oxide,[28] nickel oxide,[29–34] electrochemically active polymers, like polyaniline,[30–32,34,35] and polypyrrole,[36–38] as well as surface functional groups, like quinones.[23,39–42] Dependent on the resulting electrochemical response, we can differentiate between a battery-like or pseudocapacitive behavior.[43]

Manganese oxide is an attractive pseudocapacitive material because of its high redox activity, the low synthesis costs, and high availability/abundance.[27,44,45] The charge storage mechanism of manganese oxide is related to faradaic surface reactions, the adsorption of positively charged electrolyte ions such as H^+, Li^+, Na^+, and K^+, but also to faradaic reactions in the bulk (cation intercalation). In these cases, redox transitions between Mn(III) and Mn(IV) states occur.[27,44,46–48] The specific capacitance of manganese oxide is typically in the range of 100–200 F g^{-1} in neutral aqueous electrolytes. Much higher values have also been published,[49] for example, up to 1380 F g^{-1} for thin films (5 μm)[46] in the same order of magnitude than the maximum theoretical value of 1233 F g^{-1}.[50] The electrochemical performance of manganese oxide is not only determined by its morphology, phase, composition, and crystal structure,[51,52] but also by thickness of the electrode/coating/particles.[46,53] Although manganese oxide as supercapacitor material is already extensively studied, for example, by the groups of D. Bélanger, T. Brousse, and F. Favier,[46,48,51,54–63] remaining challenges are its low structural stability, low long-time stability, small negative voltage stability, high self-discharge, and poor electrical conductivity. A more comprehensive overview about the properties of manganese oxides for supercapacitors can be found in the literature.[49]

The low conductivity of manganese oxide (*ca.* 10^{-5} S cm^{-1})[64] limits the power performance. The latter can be improved by doping with metals or the hybridization with highly conductive carbon materials.[49] Several carbon substrates were used in combination with different types of manganese oxide, like activated carbon fiber,[24] carbon nanotubes,[65–74] graphene,[75–80] graphene oxide,[81,82] carbon nanofoams,[83,84] aerogels,[83,84] nanographite sheets,[85–87] carbon onions,[88–90] and ordered mesoporous carbon.[91–93] These carbon materials differ in crystal structure, grain/particle size, chemical composition, and oxidation state. However, the use of different electrode preparation methods, various amounts and kinds of polymer binder and conductive additive, and different electrode thicknesses make a direct comparison of electrochemical performance ratings difficult and often inconclusive. For example, Fleischmann *et al.* compared activated carbon and carbon onions as substrate for vanadium oxide coated with atomic layer deposition technique.[94] The findings regarding the influence of high internal or external surface area on the electrochemical properties were related to the synthesis process. In a study by Gambou-Bosca *et al.*, the difference between activated carbon and carbon black as substrates for manganese oxide was investigated.[95] Yet, no comprehensive set of data exists showing the influence of the carbon substrate regarding different degrees of ordering, and carbons with high internal or external porosity. Especially when comparing organic and aqueous media, this absence complicates the development of optimization strategies for this promising class of hybrid material.

In the present study, the influence of carbon on the electrochemical performance of carbon/manganese oxide hybrid electrodes is systematically investigated for organic and aqueous media. For these two types of electrolytes, we also provide, for the first time, *S*-value testing to quantify the maximum width of the electrochemical voltage window. Commercially available activated carbon (AC) and nanodiamond-derived carbon onions (OLC: onion-like carbon)[16] synthesized at 1300 °C and 1700 °C were hybridized with MnO_2 by hydrothermal synthesis. By this way, the impact of internal *vs.* external surface area on the nanohybrid material performance can be investigated. Carbon onions have recently been hybridized with MnO_2, but no comparison between different degrees of carbon ordering was presented.[88] Our data explicitly includes activated carbon because the performance of this common type of electrode material for supercapacitors combined with manganese oxide remains ill-explored.[24,62,96] Manganese oxide operated in organic and aqueous media is finally benchmarked with regard to charge and energy efficiency to assess the practicality of their implementation for energy storage applications.

2. Experimental

2.1 Materials and synthesis

Activated carbon (AC) powder YP80 was used as received (Kuraray). Carbon onions (OLC) were produced using annealing of detonation nanodiamonds (NaBond Technologies). The powder was used without further purification and placed in graphite crucibles. The typical amount of material was ~10 g. Nanodiamond powder was annealed in a high temperature furnace (Thermal Technology) in flowing argon with a purity of 4.6 and a flow rate of 1.3 L min^{-1}. Two annealing temperatures of 1300 °C for 10 h or 1700 °C for 1 h were used with heating and cooling rates of 20 °C min^{-1}. The resulting carbon onions are called OLC1300 and OLC1700.

Manganese oxide/carbon hybrids were produced by hydrothermal synthesis using potassium permanganate ($KMnO_4$, Sigma Aldrich) as precursor in aqueous solution. Carbon powders (500 mg) were dispersed in 100 mL deionized water (MilliQ) *via* tip sonication of ~4 W for 5 min. In a second step, potassium permanganate was added to the solution and continuously stirred and refluxed at 100 °C for 4 h until the color changed from purple to dark brown/black. Several mass ratios of $KMnO_4$/carbon were used to reach different loadings of manganese oxide on the carbon substrate. For example, a ratio of 3 : 1 stands for 1.5 g of $KMnO_4$ and 500 mg carbon powder. The nomenclature for the samples, for example "M–OLC1700 (3 : 1)", includes the loading with manganese oxide (M), the type of carbon substrate (AC, OLC1300, OLC1700), and the mass ratio $KMnO_4$/carbon (*e.g.*, 3 : 1). We recently described the same synthesis route and identified the manganese oxide phase as birnessite,[88] in agreement with earlier works employing permanganate as precursor.[49] For simplicity, "birnessite-type manganese oxide" is shortened to "manganese oxide" in this study, although we would like to remind that the produced phase is not pure MnO_2, but classifies rather as metal hydroxide with some amounts of potassium (~12 mass%).

To investigate structure and electrochemical performance of just manganese oxide, the latter was synthesized using an adapted co-precipitation method from ref. 51. $KMnO_4$ was dissolved in deionized water and stirred while $MnCl_2$ was added. The mass ratio of $KMnO_4 : MnCl_2$ was 2 : 3. The brown manganese oxide was directly collected. All samples were washed at least 3 times with deionized water, centrifuged, and dried at 90 °C and 20 mbar. Commercial MnO_2 was used as received (Sigma Aldrich).

2.2 Analysis of chemical composition, structure, and porosity

The elemental composition was measured using energy-dispersive X-ray analysis (EDX) with a X-Max-150 detector from Oxford Instruments in a JSM-7500F from JEOL. The electrodes containing 10 mass% polytetrafluorethylene (PTFE) binder (see Section 2.3 for details on the electrode preparation) were placed on a carbon tape and spectra were taken at three different positions using 10 kV acceleration voltage.

Transmission electron microscopy was performed with a JEOL 2100F microscope using 200 kV acceleration voltage. Powder samples were dispersed in isopropanol, tip sonicated for 10 s and drop casted on a copper grid with a lacey carbon film (Gatan).

Prior to focused ion beam (FIB) cross-sectioning in a scanning electron microscope (SEM), the samples were coated with ZnO by allowing diethyl zinc and water to react in a cyclic manner at 50 °C in a vertical-flow, hot-wall reactor (OpAL, Oxford Instruments) as described in ref. 97. This increases the contrast between pores and solid material in the SEM. Subsequently, imaging was carried out with a Zeiss Auriga 60 dual beam. The cut surface was prepared by a focused ion beam with an accelerating voltage of 30 kV and 20 pA beam current. The SEM images were acquired with the in-lens detector at 5 kV.

Thermogravimetric analysis (TGA) was used to identify the amount of manganese oxide in the hybrids. A TG 209 F1 Libra system from Netzsch was used, equipped with an automatic sample changer and alumina crucibles. Samples were heated up to 900 °C in synthetic air with a rate of 20 °C min^{-1} to avoid contaminations of the system. To investigate the difference in carbon ordering and phase in detail, the pure carbon powders were heated in synthetic air with a rate of 5 °C min^{-1}. The sample mass ranged between 5 mg and 10 mg. The amount of manganese oxide was measured by the remaining sample mass after heating to 900 °C when carbon was completely oxidized.

The skeletal density was analyzed with an AccuPyc 1330 gas pycnometer (Micromeritics) using helium gas with a purity grade of 5.0. The steel crucible had a volume of 1 cm^3 and the sample mass was between 100 mg and 200 mg. First, 20 purges were applied followed by 20 separate measurements. Both purge and analysis filling pressures were 134 Pa. An equilibration rate of 34 Pa min^{-1} was used.

Porosity and surface area were measured using nitrogen gas sorption measurements at −196 °C with an Autosorb iQ system (Quantachrome). Beforehand, the powder samples were degassed at 10^2 Pa and 300 °C for 24 h to remove any water residuals from the synthesis. During the measurement, the relative pressure was varied from 5×10^{-7} to 1.0 in 68 steps. The specific surface area (SSA) was calculated with the ASiQwin-software using the Brunauer Emmett Teller (BET) equation in the linear relative pressure range of 0.01–0.2.[43] The DFT SSA and pore size distribution (PSD) were derived *via* quenched-solid DFT (QSDFT) with a slit pore shape model between 0.56 nm and 37.5 nm.[46] Values for the total pore volume correspond to $p/p_0 = 0.95$.

Raman spectroscopy was performed with a Renishaw inVia Raman Microscope equipped with a Nd-YAG laser (532 nm). For all samples a 50× objective was used with a power of 0.2 mW at the surface of the sample. The spectra were recorded with 10 accumulations and 20 s acquisition time. For each D- and G-mode we used one Voigt-profile peak and two Voigt peaks to fit the contribution of amorphous carbon (including amorphous carbon at 1520 cm^{-1}, transpolyacetylene at *ca.* 1100 cm^{-1} and the broad signal which does not correspond to sp^2-hybridized carbon). The same methodology was used in our recent study for carbon onions.[98] All spectra were normalized and background subtracted with a linear baseline.

The electrode conductivity was measured with a custom built four-point probe. The diameter of the tips was 1.5 mm and the tip distance 1.75 mm. The areal resistance was measured at 5 different positions of the electrode. Using eqn (1) the electrode conductivity normalized to the thickness can be calculated.

$$\sigma = \frac{\ln(2)}{\pi} \frac{I}{Ud} \quad (1)$$

I is the current, U the voltage, and d the thickness of the electrode measured with a micrometer screw. The thickness was kept constant for all samples (60 ± 10 μm).

2.3 Electrochemical characterization

Free-standing and flexible PTFE-bound electrodes were used for electrochemical measurements. Carbon and hybrid powders (typically *ca.* 200 mg) were dispersed in ethanol and stirred in a mortar until most of the ethanol was evaporated and a carbon slurry resulted. For all samples 10 mass% PTFE (60 mass% aqueous solution, Sigma Aldrich) were added and mixed in a mortar until a dough-like carbon paste was formed. Using a rolling machine (MTI HR01, MTI Corp.) electrodes with a thickness of 60 μm (±10 μm) were rolled and dried over night at 90 °C and 20 mbar.

Electrochemical characterization was carried out in 1 M $LiClO_4$ in acetonitrile (ACN) from BASF or 1 M Na_2SO_4 (aqueous) from Sigma Aldrich. For all measurements, a two- and three-electrode setup was used, corresponding with full- and half-cell configuration, respectively. The electrodes were punched out to obtain discs with a diameter of 8 mm (3–5 mg) and were separated by a glass-fiber disc with diameter of 13 mm (type GF/D, GE Healthcare). The electrode/separator/electrode arrangement was compressed between two platinum disks (diameter 12 mm, thickness: 200 μm, Carl Schäfer) using spring-loaded titanium pistons, sealed by a polyether ether ketone (PEEK) body. For measurements using 1 M $LiClO_4$ in ACN, the cells

were dried at 90 °C and 20 mbar before they were put in an argon-filled glove box (MBraun Labmaster 130; O_2, H_2O < 1 ppm). The cells were vacuum back-filled with a syringe containing the electrolyte. The aqueous 1 M Na_2SO_4 electrolyte was directly vacuum filled in the cells without drying. Full-cell measurements were carried out either with a symmetric (same size, same material) or asymmetric (charge balanced counter electrode from activated carbon YP80) configuration. In a half-cell set-up, a *ca.* 5 times oversized AC counter electrode was used together with a reference electrode; the latter was a platinum wire for the aqueous electrolyte and PTFE-bound activated carbon YP50 from Kuraray for the organic electrolyte.

Electrochemical characterization was performed using a VSP300 and VMP300 potentiostat/galvanostat from Bio-Logic in cyclic voltammetry (CV) and galvanostatic mode with potential limitation (GCPL). The potential window for all full-cell measurements was 0.8 V in 1 M Na_2SO_4 and 2.2 V in 1 M $LiClO_4$ in ACN. Half-cell measurements were used to determine the capacitance of one electrode and the stability window. For data obtained with cyclic voltammetry, a scan rate of 1–10 mV s^{-1} was used and the specific capacitance of two electrodes dependent on the cell voltage (cell performance) was calculated using eqn (2):

$$C_{\text{cell}}(U) = \frac{I(U)}{\nu}\frac{1}{M} \quad (2)$$

with $I(U)$ the measured current, ν the applied scan rate, and M the active mass of both electrodes. Active mass in all cases means the mass of the carbon and the manganese oxide (without binder).

Galvanostatic measurements with potential limitation (GCPL) were used to calculate the capacitance for different specific currents as well as the specific energy and power. The current was normalized to the active mass and specific currents from 0.1 A g^{-1} to 20 A g^{-1} were applied. After charging the system to 0.8 V or 2.2 V, there was a 10 s resting time prior to discharge to 0 V cell voltage to enable facile assessment of the IR drop. Every GCPL cycle was repeated at least two times with 10 s of resting time in between. The specific discharge capacitance of two electrodes normalized to the active mass was calculated according to eqn (3):

$$C_{\text{cell}} = \frac{\int_{t_1}^{t_2} I\,\mathrm{d}t}{U_{\text{corrected}}}\frac{1}{M} \quad (3)$$

with M the active mass of both electrodes, I the applied current, t_1 and t_2 the start and end of discharging, and $U_{\text{corrected}}$ the applied voltage minus the IR-drop. The IR drop was determined as the voltage loss after 5 s of reaching the applied voltage. The same technique was used to calculate the capacitance of one electrode in a half-cell setup with a potential window of 0.5 V and normalization to the active mass of one electrode. The specific energy (E_{specific}) and specific power (P_{specific}) of the full-cell (two electrodes) were calculated using eqn (4) and (5):

$$E_{\text{specific}} = \int_{t_1}^{t_2} U\,\mathrm{d}t \times I\frac{1}{M} \quad (4)$$

$$P_{\text{specific}} = \frac{E_{\text{specific}}}{t_2 - t_1} \quad (5)$$

with M the active mass of both electrodes, I the applied current, t_1 and t_2 the start and end of discharging. The charge and energy efficiencies were calculated dividing the respective value from charging by the value from discharging and are presented in %.

3. Results and discussion

3.1 Morphology analysis

Two types of carbon onions (OLC) with different degrees of carbon ordering and one nanoporous activated carbon (AC) were selected for this study. TEM images of the carbon materials are shown in the ESI, Fig. S1.†

Both types of carbon onions were derived from nanodiamonds by thermal annealing in argon at either 1700 °C ("high temperature") or 1300 °C ("low temperature"). The primary particle size of carbon onions ranged between 4 nm and 10 nm featuring several carbon shells (ESI, Fig. S1A and B†). While differences in morphology were not observable in transmission electron micrographs, an increasing degree of carbon ordering for higher annealing temperatures is to be expected.[98–101] In contrast to OLC, AC presented a porous structure with a high level of nanocrystalline disorder (ESI, Fig. S1C†).

Even when using the same ratio of carbon and manganese oxide, different morphologies were observed for the different carbon substrates (Fig. 1). M–OLC1700 (3 : 1) had a homogenous coating of the agglomerate particles (Fig. 1D and E).

The thickness of the nanocrystalline coating was in the range of a few nanometers (~10 nm) as determined by TEM (Fig. 1F). In contrast, M–OLC1300 (3 : 1) showed a fibrous coating with nanocrystalline structure (Fig. 1A–C). The skeletal density of OLC1300 (2.2 g cm^{-3}) was 16% higher than for OLC1700 (1.9 g cm^{-3}). Therefore, the same mass content of MnO_2 would lead to a larger volumetric coating compared to the coating on the lower density substrate material. However, we see the same fibrous structure for M–OLC1300 (2 : 1) and (3 : 1) (Fig. 1A). A similar morphology was observed for M–AC (3 : 1) coated with the same amount of manganese oxide (Fig. 1J–L). Long and thin manganese oxide fibers grew on the surface of the activated carbon particle with a length of several hundred nanometers and a diameter of ~20 to 50 nm (Fig. 1L). These observations align with findings in literature: depending on the reaction ratio of permanganate and carbon,[96] as well as the reaction time,[82] the structure of manganese oxide varies from layers and nanoparticles to nanorods with differing crystallinity. Use of a much smaller amounts of permanganate for the synthesis (M–AC (1 : 2)) yielded a thin coating of around 3 nm thickness, completely covering the carbon particles (Fig. 1G–I). Etching of carbon during the formation of manganese oxide is evidenced in Fig. 1C: the graphitic shells on the outside of OLC1300 were removed, while a partially amorphous and diamond-like core remained in the center of the particles. This is in accordance with results of Raman spectroscopy in Section 3.4.

The coating of carbon by manganese oxide can also be seen in cross-sectional scanning electron micrographs of the PTFE-

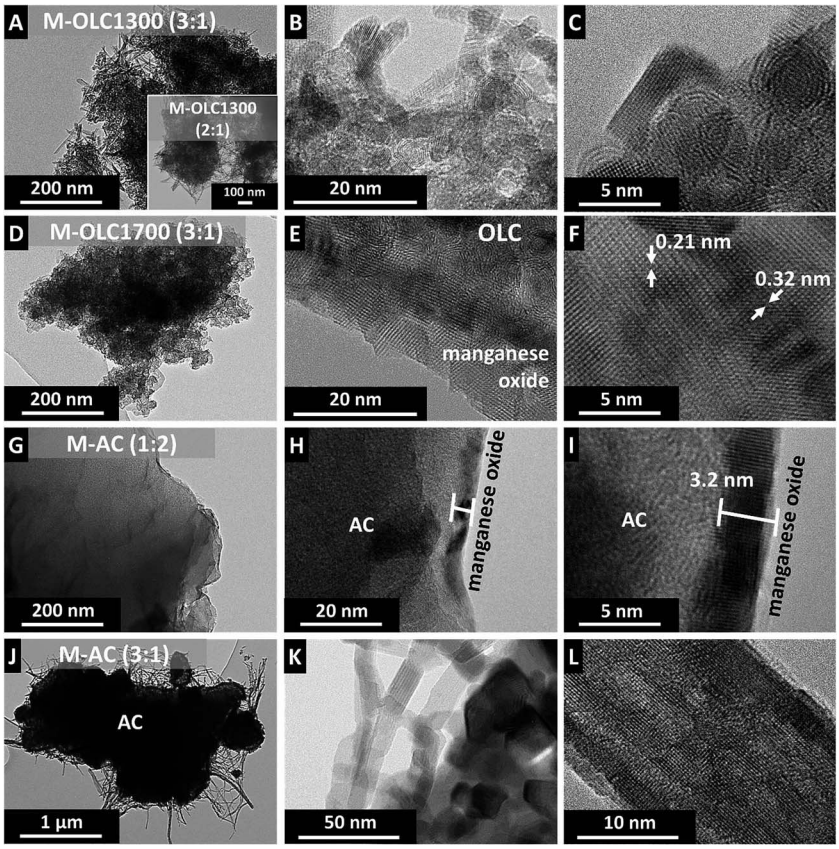

Fig. 1 Transmission electron micrographs of the carbon/manganese oxide hybrids. (A–C) M–OLC1300 (3 : 1), (D–F) M–OLC1700 (3 : 1), (G–I) M–AC (1 : 2), and (J–L) M–AC (3 : 1).

bound electrodes (Fig. 2). The initial AC electrode shows particles in the range of several micrometers in direct contact to each other (Fig. 2A–C). Additional ZnO coating was applied to increase the contrast and allow recognition of the AC particle shape. After coating with manganese oxide (M–AC (3 : 1)), an additional MnO_2 layer is visible partially covering the AC particles as depicted in Fig. 2D–F. Local inhomogeneous covering with MnO_2 as well as the existence of a few uncoated parts of the AC particles can be the result of particle agglomeration during the wet chemical synthesis. The small size of OLC and the tendency to form agglomerates of several hundred nanometers leads to more compact electrodes (Fig. 2G). Manganese oxide deposition (M–OLC1700 (3 : 1)) takes place inside the agglomerates as well as on the outside, forming a homogenous and dense composite (Fig. 2J–L).

3.2 Chemical and thermogravimetric analysis

All three carbon substrates were hydrothermally hybridized with manganese oxide using $KMnO_4$ as the precursor. This synthesis routine is well-established,[49] including work by us on the high power handling ability.[88] Different manganese oxide mass loadings were realized by using different carbon-to-$KMnO_4$ ratios. The chemical composition and the manganese oxide content were measured using EDX and TGA (Table 1).

The chemical analysis showed fluorine in addition to Mn, O, and C, which originates from the PTFE binder. Functional groups on AC account for an oxygen content of 3.3 mass%. This value is almost identical to that of low temperature carbon onions (OLC1300 : 3.1 mass%); yet, the high-temperature annealing process of OLC1700 yields a lower oxygen content (1.9 mass%) in alignment with literature.[98] The content of manganese oxide for the different samples is given in Table 1. By using a higher amount of permanganate for the synthesis, the manganese oxide content increased. For example, the amount of manganese oxide coating on OLC1700 varied from 35 mass% to 87 mass%. Different carbon substrates with the same amount of permanganate led to similar compositions with 56, 57, and 60 mass% manganese oxide for M–OLC1700 (3 : 1), M–OLC1300 (3 : 1), and AC (3 : 1).

Thermogravimetric analysis of manganese oxide showed up to *ca.* 120 °C an initial mass loss of around 4 mass% due to the loss of surface adsorbed water, followed by evaporation of interlayer water and dehydration of the manganese oxide until *ca.* 470 °C with a mass loss of ~11 mass% (Fig. 3A).[48,102] The mass loss due to progressing birnessite dehydration is dependent on the surface area and the corresponding amount of initially adsorbed water. Birnessite-type manganese oxide (K_xMnO_2) also undergoes a phase transformation to $K_xMn_2O_3$ at around 480 °C, as seen for the carbon/manganese oxide hybrids.[102] The burn-off temperatures of 631 °C for OLC1700 and 597 °C for AC were slightly higher than for OLC1300 with 566 °C, due to the higher degree of sp^2-carbon ordering.

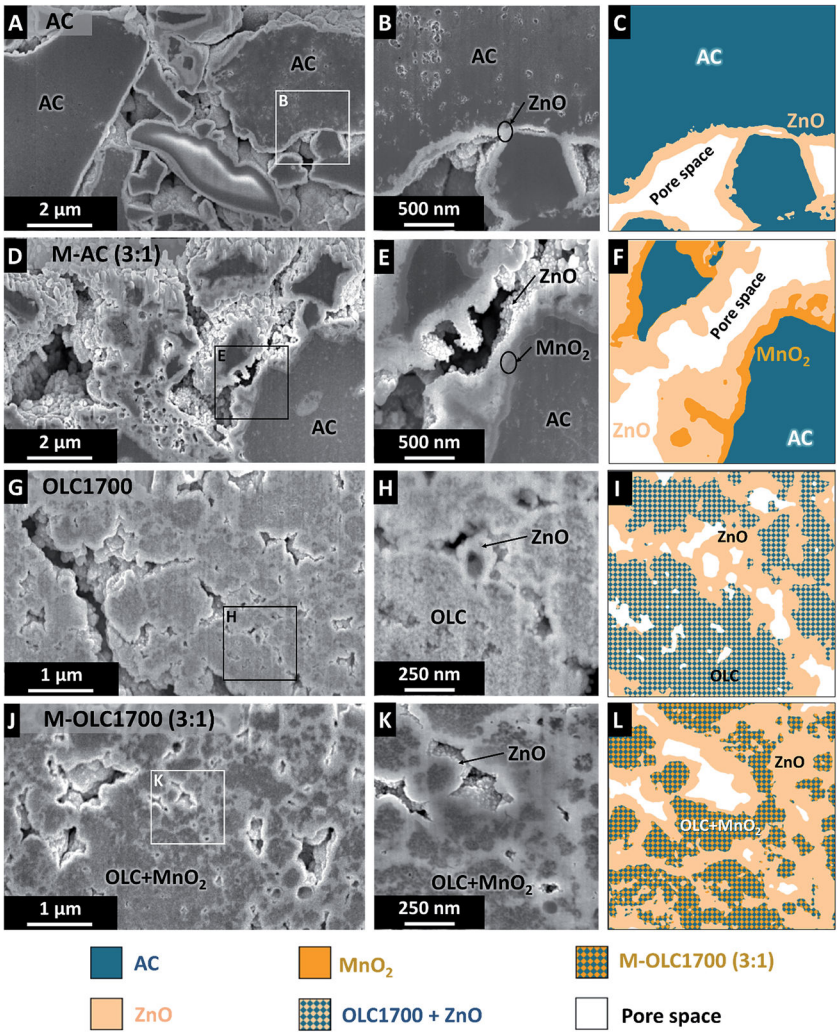

Fig. 2 Scanning electron micrographs of the cross sections prepared from electrodes containing 90 mass% active material (*i.e.*, carbon and manganese oxide) and 10 mass% PTFE as binder. ZnO was deposited by means of atomic layer deposition onto the carbon particles to increase the contrast. Colored images in C, F, I, and L were used to differentiate the carbon and manganese oxide phases in B, E, H, and K.

Table 1 Chemical composition by EDX of the samples and manganese oxide content based on EDX and TGA

	Elemental composition					Manganese oxide	
	C (mass%)	Mn (mass%)	O (mass%)	K (mass%)	F (mass%)	EDX (mass%)	TGA (mass%)
OLC1700	91.8 ± 1.8	0	1.9 ± 0.5	0	6.3 ± 2.3	0	0
M–OLC1700 (1 : 1)	64.1 ± 1.3	13.9 ± 0.5	17.2 ± 1.9	4.2 ± 0.2	0.7 ± 0.1	35 ± 3	34
M–OLC1700 (3 : 1)	40.5 ± 6.6	27.4 ± 9.3	21.9 ± 6.4	6.8 ± 2.5	3.5 ± 1.8	56 ± 18	58
M–OLC1700 (4 : 1)	28.1 ± 1.9	41.0 ± 3.7	22.4 ± 3.4	7.7 ± 0.9	0.7 ± 0.1	71 ± 8	63
M–OLC1700 (8 : 1)	12.3 ± 4.3	47.4 ± 13.7	28.2 ± 11.4	11.0 ± 2.2	1.1 ± 0.4	87 ± 27	73
OLC1300	93.6 ± 1.0	0	3.1 ± 0.1	0	3.2 ± 1.0	0	0
M–OLC1300 (2 : 1)	65.5 ± 8.6	15.5 ± 4.8	14.2 ± 2.5	3.5 ± 1.5	1.5 ± 0.8	33 ± 9	31
M–OLC1300 (3 : 1)	38.8 ± 6.9	22.8 ± 4.4	29.3 ± 3.8	5.3 ± 0.9	3.8 ± 1.3	57 ± 9	60
AC	95.5 ± 1.04	0	3.3 ± 0.5	0	1.2 ± 0.6	0	0
M–AC (1 : 2)	82.2 ± 32.0	8.9 ± 3.0	7.0 ± 1.3	1.2 ± 2.1	0.7 ± 0.4	17 ± 6	18
M–AC (1 : 1)	72.3 ± 5.8	12.6 ± 7.0	12.8 ± 3.7	1.9 ± 0.9	0.4 ± 0.2	27 ± 12	31
M–AC (3 : 1)	36.9 ± 7.2	24.9 ± 5.9	29.2 ± 1.3	6.3 ± 1.7	2.8 ± 2.5	60 ± 9	59

All carbons were completely volatized between 500 °C and 700 °C. For the hybrid materials, the burn-off temperature shifts to 300–500 °C because of an enhanced etching of carbon by evaporating water, oxygen-containing gases, and catalytic effects of the manganese oxide.[103,104] The remaining mass was identical to the amount of manganese oxide in the

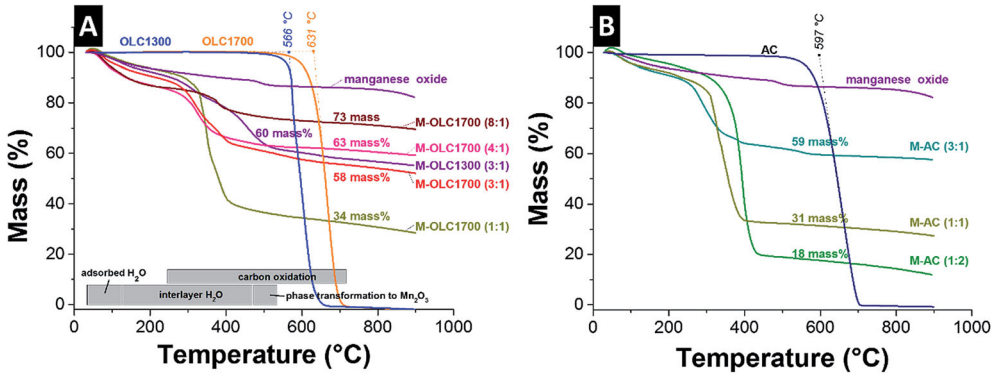

Fig. 3 TGA of the manganese oxide, the carbon powders, and the carbon/manganese oxide composites in synthetic air. All measurements were performed in synthetic air with a heating rate of 5 °C min^{-1} for the carbon powders and 20 °C min^{-1} for the hybrids. (A) Carbon onions and carbon onion/manganese oxide hybrids and (B) AC and AC/manganese oxide hybrids.

composite and was comparable to the values derived from EDX (Table 1).

3.3 Analysis of porosity, skeletal density, and electrical conductivity

Carbon onions have only outer surface area with a large fraction of mesopores (Fig. 4A), whereas activated carbon is mostly characterized by interparticle micropores (Fig. 4B). The skeletal density of both carbon onion varieties increased after adding more manganese oxide and the pore volume decreased (Fig. 4C and Table 2). The skeletal density of the AC hybrids increased from 2.2 g cm^{-3} to 2.4 g cm^{-3}, while the pore volume decreased from 1.07 cm^3 g^{-1} to 0.17 cm^3 g^{-1} similarly to carbon onions (Fig. 4C and Table 2). This finding is in agreement with TEM micrographs, showing the homogenous covering of AC by manganese oxide and blocking the pores from the outside (Fig. 1I). Pore blocking led to a decrease of the pore volume, but not to an increase in density to the same extend because the pore walls and internal pore space are not directly coated.

For all three carbon materials, we see a strong decrease in specific surface area (DFT) after hybridization with manganese oxide (Fig. 4D and Table 2). We determined a specific surface area of 323 m^2 g^{-1} and 404 m^2 g^{-1} for pristine OLC1300 and OLC1700, respectively. For a reaction ratio of (3 : 1), these values were reduced to 116 m^2 g^{-1} and 142 m^2 g^{-1}, respectively. A

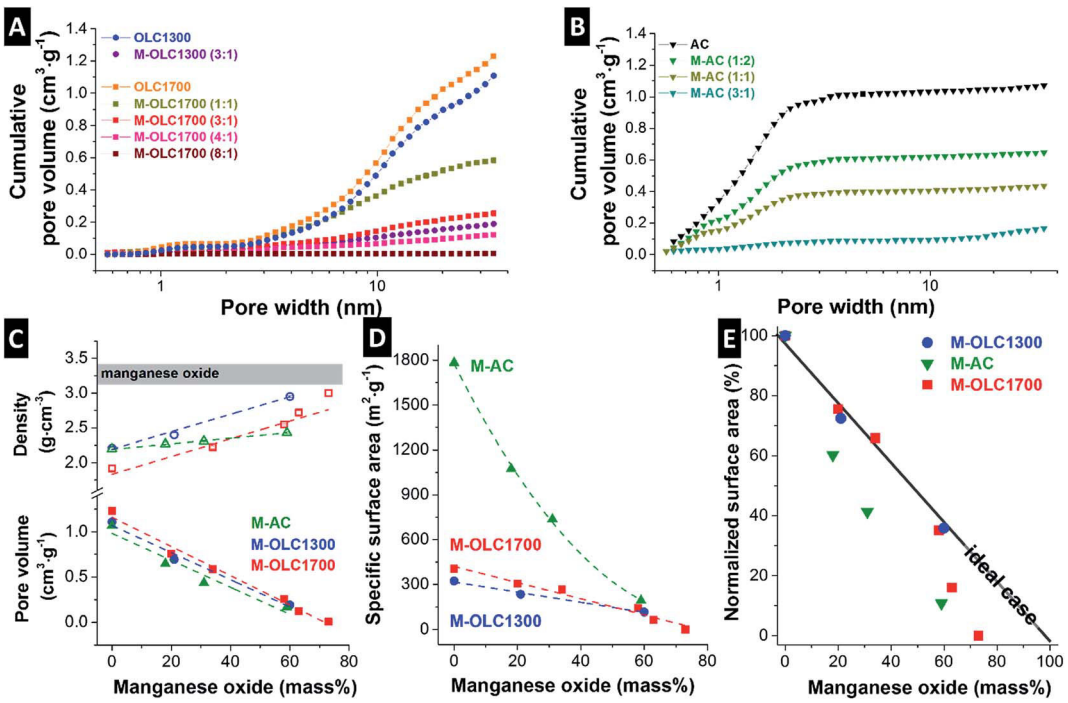

Fig. 4 (A) Cumulative pore size distributions from nitrogen gas sorption analysis of the carbon onion samples and (B) of the AC samples. (C) Skeletal densities from helium gas pycnometry and the pore volumes from nitrogen gas sorption. (D) DFT specific surface areas from gas sorption and (E) normalized surface areas.

Table 2 Surface areas, pore volumes, skeletal densities of the samples based on gas sorption analysis, gas pycnometry and 4-point probe measurements. "n.d.": not detectable (*i.e.*, the value was smaller than the detection limit of the method)

	SSA DFT ($m^2\ g^{-1}$)	Pore volume ($cm^3\ g^{-1}$)	Skeletal density ($g\ cm^{-3}$)	Conductivity ($S\ cm^{-1}$)
OLC1700	404	1.23	1.92 ± 0.03	1.78 ± 0.54
M–OLC1700 (1 : 1)	266	0.58	2.22 ± 0.02	1.98 ± 0.85
M–OLC1700 (3 : 1)	142	0.26	2.55 ± 0.01	0.09 ± 0.01
M–OLC1700 (4 : 1)	65	0.12	2.72 ± 0.03	0.02 ± 0.0
M–OLC1700 (8 : 1)	n.d.	0.01	3.01 ± 0.04	n.d.
OLC1300	323	1.11	2.21 ± 0.02	1.12 ± 0.45
M–OLC1300 (2 : 1)	234	0.70	2.40 ± 0.03	n.d.
M–OLC1300 (3 : 1)	116	0.19	2.95 ± 0.01	n.d.
AC	1783	1.07	2.20 ± 0.02	0.28 ± 0.03
M–AC (1 : 2)	1075	0.65	2.27 ± 0.03	0.05 ± 0.03
M–AC (1 : 1)	737	0.44	2.31 ± 0.01	n.d.
M–AC (3 : 1)	193	0.17	2.43 ± 0.01	n.d.

similar value (193 $m^2\ g^{-1}$) was measured for M–AC (3 : 1), which corresponds with a more than 90% decrease of the initial value (1783 $m^2\ g^{-1}$). The composition of (3 : 1) was used for further comparison of the electrochemical performance because manganese oxide loading as well as surface area are comparable for the different carbon materials.

Fig. 4E shows the relative decrease of the specific surface area after manganese oxide hybridization normalized to the initial value of the carbon materials. An ideal behavior would correspond with high manganese oxide mass loading without pore blocking. This could be approached with thin coatings while maintaining the initial accessible surface area. All studied samples deviate from ideality and pore blocking occurs to a varying degree. For carbon onion hybrids, the surface structure was retained up to a maximum loading of ~60 mass% manganese oxide due to the absence of internal pores (Fig. 2A and D),[99] preventing extensive pore blocking (Fig. 4E). For higher loadings, thick coatings engulfed the agglomerates and led to a strong decrease in specific surface area. Correspondingly, interparticle pores were almost completely filled with manganese oxide, as shown in Fig. 4A. The amount of micro- and mesopores decreased for OLC samples after manganese oxide hybridization, similar to what was observed when using AC (Fig. 4B).

3.4 Raman spectroscopy

The Raman spectra of all carbon materials showed typical features of incompletely graphitized carbon, namely the D-mode at ~1340 to 1350 cm^{-1}, the G-mode at ~1585 to 1600 cm^{-1}, and a pronounced second order spectrum (2200–3500 cm^{-1}). OLC1700 and OLC1300 showed a Raman spectrum typical for carbon onions.[98,99,105–109] Both carbon onion varieties exhibited a nanocrystalline structure and a distinct contribution from amorphous carbon at ~1520 cm^{-1} was seen in form of a broad transition between the D- and the G-mode. The latter was more pronounced for OLC1300 than for OLC1700 due to incomplete graphitization.[98] The curved shape of the G-mode for both types of carbon onions relates to the emergence of few-layer graphene between the carbon onions as a result of the synthesis from nanodiamonds in argon.[98] The Raman signal of the activated carbon presented a G-mode at 1599 cm^{-1} indicative of nanocrystalline carbon.[110] Nanocrystallinity was also seen in TEM micrographs (ESI, Fig. S1C†), showing small crystalline domains connected by amorphous/disordered carbon forms. The amount of amorphous carbon was slightly smaller than for OLC1300 and the degree of carbon ordering in the nanoscopic domains was higher, as indicated by the smaller FWHM of the G-mode.[110]

After hydrothermal synthesis, all samples showed additional Raman bands associated with manganese oxide between 250 cm^{-1} and 750 cm^{-1} (Fig. 5). For OLC1700, the G-mode position shifted from 1591 cm^{-1} to 1599 cm^{-1} for the highest manganese oxide loading (Fig. 5A). The redshift of the G-mode was a result of the hydrothermal synthesis, which led to superficial etched carbon particles resulting in smaller domain sizes.[111] The relative increase in amorphous carbon was less than 20% for the highest loading indicative for a highly ordered material (Fig. 5E). In case of OLC1300, the change of carbon structure was not characterized by a shift of the G-mode to larger wavenumbers because the initial value was already lowered to 1599 cm^{-1} due to its smaller size (Fig. 5B). The relative increase in amorphous carbon neared 100% for the highest loading of manganese oxide on OLC1300 (Fig. 5E) due to the removal of graphitic outer shells and remaining diamond-like and amorphous carbon in the core (Fig. 1C). Similar to OLC1700, the etching of outer shells led to an increase of the D- and G-mode FWHM because of the combined effect of increasing defect density and decreasing domain size (Fig. 5F). The same can be seen for AC with increasing D- and G-mode FWHM, as well as increasing relative amorphous carbon content (Fig. 5C, E and F). In contrast to OLC1300, the content of amorphous carbon did not increase linearly, but reached a constant value (+60%) once a manganese oxide loading of 30% had been reached (Fig. 5E). Obviously, the comparably small external surface area of an AC particle cannot be coated with the same amount of manganese oxide than carbon onions and the impact on the carbon structure remained limited. The birnessite-type manganese oxide phase was varied as a function of the synthesis parameters. Typically, octahedral MnO_6 layers present

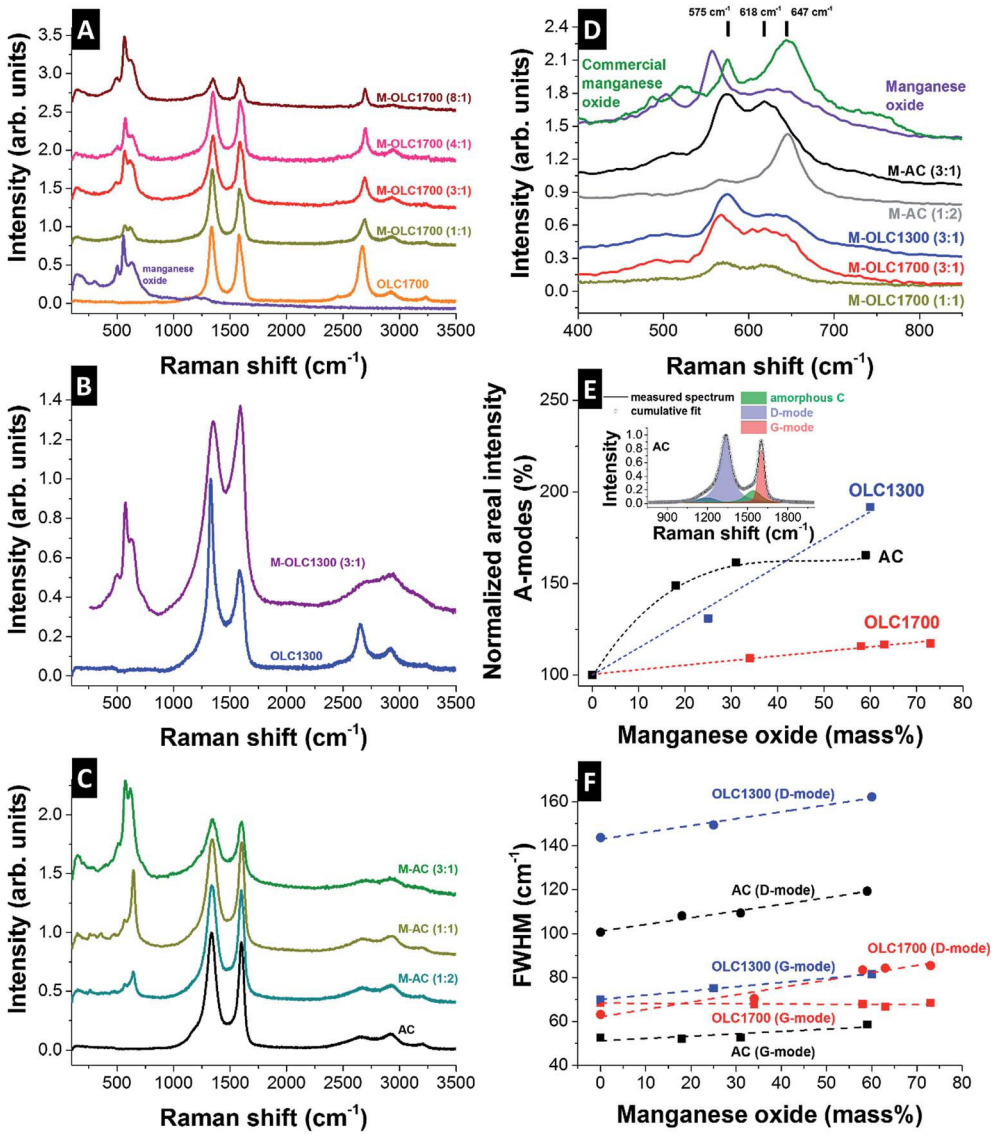

Fig. 5 (A–C) Raman spectra of manganese oxide, the carbon powders, and the carbon/manganese oxide composites. (D) Manganese oxide Raman spectra of different hybrids. (E) Normalized areal intensity of amorphous carbon plotted against the manganese oxide content. (F) FWHM of D- and G-mode dependent on the manganese oxide loading.

a vacancy in one over every six octahedral sites.[112] Between these layers, ions (Li^+, K^+, Mn^{2+}) or water molecules are intercalated depending on the synthesis and the precursor.[112] Raman spectra and the frequency positions can be analyzed according to the polymerization of the MnO_6 octahedra with modes at 506, 575, and 646 cm^{-1}.[112] All coated carbon onion samples showed a typical Raman spectrum of birnessite-type manganese oxide with vibrational frequencies typical for birnessite at 575 cm^{-1}, 618 cm^{-1}, and weak frequencies at 500 cm^{-1} and 730 cm^{-1}.[112] The Raman peak at 646 cm^{-1} is attributed to the Mn–O symmetric stretching vibration within the octahedra.

The lower frequency mode at 575 cm^{-1} comes from the stretching vibration of Mn–O in the basal plane of MnO_6 sheets and is particularly strong for Mn(IV) fraction. The higher frequency mode was shifted to 618 cm^{-1} for carbon onions because of its strong dependence on the lattice spacing in the birnessite[112] which is varied due to intercalation of potassium ions or hydration reactions.[113] The insertion of ions or molecules into the lattice resulted in a local deformation, yielding shorter Mn–O bonds and partial reduction of Mn(IV) ions, leading to a blueshift in the Raman spectrum. Manganese oxide on carbon onions exhibited particularly small domain sizes of a few nanometers, as seen by TEM (Fig. 1E and F). Grain boundaries as well as distortion due to inner-grain tension may further contribute to a variation in lattice spacing and could also explain the broadness of the high frequency mode.

While no significant difference was observed for carbon onions with different manganese oxide loadings, the birnessite Raman spectrum of activated carbon hybrids showed differences dependent on the reaction ratio of permanganate to carbon. For small loadings of manganese oxide, a rather sharp high frequency mode is observed at 647 cm^{-1} which is close to

the expected value for ideal birnessite (646 cm^{-1}).[112] Seemingly, after initial nucleation, manganese oxide layers continue to grow with rather high crystalline ordering on activated carbon. For comparison, we see much stronger nanocrystallinity with smaller manganese oxide domain sizes (*ca.* 2–3 nm) when using carbon onions. We conclude that carbon onions exhibit a much higher density of nucleation sites for the growth of manganese oxide. After using higher permanganate-to-activated carbon ratios, the Raman spectrum was similar to carbon onion hybrids due to the formation of nanocrystalline manganese oxide needles.

3.5 Electrochemical measurements

Electrochemistry was performed in aqueous (1 M Na_2SO_4) and in organic electrolyte (1 M $LiClO_4$ in ACN). The electrochemical potential window was investigated using incremental voltage window opening in half-cells using cyclic voltammetry at 1 mV s^{-1} scan rate (Fig. 6A). The electrochemical stability limit (voltage window), on first approximation, can be assessed by using *S*-value testing, as outlined by Weingarth *et al.*[114] *S*-Value testing is a quantitative measure of the irreversible charge invested during cyclic voltammetry and the limit for stable performance is conventionally set to a value of 10%. The resulting values are shown in (Fig. 6B). For the aqueous electrolyte, a potential window from −0.4 V to +0.8 V *vs.* platinum is seen. The cyclic voltammograms in Fig. 6A show irreversible reactions, well known for manganese oxide measured in aqueous media especially during negative polarization.[60,66,115] A very high initial *S*-value at −0.1 V *vs.* Pt vanishes after conditioning (*i.e.*, after several charge/discharge cycles). Using the organic electrolyte, a stable potential range from −1.2 V to +1.2 V *vs.* carbon can be identified.[114]

For full-cell setups, a cell voltage of 0.8 V and 2.2 V can be used in aqueous and organic electrolyte which is also in agreement with literature.[49] However, we note that it is not absolutely clear if *S*-value testing is the most comprehensive method to assess the maximum voltage window width for pseudocapacitive materials, because it was developed for ideal ELDC systems with the degradation mechanism related to electrolyte decomposition instead of possible electrode deterioration.[114]

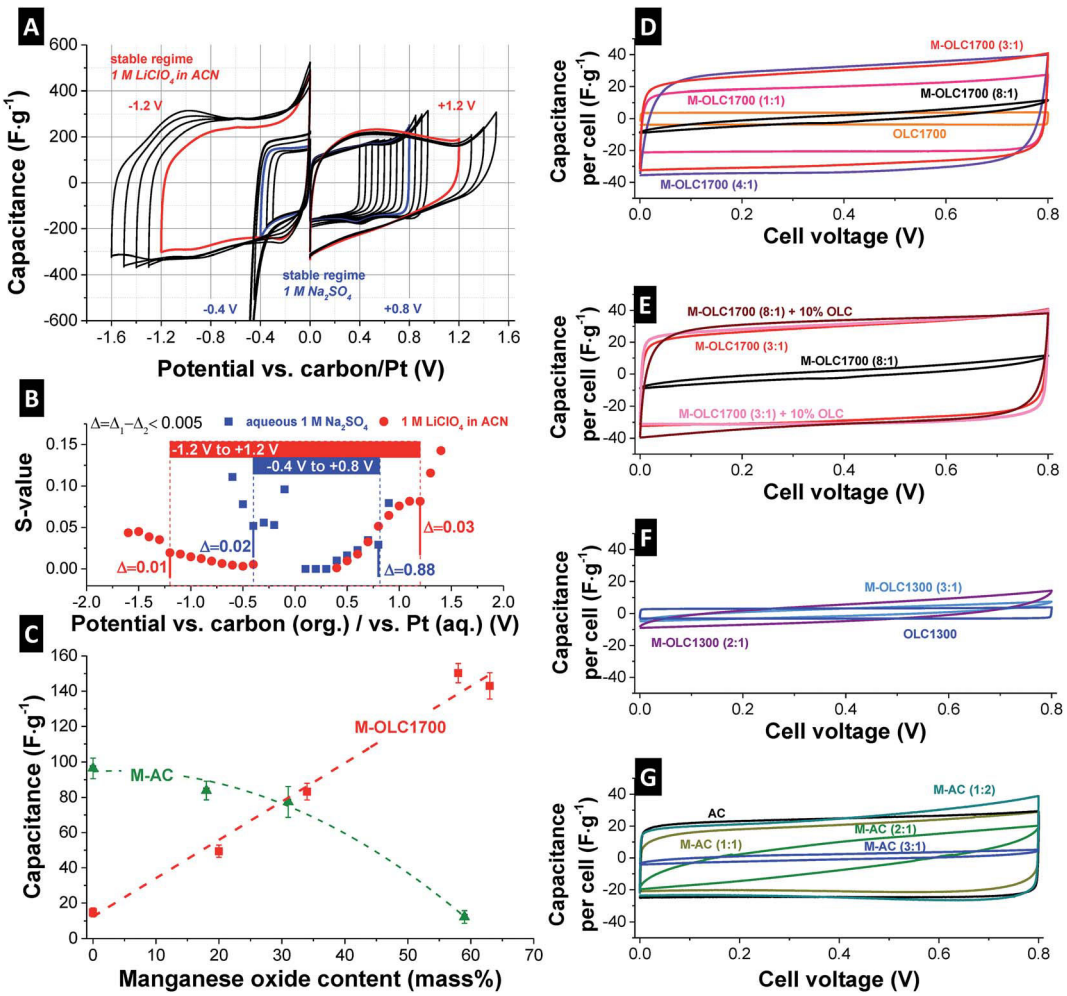

Fig. 6 (A) Potential window opening in a half-cell using M–OLC1700 (3 : 1) as working electrode, 1 mV s^{-1} as scan rate and aqueous 1 M Na_2SO_4 and 1 M $LiClO_4$ in ACN as electrolytes. (B) Corresponding *S*-values after Weingarth *et al.* (ref. 114). (C) Half-cell capacitance dependent on the manganese oxide loading. (D–G) Full-cell cyclic voltammograms at 10 mV s^{-1} in aqueous 1 M Na_2SO_4.

The capacitance of an electrode material can be measured reliably using half-cells with an oversized counter electrode (activated carbon, YP80 + 5 mass% PTFE). The capacitance was measured using galvanostatic cycling to +0.5 V *vs.* carbon with a rate of 0.1 A g^{-1}. By increasing the manganese oxide loading on OLC1700, the specific capacitance increased linearly until the maximum value of 150 F g^{-1} for 58 mass% manganese oxide (M–OLC1700 (3 : 1)) was reached (Fig. 6C). By further increasing the metal oxide content, the capacitance decreased. Ultimately, we see a very high electrical resistance (*e.g.*, for M–OLC1700 (8 : 1)) similar to that of pure manganese oxide and no charge storage capacity was able to be determined anymore.[66] The maximum value of 150 F g^{-1} in aqueous medium is somewhat smaller compared to other studies with maximum reported values between 200 and 400 F g^{-1} (Table 3). However, a fair comparison of capacitance values is only possible when similar materials and same normalizations and measurement techniques are used. Table 3 presents capacitance values of different birnessite or manganese oxide materials with $KMnO_4$ as precursor, measured in half-cells and neutral aqueous electrolytes. Different manganese oxide contents in the composite as well as different amounts of conductive additive and binder were used. To compare the data, all capacitance values were normalized either to the MnO_2 content or to the electrode without binder. After normalizing to the amount of manganese oxide, the literature values ranged from 61 to 420 F g^{-1}. The capacitance values reported in this study are comparably high between 226 and 309 F g^{-1}, and are attributed to the high conductivity and easy ion accessibility of the composite. The high value of 868 F g^{-1} reported by Makgopa *et al.* might stem from the use of ultrathin electrodes.[88] When comparing data normalized to manganese oxide and carbon content, the capacitances are in line with most of the studies showing values in the range of 48–408 F g^{-1} (Table 3).

Fig. 6D depicts CVs of the full-cells of OLC1700. The rectangular shape of OLC1700 demonstrates nearly ideal double-layer capacitor behavior, in alignment with literature.[16,17] By increasing the metal oxide loading, the cell capacitance increased by maintaining the quasi rectangular shape, which evidences the highly pseudocapacitive behavior of the hybrid electrodes.[43,44,46] With a loading of 73 mass% manganese oxide, the resistivity of the electrode was too high and no significant capacitance could be measured (Fig. 6D and Table 2). The conductivity of the electrodes followed the same trend with 1.78 $\pm$ 0.54 S cm^{-1} for OLC1700, 1.98 $\pm$ 0.85 S cm^{-1} for M–OLC1700 (1 : 1), and decreasing values until the conductivity for the highest loading was smaller than the detection limit (Table 2). By adding 10 mass% OLC1700 as conductive additive during electrode fabrication to the material (M–OLC1700 (8 : 1) + 10% OLC), the conductivity of the electrode was enhanced to 1.52 $\pm$ 0.44 S cm^{-1}, leading to a pronouncedly rectangular shape of the CV (Fig. 6E).

During the synthesis, manganese oxide first nucleates on the carbon substrate leading to a thin layer with low resistivity and rather low electrode capacitance (M–OLC1700 (1 : 1)). Further coating increases the layer thickness until a balance of electrical conductivity and electrochemical response (*i.e.*, maximum capacitance) is reached (M–OLC1700 (3 : 1)). As this process continues, the conductivity decreases significantly (M–OLC1700 (8 : 1)) (Table 2). This is also supported by the growth of manganese oxide needles which are not directly in contact with conductive carbon. Adding carbon onions as conductive additive between the non-conductive parts of thick layer or needle-like manganese oxide (M–OLC1700 (8 : 1) + 10% OLC) is a facile approach to significantly increase conductivity and capacitance (Table 2). The direct influence of conductivity and electron support of the manganese oxide by the conductive carbon is supported by the low performance of OLC1300 in the composite (Fig. 6D).

Low temperature carbon onions (OLC1300) present a lower degree of carbon ordering than OLC1700 (Fig. 5D), explaining the lower electrode conductivity of 1.12 $\pm$ 0.45 S cm^{-1} and inferior rate handling.[98,100,101,125] The cyclic voltammogram of OLC1300 is similar to OLC1700 with a nearly perfect rectangular shape (Fig. 6D). After adding manganese oxide, the capacitive behavior vanished. Even for very small manganese oxide loadings, the high resistivity (Table 2) of the electrode prevents the emergence of a characteristic pseudocapacitive behavior and results in negligible capacitance. As shown by Raman spectroscopy and TEM analysis, the hydrothermal synthesis of manganese oxide coating on carbon involves etching of outer graphitic layers, resulting in less conductive amorphous carbon cores. Consequently, the electrochemical performance of carbon/manganese oxide hybrids is directly influenced by the degree of carbon ordering and the electrical conductivity, since all other parameters were kept constant.

For AC, using the same synthesis, no significant increase in capacitance was observed after variation of the manganese oxide loading (Fig. 6B and E). The highest value of 96 F g^{-1} at 0.5 V in a half-cell is seen for the initial AC without additional redox activity and 84 F g^{-1} for M–AC (1 : 2). In recent literature, somewhat larger values of 117 F g^{-1} (ref. 24) and 252 F g^{-1} (ref. 96) were reported for activated carbon (fiber)/manganese oxide composites. Coating of the porous particles with a dense layer of metal oxide resulted in pore blocking, leading to a decrease in surface area as shown by TEM, gas sorption, and gas pycnometry. Still, for thin layers (*i.e.*, M–AC (1 : 2) and M–AC (1 : 1)), the capacitance was similar to the initial AC, even if the surface area decreases to ~60% of the initial value (731 m^2 g^{-1}). Cyclic voltammograms indicate a sufficiently high conductivity (Table 2) in comparison with OLC1300/manganese oxide hybrids and a rectangular shape (Fig. 6E). For higher manganese oxide loadings, the capacitance quickly drops and the electrochemical response becomes more resistive. The layer thickness as well as the growth of needles starts at much lower amounts of manganese oxide precursor compared to OLC. For M–OLC1700 (3 : 1), the best performance was measured with the highest capacitance of 150 F g^{-1}, whereas the same amount of metal oxide with AC as substrate showed a negligible capacitance (*ca.* 10 F g^{-1}).

Coating thickness,[46,53] morphology,[71] and structure[51] of the manganese oxide phase not only influence the (equilibrium = low-rate) capacitance, but also result in differing power performances. Fig. 7A and B present the rate handling by applying

Table 3 Literature half-cell values of manganese oxides. The compared data are for birnessite-type manganese oxides or similar manganese oxides with $KMnO_4$ as precursor. CB means carbon black, AC activated carbon, OLC onion-like carbon, and rGO reduced graphene-oxide. MnO_2 "+" carbon describes physical mixing and "on" carbon a coating with MnO_2

	MnO_2 in the composite (mass%)	Electrolyte	Rate	Voltage window (V)	Conductive additive (mass%)	Amount of binder (mass%)	Reported capacitance ($F\ g^{-1}$)	Normalization	Capacitance per MnO_2 ($F\ g^{-1}$)	Capacitance per electrode w/o binder ($F\ g^{-1}$)	Ref.
Birnessite on OLC	63	1 M Na_2SO_4	0.1 A g^{-1}	0/+0.5	0	10	143	MnO_2 + C	226	143	This study
Birnessite on OLC	58	1 M $LiClO_4$ in ACN	0.1 A g^{-1}	0/+1	0	10	179	MnO_2 + C	309	179	This study
Birnessite on OLC	58	1 M Na_2SO_4	0.1 A g^{-1}	0/+0.5	0	10	150	MnO_2 + C	259	150	This study
Birnessite on OLC	34	1 M Na_2SO_4	0.1 A g^{-1}	0/+0.5	0	10	83	MnO_2 + C	244	83	This study
Birnessite on OLC	20	1 M Na_2SO_4	0.1 A g^{-1}	0/+0.5	0	10	49	MnO_2 + C	245	49	This study
Birnessite on OLC	47	1 M Na_2SO_4	0.1 A g^{-1}	0/+0.5	0	10	408	MnO_2 + C	868	408	88
Birnessite nanotubes		1 M Na_2SO_4	0.25 A g^{-1}	−0.2/+0.8	20	10	365	MnO_2	365	284	116
Birnessite on AC	60	1 M Na_2SO_4	0.5 A g^{-1}	−0.2/+0.8	20	10	252	MnO_2 + C	420	196	96
Birnessite nanosheets		1 M Na_2SO_4	0.3 A g^{-1}	−0.1/+0.9	20	10	269	MnO_2	269	209	117
Birnessite on OLC	80	1 M Na_2SO_4	0.2 A g^{-1}	0/+0.8	10	10	178	MnO_2	178	127	118
(Na)–birnessite nanowires		0.5 M Na_2SO_4	1 mV s^{-1}	0/+1	10	10	191	MnO_2	191	170	119
Birnessite on rGO		1 M Na_2SO_4	0.1 A g^{-1}	0/+1	15	5	194	Electrode	243	204	120
Birnessite nanobelt bundle		1 M Na_2SO_4	5 mV s^{-1}	−0.2/+0.8	15	5	268	MnO_2	268	226	121
Different types of birnessite		0.1 M K_2SO_4	5 mV s^{-1}	0/+0.9	25	7	80–110	MnO_2	80–110	58–80	61
Birnessite		0.1 M Na_2SO_4	5 mV s^{-1}	0/+0.9	15	5	150	MnO_2	150	126	46
Birnessite on AC fiber	63	1 M Na_2SO_4	10 mA cm^{-2}	−0.2/+0.8	10	5	117	MnO_2 + C	186	105	24
Graphene-wrapped MnO_2	91	1 M Na_2SO_4	0.5 A g^{-1}	0/+1	20	10	210	MnO_2 + C	231	180	122
Nanostructured MnO_2		1 M Na_2SO_4	5 mV s^{-1}	−0.2/+0.8	20	5	72–168	MnO_2	72–168	57–133	71
Nanostructured MnO_2		0.1 M Na_2SO_4	0.5 mA cm^{-2}	0/+1	20	5	61–250	MnO_2	61–250	48–133	123
Nanostructured α-MnO_2		0.1 M Na_2SO_4	0.5 mA cm^{-2}	0/+1	20	10	297	MnO_2	297	231	124
Amorphous MnO_2 + CB	60–80	0.65 M K_2SO_4	2 mV s^{-1}	−0.1/+0.9	0	10	100–141	Electrode	164–175	111–157	95
Amorphous MnO_2 + AC	60–80	0.65 M K_2SO_4	2 mV s^{-1}	−0.1/+0.9	0	10	134–150	Electrode	174–183	149–167	95
Amorphous MnO_2 + AC	60	0.65 M K_2SO_4	2 mV s^{-1}	0/+0.9	0	10	129	Electrode	239	143	62
Amorphous MnO_2 on AC	60	0.65 M K_2SO_4	2 mV s^{-1}	0/+0.9	0	10	122	Electrode	227	136	62

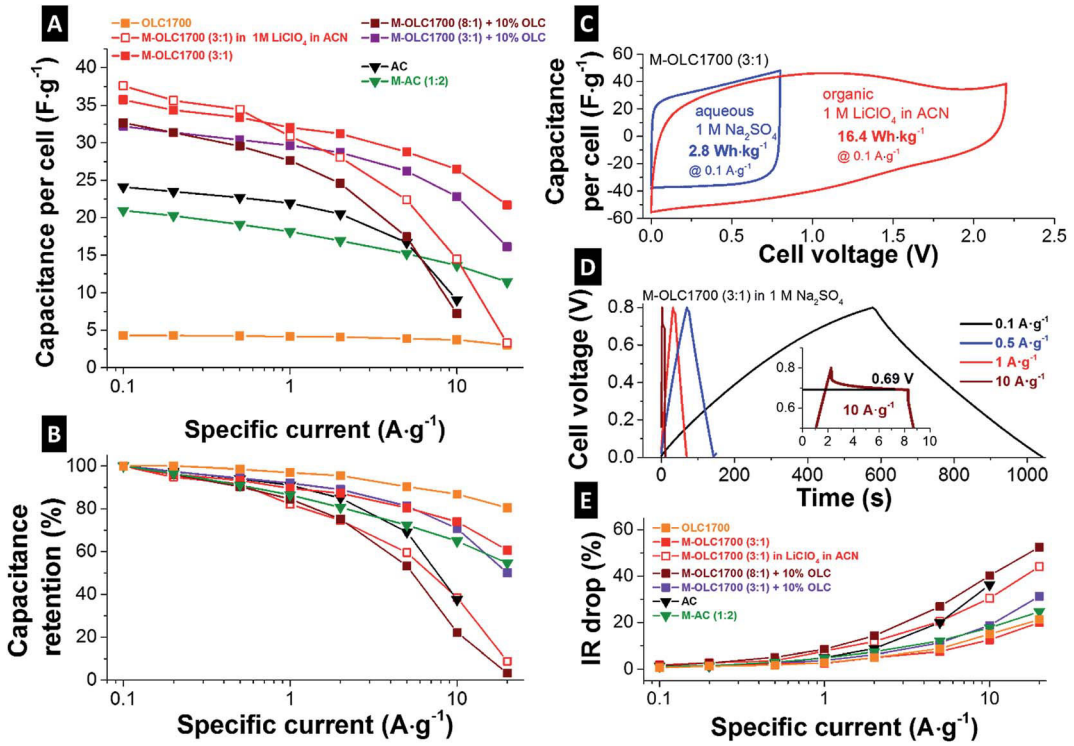

Fig. 7 (A) Rate handling plot: full-cell capacitance dependent on the applied current density. (B) Normalized rate handling plot. (C) Cyclic voltammograms of M–OLC1700 (3 : 1) in full-cell mode using aqueous 1 M Na_2SO_4 and 1 M $LiClO_4$ in ACN. (D) Galvanostatic cycling plots of M–OLC1700 (3 : 1) aqueous 1 M Na_2SO_4 using different specific currents. The inset shows the IR drop by applying a specific current of 10 A g^{-1}. (E) Normalized IR drop: normalized to IR drop at 0.1 A g^{-1} (0.8 V and 2.2 V for aqueous and organic electrolyte). All measurements were done in aqueous 1 M Na_2SO_4 electrolyte if not otherwise declared.

different current densities in full-cell mode. In agreement with literature, the rate behavior of OLC was demonstrated to be superior to AC with a capacitance retention of more than 80% at 20 A g^{-1} compared to less than 40% at 10 A g^{-1}.[101] For M–AC (1 : 2) with a surface area > 1000 m^2 g^{-1}, a significant contribution of double-layer capacitance can be assumed. However, the thin and highly conductive coating enabled a very fast system response due to fast surface redox and intercalation effects. Therefore, OLC1700 hybrids resulted in a higher capacitance and in a better rate handling due to higher conductivity and highly accessible outer surface area (Fig. 7A and B). For M–OLC1700 (8 : 1), thick metal oxide layers resulted in high contact resistances between the particles and less facile electron support. After adding 10 mass% OLC (M–OLC1700 (8 : 1) + 10 mass% OLC), the conductivity of the manganese oxide surface coating was increased. M–OLC1700 (3 : 1) with a manganese oxide content of 58 mass% exhibited the best performance with the highest measured capacitance of 150 F g^{-1} and good rate handling. However, the specific energy for 0.8 V cell voltage in aqueous electrolyte results in only 2.8 W h kg^{-1}, 40% larger than for AC (~2 W h kg^{-1}). To further improve the specific energy, the maximum cell voltage can be increased when using an organic electrolyte instead of an aqueous medium. In our case, we investigated 1 M $LiClO_4$ in ACN. The capacitance of M–OLC1700 (3 : 1) was increased to 176 F g^{-1} at 0.5 V and 179 F g^{-1} at 1 V and 0.1 A g^{-1} (measured in a half-cell). Corresponding cyclic voltammograms for the full-cell setup are given in Fig. 7C. The extended voltage window translates to an enhanced specific energy of 16.4 W h kg^{-1} which is more than 5-times higher than in aqueous media.

Up to a specific current of 1 A g^{-1}, the cell capacitance in the organic medium was comparable to the same material operated in the aqueous electrolyte (Fig. 7A and B). For higher rates, the capacitance retention dropped more severely compared to aqueous medium. The normalized IR drop is shown in Fig. 7E and the corresponding charge–discharge curves in Fig. 7D present higher values in organic medium compared to the aqueous electrolyte. For electrodes with higher conductivity (Table 2), the IR drop was smaller and the resulting cell voltage larger (Fig. 7E). The initial carbon onions (OLC1700) presented an increase in IR drop of ~20% when increasing the specific current from 0.1 A g^{-1} to 20 A g^{-1} due to high conductivity and high ion accessibility. The same was measured for M–OLC1700 (3 : 1) with a thin manganese oxide coating.

Electrochemical energy storage devices can be compared conveniently *via* Ragone plots.[126] Fig. 8A shows the specific energy of the cell normalized to the active mass of both electrodes *versus* the specific power derived from galvanostatic cycling by using different rates. Carbon onions (OLC1700) present excellent specific power of more than 10 kW kg^{-1}, but with a comparable low specific energy of less than 0.4 W h kg^{-1} in aqueous electrolyte. Values for the specific energy were at 2.8 W h kg^{-1} for M–OLC1700 (3 : 1), which is larger than activated carbon with ~2 W h kg^{-1}. The energy capacity can be increased

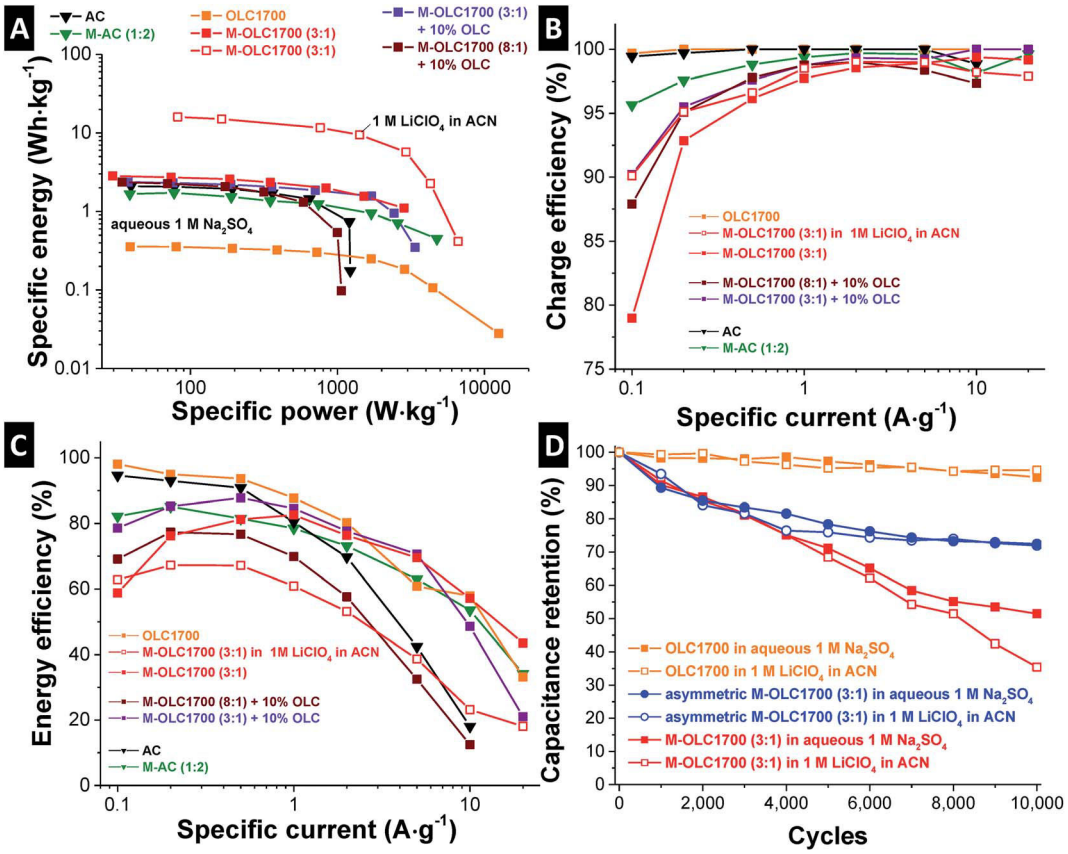

Fig. 8 (A) Ragone plot derived from galvanostatic cycling with potential limitation using 0.8 V and 2.2 V cell voltage for aqueous and organic electrolyte. All values are normalized to two electrodes. (B) Charge efficiency and (C) energy efficiency dependent on the applied specific currents. (D) Long-time stability test using 10 000 galvanostatic cycles using symmetric and asymmetric full-cells. All measurements were done in aqueous 1 M Na_2SO_4 electrolyte if not otherwise stated.

when using organic electrolyte with 2.2 V cell voltage to 16.4 W h kg^{-1}. By adding carbon onions as conductive additive, the specific power can be slightly increased for the manganese oxide hybrid (M–OLC1700 (3 : 1) + 10 mass% OLC), but the specific energy is decreased due to smaller capacitance. Additional manganese oxide loading (M–OLC1700 (8 : 1) + 10 mass% OLC) decreased the specific power as well as the specific energy.

The optimum performance was found for 58 mass% manganese oxide, which is in agreement with recent studies using similar amounts.[24,88,96] Good performance at low and high rates is important, but only when also sufficient long-time stability is maintained. For manganese oxide in organic and neutral aqueous media, the potential window in the negative range is limited to −1.2 V *vs.* carbon and −0.4 V *vs.* Pt (Fig. 6A and B). For aqueous media, the stability is rather low due to the dissolution of manganese oxide in the negative range.[60,66,115] This potential-dependent stability makes manganese oxide an attractive electrode material for positive polarization, but not for the negative side in aqueous media.[44] Although a small cell voltage of 0.8 V for aqueous electrolyte and 2.2 V for organic electrolyte was used, the electrodes lost more than 40% of capacitance after 10 000 galvanostatic cycles, in agreement with the measured stability range in Fig. 6A and B. Even in organic electrolyte at 2.2 V, the material had a capacitance retention of less than 40%. This clearly shows that *S*-value stability testing for pseudocapacitive materials, including faradaic reactions, may overestimate the actual potential windows.

For low rates and high loadings, the charge efficiency falls below 80% (Fig. 8B). Irreversible reactions take place, for example influenced by electrode dissolution like the Mn(IV) reduction, whereas the charge efficiency for the pristine carbon powders remains constant. For higher rates, these reactions still occur, but are not visible in the electrochemical data because of the high currents related to fast reactions. Taking into account the increase in IR drop in Fig. 7E and the charge efficiency (as a result of irreversible reactions; *e.g.*, dissolution of the material) in Fig. 8B, the change of energy efficiency (Fig. 8C) can be explained. The latter shows low values for low and high rates coming from a voltage loss at high rates and low charge efficiency at low rates.

The low stability of manganese oxide in the negative range can be avoided by using an asymmetric fabrication technique.[44,59,60,115] In this study, a charge balanced AC counter electrode was used (negative polarization) and the carbon onion/manganese oxide hybrid (positive polarization). Fig. 8D demonstrates the improved long-time stability of asymmetric devices in aqueous and organic electrolyte, with a capacitive retention of around 72% after 10 000 charge/discharge cycles.

Clearly, the instability of manganese oxide remains a key challenge for further adaption of the technology, but asymmetric device architectures can greatly improve the performance stability.

4. Conclusions

This study provides a comprehensive data set of hydrothermally synthesized birnessite-type manganese oxide on different carbon substrates for supercapacitor applications. As observable in our data, the metal oxide coatings block the internal pores of activated carbon. Depending on the amount of manganese oxide loading, its specific surface area decreased by more than 80%. The very low external surface area of AC did not provide enough active sites for the reaction with permanganate (*i.e.*, the manganese oxide precursor), so that needle-like structures with high resistivity form which protrude into the interparticle space of the electrode. For comparison, high temperature carbon onions, with accessible surface area only on the outer side were homogenously coated, resulting in a strong increase in capacitance and overall good rate behavior with ~75% capacitance retention at 10 A g^{-1} applied specific current.

Besides porosity and morphology of the carbon substrate, also the degree of carbon ordering strongly influences the electrochemical performance of carbon/manganese oxide hybrids. High and low temperature carbon onions (OLC1700 and OLC1300) with different degrees of carbon ordering were compared. The lower conductivity of OLC1300 was found to be insufficient to overcome the low conductivity of manganese oxide, resulting in a very high resistance of the system. For OLC1700, a strong increase in capacitance from ~20 F g^{-1} to 150 F g^{-1} was measured with a specific energy of 2.8 W h kg^{-1} in aqueous and 16.4 W h kg^{-1} in organic electrolyte, while showing a good rate handling behavior. The limited long-time stability, a well-known problem of manganese oxide, was strongly improved by building asymmetric full-cells with activated carbon on the negative side. However, the stability remains a key challenge for further advancements of the technology.

Acknowledgements

This work was supported by the CREATe-Network Project, Horizon 2020 of the European Commission (RISE Project No. 644013). This work was carried out within the framework of the graduate course "Materials for the efficient use of energy" at Saarland University. The authors thank Prof. Eduard Arzt (INM) for his continuing support. Nicolas Jäckel (INM) is thanked for initiating collaboration with the Thiele Group and for helpful comment and discussions. We thank Jan Laube and Prof. Zacharias from the Laboratory for Nanotechnology (University of Freiburg) for the atomic layer deposition of ZnO.

References

1 F. Béguin, V. Presser, A. Balducci and E. Frackowiak, *Adv. Mater.*, 2014, **26**, 2219–2251.
2 P. Simon and Y. Gogotsi, *Nat. Mater.*, 2008, **7**, 845–854.
3 J. B. Goodenough, *Energy Environ. Sci.*, 2014, **7**, 14–18.
4 Z. Yang, J. Zhang, M. C. Kintner-Meyer, X. Lu, D. Choi, J. P. Lemmon and J. Liu, *Chem. Rev.*, 2011, **111**, 3577–3613.
5 N. S. Choi, Z. Chen, S. A. Freunberger, X. Ji, Y. K. Sun, K. Amine, G. Yushin, L. F. Nazar, J. Cho and P. G. Bruce, *Angew. Chem., Int. Ed.*, 2012, **51**, 9994–10024.
6 C. Liu, F. Li, L. P. Ma and H. M. Cheng, *Adv. Mater.*, 2010, **22**, E28–E62.
7 P. Simon, Y. Gogotsi and B. Dunn, *Science Magazine*, 2014, p. 343.
8 E. Frackowiak and F. Beguin, *Carbon*, 2001, **39**, 937–950.
9 N. Jäckel, M. Rodner, A. Schreiber, J. Jeongwook, M. Zeiger, M. Aslan, D. Weingarth and V. Presser, *J. Power Sources*, 2016, **326**, 660–671.
10 D. Qu and H. Shi, *J. Power Sources*, 1998, **74**, 99–107.
11 H. Shi, *Electrochim. Acta*, 1996, **41**, 1633–1639.
12 Y. Gogotsi, A. Nikitin, H. Ye, W. Zhou, J. E. Fischer, B. Yi, H. C. Foley and M. W. Barsoum, *Nat. Mater.*, 2003, **2**, 591–594.
13 A. Jänes, L. Permann, M. Arulepp and E. Lust, *Electrochem. Commun.*, 2004, **6**, 313–318.
14 V. Presser, L. Zhang, J. J. Niu, J. McDonough, C. Perez, H. Fong and Y. Gogotsi, *Adv. Energy Mater.*, 2011, **1**, 423–430.
15 A. Fuertes, G. Lota, T. Centeno and E. Frackowiak, *Electrochim. Acta*, 2005, **50**, 2799–2805.
16 M. Zeiger, N. Jäckel, V. N. Mochalin and V. Presser, *J. Mater. Chem. A*, 2016, **4**, 3172–3196.
17 M. E. Plonska-Brzezinska and L. Echegoyen, *J. Mater. Chem. A*, 2013, **1**, 13703–13714.
18 A. Bello, K. Makgopa, M. Fabiane, D. Dodoo-Ahrin, K. I. Ozoemena and N. Manyala, *J. Mater. Sci.*, 2013, **48**, 6707–6712.
19 C. J. Jafta, F. Nkosi, L. le Roux, M. K. Mathe, M. Kebede, K. Makgopa, Y. Song, D. Tong, M. Oyama and N. Manyala, *Electrochim. Acta*, 2013, **110**, 228–233.
20 E. Frackowiak, K. Jurewicz, S. Delpeux and F. Beguin, *J. Power Sources*, 2001, **97**, 822–825.
21 E. Frackowiak, K. Metenier, V. Bertagna and F. Beguin, *Appl. Phys. Lett.*, 2000, **77**, 2421–2423.
22 E. Ra, E. Raymundo-Piñero, Y. Lee and F. Béguin, *Carbon*, 2009, **47**, 2984–2992.
23 M. Zeiger, D. Weingarth and V. Presser, *ChemElectroChem*, 2015, **2**, 1117–1127.
24 K. Zhu, Y. Wang, J. A. Tang, H. Qiu, X. Meng, Z. Gao, G. Chen, Y. Wei and Y. Gao, *RSC Adv.*, 2016, **6**, 14819–14825.
25 U. Fischer, R. Saliger, V. Bock, R. Petricevic and J. Fricke, *J. Porous Mater.*, 1997, **4**, 281–285.
26 O. Barbieri, M. Hahn, A. Herzog and R. Kötz, *Carbon*, 2005, **43**, 1303–1310.
27 C. Xu, F. Kang, B. Li and H. Du, *J. Mater. Res.*, 2010, **25**, 1421–1432.
28 J. Zheng, P. Cygan and T. Jow, *J. Electrochem. Soc.*, 1995, **142**, 2699–2703.
29 M. E. Plonska-Brzezinska, D. M. Brus, A. Molina-Ontoria and L. Echegoyen, *RSC Adv.*, 2013, **3**, 25891–25901.

30 W.-C. Chen and T.-C. Wen, *J. Power Sources*, 2003, **117**, 273–282.
31 Q. Cheng, J. Tang, J. Ma, H. Zhang, N. Shinya and L.-C. Qin, *J. Phys. Chem. C*, 2011, **115**, 23584–23590.
32 I. Kovalenko, D. G. Bucknall and G. Yushin, *Adv. Funct. Mater.*, 2010, **20**, 3979–3986.
33 M. E. Plonska-Brzezinska, J. Mazurczyk, B. Palys, J. Breczko, A. Lapinski, A. T. Dubis and L. Echegoyen, *Chem.–Eur. J.*, 2012, **18**, 2600–2608.
34 H. Zengin, W. Zhou, J. Jin, R. Czerw, D. W. Smith, L. Echegoyen, D. L. Carroll, S. H. Foulger and J. Ballato, *Adv. Mater.*, 2002, **14**, 1480–1483.
35 K.-S. Kim and S.-J. Park, *J. Solid State Electrochem.*, 2012, **16**, 2751–2758.
36 L.-Z. Fan and J. Maier, *Electrochem. Commun.*, 2006, **8**, 937–940.
37 K. Jurewicz, S. Delpeux, V. Bertagna, F. Béguin and E. Frackowiak, *Chem. Phys. Lett.*, 2001, **347**, 36–40.
38 O. Mykhailiv, M. Imierska, M. Petelczyc, L. Echegoyen and M. E. Plonska-Brzezinska, *Chem.–Eur. J.*, 2015, **21**, 5783–5793.
39 D. M. Anjos, J. K. McDonough, E. Perre, G. M. Brown, S. H. Overbury, Y. Gogotsi and V. Presser, *Nano Energy*, 2013, **2**, 702–712.
40 S. Bailey, I. Ritchie, N. Searcy and P. Singh, *J. Appl. Electrochem.*, 1988, **18**, 368–373.
41 X. Chen, H. Wang, H. Yi, X. Wang, X. Yan and Z. Guo, *J. Phys. Chem. C*, 2014, **118**, 8262–8270.
42 A. Le Comte, D. Chhin, A. Gagnon, R. Retoux, T. Brousse and D. Belanger, *J. Mater. Chem. A*, 2015, **3**, 6146–6156.
43 T. Brousse, D. Bélanger and J. W. Long, *J. Electrochem. Soc.*, 2015, **162**, A5185–A5189.
44 D. Bélanger, L. Brousse and J. W. Long, *Electrochem. Soc. Interface*, 2008, **17**, 49.
45 L. Pan, K.-X. Wang, X.-D. Zhu, X.-M. Xie and Y.-T. Liu, *J. Mater. Chem. A*, 2015, **3**, 6477–6483.
46 M. Toupin, T. Brousse and D. Bélanger, *Chem. Mater.*, 2004, **16**, 3184–3190.
47 T.-H. Wu, D. Hesp, V. R. Dhanak, C. Collins, F. Braga, L. Hardwick and C.-C. Hu, *J. Mater. Chem. A*, 2015, **3**, 12786–12795.
48 L. Athouël, F. Moser, R. Dugas, O. Crosnier, D. Bélanger and T. Brousse, *J. Phys. Chem. C*, 2008, **112**, 7270–7277.
49 W. Wei, X. Cui, W. Chen and D. G. Ivey, *Chem. Soc. Rev.*, 2011, **40**, 1697–1721.
50 A. Gambou-Bosca and D. Bélanger, *ECS Trans.*, 2015, **64**, 13–20.
51 M. Toupin, T. Brousse and D. Bélanger, *Chem. Mater.*, 2002, **14**, 3946–3952.
52 O. Ghodbane, J.-L. Pascal, B. Fraisse and F. Favier, *ACS Appl. Mater. Interfaces*, 2010, **2**, 3493–3505.
53 M. Wu, L. Zhang, J. Gao, C. Xiao, D. Wang, A. Chen and S. Zhang, *J. Electroanal. Chem.*, 2008, **613**, 125–130.
54 T. Brousse, P.-L. Taberna, O. Crosnier, R. Dugas, P. Guillemet, Y. Scudeller, Y. Zhou, F. Favier, D. Bélanger and P. Simon, *J. Power Sources*, 2007, **173**, 633–641.
55 O. Ghodbane, F. Ataherian, N.-L. Wu and F. Favier, *J. Power Sources*, 2012, **206**, 454–462.
56 O. Ghodbane, J.-L. Pascal and F. Favier, *ACS Appl. Mater. Interfaces*, 2009, **1**, 1130–1139.
57 D. J. Jones, E. Wortham, J. Roziere, F. Favier, J.-L. Pascal and L. Monconduit, *J. Phys. Chem. Solids*, 2004, **65**, 235–239.
58 Y. Lei, C. Fournier, J.-L. Pascal and F. Favier, *Microporous Mesoporous Mater.*, 2008, **110**, 167–176.
59 L. Athouël, F. Moser, R. Dugas, O. Crosnier, D. Bélanger and T. Brousse, *ECS Trans.*, 2008, **16**, 119–123.
60 T. Brousse, M. Toupin and D. Belanger, *J. Electrochem. Soc.*, 2004, **151**, A614–A622.
61 T. Brousse, M. Toupin, R. Dugas, L. Athouël, O. Crosnier and D. Bélanger, *J. Electrochem. Soc.*, 2006, **153**, A2171–A2180.
62 A. Gambou-Bosca and D. Bélanger, *J. Electrochem. Soc.*, 2015, **162**, A5115–A5123.
63 C. Ramirez-Castro, O. Crosnier, L. Athouël, R. Retoux, D. Bélanger and T. Brousse, *J. Electrochem. Soc.*, 2015, **162**, A5179–A5184.
64 T. M. McEvoy, J. W. Long, T. J. Smith and K. J. Stevenson, *Langmuir*, 2006, **22**, 4462–4466.
65 V. Subramanian, H. Zhu and B. Wei, *Electrochem. Commun.*, 2006, **8**, 827–832.
66 E. Raymundo-Pinero, V. Khomenko, E. Frackowiak and F. Beguin, *J. Electrochem. Soc.*, 2005, **152**, A229–A235.
67 C. Y. Lee, H. M. Tsai, H. J. Chuang, S. Y. Li, P. Lin and T. Y. Tseng, *J. Electrochem. Soc.*, 2005, **152**, A716–A720.
68 Y.-T. Wu and C.-C. Hu, *J. Electrochem. Soc.*, 2004, **151**, A2060–A2066.
69 S.-B. Ma, K.-Y. Ahn, E.-S. Lee, K.-H. Oh and K.-B. Kim, *Carbon*, 2007, **45**, 375–382.
70 J. Li and I. Zhitomirsky, *J. Mater. Process. Technol.*, 2009, **209**, 3452–3459.
71 V. Subramanian, H. Zhu, R. Vajtai, P. Ajayan and B. Wei, *J. Phys. Chem. B*, 2005, **109**, 20207–20214.
72 Z. Fan, J. Chen, B. Zhang, F. Sun, B. Liu and Y. Kuang, *Mater. Res. Bull.*, 2008, **43**, 2085–2091.
73 S.-L. Chou, J.-Z. Wang, S.-Y. Chew, H.-K. Liu and S.-X. Dou, *Electrochem. Commun.*, 2008, **10**, 1724–1727.
74 Z. Fan, J. Chen, B. Zhang, B. Liu, X. Zhong and Y. Kuang, *Diamond Relat. Mater.*, 2008, **17**, 1943–1948.
75 B. G. Choi, M. Yang, W. H. Hong, J. W. Choi and Y. S. Huh, *ACS Nano*, 2012, **6**, 4020–4028.
76 J. Yan, Z. Fan, T. Wei, W. Qian, M. Zhang and F. Wei, *Carbon*, 2010, **48**, 3825–3833.
77 Z. Li, Y. Mi, X. Liu, S. Liu, S. Yang and J. Wang, *J. Mater. Chem.*, 2011, **21**, 14706–14711.
78 Z. Fan, J. Yan, T. Wei, L. Zhi, G. Ning, T. Li and F. Wei, *Adv. Funct. Mater.*, 2011, **21**, 2366–2375.
79 Q. Cheng, J. Tang, J. Ma, H. Zhang, N. Shinya and L.-C. Qin, *Carbon*, 2011, **49**, 2917–2925.
80 Y. He, W. Chen, X. Li, Z. Zhang, J. Fu, C. Zhao and E. Xie, *ACS Nano*, 2012, **7**, 174–182.
81 A. Sumboja, C. Y. Foo, X. Wang and P. S. Lee, *Adv. Mater.*, 2013, **25**, 2809–2815.
82 S. Chen, J. Zhu, X. Wu, Q. Han and X. Wang, *ACS Nano*, 2010, **4**, 2822–2830.

83 A. E. Fischer, K. A. Pettigrew, D. R. Rolison, R. M. Stroud and J. W. Long, *Nano Lett.*, 2007, **7**, 281–286.
84 J. W. Long, M. B. Sassin, A. E. Fischer, D. R. Rolison, A. N. Mansour, V. S. Johnson, P. E. Stallworth and S. G. Greenbaum, *J. Phys. Chem. C*, 2009, **113**, 17595–17598.
85 C. Wan, K. Azumi and H. Konno, *J. Appl. Electrochem.*, 2007, **37**, 1055–1061.
86 C. Wan, K. Azumi and H. Konno, *Electrochim. Acta*, 2007, **52**, 3061–3066.
87 J. Yan, Z. Fan, T. Wei, Z. Qie, S. Wang and M. Zhang, *Mater. Sci. Eng., B*, 2008, **151**, 174–178.
88 K. Makgopa, P. M. Ejikeme, C. J. Jafta, K. Raju, M. Zeiger, V. Presser and K. I. Ozoemena, *J. Mater. Chem. A*, 2015, **3**, 3480–3490.
89 R. Borgohain, J. Li, J. P. Selegue and Y.-T. Cheng, *J. Phys. Chem. C*, 2012, **116**, 15068–15075.
90 R. Borgohain, J. P. Selegue and Y.-T. Cheng, *J. Mater. Chem. A*, 2014, **2**, 20367–20373.
91 X. Dong, W. Shen, J. Gu, L. Xiong, Y. Zhu, H. Li and J. Shi, *J. Phys. Chem. B*, 2006, **110**, 6015–6019.
92 L. L. Zhang, T. Wei, W. Wang and X. Zhao, *Microporous Mesoporous Mater.*, 2009, **123**, 260–267.
93 S. Yoon, C. Lee, S. M. Oh, Y.-K. Park and W. C. Choi, *J. Non-Cryst. Solids*, 2009, **355**, 252–256.
94 S. Fleischmann, N. Jäckel, M. Zeiger, B. Krüner, I. Grobelsek, P. Formanek, S. Choudhury, D. Weingarth and V. Presser, *Chem. Mater.*, 2016, **28**, 2802–2813.
95 A. Gambou-Bosca and D. Bélanger, *J. Mater. Chem. A*, 2014, **2**, 6463–6473.
96 X. Zhang, X. Sun, H. Zhang, D. Zhang and Y. Ma, *Mater. Chem. Phys.*, 2012, **137**, 290–296.
97 S. Vierrath, F. Güder, A. Menzel, M. Hagner, R. Zengerle, M. Zacharias and S. Thiele, *J. Power Sources*, 2015, **285**, 413–417.
98 M. Zeiger, N. Jäckel, D. Weingarth and V. Presser, *Carbon*, 2015, **94**, 507–517.
99 M. Zeiger, N. Jäckel, M. Aslan, D. Weingarth and V. Presser, *Carbon*, 2015, **84**, 584–598.
100 D. Weingarth, M. Zeiger, N. Jäckel, M. Aslan, G. Feng and V. Presser, *Adv. Energy Mater.*, 2014, **4**, 1400316.
101 J. K. McDonough, A. I. Frolov, V. Presser, J. Niu, C. H. Miller, T. Ubieto, M. V. Fedorov and Y. Gogotsi, *Carbon*, 2012, **50**, 3298–3309.
102 S. Bach, J. Pereira-Ramos, N. Baffier and R. Messina, *Electrochim. Acta*, 1991, **36**, 1595–1603.
103 B. Shen, *Energy Convers. Manage.*, 2006, **47**, 1429–1437.
104 Y. Peng, Z. Chen, J. Wen, Q. Xiao, D. Weng, S. He, H. Geng and Y. Lu, *Nano Res.*, 2011, **4**, 216–225.
105 O. O. Mykhaylyk, Y. M. Solonin, D. N. Batchelder and R. Brydson, *J. Appl. Phys.*, 2005, **97**, 074302.
106 E. D. Obraztsova, M. Fujii, S. Hayashi, V. L. Kuznetsov, Y. V. Butenko and A. L. Chuvilin, *Carbon*, 1998, **36**, 821–826.
107 D. Roy, M. Chhowalla, H. Wang, N. Sano, I. Alexandrou, T. W. Clyne and G. A. J. Amaratunga, *Chem. Phys. Lett.*, 2003, **373**, 52–56.
108 X. Wang, B. Xu, X. Liu, H. Jia and I. Hideki, *Phys. B*, 2005, **357**, 277–281.
109 Q. Zou, M. Z. Wang, Y. G. Li, B. Lv and Y. C. Zhao, *J. Exp. Nanosci.*, 2010, **5**, 473–487.
110 A. C. Ferrari and J. Robertson, *Philos. Trans. R. Soc., A*, 2004, **362**, 2477–2512.
111 A. Ferrari and J. Robertson, *Phys. Rev. B: Condens. Matter Mater. Phys.*, 2000, **61**, 14095.
112 C. M. Julien, M. Massot and C. Poinsignon, *Spectrochim. Acta, Part A*, 2004, **60**, 689–700.
113 C. Julien, M. Massot, R. Baddour-Hadjean, S. Franger, S. Bach and J. Pereira-Ramos, *Solid State Ionics*, 2003, **159**, 345–356.
114 D. Weingarth, H. Noh, A. Foelske-Schmitz, A. Wokaun and R. Kötz, *Electrochim. Acta*, 2013, **103**, 119–124.
115 V. Khomenko, E. Raymundo-Pinero and F. Béguin, *J. Power Sources*, 2006, **153**, 183–190.
116 M. Huang, Y. Zhang, F. Li, L. Zhang, R. S. Ruoff, Z. Wen and Q. Liu, *Sci. Rep.*, 2014, **4**, 3878.
117 X. Zhang, P. Yu, H. Zhang, D. Zhang, X. Sun and Y. Ma, *Electrochim. Acta*, 2013, **89**, 523–529.
118 Y. Wang, S. F. Yu, C. Y. Sun, T. J. Zhu and H. Y. Yang, *J. Mater. Chem.*, 2012, **22**, 17584–17588.
119 O. Vargas, A. Caballero, L. Hernán and J. Morales, *J. Power Sources*, 2011, **196**, 3350–3354.
120 Z. Li, J. Wang, Z. Wang, H. Ran, Y. Li, X. Han and S. Yang, *New J. Chem.*, 2012, **36**, 1490–1495.
121 X. Tang, H. Li, Z.-H. Liu, Z. Yang and Z. Wang, *J. Power Sources*, 2011, **196**, 855–859.
122 J. Zhu and J. He, *ACS Appl. Mater. Interfaces*, 2012, **4**, 1770–1776.
123 P. Ragupathy, D. H. Park, G. Campet, H. Vasan, S.-J. Hwang, J.-H. Choy and N. Munichandraiah, *J. Phys. Chem. C*, 2009, **113**, 6303–6309.
124 S. Devaraj and N. Munichandraiah, *J. Electrochem. Soc.*, 2007, **154**, A80–A88.
125 C. Portet, G. Yushin and Y. Gogotsi, *Carbon*, 2007, **45**, 2511–2518.
126 D. V. Ragone, *SAE [Tech. Pap.]*, 1968, 680453.

Electronic Supplementary Material (ESI) for RSC Advances.

Supporting Information

Influence of carbon substrate on the electrochemical performance of carbon/manganese oxide hybrids in aqueous and organic electrolytes

Marco Zeiger,[1,2] Simon Fleischmann,[1,2] Benjamin Krüner,[1,2] Aura Tolosa,[1,2]

Stephan Bechtel,[1,2] Mathias Baltes,[2] Anna Schreiber,[1] Riko Moroni,[3] Severin Vierrath,[3]

Simon Thiele,[3,4] and Volker Presser[1,2,]*

[1] *INM - Leibniz Institute for New Materials, Campus D2 2, 66123 Saarbrücken, Germany*

[2] *Department of Materials Science and Engineering, Saarland University, Campus D2 2, 66123 Saarbrücken, Germany*

[3] *IMTEK Department of Microsystems Engineering, University of Freiburg, Georges-Koehler-Allee 103, 79110 Freiburg, Germany*

[4] *FIT, University of Freiburg, Georges-Koehler-Allee 103, 79110, 79104 Freiburg, Germany*

** Corresponding author's email address:* volker.presser@leibniz-inm.de

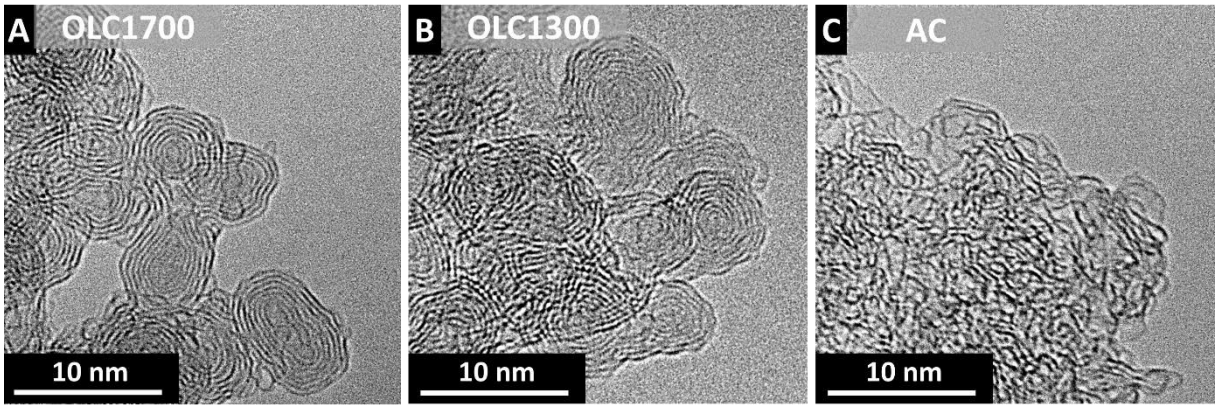

Figure S1: (A-C) Transmission electron micrographs of the carbon powders. (A) Carbon onions synthesized at 1700 °C (OLC1700). (B) Carbon onions synthesized at 1300 °C (OLC1300). (C) Activated carbon (Kuraray YP80).

3.5 Carbon onion-sulfur hybrid cathodes for lithium-sulfur batteries

Soumyadip Choudhury,[1,2] Marco Zeiger,[1,3] Pau Massuti-Ballester,[1,3] Simon Fleischmann,[3] Peter Formanek,[2] Lars Borchardt,[4] and Volker Presser[1,3,*]

1 *INM - Leibniz Institute for New Materials, Campus D2 2, 66123 Saarbrücken, Germany*
2 *Leibniz-Institut für Polymerforschung Dresden e.V., Hohe Str. 6, 01069 Dresden, Germany*
3 *Department of Materials Science and Engineering, Saarland University, Campus D2 2, 66123 Saarbrücken Germany*
4 *Department of Inorganic Chemistry, Technische Universität Dresden, Bergstraße 66, 01062 Dresden, Germany*

Citation:
Choudhury, S.; Zeiger, M.; Massuti-Ballester, P.; Fleischmann, S.; Formanek, P.; Borchardt, L.; Presser, V., Carbon onion-sulfur hybrid cathodes for lithium-sulfur batteries. *Sustainable Energy & Fuels* **2017,** 1, 84-94. (DOI: 10.1039/C6SE00034G)

Own contribution: Design, planning, writing, carbon onion synthesis, Raman spectroscopy, transmission electron microscopy, thermogravimetric analysis.

Abstract:
In this study, we explore carbon onions (diameter below 10 nm), for the first time, as a substrate material for lithium sulfur cathodes. We introduce several scalable synthesis routes to fabricate carbon onion-sulfur hybrids by adopting in situ and melt diffusion strategies with sulfur fractions up to 68 mass%. The conducting skeleton of agglomerated carbon onions proved to be responsible for keeping active sulfur always in close vicinity to the conducting matrix. Therefore, the hybrids are found to be efficient cathodes for Li-S batteries, yielding 97-98% Coulombic efficiency over 150 cycles with a slow fading of the specific capacity (ca. 660 mA h g^{-1} after 150 cycles) in long term cycle test and rate capability experiments.

Volume 1 | Number 1 | March 2017 | Pages 1–218

Sustainable Energy & Fuels

Interdisciplinary research for the development of sustainable energy technologies

rsc.li/sustainable-energy

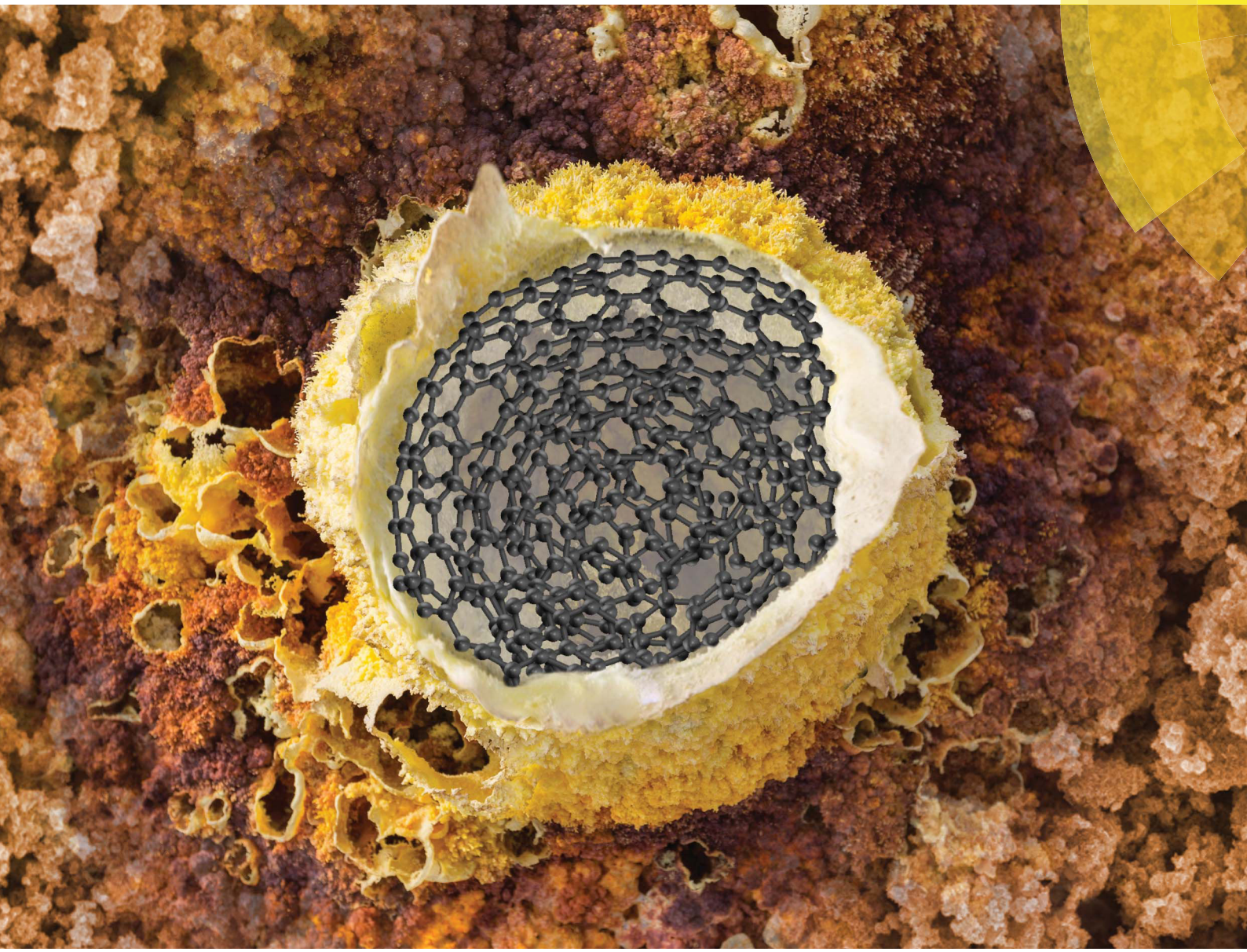

ISSN 2398-4902

ROYAL SOCIETY OF CHEMISTRY

PAPER

Volker Presser *et al.*

Carbon onion–sulfur hybrid cathodes for lithium–sulfur batteries

Sustainable Energy & Fuels

PAPER

View Article Online
View Journal | View Issue

Cite this: *Sustainable Energy Fuels*, 2017, **1**, 84

Carbon onion–sulfur hybrid cathodes for lithium–sulfur batteries†

Soumyadip Choudhury,[ab] Marco Zeiger,[ac] Pau Massuti-Ballester,[ac] Simon Fleischmann,[c] Petr Formanek,[b] Lars Borchardt[d] and Volker Presser*[ac]

Received 2nd November 2016
Accepted 3rd January 2017

DOI: 10.1039/c6se00034g

rsc.li/sustainable-energy

In this study, we explore carbon onions (diameter below 10 nm), for the first time, as a substrate material for lithium sulfur cathodes. We introduce several scalable synthesis routes to fabricate carbon onion–sulfur hybrids by adopting *in situ* and melt diffusion strategies with sulfur fractions up to 68 mass%. The conducting skeleton of agglomerated carbon onions proved to be responsible for keeping active sulfur always in close vicinity to the conducting matrix. Therefore, the hybrids are found to be efficient cathodes for Li–S batteries, yielding 97–98% Coulombic efficiency over 150 cycles with a slow fading of the specific capacity (*ca.* 660 mA h g^{-1} after 150 cycles) in long term cycle test and rate capability experiments.

1. Introduction

The increase in global energy demand and limited reserve of fossil fuel resources have led to intense research efforts for efficient and mobile energy storage technologies, especially rechargeable batteries.[1] The further implementation of current lithium-ion battery technology is impeded by high costs, safety concerns, and the limited energy density associated with state-of-the-art insertion-compound electrodes like layered $LiCoO_2$, spinel $LiMn_2O_4$, olivine $LiFePO_4$ cathodes, and graphite anodes.[2,3] The development of alternative low-cost, abundant electrode materials with high energy and power densities is crucial for widely employing rechargeable batteries for the storage of renewable energies and the transportation sectors.[4,5]

Lithium–sulfur (Li–S) systems have emerged in recent years as a promising battery class.[6–9] In addition to the high specific capacity, using sulfur as a cathode material has the advantages of high natural abundance, low cost, and high environmental friendliness.[7] Although the lithium–sulfur system operates at a relatively low average potential of 2.1 V against Li/Li^+, it shows a very high theoretical specific capacity of 1675 mA h g^{-1} and a high theoretical specific energy of 2600 W h kg^{-1}.[5,10] A remaining hindrance to reach the theoretical limit is the low sulfur utilization for Li–S rechargeable systems. Still, Li–S batteries suffer from the isolative behavior of the start (S_8) and end product (Li_2S), active material loss by dissolution of intermediate species (polysulfides) in the electrolyte, and shuttle mechanisms leading to anode passivation by the deposition of Li_2S_2 and Li_2S.[11,12]

Several studies have shown different carbons as a conductive substrate for insulating sulfur including a variety of carbons with a high surface area and conductivity. Among others, researchers have investigated multi-walled carbon nanotubes,[13–15] mesoporous carbon,[16] graphene,[14,17] carbide-derived carbon,[18] biomass derived carbon,[19,20] three-dimensional bicontinuous gyroidal carbon,[21,22] carbon from polyacrylonitrile,[23] activated carbon fiber cloth,[24] and hard[25] or soft templated carbons[26] as substrates for sulfur in lithium–sulfur batteries.

In this work, we explore carbon onions for lithium sulfur batteries. Carbon onions, also known as onion-like carbon (OLC), consist of several concentrically stacked graphitic carbon spheres.[27] A facile and scalable synthesis route for carbon onions is thermal annealing of nanodiamond powder in an inert atmosphere or vacuum.[28] During the annealing process at temperatures above 1300 °C, the sp^3-hybridized nanodiamond is progressively converted to quasi-spherical sp^2-carbon onions.[29] The high electrical conductivity of carbon onion aggregates (*ca.* 4 S cm^{-1}) provides a conductive network for sulfur, while the enhanced surface area (200–600 m^2 g^{-1}) and nanoscopic size (5–10 nm),[30] hierarchical porous structure, and possibility to create a mechanically robust electrode structure are attractive for creating a large sulfur/electrolyte interface, mitigating polysulfide shuttling. Our work compared different synthesis approaches for obtaining carbon onion/sulfur electrodes, provides structural and chemical characterization, and benchmarks the resulting electrochemical performance.

[a]*INM – Leibniz Institute for New Materials, Campus D2 2, 66123 Saarbrücken, Germany. E-mail: volker.presser@leibniz-inm.de*

[b]*Leibniz-Institut für Polymerforschung Dresden e.V., Hohe Str. 6, 01069 Dresden, Germany*

[c]*Department of Materials Science and Engineering, Saarland University, Campus D2 2, 66123 Saarbrücken, Germany*

[d]*Department of Inorganic Chemistry, Technische Universität Dresden, Bergstraße 66, 01062 Dresden, Germany*

† Electronic supplementary information (ESI) available. See DOI: 10.1039/c6se00034g

2. Experimental description

Materials

Nanodiamond powder was purchased from NaBond Technologies. Battery-grade conductive carbon black (C65) was purchased from Imerys. Sodium thiosulfate pentahydrate ($Na_2S_2O_3 \cdot 5H_2O$), elemental sulfur (S_8), polyvinylidene fluoride (PVDF) powder (molecular mass *ca.* 534 000 g mol^{-1}), *N*-methyl-2-pyrrolidone (NMP), bis(trifluoromethane)sulfonimide lithium salt (LiTFSI), 1,2-dimethoxyethane (DME), 1,3-dioxolane (DOL), and lithium nitrate ($LiNO_3$) were purchased from Sigma Aldrich, and used without any further purification. Nickel foil with a thickness of 20 μm was procured from Schlenk Metallfolien. Electrochemical grade high purity (99.9%) lithium was purchased from PI-Kem. A trilayer porous polyolefine separator was obtained from Celgard and we used non-woven polypropylene separators from Freudenberg.

Synthesis of carbon onions

Carbon onions were synthesized by thermal annealing of the detonation nanodiamond with a diameter in the range of 4–6 nm (NaBond Technologies). The nanodiamond powder was annealed in an argon atmosphere in a graphite crucible using a water cooled high temperature furnace with a tungsten heater (Thermal Technology) at 1700 °C for 1 h (heating/cooling rate: 20 °C min^{-1}). For more information, see ref. 28.

Preparation of carbon onion–sulfur composites

Herein, three different approaches were investigated (Fig. 1): (1) mechanical melt mixing of sulfur with carbon onions, (2) *in situ* formation of sulfur nanoparticles on the carbon surface, and (3) melting of the covering nanoparticles to form homogenous layers around the carbon onions. The melt mixing carbon onion–sulfur composite was prepared as follows: 65 mass% elemental sulfur (S_8) were added to 35 mass% of carbon onions. It was primarily mixed in a mortar, and afterwards ball milled to get nearly uniform distribution of the sulfur. The carbon–sulfur composite powder was thermally annealed at 155 °C for 5 h under an argon atmosphere. Using this treatment sulfur is fluid and attains minimum viscosity (ref. 16) so that uniform coverage of sulfur over all the available surface of carbon onion particles was obtained.

For *in situ* formation of sulfur nanoparticles on the carbon onion surface, 1.55 g of sodium thiosulfate was first dissolved in 40 mL of water. Afterwards, 100 mg of carbon onions was added with subsequent sonication for 30 min under ice-cold water. In the next step, 2.5 mL of 5 M HCl was added dropwise to the system. By this time, sulfur nanoparticles were formed in the mixture. The mixture was left to react for 2 h and was filtered through a 0.2 μm hydrophilic PVDF filter. It was washed with copious amounts of water until pH 7 was achieved. The carbon onion/sulfur mixture was dried at 80 °C under vacuum for 12 h.

For the third OLC-S hybrid, the carbon onions/sulfur nanoparticle mixture was thermally annealed at 155 °C following the same protocol maintained for the first set of samples.

For comparison, electrodes of the same thickness were made with sulfur nanoparticles along with 10 mass% conductive additive (Super C65) and 8 mass% PVDF binder. The slurry was cast onto nickel foil following the same way as done for carbon onion/sulfur hybrids. This electrode is designated as SNP (sulfur nanoparticle) electrode.

Electrode preparation

The three sets of carbon–sulfur composite powders were individually mixed with 8 mass% of PVDF binder in NMP to attain the desired slurry viscosity. The slurry was cast on a nickel current collector, achieving a 300 μm wet electrode thickness, and afterwards dried in an oven operated under vacuum at 60 °C for 12 h to get rid of any traces of solvent. In the dry state, each electrode has a mass loading of 3–4 mg cm^{-2} (corresponding sulfur loading is 2–3 mg cm^{-2}) which is at the level to attain the required areal capacity desired for applications in electrically driven vehicles.[31]

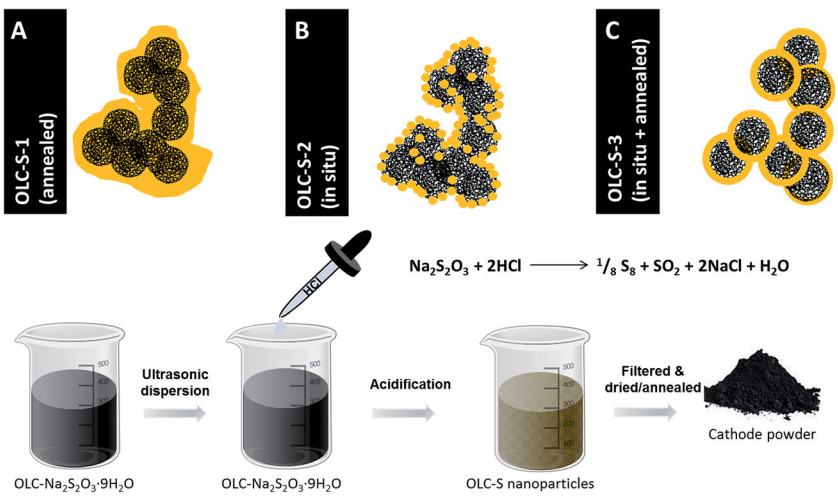

Fig. 1 Schematic representation of fabrication of OLC-S hybrids following three different approaches.

Conductivity measurements

The same slurries for each set of samples for preparing electrodes were again cast over 50 μm thin polyimide foil for conductivity measurements. Sheet resistance measurements were made with a custom-built spring-loaded four-point probe with blunt gold contacts (tip diameter: 1.5 mm, tip distance: 3 mm).

Raman spectroscopy

Raman spectra were recorded with a Renishaw inVia Raman Microscope employing an Nd:YAG laser with an excitation wavelength of 532 nm or HeNe laser operating at 633 nm. A grating with 2400 lines per mm and a 50× objective were used to reach a spectral resolution of about 1.2 cm^{-1}. The laser spot on the sample was about 2 μm in diameter at a power of 0.2 mW. The acquisition time of each spectrum was 30 s, and 10 accumulations were averaged.

X-ray diffraction

The crystalline structure of the carbon–sulfur hybrids was analyzed by X-ray diffraction employing a D8 Advance diffractometer (Bruker AXS) with a copper X-ray source ($Cu_{K\alpha}$, 40 kV, 40 mA), a Göbel mirror, and a 2D area detector (VANTEC-500) that covers about 25° 2θ. All samples were measured in a range from 10 to 60° 2θ in 3 steps, with a step duration of 24 min.

Gas sorption measurements

Porosity analysis was carried out using an Autosorb iQ nitrogen gas sorption system (Quantachrome). The carbon onion powder was first outgassed at 300 °C for 10 h under vacuum (10^2 Pa). The nitrogen gas sorption analysis was performed at a temperature of −196 °C in the relative pressure range from 5×10^{-7} to 1.0 in 68 steps. The pore size distribution (PSD) was calculated using the quenched-solid density functional theory (QSDFT)[32,33] supplied by Quantachrome assuming a slit-shape pore geometry. The BET SSA after Brunauer–Emmett–Teller[34] was calculated in the linear regime of the measured isotherms between 0.1 and 0.3P/P_0. Carbon onion sulfur hybrids were not measured using gas sorption analysis due to the evaporation of sulfur and the possible contamination of the system.

Thermogravimetric analysis

To estimate the loading of sulfur in each carbon–sulfur hybrid, thermogravimetric analysis (TGA) was adopted. As sulfur sublimes when heated to 500 °C, TGA of the carbon–sulfur hybrids was performed using a Netzsch Libra TG 209 F1 in the temperature range of 30–500 °C with a heating rate of 10 °C min^{-1} under continuous flow of argon.

CHNS elemental analysis

The chemical composition was further investigated with CHNS elemental analysis with a Vario Micro Cube system (Elementar Analysensysteme). After combustion, the samples were measured under oxygen at 1150 °C in a tin holder. The CHNS analyzer was calibrated with sulfanilic acid using different masses (41.6 mass% C, 4.1 mass% H, 8.1 mass% N, 18.5 mass% S).

Energy filtered transmission electron microscopy

The specimen was prepared by dispersing the powders in ethanol followed by placing a drop on a lacey carbon film TEM grid (Plano GmbH). The TEM grid was dried at 50 °C to remove traces of ethanol before inserting into the TEM instrument. Transmission electron micrographs were recorded with a JEOL 2100F microscope at 200 kV. Energy filtered imaging (EFTEM) was conducted on a Libra 120 transmission electron microscope (Carl Zeiss) operated at 120 keV.

Electrochemical benchmarking

The coin-cell type cathodes were cut as discs of 14.2 mm diameter from the entire piece and 2032 coin cells were assembled in an argon filled glovebox (O_2 & H_2O: <1 ppm) with carbon onion/sulfur hybrid cathodes, lithium metal discs as the anode, and a porous trilayer PP–PE–PP membrane from Celgard and Freudenberg non-woven PP mat together as the separator (PP = polypropylene; PE = polyethylene). Each electrode has a sulfur loading of *ca.* 60 mass% (excluding binder). The separators were soaked with 100 μL of 1 M LiTFSI in 1 : 1 (by volume; v/v) 1,2-dimethoxyethane (DME) and 1,3-dioxolane (DOL) along with 0.25 M $LiNO_3$ serving as the electrolyte. Cyclic voltammetry was performed with a Biologic VPM-300 potentiostat–galvanostat within the potential range of 1 V to 3 V *versus* Li/Li^+ at a scan rate of 100 μV s^{-1} (equivalent to 0.2C). Galvanostatic charge/discharge tests were carried out with an Astrol BatSmall battery analyzer at a constant current density of 336 mA g^{-1} (=0.2C) for charging and 168 mA g^{-1} (=0.1C) for discharging within the potential window of 1.8 V to 2.6 V *versus* Li/Li^+. The rate capability experiments were done at different rates from 0.1C (discharge)/0.2C (charge) for 20 cycles, 0.2C (discharge)/0.4C (charge) for the next 10 cycles, 0.5C (discharge)/1C (charge) for further 10 cycles, 1C (discharge)/2C (charge) and then brought back to 0.1C (discharge)/0.2C (charge), and allowed to run for the next 20 charging–discharging cycles. For high rate cycle stability tests, the carbon onion hybrid cathode containing cells were subjected to discharge at 1C and charged at 2C for 500 cycles. In all our galvanostatic charge–discharge experiments, we set the charging rate at two times the discharge rate to simulate the actual usage of battery where a faster charging is required.[21]

3. Results and discussion

Carbon onions (OLC) were synthesized by thermal annealing of nanodiamonds (ND) at 1700 °C in argon.[29,30] Using these conditions, ND particles with a mean size of ~5 nm completely transform to sp^2-hybridized carbon onions. During this process, the diamond structure with a lattice spacing of 0.21 nm rearranges to a graphitic multi-shell carbon onion with an outer lattice spacing of 0.34 nm (Fig. S1, ESI†). Between the single carbon onions with a diameter between 5 and 10 nm, we also

see few-layer graphene nanoribbons as a result of the annealing process (Fig. S1, ESI†).[28]

Carbon onion/sulfur (OLC-S) hybrids were synthesized using three different approaches, as described in the Experimental section. The overall distribution of sulfur on the carbon onion surface and in the interparticle voids was surveyed with energy filtered transmission electron microscopy (EFTEM). The sulfur signal was confirmed by comparing energy filtered images below (153 eV) and above (200 eV) the sulfur ionization edge (165 eV). As seen from Fig. 2B, the *in situ* deposition of sulfur on OLC (OLC-S-2) shows the most uniform sulfur distribution, whereas the melt-mixing (OLC-S-1) leads to a larger degree of localized sulfur clustering (Fig. 2A). Further annealing of *in situ* deposited sulfur on OLC (OLC-S-3) resulted in a low degree of sulfur clustering. Carbon onions act as nucleating surfaces for sulfur nanoparticle deposition, whereas the melt diffusion strategy results in non-uniform spreading of molten sulfur in a random manner. However, the *in situ* sulfur nanoparticle deposition on carbon onion surfaces followed by thermal annealing leads to a low extent of sulfur clustering compared to the mechanical melt mixing pathway, as evident from the carbon–sulfur colored overlay images (Fig. 2C).

The nitrogen gas sorption measurement of carbon onions shows a surface area of 425 $m^2 g^{-1}$ (BET) and 402 $m^2 g^{-1}$ (DFT) with a pore volume of 1.21 $cm^3 g^{-1}$. The pore size distribution pattern can be differentiated into three regimes: pores related to particles in direct contact (for pores <1 nm), particles separated by spacer particles (at 1 nm pore size and in the mesopore range), and pores between particle agglomerates (Fig. 3A). These spaces among the particle interstices were utilized to embed insulating sulfur to attain a high degree of intimate contact with the carbon onion surfaces. Additionally, the pore hierarchy also plays a crucial role in functioning of lithium–sulfur batteries by accommodating a large quantity of sulfur mass as well as electrolyte wetting together with lowering the tendency of polysulfide migration out of the cathode to the bulk electrolyte.[15,35–39]

Thermogravimetric analysis of pristine carbon onions undergoes a very little mass loss of *ca.* 1% up to 500 °C. This mass loss is attributed to the decomposition of functional groups on the surface of carbon onions. The thermogravimetric measurements of OLC-S hybrids demonstrate one step mass loss at around 300 °C for all samples with a mass loss of 68% OLC-S-1 and 65% for OLC-S-2 and OLC-S-3 (Fig. 3B). The respective mass loss corresponds to the sulfur content from CHNS elemental analysis (Table 1). The absence of any other step in the thermogram indicates that sulfur is only coated onto the carbon onions and does not penetrate the inside of the particles, irrespective of the deposition process. For contrast, hierarchical porous carbons exhibit more than one step of mass loss during thermogravimetry.[40,41] It is reported in the literature that the sulfur confined in micropores requires a higher thermal energy and is released at much higher temperature than the sulfur present outside the micropores.[40,41]

The structure of carbon onions was not changed by the synthesis procedures as indicated by Raman spectroscopy (Fig. 3C, Table 2, and Fig. S2, ESI†) and XRD (Fig. 3D). Independent of the treatment, carbon onions are characterized by their typical Raman spectrum with the carbon D-mode at 1338 cm^{-1}, the G-mode at 1577 cm^{-1}, and a distinct second order spectrum (Fig. S2, ESI†). The G-mode, representative for sp^2-hybridized carbon, is measured at 1577 cm^{-1}, indicating nanocrystalline and partially amorphous carbon. Amorphous carbon is mostly located between the particles (Fig. S1B, ESI†), leading to partially connected particles and a strong degree of agglomeration. Carbon onions present a rather high degree of

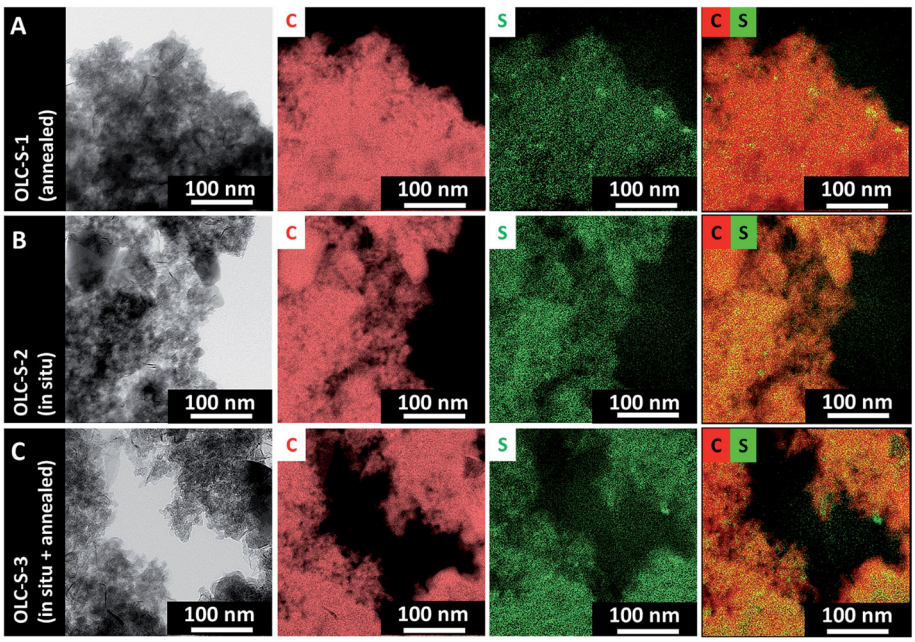

Fig. 2 (A–C) Energy filtered transmission electron micrographs of carbon onion/sulfur hybrid materials, their corresponding elemental maps, and the overlay of carbon and sulfur elemental mappings.

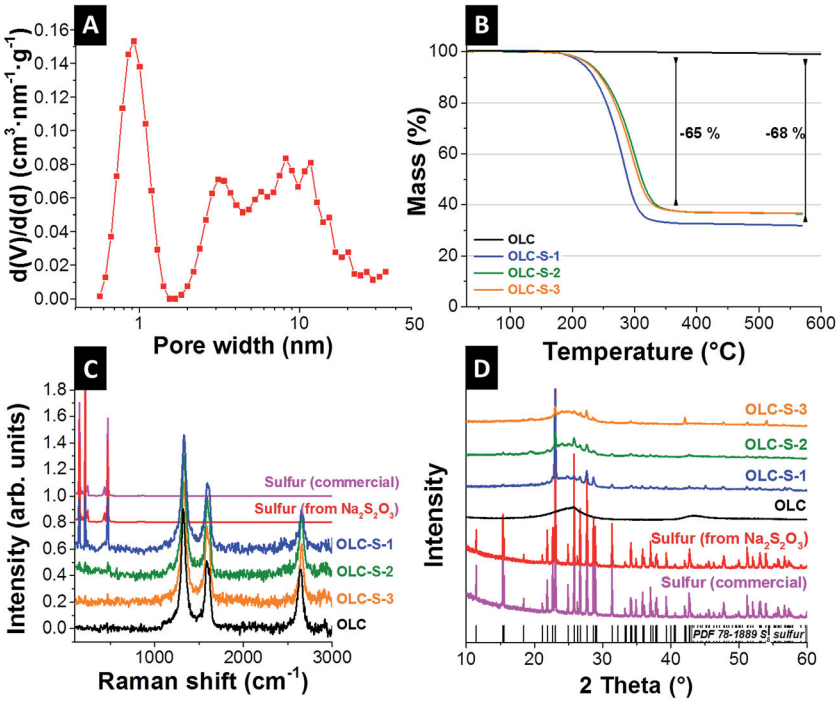

Fig. 3 (A) Pore size distribution of OLC calculated from QSDFT assuming slit pores, (B) sulfur contents from TGA, (C) Raman spectra (633 nm excitation wavelength) and (D) X-ray diffractograms of carbon onions and carbon onion/sulfur hybrids.

Table 1 Estimation of sulfur contents from TGA and CHNS elemental analysis

	Sulfur (mass%)	
Sample	TGA	CHNS
OLC-S-1	68	68 ± 1
OLC-S-2	65	62 ± 5
OLC-S-3	65	64 ± 1

ordering as demonstrated by the sharp G-mode (FWHM of 44 cm^{-1}) and the distinct second order peaks at 2675 cm^{-1}. By virtue of the instability under laser irradiation, we did not detect any sulfur when using a laser wavelength of 532 nm. To avoid such degradation, we conducted also experiments at 633 nm excitation wavelength (Fig. 3C). Commercial sulfur and sulfur derived from sodium thiosulfate were also characterized by Raman spectroscopy. Sulfur shows three distinct peaks at 156, 219, and 473 cm^{-1}, which are related to the vibrations of the S–S bonds.[14,19,42] When measuring the OLC-S hybrids by Raman spectroscopy, OLC-S-2 and OLC-S-3 showed very weak sulfur signals, whereas OLC-S-1 demonstrated very clearly all three characteristic sulfur peaks. This indicates the presence of non-uniform distributions of sulfur onto the carbon onion surfaces whereas the two other hybrids claim to have nearly homogeneous coverage of sulfur on OLC. As a result, the Raman signals from carbon predominate over sulfur signals although all three hybrids contain *ca.* 65 mass% of sulfur (relative to the carbon mass).

The incompletely crystalline structure of carbon onions was further assessed by XRD (Fig. 3D). The broadening of the (002) graphitic carbon peak at ~26° 2θ is a consequence of the nanoscopic carbon particle size of 5–7 nm. In all three OLC-S hybrids, all crystalline peaks of sulfur are detected in alignment with PDF 78-1889. This confirms the growth of crystalline sulfur domains on the carbon onion substrates and ensures the allocation of sulfur in interparticle voids. When carbon with a large inner porosity is used as the host for sulfur, molten sulfur or nanoparticle precursor solutions tend to infiltrate into the pores driven by capillary forces.[16,24] In such a case, the imbibed sulfur in the pores does not display the well-resolved crystalline

Table 2 Raman spectroscopy results of OLC and OLC-S hybrids

Sample	Position D-band (cm^{-1})	Position G-band (cm^{-1})	FWHM D-band (cm^{-1})	FWHM G-band (cm^{-1})	I_D/I_G
OLC	1338	1580	57	44	1.43
OLC-S-1	1339	1579	67	48	1.79
OLC-S-2	1339	1577	62	46	1.70
OLC-S-3	1338	1576	62	48	1.69

peaks.[16,24] In the OLC-S hybrids, sulfur remains at the exterior surfaces of OLC particles. For this reason, no significant differences were visible in the XRD pattern of three different hybrid types.

The usefulness of the carbon onions as a host for embedding sulfur was further tested by sheet resistance measurements of the 80–100 μm (dry) thick electrodes coated on polyimide foil (Table 3). Using a four-point-probe, the measured electrical conductivity of all samples showed little difference, with values around 0.2 S cm^{-1}.

Electrochemical characterization including cyclic voltammetry (three-electrode setup) and galvanostatic charge–discharge measurements (two-electrode setup) was performed by using the OLC-S composite electrode as the working electrode (cathode) and lithium as the counter electrode (anode) and reference electrode. The cyclic voltammograms show the characteristic shape of sulfur oxidation and reduction (Fig. 4A, C and E). During discharge, the characteristic two reduction peaks at around 2.4 V and 2.0 V *vs.* Li appear (Fig. 4A, C and E). These peaks correspond to the ring opening reduction of sulfur to Li_2S_n ($n > 4$) and the subsequent reduction of higher order polysulfides to short chain polysulfide species, respectively.[43] The anodic sweep shows a characteristic single peak at around 2.4 V *vs.* Li. The relatively narrow peaks for OLC-S-2 and stable peak positions for oxidation and reduction indicate good reaction kinetics for reduction and oxidation reactions in the first cycle and run in a comparable range for all cycles. The two other hybrids OLC-S-1 and OLC-S-3 have much broader oxidation and reduction peaks which are indicative of relatively slow and inferior reaction kinetics compared to OLC-S-2. Such broadening of redox peaks arises from uneven distribution of sulfur in the OLC matrix. Thus, the reaction steps are overlapping and yield broader redox peaks, which indicate poor performances such as low energy efficiency and slow kinetics. The poorer performance can be related to larger amounts of inactive sulfur insufficiently connected to the conductive carbon onion substrate. In the case of OLC-S-3, due to the thermal treatment after nanoparticle formation, the molten sulfur moves to some extent from the surface and reorganizes as larger sulfur

Table 3 Conductivity measurements *via* the four-point-probe of OLC-S hybrids

Sample	Conductivity (S cm^{-1})
OLC-S-1 electrode	19.8×10^{-2}
OLC-S-2 electrode	23.3×10^{-2}
OLC-S-3 electrode	20.8×10^{-2}

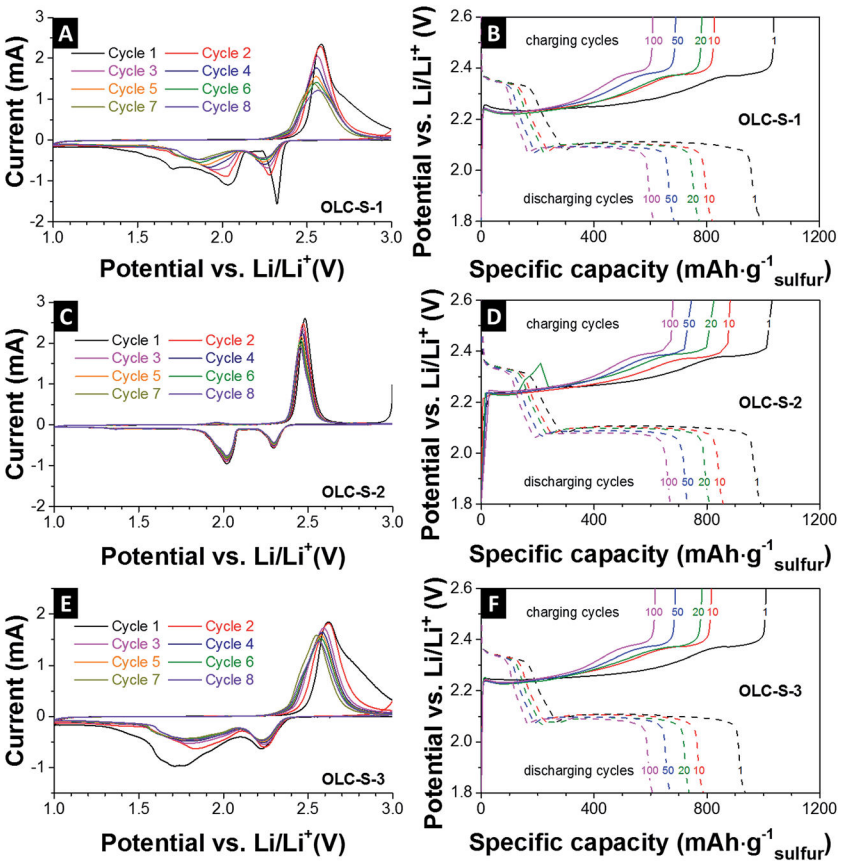

Fig. 4 Cyclic voltammograms at a rate of 0.1 mV s^{-1} and galvanostatic charge–discharge curves at 336 mA g^{-1} (0.2C) for charging and 168 mA g^{-1} (0.1C) for discharging within the potential window of 1.8 V to 2.6 V *versus* Li/Li^+ of (A and B) OLC-S-1, (C and D) OLC-S-2, and (E and F) OLC-S-3.

particles, which are not ideally covering the carbon onion surfaces anymore. Those agglomerated parts remain electrochemically inactive, thus demonstrating poorer performance compared to OLC-S-2.

The reversible galvanostatic charge–discharge tests of the OLC-S hybrids were carried out in 2032 coin cells at 0.1C discharge rate (167 mA g^{-1}) and 0.2C charging rate (334 mA g^{-1}). The plateaus in the voltage profiles (Fig. 4B, D and F) match the peak voltages of the cyclic voltammograms for reduction and oxidation (Fig. 4A, C and E). We identify two plateaus in the discharge process, as summarized by Ji *et al.* (ref. 16):

- The first one contributes a minor part to the overall capacity from 2.4 V to *ca.* 2.1 V *vs.* Li. This plateau corresponds to the ring opening conversion of elemental sulfur (S_8) to Li polysulfide anions (Li_2S_x; where x is typically 4–5).[6,7,11] The kinetics of this step are fast.
- The second plateau appears at around 2.1 V *vs.* Li due to the conversion reaction of higher order polysulfides to Li_2S_2 and then to Li_2S. This reaction occurs at a much slower rate and contributes to the large fraction of the overall capacity.

The similarity of voltage profiles at different cycles is indicative of slower capacity fading with prolonged cycling. Additionally, the voltage plateaus of all samples that appear at the same potential during discharge and charge reflect the mitigation of active mass loss per charging–discharging cycles.

The corresponding specific capacities for charging and discharging are represented normalized to the sulfur mass (Fig. 5A). The specific capacities of all hybrids present values of 900–1200 mA h g_{sulfur}^{-1} in the initial cycles (up to 5 cycles). After 10 charge–discharge cycles, OLC-S-2 and OLC-S-3 hybrids showed only a slow capacity fading per cycles. The capacity stabilized at 800 mA h g_{sulfur}^{-1} and 600 mA h g_{sulfur}^{-1} up to 150 charging–discharging cycles for OLC-S-2 and OLC-S-3 hybrids, respectively. Cathodes containing carbon onions/sulfur hybrids, where the melt diffusion route was followed, demonstrated severe capacity fading within 50 cycles and remained with only 400 mA h g_{sulfur}^{-1} at the end of 150 cycles of charge–discharge. The electrode prepared from sulfur nanoparticles (SNPs) with 10 mass% conductive additive showed a low specific capacity in the initial cycles. After 20 cycles, the specific capacity was stabilized at 200 mA h g_{sulfur}^{-1} for the following 150 cycles. The relatively low specific capacity values are because of an insufficient amount of conducting carbon with a high surface area around the sulfur nanoparticles.

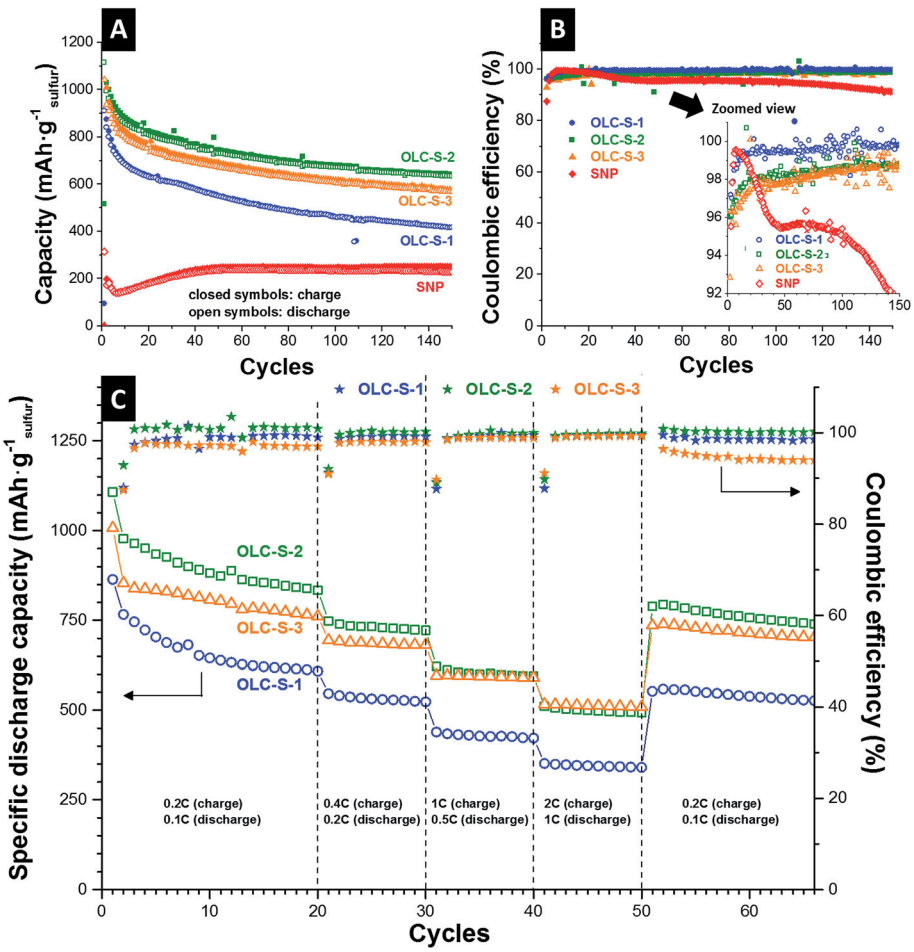

Fig. 5 Cycling performance (0.2C charge, 0.1C discharge) for the (A) specific capacity and (B) Coulombic efficiency (inset shows the zoomed range of 92–100%). (C) Rate capability study of the carbon onion/sulfur hybrid and sulfur nanoparticle (SNP) cathodes.

Table 4 Reported values for selected carbon/sulfur electrodes in comparison to this work. In all reports, metallic Li was used as the anode. Used abbreviations: PC = propylene carbonate; EC = ethyl carbonate; DEC = diethyl carbonate; DME = dimethoxyethane; DOL = 1,3-dioxolane; LiTFSI = Li salt of bis(trifluoromethanesulfonyl)imide; PEGDME = polyethylene glycol dimethyl ether; PYR_{14} = 1-butyl-1-methylpyrrolidinium; TEGDME = tetraethylene glycol dimethyl ether; (w = mass; v = volume)

Carbon for cathode	Surface area ($m^2\ g^{-1}$)	Sulfur loading (mg cm^{-2})	Separator	Electrolyte	Specific capacity (mA h g_{sulfur}^{-1})			Potential window	C-Rate	Ref.
					Cycle 5	Cycle 50	Cycle 100			
This work	*ca.* 400	2–3	Polyolefin separators	1 M LiTFSI in 1 : 1 (v/v) DME/DOL + 0.25 M $LiNO_3$	*ca.* 950 (OLC-2)	*ca.* 730 (OLC-2)	*ca.* 670 (OLC-2)	1.8–2.6 V	0.1C (discharge), 0.2C (charge)	—
Acetylene black	*ca.* 65	1.5	Polypropylene separator	1 M $LiPF_6$ PC/EC/DEC 1 : 4 : 5 (v/v)	*ca.* 600	*ca.* 500	—	1.8–2.8 V	0.02C	45
Ketjen black	*ca.* 800	0.81	Unknown	0.5 M $LiSO_3CF_3$ in 8 : 2 (v/v) DME/DOL + imidazolium salts	*ca.* 770	*ca.* 700	*ca.* 600	1.8–2.8 V	0.5C	46
Multi-walled carbon nanotube	*ca.* 107	Unknown	Celgard	0.5 M LiTFSI in 1 : 1 (v/v) DME/DOL + 0.5 M $LiNO_3$	*ca.* 1100	*ca.* 1000	*ca.* 950	1.7–2.7 V	0.18C	35
Vertically aligned CNTs	—	Unknown	Celgard and glass fiber mat	1 M LiTFSI in 1 : 1 (v/v) DME/DOL + 0.25 M $LiNO_3$	*ca.* 850	*ca.* 750 (cycle 40)	—	1–3 V	0.08C	47
Small CNTs confined inside a large CNT	*ca.* 150	1.36	Unknown	1 M LiTFSI in 1 : 1 (v/v) DME/DOL	*ca.* 1250	*ca.* 1100	*ca.* 1000	1.5–3 V	0.1C	43
Carbon aerogel	*ca.* 1395	Unknown	Polypropylene separator	1 M LiTFSI in 1 : 1 (v/v) DME/DOL + 0.1 M $LiNO_3$	*ca.* 790	*ca.* 650	*ca.* 600	1.8–2.8 V	0.1C	40
Ordered mesoporous carbon	2445	0.45	Not mentioned	1 M LiTFSI in 1 : 1 (v/v) DME/DOL	*ca.* 1000	*ca.* 900	*ca.* 800	1.5–3 V	1C	48
Ordered mesoporous carbon (KOH activated)	*ca.* 1566	0.25	Celgard	1 M LiTFSI in 55 : 40 (v/v) DME/DOL	*ca.* 500 (51.5% S)	*ca.* 300	—	1–3.6 V	1.5C	37
Sulphur–TiO_2 yolk–shell	—	0.4–0.6	Unknown	1 M LiTFSI in 1 : 1 (v/v) DME/DOL + 0.14 M $LiNO_3$	*ca.* 1000	*ca.* 800	*ca.* 900	1.7–2.6 V	0.5C	49
Hydrothermal carbon from monosaccharides	*ca.* 300		Unknown	1 M LiTFSI in 1 : 1 (v/v) DME/DOL	*ca.* 780	*ca.* 580	—	1.5–3.2 V	1C	50
Reduced graphene oxide	—	Unknown	Celgard	LiTFSI in PYR_{14}TFSI/PEGDME (1 : 1 w/w)	*ca.* 900	*ca.* 900	—	1–3 V	0.02C (3 cycles) then 0.1C for 47 cycles	51
Graphene-enveloped sulfur	—	Unknown	Unknown	1 M LiTFSI in TEGDME	*ca.* 690	*ca.* 520	—	1.5–3 V	0.2C	17
Nafion coated sandwich type graphene sheets	*ca.* 578	Unknown	Celgard	1 M LiTFSI in 1 : 1 (v/v) DME/DOL	*ca.* 950	*ca.* 800	—	1–3 V	0.1C	52
Activated carbon fiber cloth	2000	6.5	Celgard	0.35 M LiTFSI in 1 : 1 (v/v) DME/DOL + 0.29 M $LiNO_3$	*ca.* 1000	*ca.* 950	—	1.7–2.5 V	0.09C	24
Inverse opal carbon	*ca.* 1300	2–3	Polyolefin separator	1 M LiTFSI in 1 : 1 (v/v) DME/DOL + 0.25 M $LiNO_3$	*ca.* 1650	*ca.* 400	—	1.5–2.8 V	0.1C	26
3D gyroidal carbon	*ca.* 900	2–3	Polyolefin separator	1 M LiTFSI in 1 : 1 (v/v) DME/DOL	*ca.* 650	*ca.* 600	*ca.* 520	1.5–2.8 V	0.1C (discharge), 0.2C (charge)	21
3D gyroidal carbon (activated)	*ca.* 2000	0.8	Celgard	1 M LiTFSI in TEGDME + 0.15 M $LiNO_3$	*ca.* 1100	*ca.* 1000	*ca.* 830	1.5–2.8 V	0.1C	22

Additionally, a comparison of specific capacities from the literature with different types of carbon substrates can be found in Table 4.

The capacity loss in the initial cycles can be attributed to the irreversible diffusion of polysulfides possibly from the dissociative sulfur on the surface of OLC particles. This irreversible reaction leads to slightly lower Coulombic efficiency close to 97–99% in reversible (Fig. 5B) or irreversible mode (Fig. 5C). For comparison, the SNP electrodes demonstrated a Coulombic efficiency below 95% after 30 cycles and after 100 cycles, the Coulombic efficiency dropped below 90%. This behavior can be explained by a lack of structural integrity and loss of electrical connectivity between the additive and sulfur nanoparticles. The relatively high specific capacity in the beginning and the slow capacity fading of OLC-S hybrids can be attributed to the benefits of the enhanced surface area of carbon onions and the accessible interparticle space. The interconnecting feature of carbon onion agglomerates provides a high electrical conductivity and is beneficial to ensure accessibility of the active material by the electrolyte and the Li^+ ions with prolonged cycling.

The rate capability tests of the carbon onion–sulfur hybrids were carried out in 2032 coin cells at multiple C-rates (Fig. 5C). The respective charge and discharge protocol is explained in the experimental part. After 20 cycles at a low rate (0.2C charge and 0.1C discharge) and 30 cycles at a high rate (up to 2C charge and 1C discharge) the specific capacity was recovered close to the level of the initial 20th cycles after multiple irreversible charging–discharging fluctuations. From the irreversible capacity retention ability, it can be concluded that the carbon onion–sulfur composite nanostructures were not ruptured and the sulfur distribution was restored even after such stringent charging–discharging conditions.

Finally, we investigated the long-term cycle performance of the OLC-S hybrids at very high C-rates, for instance, 2C (equivalent to 3350 mA g^{-1} with respect to sulfur) for charging and 1C (equivalent to 1675 mA g^{-1} with respect to sulfur) for discharging (Fig. 6). Among all three OLC-S hybrids, the onion-like carbon hybrid fabricated by the *in situ* routine followed by thermal annealing demonstrated an initial specific discharge capacity of 800 mA h g^{-1}. After 25 cycles, the battery showed a very high stability over 500 cycles with a slow rate of capacity fading (Fig. 6). For the latter, we measured a remaining capacity of 400 mA h g^{-1} after 500 cycles. The other *in situ* hybrid (*i.e.*, without annealing) followed a similar trend, yielding 300 mA h g^{-1} after 500 cycles. The OLC-S hybrid fabricated *via* the melt diffusion strategy had been showing poorest performances amongst all three hybrids due to random distribution of sulfur in the hybrid. The better performance of the OLC-S-3 at higher rates relative to other hybrids was also observed in rate capability experiments (Fig. 5C). The slower capacity fading at such high specific currents is mainly ascribed to the excellent electrical conductivity of the OLC-S hybrids, which are capable of satisfying the requirement for such fast discharge and charge during repetitive cycling.[41,43] We attribute the better performance at higher charge/discharge rates of OLC-S-3 to the much more integrated hybrid nanostructure by melting of the *in situ* deposited sulfur on the surface of OLC. Our findings are also in good agreement with the published reports by Nazar *et al.* performed at high C rates (cut-off voltage limit 1.5–3 V *vs.* Li/Li^+) exploiting bimodal porous carbon possessing over 2000 m^2 g^{-1} surface area.[44]

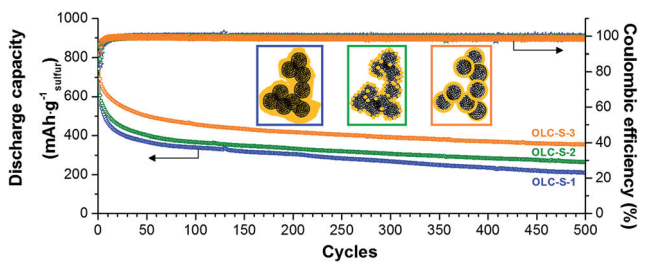

Fig. 6 Long term cycle stability at high C-rates (charging at 2C/discharging at 1C) study of the carbon onion/sulfur hybrids.

4. Conclusions

Our work introduces carbon onions for the fabrication of carbon/sulfur hybrid cathodes for lithium–sulfur batteries with sulfur loading up to 68 mass% and without any further addition of a conducting aid such as carbon black. Three different approaches were explored: (1) melt diffusion, (2) *in situ* generation of sulfur nanoparticles on the surface of onion-like carbon, and (3) *in situ* generation of sulfur nanoparticles on the surface of onion-like carbon followed by thermal annealing.

The electrochemical performance of these hybrid materials has been tested by electrochemical characterization. Carbon onion–sulfur hybrids prepared *via* the *in situ* approach (OLC-S-2 and OLC-S-3) had an optimum interaction between the hybrid components exhibiting a specific capacity of *ca.* 700 mA h g^{-1} even after 150 charge–discharge cycles at 167 mA g^{-1} specific current (corresponds to 0.1C discharge rate). In addition, the capacity restoration ability of OLC-S *in situ* hybrids right after running with a high current density of 1675 mA g^{-1} (corresponds to 1C discharge rate) demonstrated a specific capacity of 740 mA h g^{-1} close to its earlier capacity at 0.1C rate (800 mA h g^{-1}) when the current density was reduced to 167 mA g^{-1} (corresponds to 0.1C discharge rate). This hybrid material showed enhanced performance compared to the other OLC-S hybrids studied at slow discharge rates. In addition, these hybrids demonstrate good cycle performances operated with very high C-rates (1C for discharge and 2C for charge). Amongst them, the hybrid fabricated *via in situ* generation of sulfur nanoparticles on the surface of onion-like carbon followed by thermal annealing (OLC-S-3) has been found to be superior (800 mA h g^{-1} at cycle 1, 600 mA h g^{-1} at cycle 20, and 400 mA h g^{-1} at cycle 500).

The high electrochemical stability and attractive rate handling can be attributed to carbon onion aggregates which contribute a high electronic conductivity and provide an exclusively outer surface, which enables the synergy of high sulfur mass loading and high percentage of electrochemically active sulfur.

Acknowledgements

V. P., S. C., and M. Z. gratefully acknowledge funding from the German Federal Ministry for Research and Education (BMBF) in support of the nanoEES^{3D} project (award number 03EK3013) and L. B. in support of the Mechanocarb project (award number 03SF0498), both as part of the strategic funding initiative energy storage framework. This work was supported by the CREATe-Network Project, Horizon 2020 of the European Commission (RISE Project No. 644013). The authors thank Prof. Eduard Arzt (INM) for his continuing support.

References

1 B. Dunn, H. Kamath and J.-M. Tarascon, *Science*, 2011, **334**, 928–935.
2 P. G. Bruce, B. Scrosati and J. M. Tarascon, *Angew. Chem., Int. Ed.*, 2008, **47**, 2930–2946.
3 C. M. Hayner, X. Zhao and H. H. Kung, *Annu. Rev. Chem. Biomol. Eng.*, 2012, **3**, 445–471.
4 J. M. Tarascon and M. Armand, *Nature*, 2001, **414**, 359–367.
5 M. M. Thackeray, C. Wolverton and E. D. Isaacs, *Energy Environ. Sci.*, 2012, **5**, 7854–7863.
6 A. Manthiram, S. H. Chung and C. Zu, *Adv. Mater.*, 2015, **27**, 1980–2006.
7 L. Borchardt, M. Oschatz and S. Kaskel, *Chem.–Eur. J.*, 2016, **22**, 7324–7351.
8 G.-L. Xu, Y.-F. Xu, J.-C. Fang, X.-X. Peng, F. Fu, L. Huang, J.-T. Li and S.-G. Sun, *ACS Appl. Mater. Interfaces*, 2013, **5**, 10782–10793.
9 J. Tang, J. Yang and X. Zhou, *RSC Adv.*, 2013, **3**, 16936–16939.
10 M. Wild, L. O'Neill, T. Zhang, R. Purkayastha, G. Minton, M. Marinescu and G. J. Offer, *Energy Environ. Sci.*, 2015, **8**, 3477–3494.
11 M. K. Song, E. J. Cairns and Y. Zhang, *Nanoscale*, 2013, **5**, 2186–2204.
12 X. Ji and L. F. Nazar, *J. Mater. Chem.*, 2010, **20**, 9821–9826.
13 Y.-S. Su, Y. Fu and A. Manthiram, *Phys. Chem. Chem. Phys.*, 2012, **14**, 14495–14499.
14 J. Guo, Y. Xu and C. Wang, *Nano Lett.*, 2011, **11**, 4288–4294.
15 K. Mi, Y. Jiang, J. K. Feng, Y. T. Qian and S. L. Xiong, *Adv. Funct. Mater.*, 2016, **26**, 1571–1579.
16 X. Ji, K. T. Lee and L. F. Nazar, *Nat. Mater.*, 2009, **8**, 500–506.
17 S. Evers and L. F. Nazar, *Chem. Commun.*, 2012, **48**, 1233–1235.
18 T. J. Lee, Y. Zhao, S. Thieme, H. Kim, M. Oschatz, L. Borchardt, A. Magasinski, W. I. Cho, S. Kaskel and G. Yushin, *Adv. Mater.*, 2013, **25**, 4573–4579.
19 F. Chen, J. Yang, T. Bai, B. Long and X. Zhou, *Electrochim. Acta*, 2016, **192**, 99–109.
20 M. Raja, N. Angulakshmi and A. M. Stephan, *RSC Adv.*, 2016, **6**, 13772–13779.
21 S. Choudhury, M. Agrawal, P. Formanek, D. Jehnichen, D. Fischer, B. Krause, V. Albrecht, M. Stamm and L. Ionov, *ACS Nano*, 2015, **9**, 6147–6157.
22 J. G. Werner, S. S. Johnson, V. Vijay and U. Wiesner, *Chem. Mater.*, 2015, **27**, 3349–3357.
23 C. Lai, X. Gao, B. Zhang, T. Yan and Z. Zhou, *J. Phys. Chem. C*, 2009, **113**, 4712–4716.
24 R. Elazari, G. Salitra, A. Garsuch, A. Panchenko and D. Aurbach, *Adv. Mater.*, 2011, **23**, 5641–5644.
25 N. Jayaprakash, J. Shen, S. S. Moganty, A. Corona and L. A. Archer, *Angew. Chem., Int. Ed.*, 2011, **123**, 6026–6030.
26 M. Agrawal, S. Choudhury, K. Gruber, F. Simon, D. Fischer, V. Albrecht, M. Göbel, S. Koller, M. Stamm and L. Ionov, *J. Power Sources*, 2014, **261**, 363–370.
27 M. Zeiger, N. Jäckel, V. N. Mochalin and V. Presser, *J. Mater. Chem. A*, 2016, **4**, 3172–3196.
28 M. Zeiger, N. Jäckel, D. Weingarth and V. Presser, *Carbon*, 2015, **94**, 507–517.
29 V. L. Kuznetsov, A. L. Chuvilin, Y. V. Butenko, I. Y. Mal'kov and V. M. Titov, *Chem. Phys. Lett.*, 1994, **222**, 343–348.
30 M. Zeiger, N. Jäckel, M. Aslan, D. Weingarth and V. Presser, *Carbon*, 2015, **84**, 584–598.
31 D. Lv, J. Zheng, Q. Li, X. Xie, S. Ferrara, Z. Nie, L. B. Mehdi, N. D. Browning, J.-G. Zhang, G. L. Graff, J. Liu and J. Xiao, *Adv. Energy Mater.*, 2015, **5**, 1402290.
32 X. Chen, E. Pomerantseva, P. Banerjee, K. Gregorczyk, R. Ghodssi and G. Rubloff, *Chem. Mater.*, 2012, **24**, 1255–1261.
33 P. I. Ravikovitch, A. Vishnyakov and A. V. Neimark, *Phys. Rev. E: Stat., Nonlinear, Soft Matter Phys.*, 2001, **64**, 011602.
34 S. Brunauer, P. H. Emmett and E. Teller, *J. Am. Chem. Soc.*, 1938, **60**, 309–319.
35 J.-J. Chen, Q. Zhang, Y.-N. Shi, L.-L. Qin, Y. Cao, M.-S. Zheng and Q.-F. Dong, *Phys. Chem. Chem. Phys.*, 2012, **14**, 5376–5382.
36 B. Ding, C. Yuan, L. Shen, G. Xu, P. Nie and X. Zhang, *Chem.–Eur. J.*, 2013, **19**, 1013–1019.
37 C. Liang, N. J. Dudney and J. Y. Howe, *Chem. Mater.*, 2009, **21**, 4724–4730.
38 C. Tang, B. Q. Li, Q. Zhang, L. Zhu, H. F. Wang, J. L. Shi and F. Wei, *Adv. Funct. Mater.*, 2016, **26**, 577–585.
39 Y. J. Zhong, S. F. Wang, Y. J. Sha, M. L. Liu, R. Cai, L. Li and Z. P. Shao, *J. Mater. Chem. A*, 2016, **4**, 9526–9535.
40 K. Balakumar and N. Kalaiselvi, *RSC Adv.*, 2015, **5**, 34008–34018.
41 G. Li, J. Sun, W. Hou, S. Jiang, Y. Huang and J. Geng, *Nat. Commun.*, 2016, **7**, 10601.
42 H. Wang, C. Zhang, Z. Chen, H. K. Liu and Z. Guo, *Carbon*, 2015, **81**, 782–787.
43 F. Jin, S. Xiao, L. Lu and Y. Wang, *Nano Lett.*, 2016, **16**, 440–447.
44 G. He, X. Ji and L. Nazar, *Energy Environ. Sci.*, 2011, **4**, 2878–2883.
45 B. Zhang, C. Lai, Z. Zhou and X. Gao, *Electrochim. Acta*, 2009, **54**, 3708–3713.
46 S. Kim, Y. Jung and S.-J. Park, *J. Power Sources*, 2005, **152**, 272–277.
47 S. Dörfler, M. Hagen, H. Althues, J. Tübke, S. Kaskel and M. J. Hoffmann, *Chem. Commun.*, 2012, **48**, 4097–4099.
48 J. Schuster, G. He, B. Mandlmeier, T. Yim, K. T. Lee, T. Bein and L. F. Nazar, *Angew. Chem., Int. Ed.*, 2012, **51**, 3591–3595.

49 Z. W. Seh, W. Li, J. J. Cha, G. Zheng, Y. Yang, M. T. McDowell, P.-C. Hsu and Y. Cui, *Nat. Commun.*, 2013, **4**, 1331.
50 N. Brun, K. Sakaushi, L. Yu, L. Giebeler, J. Eckert and M. M. Titirici, *Phys. Chem. Chem. Phys.*, 2013, **15**, 6080–6087.
51 L. Ji, M. Rao, H. Zheng, L. Zhang, Y. Li, W. Duan, J. Guo, E. J. Cairns and Y. Zhang, *J. Am. Chem. Soc.*, 2011, **133**, 18522–18525.
52 Y. Cao, X. Li, I. A. Aksay, J. Lemmon, Z. Nie, Z. Yang and J. Liu, *Phys. Chem. Chem. Phys.*, 2011, **13**, 7660–7665.

Electronic Supplementary Material (ESI) for Sustainable Energy & Fuels.

SUPPORTING INFORMATION

CARBON ONION - SULFUR HYBRID CATHODES FOR LITHIUM-SULFUR BATTERIES

Soumyadip Choudhury,[1,2] Marco Zeiger,[1,3] Pau Massuti-Ballester,[1,3]

Simon Fleischmann,[3] Petr Formanek,[2] Lars Borchardt,[4] Volker Presser[1,3,*]

[1] *INM - Leibniz Institute for New Materials, Campus D2 2, 66123 Saarbrücken, Germany*

[2] *Leibniz-Institut für Polymerforschung Dresden e.V., Hohe Str. 6, 01069 Dresden, Germany*

[3] *Department of Materials Science and Engineering, Saarland University, Campus D2 2, 66123 Saarbrücken Germany*

[4] *Department of Inorganic Chemistry, Technische Universität Dresden, Bergstraße 66, 01062 Dresden, Germany*

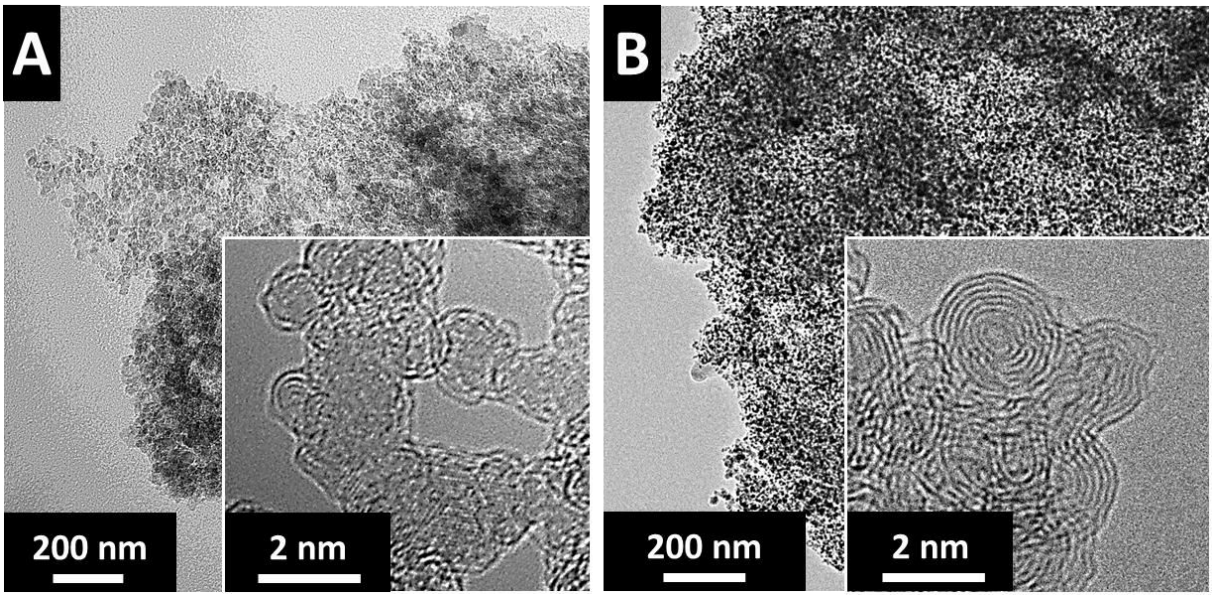

Figure S1. TEM micrographs of (A) nanodiamonds and (B) carbon onions obtained from thermal annealing of nanodiamonds.

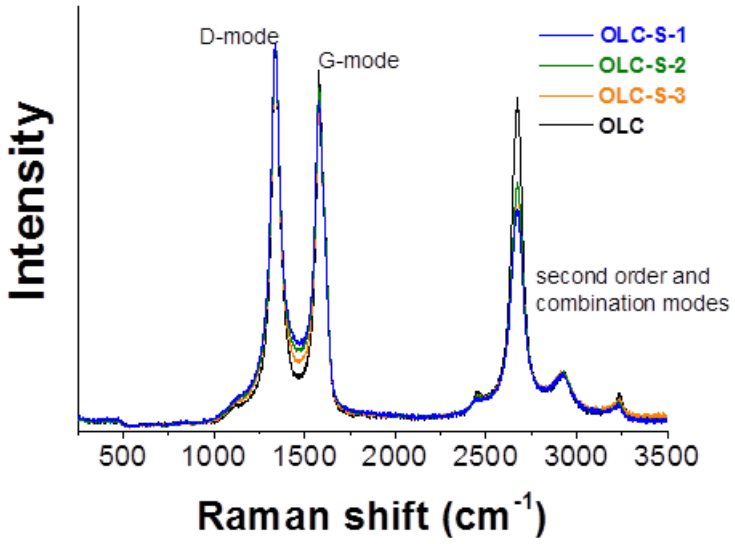

Figure S2. Raman spectra of the carbon onion / sulfur hybrids (using a 532 nm excitation wavelength).

3.6 Quinone-decorated onion-like carbon/carbon fiber hybrid electrodes for high-rate supercapacitor applications

Marco Zeiger,[1,2] Daniel Weingarth,[1] and Volker Presser[1,2]

[1] *INM - Leibniz Institute for New Materials, Campus D2 2, 66123 Saarbrücken, Germany*
[2] *Department of Materials Science and Engineering, Saarland University, Campus D2 2, 66123 Saarbrücken, Germany*

Citation:
Zeiger, M.; Weingarth, D.; Presser, V., Quinone-Decorated Onion-Like Carbon/Carbon Fiber Hybrid Electrodes for High-Rate Supercapacitor Applications. *ChemElectroChem* **2015,** 2, 1117-1127. (DOI: 10.1002/celc.201500130)

Own contribution: Design, planning, writing, synthesis, Raman spectroscopy, scanning- and transmission electron microscopy, conductivity measurements, particle size analysis, electrochemistry.

Abstract:
The energy performance of carbon onions can be significantly enhanced by introducing pseudocapacitive materials, but this is commonly at the cost of power handling. In this study, a novel synergistic electrode preparation method was developed by using carbon-fiber substrates loaded with quinone-decorated carbon onions. The electrodes are free standing, binder free, extremely conductive, and the interfiber space filling overcomes the severely low apparent density commonly found for electrospun fibers. Electrochemical measurements were performed in organic and aqueous electrolytes. For both systems, a high electrochemical stability after 10,000 cycles was measured, as well as a long-term voltage floating test for the organic electrolyte. The capacitance in 1M H_2SO_4 was 288 Fg^{-1} for the highest loading of quinones, which is similar to literature values, but with a very high power handling, showing more than 100 Fg^{-1} at a scan rate of 2 Vs^{-1}.

FUNDAMENTALS & APPLICATIONS

CHEMELECTROCHEM

ANALYSIS & CATALYSIS, BIO & NANO, ENERGY & MORE

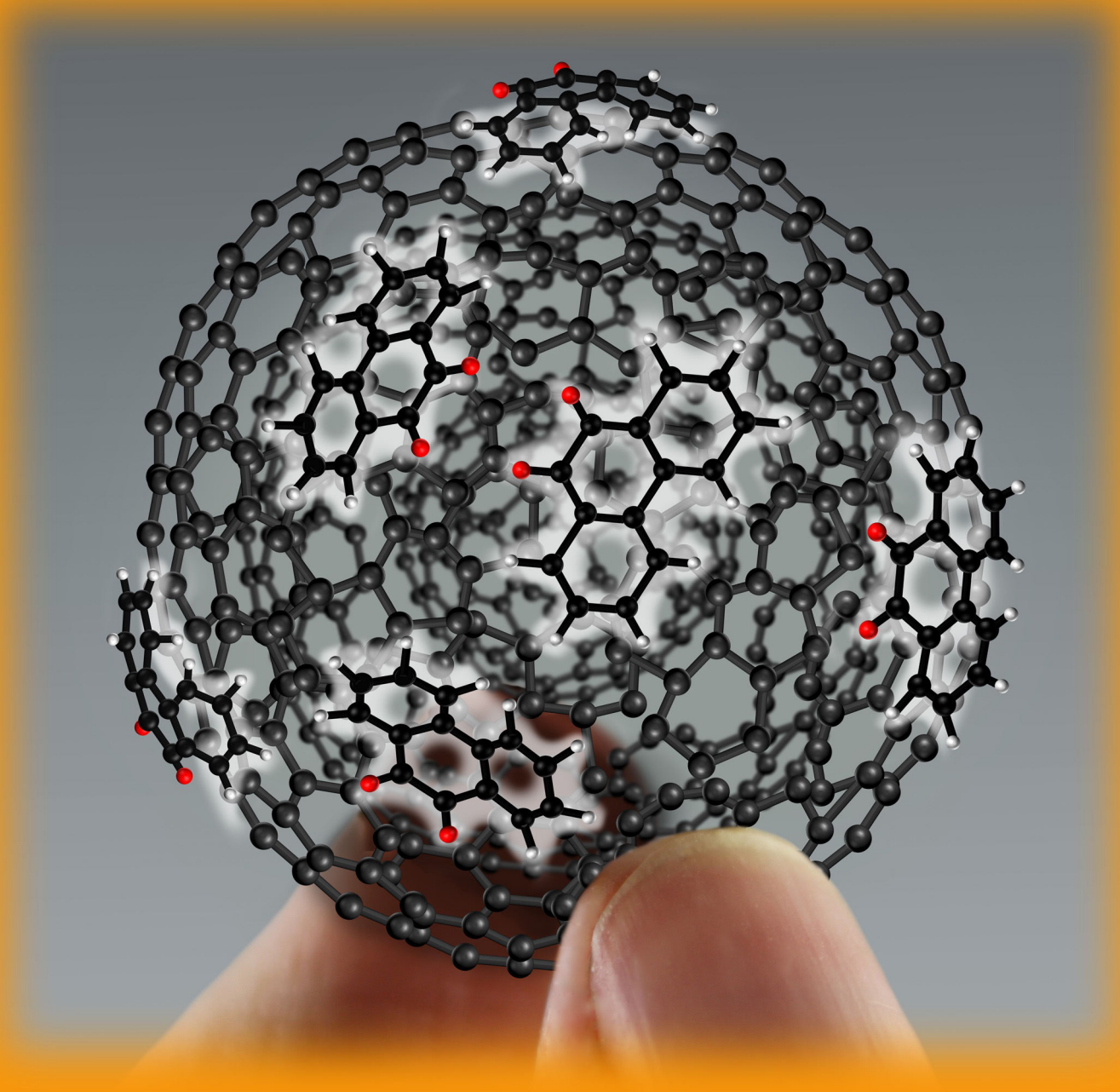

8/2015

Cover Picture:

V. Presser et al.

Quinone-Decorated Onion-Like Carbon/Carbon Fiber Hybrid Electrodes for High-Rate Supercapacitor Applications

A Journal of

ChemPubSoc Europe

WILEY-VCH

www.chemelectrochem.org

ChemPubSoc Europe

DOI: 10.1002/celc.201500130

CHEMELECTROCHEM Articles

Quinone-Decorated Onion-Like Carbon/Carbon Fiber Hybrid Electrodes for High-Rate Supercapacitor Applications

Marco Zeiger,[a, b] Daniel Weingarth,[a] and Volker Presser*[a, b]

The energy performance of carbon onions can be significantly enhanced by introducing pseudocapacitive materials, but this is commonly at the cost of power handling. In this study, a novel synergistic electrode preparation method was developed by using carbon-fiber substrates loaded with quinone-decorated carbon onions. The electrodes are free standing, binder free, extremely conductive, and the interfiber space filling overcomes the severely low apparent density commonly found for electrospun fibers. Electrochemical measurements were performed in organic and aqueous electrolytes. For both systems, a high electrochemical stability after 10000 cycles was measured, as well as a long-term voltage floating test for the organic electrolyte. The capacitance in 1 M H_2SO_4 was 288 F g^{-1} for the highest loading of quinones, which is similar to literature values, but with a very high power handling, showing more than 100 F g^{-1} at a scan rate of 2 V s^{-1}.

1. Introduction

Electrical double-layer capacitors (EDLCs), or supercapacitors, are energy-storage devices with high power density compared to other electrochemical energy-storage technologies.[1–3] This high power handling is accomplished by the physical energy-storage mechanism of highly efficient ion electrosorption at the charged interface of an electrolyte with high-surface-area carbon electrodes.[1,2] However, EDLCs show a very moderate energy density compared to batteries, with the latter capitalizing electrochemical redox reactions and current research efforts aim to overcome this limitation.[4,5] Most commonly, EDLC electrodes are composed of activated carbon (AC), considering its moderate-to-low cost and high natural abundance in organic precursors.[6] In addition, a plethora of other carbon materials has been explored, such as carbon nanotubes,[7] graphene,[8] carbide-derived carbon,[9] templated carbons,[10] carbon black,[11] and carbon onions.[1,12]

Carbon onions, also known as onion-like carbons (OLCs), are an intriguing class of carbon nanomaterials that consist of spherical carbon nanoparticles, which can be seen as mostly sp^2-hybridized multishell fullerenes.[13] OLC has been investigated as a promising material for extremely high power-handling applications[14–17] and a performance up to 200 V s^{-1} has been described in the literature for OLC micro-supercapacitors (i.e. ultrathin electrodes of just a few micrometers).[18] Although there are many different synthesis methods for OLCs, currently the only scalable synthesis route employs thermal annealing of detonation nanodiamond above 1000 °C, yielding a high level of control over the resulting OLC structures.[19] The excellent power-handling ability of OLC is related to the absence of intraparticle porosity and the dominance of external surface area, giving rise to beneficially high ion mobility,[20] even at operational temperatures below 0 °C.[21] However, the absence of internal particle porosity[22] and the nanoscopic particle diameter of around 5–10 nm limits the total specific surface area (SSA) to around 200–600 $m^2 g^{-1}$.[14,16,17] Consequently, only a moderate specific capacitance between 20 and 60 F g^{-1} can be found in organic electrolyte, which corresponds to a low energy density of, typically, below 10 Wh kg^{-1}.[17] Such performance is low compared to AC or other porous carbons, with typically more than 1200 $m^2 g^{-1}$and more than 100 F g^{-1}.[23] Yet, even the latter value corresponds to an energy density roughly one order of magnitude below that of lithium-ion batteries, which results in vast research efforts being invested in exploring facile ways to enhance the energy-storage capacity of supercapacitors.[5,24]

Currently, the literature shows two general approaches to increase the capacitance of carbon materials: 1) increasing the operation voltage by using advanced electrolytes or 2) adding redox-active materials for so-called pseudocapacitors. In the case of carbons with moderate or non-optimized pore structures, there is a third approach: 3) increasing the SSA through chemical or physical activation. For example, physical activation in air[22] or chemical activation with H_2SO_4/HNO_3 or KOH mixtures[25] was demonstrated to increase the surface area of OLCs to 650–820 $m^2 g^{-1}$ with a capacitance of more than 120 F g^{-1} in aqueous electrolytes. The finite ability of nanoporous carbons to screen electric charges, however, presents an upper capacitance limit in this approach.[26]

[a] M. Zeiger, Dr. D. Weingarth, Prof. Dr. V. Presser
INM - Leibniz Institute for New Materials
Campus D2 2, 66123 Saarbrücken (Germany)
E-mail: volker.presser@leibniz-inm.de

[b] M. Zeiger, Prof. Dr. V. Presser
Department of Materials Science and Engineering
Saarland University, Campus D2 2, 66123 Saarbrücken (Germany)

Supporting Information for this article is available on the WWW under http://dx.doi.org/10.1002/celc.201500130.

Pseudocapacitors capitalize the high energy density inherent to reversible redox reactions and provide another facile way to enhance the energy ratings of supercapacitors. Motivated by the excellent electrical conductivity and fast ion electrosorption dynamics in OLC electrodes, OLC pseudocapacitors are a promising technology. In particular, three systems have been investigated: 1) adding redox-active metal oxides to OLCs,[27,28] 2) functionalization with electrochemically active polymers like polyaniline,[29] and 3) decorating the onion surface with redox-active surface groups such as quinones.[15] The latter provides a particularly attractive approach, as simple addition of quinones to the electrolyte[30] or dispersion of the carbon powder in quinone-containing solution can be used instead of more elaborate hydrothermal syntheses of metal-oxide particles.[15]

The redox activity and high electrochemical reversibility of quinones has been studied before.[31,32] For example, Roldán et al. added hydroquinones directly to the aqueous electrolyte (1 M H_2SO_4) to increase the capacitance of an AC supercapacitor by more than 300% (i.e., up to 900 F g^{-1}, but only at very small current densities).[33] Another synthesis procedure was described by Balach et al. by immersing porous carbon microparticles into different types of quinone-containing solutions to reach values of approximately 900 F g^{-1} in 1 M $HClO_4$.[34] Other carbon materials used in combination with quinones include carbon fabrics,[35] graphene nanosheets,[36] and carbon nanotubes.[37] Recently, quinone decoration on OLCs was explored in Ref. [15], achieving a specific capacitance of 267 F g^{-1} at 5 mV s^{-1} for a high loading of 9,10-phenanthrenequinones (PQ) in a three-electrode setup (half-cell experiment); yet, the material showed a limited power-handling ability with a drop in the specific capacitance to just 50 F g^{-1} at 2 V s^{-1}. The latter study employed small amounts of quinone-decorated onions that were drop-casted onto glassy carbon, whereas, for the practical implementation of this material, data on electrode films is needed and the performance of a full cell (two-electrode setup) is necessary. All aforementioned approaches were based on the conventional electrode concept of using carbon particles glued together with a polymer binder, which, in turn, adds resistance and dead mass to the system.

The literature documents a promising improvement in energy-storage capacity through quinone modification of carbon surfaces; yet, the highest benefit for supercapacitors is only achieved when addressing both energy rating and power handling. The latter is commonly limited in AC or other materials with a large intraparticle porosity and, as a consequence, often large amounts of conductive additive or binder were used, often reaching only 75 wt% of active material.[36,37] Specifically, for OLCs, binder-free electrodes are desirable to preserve the high intrinsic electrical conductivity of OLCs, which is effectively lowered when significant amounts of polymer binder are added. In general, the preparation technique and specifics of carbon electrodes have strong impacts on the supercapacitor performance.[38] Most commonly, electrodes are produced by mixing carbon powders with 5–10 wt% polytetrafluoroethylene (PTFE),[33] whereas exploratory studies on the electrochemical performance of materials may rely on drop casting sulfonated tetrafluoroethylene-based fluoropolymer–copolymer/carbon ink on glassy carbon.[34] These methods that use drop casting on conductive substrates are suitable for electrochemical testing, but are disadvantageous for a large-scale preparation, problematic to handle, and the substrate is typically not included in the capacitance or energy density calculations.

In our study, we present a new synthesis method to obtain binder-free, free-standing, and highly conductive electrodes consisting of OLC and well-established carbonized polyacrylonitrile (PAN) fibers derived from electrospinning. Electrospinning presents a facile way to obtain polymer-fiber mats with a high level of control over the fiber diameter and chemical composition.[39,40] By using further thermal treatment, polymer fibers can be carburized without losing the shape and mechanical stability; yet, the remaining large interfiber space typically remains unused. Our approach entails utilizing both the high connectivity of carburized PAN fibers and filling the interfiber space with OLCs to capitalize on superior electrical conductivity and to eliminate the need for a polymer binder. To advance beyond merely designing an improved concept for OLC electrodes, we utilize our novel OLC/carbon fiber (OLC/CF) hybrid mats as a substrate for facile quinone decoration.

2. Results and Discussion

2.1. Morphological and Structural Characterization

Electrospinning of PAN fibers is a well-established and extensively investigated procedure.[40,41] As (partially) graphitic carbon electrodes are needed for electrochemical applications, the as-spun PAN fibers need to undergo thermochemical treatment: first, oxidation in air; second, carburization in argon. As seen in Figures 1 A–C, this two-step process preserves the structural integrity and the continuous, highly interconnected network of fibers of the fiber mats. The high-temperature treatment in argon at 1700 °C also causes a significant reduction in fiber diameter from 264 ± 53 nm (as-spun) and 303 ± 84 nm (after oxidation) to 144 ± 33 nm (Figure 1 D) with a total fiber mat thickness of approximately 50 μm (see Figure S1 A in the Supporting Information).

The starting material for OLC is nanodiamond (ND) used in the form of a stable dispersion in water, with an average (particle) size of around 8 nm for the simplicity of introducing it later into the interfiber space of oxidized PAN fibers (Figure 1 E). This is in agreement with the primary particle size of around 5 nm, as seen with TEM (Figure 1 F). The ND particles showed a diamond core with a (111)-plane lattice spacing of 0.21 nm and were covered with sp^2-hybridized carbon shells, as seen from Figure 1 F. Like PAN, ND particles also need to be transformed to sp^2-hybridized carbon prior to use in supercapacitors. This is accomplished by thermal annealing in vacuum or inert-gas atmospheres. By using the same conditions needed for the transition of oxidized PAN fibers to carbon nanofibers (i.e. 1700 °C), we obtained highly graphitic OLC particles, exhibiting a highly defective fullerene-like structure with several shells (Figure 1 G) and a lattice spacing of 0.34 nm for the graphite (002) plane.

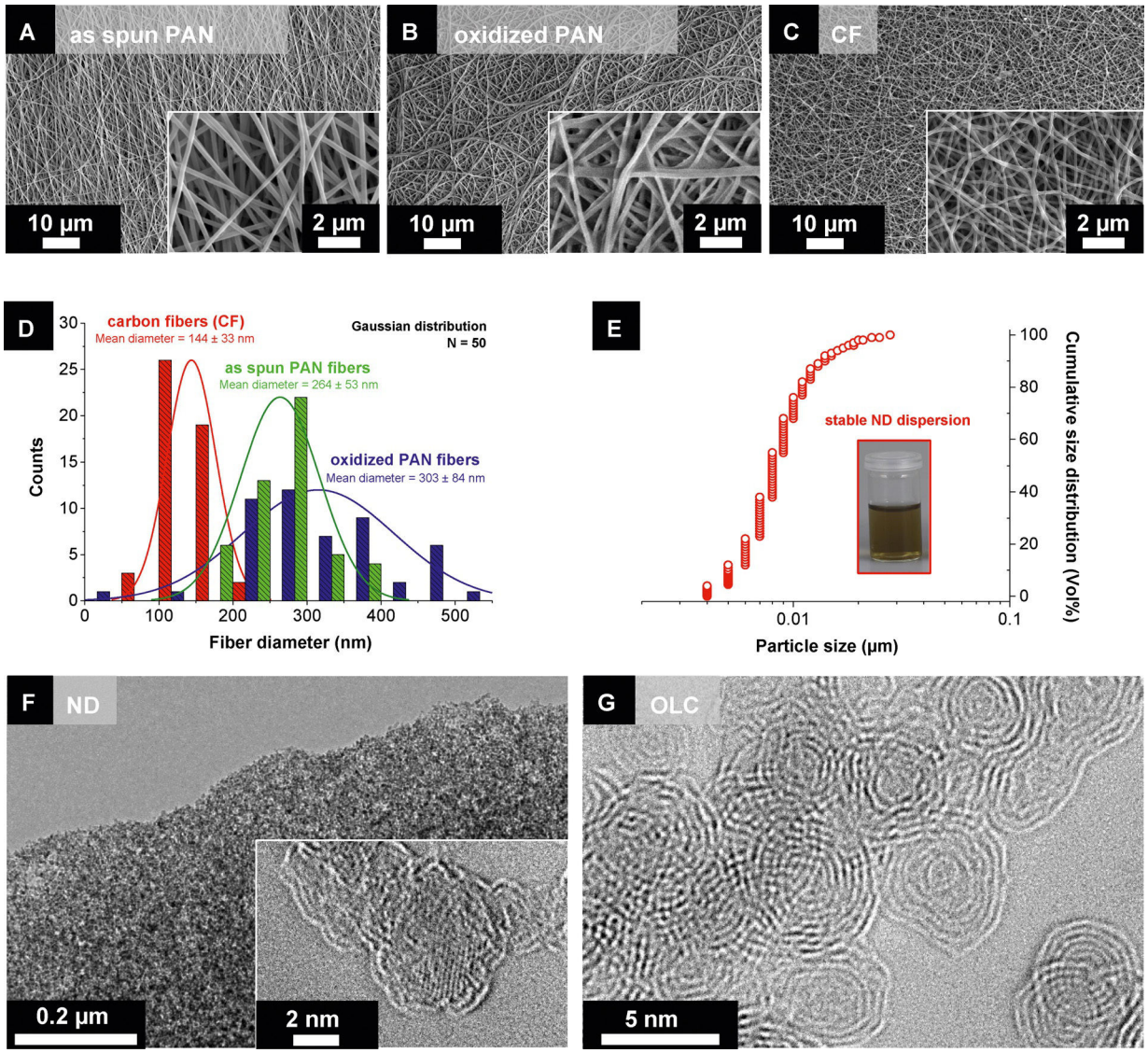

Figure 1. SEM images of A) as-spun PAN fibers, B) oxidized PAN fibers, and C) CFs annealed at 1700 °C in argon. D) The fiber diameter distribution for the three synthesis steps (as spun, oxidized, and carburized). E) Centrifugal sedimentation analysis of a stable ND dispersion measured in a 0.5 wt% water dispersion. TEM images of F) NDs and G) OLCs.

We see from these TEM images that annealing either NDs or oxidized PAN fibers in argon at 1700 °C yields highly graphitic carbon materials. Thus, our approach was to synergistically combine the final heat-treatment process by drop-casting ND particles of a stable dispersion into the interfiber space of oxidized PAN fibers (Figure 2). As seen visually from the photograph, oxidation at 250 °C in air changes the color of white electrospun PAN fibers mats (Figure 2A) to amber (Figure 2B). After drop-casting ND particles, an additional color change to dark brown occurs and finally to black after high-temperature annealing (Figure 2C and D). During this process, ND powders alone lose around 30% of their initial mass, owing to the desorption of oxygen-containing surface functional groups and carbon etching.[22] For comparison, the mass loss of PAN alone is even more dramatic, with levels around 60% coming from the evolution of oxygen-, nitrogen-, and hydrogen-containing gases.[42] The hybrid systems of PAN50, PAN250, and PAN500 show a mass loss of approximately 70% after thermal annealing at 1700 °C. Interestingly, all OLC/CF hybrid mats show approximately the same mass loss, even though they mostly consist of ND, which is related to enhanced OLC etching by reactive gases coming from the ND and the PAN. Oxygen-containing functional groups are released during annealing in argon and readily react with carbon; this results in the evolution of CO and CO_2, which lead to carbon etching through the Boudouard reaction.[43] The thickness of the hybrid mats did not change significantly after heat treatment and we measured values between 20 and 60 µm for the different filling states (see Figure S1 A).

After drop casting and drying in a vacuum, the interfiber space is partially filled with ND and we find an additional adlayer of ND particles on top of the fiber mat (Figures 3A and C). The final heat-treatment step at 1700 °C then transitions the oxidized PAN fibers and the infiltrated ND particles to the

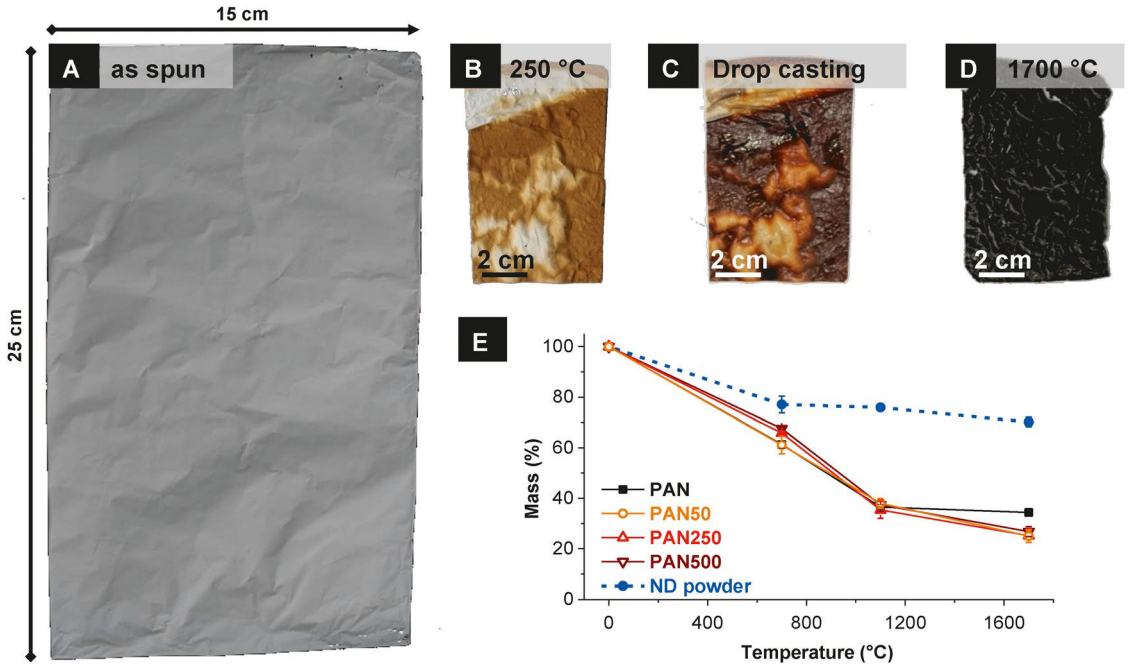

Figure 2. As-spun PAN fiber mat A) on aluminum foil, B) after oxidation in air at 250 °C, C) after drop casting of NDs (5 wt% water dispersion), and D) after joint thermal annealing in argon at 1700 °C. E) Mass loss for fiber mats with different ND filling degrees and the ND powder as a function of the synthesis temperature.

CFs and OLCs, respectively. We see a shrinkage in the fiber diameters (Figures 1C and D) and, in particular, the cross-sectional SEM images show shrunken CFs in channels of the former size of the original PAN fibers within a consolidated matrix of OLCs (Figure 3B). Mechanical tension during thermal annealing also causes larger pore openings in the range of 1–2 μm (Figure 3D).

TEM images further corroborate the synergistic co-transformation of oxidized PAN to CFs and ND to OLCs (Figure 3E–H). Structurally and morphologically, the OLC/CF hybrid mats exhibit the same features as CF or OLC synthesized separately (Figure 1). Both CFs and OLCs show a high degree of structural ordering, which is characteristic for both materials synthesized at an elevated temperature of 1700 °C.[42] However, the loading with onions is not just filling the free interfiber space, but is also interconnected through local sintering of the OLCs (Figure 3F), as shown in a recent study.[22]

The partially graphitic state of OLC and CF, and also the OLC/CF hybrid fiber mats, is shown by the presence of characteristic D and G modes between 1200 and 1700 cm^{-1}, and a distinct range of overtones and combinational modes between 2300 and 3400 cm^{-1} (Figure 4A). The G mode between 1580 and 1600 cm^{-1} is a first-order peak with E_{2g} symmetry and representative of sp^2-hybridized carbon.[44] The D mode between 1340 and 1345 cm^{-1} relates to defects and disorder-induced phonon transitions.[45] The D-to-G band intensity (I_D/I_G) ratios of carburized PAN and OLCs are 1.36±0.02 and 1.24±0.03, respectively, which are typical for a high degree of carbon ordering. This result is supported by presence of sharp D and G peaks with a rather narrow full-width at half maximum of 40–70 cm^{-1} (Figure 4B).[44] By adding quinones to the composite electrode (PQ-max) through drop casting followed by extensive washing, the Raman signal of PQ is still visible in the composite, indicating the stable adsorption and high degree of functionalization (Figure 4A).

As expected for a high degree of graphitization, we also observe a high electrical conductivity, as measured with a four-point-probe (Figure 4C). OLC powders, after compressing to free-standing pellets, show conductivities between 0.9 and 1.8 $S\,cm^{-1}$, whereas PTFE-bound OLC electrodes show values of 0.5–1.1 $S\,cm^{-1}$, which is in excellent agreement with the literature.[14,17] For comparison, the electrical conductivity of film electrodes of pure carbon black with 10 wt% PTFE and AC with 5 wt% PTFE are approximately 2 and 0.1 $S\,cm^{-1}$, respectively.[46] Although the degree of carbon ordering for CF and OLC is very similar based on our Raman investigation, we see that CF mats have a conductivity an order of magnitude higher (ca. 26 $S\,cm^{-1}$). Even higher values are obtained for OLC/CF hybrid mats with a maximum of approximately 54 $S\,cm^{-1}$ for CF500, and it is important to note that this value is not reduced when adding PQ to the latter (Figure 4C). These findings exemplify that the conductivity of the composite electrode is sensitive to particle–particle resistance, and the high conductivities of CF and OLC/CF hybrid mats are afforded by the high interconnectivity and the continuous network of fused carbon material.

The SSA of OLCs, typically in the range of 200–600 $m^2\,g^{-1}$,[22] represents the large external surface and does not stem from internal porosity. In this study, the surface area of OLCs synthesized at 1700 °C is 387 $m^2\,g^{-1}$ (BET) and 353 $m^2\,g^{-1}$ (DFT), which are in agreement with the literature.[17,22,47] The carbonized PAN fibers show a surface area of less than 50 $m^2\,g^{-1}$, which

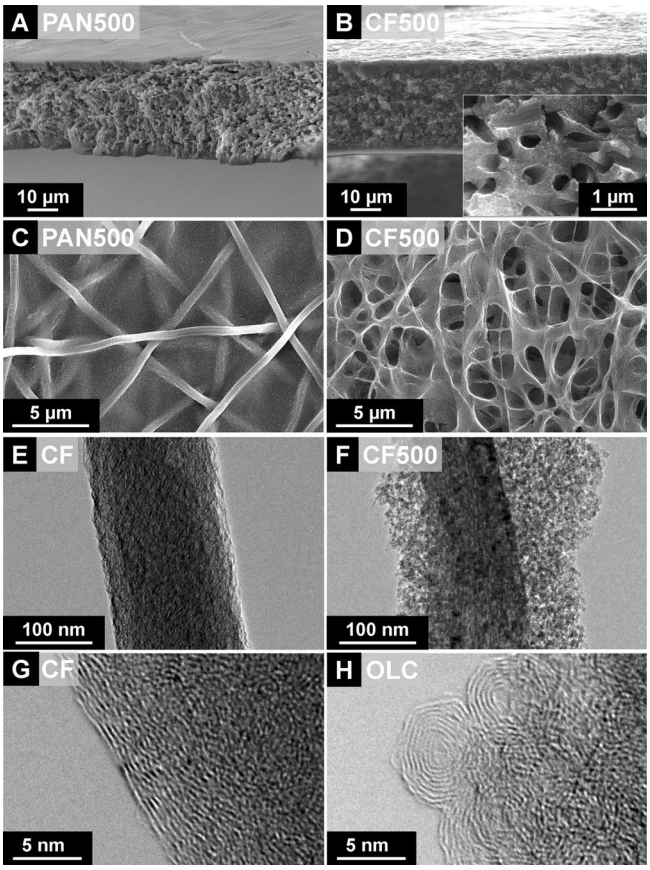

Figure 3. Cross-sectional and top-view SEM images of composites electrodes consisting of A, C) oxidized PAN with 500 wt% ND after drop casting and B, D) after annealing at 1700 °C in argon. TEM images of E, G) CFs and F, H) the composite electrode with 500 wt% ND annealed in argon at 1700 °C.

prohibits their use for supercapacitors (at least without additional physical or chemical activation). With an increasing amount of OLCs in the hybrid-mat electrode, the surface area continuously increases for CF500 to maximum values of 313 $m^2 g^{-1}$ (BET) and 291 $m^2 g^{-1}$ (DFT). This value is still slightly smaller than the surface area of loose OLC powder, because of the sintering to other OLCs and superficial fusing to CFs. This is accomplished by carbon redistribution related to reactive gases coming from the ND precursor, ultimately giving rise to the formation of larger graphitic particles, as shown in a recent study (cf. Figure S2).[22]

2.2. Electrochemical Characterization

Electrochemical testing was performed on PTFE-bound OLC electrodes and free-standing CF and OLC/CF hybrid mats in 1 M tetraethylammonium tetrafluoroborate (TEA–BF_4) in acetonitrile (ACN). Cyclic voltammograms (CVs) at different scan rates in a half-cell were used to demonstrate the electrochemical performance at 10 $mV s^{-1}$ (Figure 5A) and 2 $V s^{-1}$ (Figure 5B). In the case of the latter, high scan rate, the rectangular CV shape of the CF and OLC/CF hybrid mats is still present, whereas the CV for the PTFE-bound electrode indicates a significant resistive behavior (Figure 5B). We also note a pronounced butterfly shape of CVs for all samples as a result of the non-constant differential capacitance.[47,48] In detail, applying a higher potential introduces additional states, increases the electrical conductivity of the carbon, and improves the ability to screen ionic charges. This phenomenon is known as electrochemical doping and has been described in the literature for graphite, ACs, carbon nanotubes, and OLCs.[48,49]

Dependent on the amount of OLC, the capacitance increases from below 1 $F g^{-1}$ to a maximum of 19.5 $F g^{-1}$ (CF500) at 1 V. The increase in capacitance with the amount of OLC stems from the higher SSA of CF500 (313 $m^2 g^{-1}$ BET SSA) compared to the carbonized PAN fibers (36 $m^2 g^{-1}$ BET SSA). The PTFE-bound electrode has a slightly larger capacitance of 20.5 $F g^{-1}$, because of the larger surface area; yet, we see that this initially higher capacitance is readily lost at higher scan rates with a crossover to CF500 at around 100 $mV s^{-1}$ (Figure 5C). However, CF500 loses just 15% of its initial low-scan-rate capacitance, whereas the PTFE-bound OLC electrode shows a reduced specific capacitance of approximately 60% at 2 $V s^{-1}$ (Figure 5C). An overview of the measured electrode capacitances is given in Table 1.

The observations made for CVs of half-cell operation are confirmed for full-cell experiments (Figure 5D). Direct compari-

Table 1. Capacitance and capacity values for different types of electrodes. All values were determined at 10 $mV s^{-1}$ at 1 V in organic electrolyte and at −0.4 V in aqueous electrolyte with half cells. Values for pseudocapacitive energy storage are given in $F g^{-1}$ and $mAh g^{-1}$.

Electrode	1 M H_2SO_4 Capacitance [$F g^{-1}$]	Capacity [$mAh g^{-1}$]	1 M TEA–BF_4 in ACN Capacitance [$F g^{-1}$]	Ref.
OLC	–	–	21	this work
OLC	–	–	20–27[a]	[14]
CF	–	–	1	this work
CF50	–	–	3	this work
CF250	–	–	9	this work
CF500	34	4	20	this work
PQ-20	46	5	–	this work
PQ-200	112	13	–	this work
PQ-max	288	32	–	this work
AC-HQ	280[b]	–	–	[30]
PQ-CB-max	257[c]	–	–	[59]
CF-PQ-max	21	2	–	this work
OLC-PQ-max	221	25	–	this work
OLC-PQ	264[d]	–	–	[15]

[a] Measured in 1.5 M TEA–BF_4 in ACN. [b] Measured for hydroquinone = 1,4-dihydroxybenezene, not for PQ, using AC. [c] Measured in 1 M KOH; PQ was electrochemically grafted on carbon black (CB). [d] Measured in a three-electrode configuration (half-cell) drop cast with Nafion on glassy carbon.

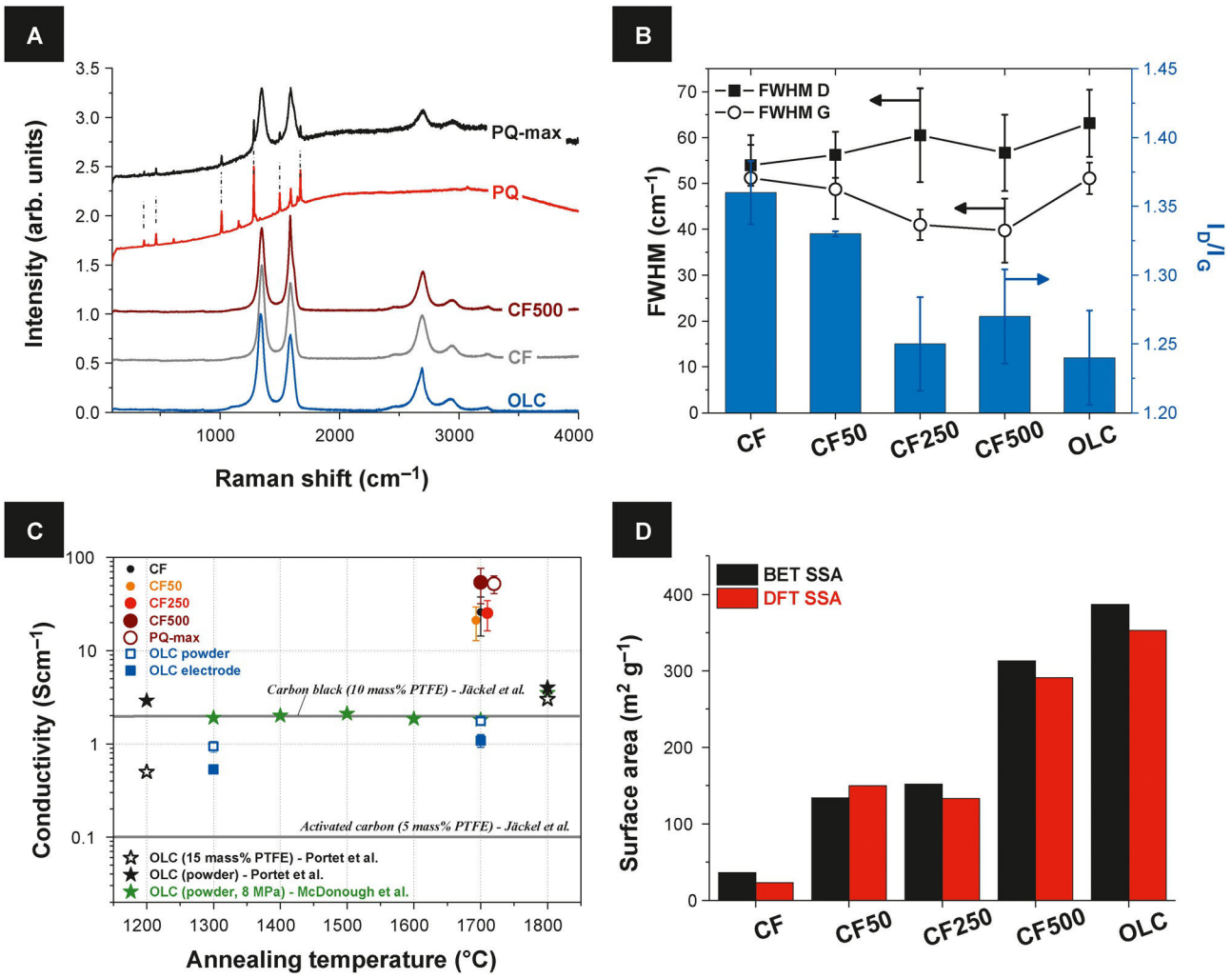

Figure 4. A) Raman spectra of OLC, CF, the composite electrode with 500 wt% ND (CF500), PQ, and the maximum loading of PQ on CF500 (PQ-max). B) FWHM of the D and G modes and the I_D/I_G ratio from Lorentzian peak fitting. C) Conductivities normalized to the electrode thickness for experimental and literature values and D) the BET and DFT SSAs The references in (C) are from Refs. [14, 17, 46].

son of PTFE-bound OLC electrode performance with CF500 shows that the latter exhibits a significantly higher rate-handling ability when cycling up to a cell voltage of 2.5 V (Figure 5D). When employing galvanostatic charge/discharge testing, we see that CF500 and PTFE-bound OLC electrodes show a comparable performance up to approximately 1 A g^{-1}. With increasing current density up to 50 A g^{-1} the relative capacitance is as low as 25% for the PTFE-bound OLC electrode, but still more than 70% for the OLC/CF hybrid mat. Even for a current density of 100 A g^{-1}, the composite electrode shows a relative capacitance of more than 60% of the low-current-density value. Thus, at higher current densities, CF500 shows superior capacitive performance, and this performance remains highly stable (Figure 5F). In particular, we tested the cycling stability over 10000 cycles at 200 mV s^{-1} and for 100 h holding time at 2.5 V without any degradation, especially for the CF500.

Yet, it is clear that, with such a low specific capacitance, even CF500 or PTFE-bound OLC electrodes have limited potential as electrode materials for carbon supercapacitors. Thus, we used our well-characterized OLC/CF hybrid mats as a substrate for modification with PQ. Electrochemical characterization in aqueous 1 M H_2SO_4, using CF500 with different loadings of PQ, the PTFE-bound electrode with PQ, as well as the carburized PAN electrode with PQ, is presented in Figure 6. Cyclic voltammetry from 0 to −0.4 V versus Pt of the CF500 composite electrode shows a rectangular shape with a capacitance of 34 F g^{-1} (Figure 6A), which is 70% higher than in organic electrolyte (Figure 5A). With addition and subsequent increasing loadings of PQ, the quinone redox peaks between −0.15 and −0.25 V versus Pt appear and grow in intensity and area (Figure 6A).

As inferred from the literature, the drop-casted quinone molecules arrange parallel to the OLC surface, most probably because of π–π interactions.[50] The mechanism of the proton-coupled electron-transfer reaction ($2e^-/2H^+$) between the surface-bound quinones and electrolyte is described elsewhere.[32,51] With the maximum loading of CF500 with PQ (PQ-max), a capacitance of 288 F g^{-1} is measured with a maximum energy density of approximately 6.4 Wh kg^{-1} and a maximum power density of 19.2 kW kg^{-1}. For comparison, using the same

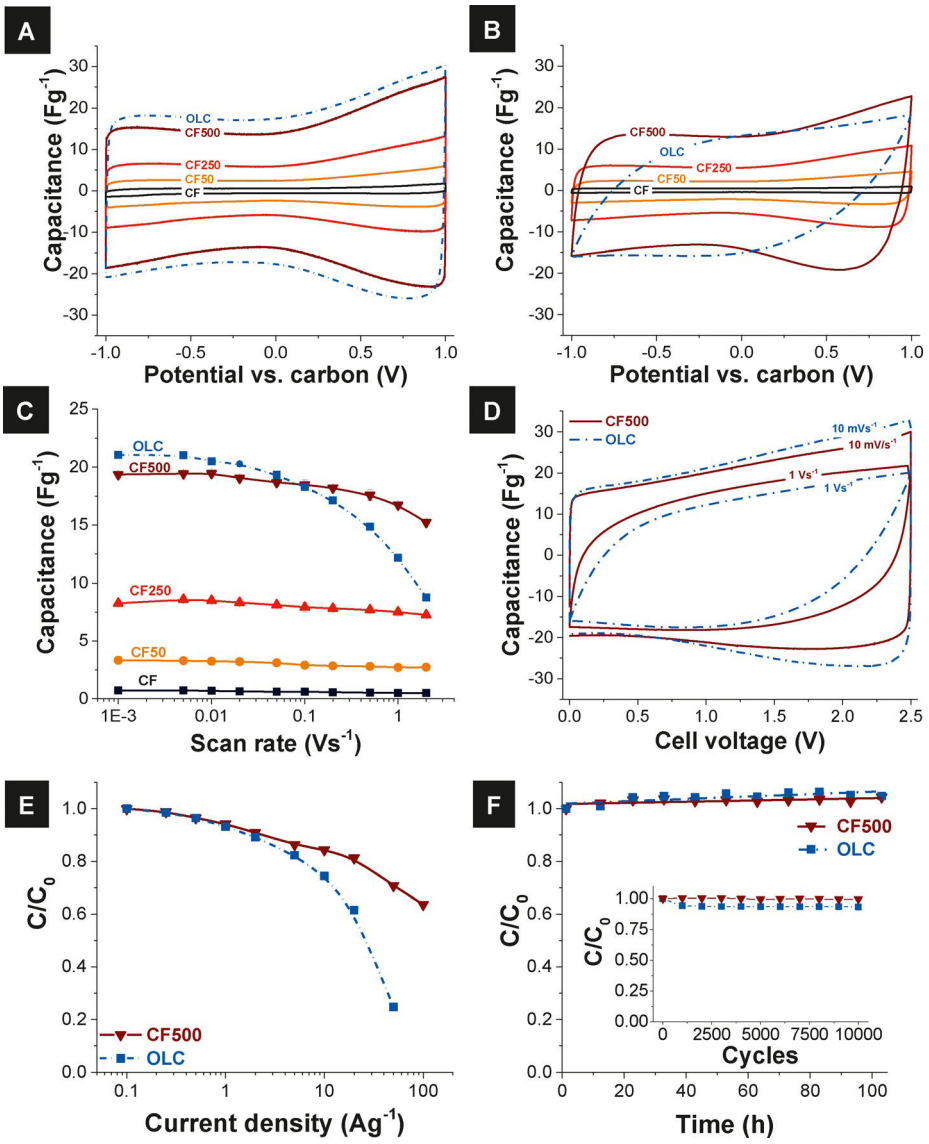

Figure 5. CVs from −1 to +1 V versus carbon for the composite electrodes and the PTFE-bound OLC electrode, using a three-electrode setup with a scan rate of A) 10 mV s^{-1} and B) 1 V s^{-1}. C) Capacitance measured at 1 V versus carbon as a function of the scan rate. D) CVs from 0 to 2.5 V in a full cell at 10 mV s^{-1} and 1 V s^{-1} for CF500 and the PTFE-bound OLC electrode. E) Rate handling measured in a two-electrode setup with galvanostatic cycling and a potential limitation of 2.5 V. F) Long-term voltage floating test at 0.5 A g^{-1}, 2.5 V potential limitation, and a holding time of 10 h. The inset in (F) shows a stability test with 10000 CVs at 200 mV s^{-1}. All samples were measured in in 1 M TEA–BF_4 in ACN.

synthesis and experimental conditions, the PTFE-bound OLC electrode (OLC-PQ-max) and the CF electrode (CF-PQ-max) have lower capacitances of 221 and 21 F g^{-1}, respectively, with a maximum energy density of approximately 4.9 Wh kg^{-1} and a maximum power density of 4.3 kW kg^{-1} for OLC-PQ-max. Commercial AC electrodes present much lower values with a capacitance of 115 F g^{-1}, energy density of 2.5 Wh kg^{-1}, and power density of 1.8 kW kg^{-1} (Figure 6A and Figure S3B). All capacitance and capacity values are presented in Table 1. Figure 6B also shows the performance of conventional AC in the form of a PTFE-bound electrode; as expected, the capacitive performance of an AC electrode drops rapidly when transitioning beyond 100 mV s^{-1}. Up to a scan rate of 200 mV s^{-1}, our data is in excellent agreement with our previous study (Ref. [15]) on drop-casted quinone-decorated onions on glassy carbon. For higher scan rates, for example 2 V s^{-1}, our OLC/CF hybrid mats have twice the capacitance, despite the smaller surface area and lower synthesis temperature (this work: 1700 °C, Anjos et al.: 1800 °C).[15]

These findings are supported by the electrochemical characterization in organic electrolyte. As shown before (Figure 5), using 1 M TEA–BF_4 in ACN, the PTFE-bound OLC electrode exhibited a lower rate handling with only 40% initial capacitance at a scan rate of 2 V s^{-1} (half-cell) and 25% at 50 A g^{-1} (full cell) compared to approximately 75 and 70% for CF500. The same result was observed in 1 M H_2SO_4 with an enormously high capacitance of more than 100 F g^{-1} for the PQ-loaded composite (PQ-max), only 25 F g^{-1} for the PTFE-bound electrode, and 3 F g^{-1} for a standard AC electrode at 2 V s^{-1}. Even without PQ loading, the OLC/CF hybrid mats (CF500) show higher values (ca. 35 F g^{-1}) than the PTFE-bound OLC electrode and AC (Figure 6B). These findings are additionally supported by impedance spectroscopy (Figure S3A), where a clear reduction in equivalent distributed resistance (EDR) can be seen for composite electrodes compared to PTFE-bound OLC electrodes.

Electrochemical long-term stability was measured by using cyclic voltammetry from 0 to −0.4 V versus Pt for 10000 cycles (Figure 6C). The AC electrolyte and CF500 composite electrode demonstrate a high stability after 10000 cycles. After PQ loading of the composite electrode (PQ-max), the capacitance decrease by approximately 10% after 10000 cycles, which is similar to previous reported literature values around 6%.[15] The maximum potential window is limited to 1 V, as shown in Figure 6D. The full-cell arrangement for both the CF500 electrode as well as the high-loading PQ-max electrodes shows similar data compared to the half-cell experiments. By successively opening the potential window in 0.1 V steps, between −0.5 and 0.5 V, electrode degeneration starts. This is indicated by the higher slope of

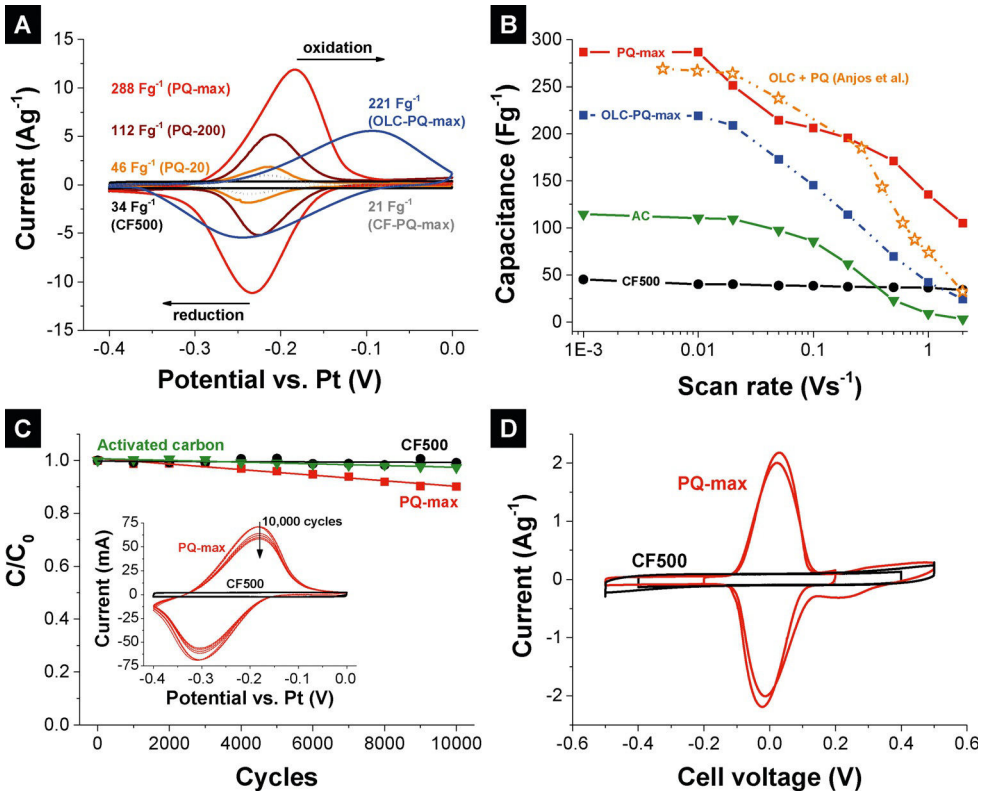

Figure 6. A) CVs from −0.4 to 0 V versus Pt for the composite electrode CF500, with different loadings of PQ, PTFE-bound OLC, AC electrodes, and the PQ-loaded CF electrode. A three-electrode setup with a platinum wire as the reference electrode and a scan rate of 10 mV s^{-1} was used. B) Plot of the capacitance versus the scan rate. C) The stability was measured by using cyclic voltammetry from −0.4 to 0 V versus Pt, applying 10 000 cycles at 200 mV s^{-1}. CVs when using a full cell with the potential window successively opened up to −0.5 and +0.5 V for CF500 and PQ-max. All samples were measured in aqueous 1 M H_2SO_4.

CF500, when using a cell voltage of 1 V, and the appearance of additional peaks for PQ-max.

3. Conclusions

A new electrode synthesis method was developed by using a CF network filled with OLCs. For the first time, OLC electrodes were free standing and binder free with superior rate handling in organic as well as aqueous electrolytes compared to standard PTFE-bound or drop-casted OLCs. The filling of the interfiber spacing of CF networks presents a facile way to synergistically combine the high conductivity of a continuous fiber network with the higher surface area of carbon nanoparticles (i.e. OLCs). This method may also work as a platform to prepare electrodes with other carbon or hybrid nanoparticles. The high conductivity combined with a moderate surface area is also a suitable platform for effective functionalization with pseudocapacitive materials like quinones. The maximum decoration of the composite electrode with quinones increases the capacitance more than eight times to 288 F g^{-1} in 1 M H_2SO_4. The electrode demonstrates a stable performance for 10 000 cycles and a fast response, resulting in more than 100 F g^{-1} at a scan rate of 2 V s^{-1}.

Experimental Section

Synthesis of CF, OLC, and Composite Electrodes

CF mats were synthesized through the thermal annealing of electrospun polymer fibers of PAN (Sigma Aldrich). For electrospinning, the polymer powder was dissolved in dimethylformamide (DMF; Sigma Aldrich, anhydrous 99.8%) in an 8 wt% solution, resulting in a viscous liquid. A 5 mL aliquot of the polymer solution was spun with a MECC electrospinning system (MECC Co.) at 15 kV by using a feed rate of 0.4 mL h^{-1} and 250 mm fly distance for 10 h, using a transverse speed of 20 mm s^{-1} over a travel distance of 250 mm. The electrospinning setup consisted of a syringe and a needle connected with PTFE tubing and a plate collector coated with conventional alumina foil as the substrate. After electrospinning, polymer-fiber mats were converted to CFs by using a two-step treatment. First, the polymer fibers were oxidized in air in a furnace at 250 °C for 30 min by using a heating rate of 5 °C min^{-1}. To avoid large temperature variations and deformation of the mats during heating, the samples were placed between two graphite plates. Second, the oxidized PAN fiber mats were thermally annealed in a water-cooled high-temperature furnace with tungsten heater (Thermal Technology Inc.) in pure argon (purity 4.6). The temperature profile exhibited three holding temperatures of 700 and 1100 °C for 1 h, and 1700 °C for 3 h. The heating rate was 5 °C min^{-1} and the cooling rate 15 °C min^{-1}.

Composite electrodes consisting of CFs and OLCs were made through a two-step approach: drop casting of NDs into the polymer-fiber mats, followed by a thermal annealing process to synergistically convert the composite to conductive CFs and OLCs. The NDs were supplied in a 5 wt% dispersion in water (Single-digit NDs 5 wt% in water, PlasmaChem), and the supplier used a post-synthesis treatment to produce a dispersion composed of so-called single-digit NDs that were fully dispersed and de-agglomerated in water with an average aggregate size of 5–15 nm and a SSA of 350–390 m^2 g^{-1}. The dispersion was drop cast in several steps on the oxidized PAN polymer-fiber mats until the desired mass loading had been reached. Between the casting steps, the fiber mats were dried in a vacuum furnace at 120 °C for 1 h at 10 mbar to evaporate the solvent (H_2O). The filling degrees with ND were 50, 250, or 500 wt% (related to the mass of oxidized polymer fibers). The samples are referred to as PAN50, PAN250, or PAN500, respectively. After placing the NDs in the interfiber space, the same thermal annealing process, as already mentioned for the electrospun PAN fibers, was used to create free-standing and binder-free CF electrodes filled with OLC (CF–CF500).

For comparison, conventional PTFE-bound electrodes were prepared with OLCs synthesized with the same temperature-treatment protocol as outlined before. Free-standing OLC electrodes were prepared by mixing 90 wt% of OLCs with 10 wt% polytetrafluoroethylene (60 wt% PTFE in water, Sigma Aldrich) together with ethanol to make a slurry. For the AC electrode, 95 wt% carbon and 5 wt% PTFE were used. The slurries were tip-sonicated for 10 min at approximately 4 W, and then constantly stirred until a dough-like mass was developed. By using a twin roller (MTI HR01, MTI Corporation), the PTFE-bound mass was rolled into free-standing sheets with a thickness of approximately 100 μm. Prior to use, the electrodes were dried at 120 °C in vacuum at 2 kPa for 24 h. For half-cell experiments, the oversized counter electrode was composed of AC (YP80, Kuraray Chemical Co.) and 5 wt% PTFE with a thickness of approximately 300 μm. After drying, the working electrodes were prepared by punching out 6 mm disks of CF mats, OLC/CF hybrid-fiber mats, and PTFE-bound OLC and AC electrodes.

Decoration of Composite Electrodes with PQ

The CF500 hybrid-fiber mats were functionalized with PQ. First, the PQ powder (Sigma Aldrich) was dissolved in ethanol (1.1 mg mL^{-1}) and filtered several times with a syringe filter (0.1 μm pore size). The resulting solution was drop cast on the electrodes by using a volume of 20 μL and drying at room temperature; this process was repeated several times to prepare two different levels of PQ loading. For the PQ-20 sample, only one casting step was used, resulting in an overall volume of 20 μL. For the PQ-200 sample, ten casting steps were used with an overall volume of PQ-solution of 200 μL. To prepare a composite electrode with the maximum loading of PQ (PQ-max), the electrode was put into 5 mL of the solution for 24 h. For comparison, the PTFE-bound OLC electrode (OLC-PQ-max) and the CF electrode (CF-PQ-max) were also soaked in the 5 mL solution for 24 h. After decoration with PQ, all samples were rinsed with ethanol several times and dried at room temperature in vacuum at 2 kPa for 24 h. This step was adopted to remove any PQ that was not adsorbed on the electrode surface in order to avoid the addition of (electrochemically) dead mass.

Structural Characterization

Electron Microscopy

SEM images were taken with a FEI Versa 3D Dual Beam (FEI) at 10 kV. Free-standing electrodes as well as OLC powders were mounted on a steel sample holder with sticky carbon tape. For cross-sectional images, the samples were cut with a razor blade and fixed with carbon tape on a 90° tilted sample holder. Samples consisting of polymer or NDs were sputter-coated with gold for 60 s with an Autofine Coater (JEOL) prior to imaging. The fiber diameter distribution was derived from SEM images by using ImageJ software. For each sample, two different batches were prepared and the diameters were manually read at five different positions on the sample. The total number of measured diameters was 50 and a Gaussian function was used to fit the data.

Samples for TEM were prepared by dispersing powders or fibers in ethanol and drop-casting them on a copper grid with a lacey carbon film (Gatan). All measurements were carried out with a JEOL 2100F operating at 200 kV. CF mats or composite mats were first tip-sonicated in ethanol for 5 min to make a drop cast on the copper grids possible.

Raman Spectroscopy

Raman spectra were measured with a Renishaw inVia Raman Microscope by using an Nd-YAG laser with an excitation wavelength of 532 nm. The grating was 2400 lines mm^{-1}, yielding a spectral resolution of approximately 1.2 cm^{-1}, and the spot size on the sample in the focal plane was approximately 2 μm with an output power of 0.2 mW. Spectra were recorded for 20 s and accumulated 50 times to obtain high signal-to noise and signal-to-background ratios. Peak fitting was performed by employing two Lorentzian peaks, one for the D mode and the other for the G mode.

Conductivity Measurements with a Four-Point Probe

The conductivity of the electrodes was determined with a custom-built four-point probe (tip diameter: 1.5 mm; tip distance 1.75 mm). The areal resistance was measured ten times on different positions of the electrode material (3×3 cm^2), and Equation (1) was used to calculate the electrode conductivity (σ) normalized to the thickness:[52]

$$\sigma = \frac{\ln(2)}{\pi}\frac{I}{U \cdot d} \quad (1)$$

where I is the current, U the voltage, and d the thickness of the electrode measured with a micrometer screw.

Gas Sorption Analysis

To remove adsorbed molecules from the surface, all samples were degassed at 200 °C for 30 min and subsequently at 300 °C for 20 h at a relative pressure of 0.1 Pa. Nitrogen-gas sorption analysis at −196 °C was performed with a Quantachrome Autosorb 6B system. The pore-size distribution (PSD) was derived by using quenched-solid density functional theory (QSDFT) supplied by Quantachrome, assuming a slit-shape pore model.[53] The SSA obtained by using the BET equation was calculated in the linear regime of the measured isotherms at a partial pressure (P/P_0) between 0.1 and 0.3.[54]

Particle-Size Analysis

Particle-size analysis was performed by using centrifugal sedimentation analysis (LUMiSizer; LUM GmbH, Germany). The ND powder was dispersed in water (0.5 wt%) by using tip sonication at approximately 4 W for 1 h and tested in a range from 200 to 4000 rpm.

Electrochemical Characterization

TEA–BF_4 (1 M) in ACN from BASF and aqueous sulfuric acid (1 M) from Sigma Aldrich were used as electrolytes. We used two-electrode and three-electrode setups in this study to provide, for the first time, comparative half- and full-cell performance data, respectively. The prepared electrodes (6 mm in diameter) were separated by a glass-fiber separator with a diameter of 13 mm (type GF/D, Whatman). By using 1 M TEA–BF_4 in ACN, the electrode/separator/electrode arrangement was placed between two carbon-coated aluminum foils (diameter 12 mm, type Zflo 2653, Exopack technologies) and compressed with spring-loaded titanium pistons. For the aqueous system, in this case using 1 M H_2SO_4, the electrode/separator/electrode sandwich was placed between platinum disks as current collectors (12 mm in diameter and 100 μm thick,

Mateck) and compressed with spring-loaded polyether ether ketone (PEEK) pistons. In the three-electrode setup, the counter electrode consisted of AC (YP80, Kuraray) with 5 wt% PTFE and a thickness of 300 μm. The reference electrode in the organic system was AC (YP50, Kuraray) with 5 wt% PTFE, and in the aqueous system a platinum wire (Carl Schaefer) with a diameter of 0.5 mm. The cells for organic electrolyte were dried at 120 °C and a vacuum of 2 kPa for 12 h before they were put in an argon-filled glove box (MBraun Labmaster 130; O_2, H_2O < 1 ppm), where they were vacuum filled with a syringe containing 1 M TEA–BF_4 in ACN. The cells for the aqueous system were directly, without further drying, vacuum filled with a syringe and the mentioned electrolyte.

All electrochemical measurements were carried out by using a VSP300 or VMP300 potentiostat/galvanostat from Bio-Logic in cyclic voltammetry or galvanostatic (GCPL) mode. In the organic system, CVs at different scan rates from 1 mV s^{-1} to 2 V s^{-1} between −1 and +1 V versus AC were conducted in a half cell.[47,55] Each voltage was applied three times and the capacitance at 1 V for each scan rate was calculated by using Equation (2):[56]

$$C = \frac{\int_{t_0}^{t_{end}} I(t)\mathrm{d}t}{U} \quad (2)$$

where C is the capacitance, t the time (t_0: start of discharge; t_{end}: end of discharge), and U the potential. The specific capacitance in the three-electrode setup was determined with Equation (3):[57,58]

$$C_{sp} = \frac{C}{m} \quad (3)$$

in which m is the mass of the working electrode. By using GCPL mode in a full-cell arrangement (two electrodes), the current was varied to apply different current densities from 0.1 to 100 A g^{-1} with 10 s resting time between charging/discharging and a potential limitation of 2.5 V. For PTFE-bound electrodes, the maximum current density was 50 A g^{-1}, owing to current limitations of the potentiostat. The specific current relates in this case to the mass of both electrodes, and the resulting capacitance was calculated from the current and the time for discharge with respect to the *IR* drop of the cell. Stability was measured by using both long-time voltage floating tests and voltammetric cycling. The long-time voltage floating test in a full cell was performed between 0 and 2.5 V with a constant current of 0.5 A g^{-1} and a holding time of 10 h. After galvanostatic cycling three times, the voltage was held for 10 h at 2.5 V and the procedure was repeated to an overall holding time of 100 h. Voltammetric cycling from 0 to 2.5 V at 200 mV s^{-1} was repeated 10 000 times, and every 200 cycles were recorded.

In the aqueous system, only cyclic voltammetry was used for electrochemical characterization. By using a three-electrode setup, different scan rates over a range of three orders of magnitude from 1 mV s^{-1} to 2 V s^{-1} were applied between 0 and −0.4 V. In the two-electrode configuration, the potential window was successively opened from −0.2 to +0.2 V in 100 mV steps to the maximal potential window of −0.5 to +0.5 V. Electrochemical stability was tested by using cyclic voltammetry from 0 to −0.4 V versus Pt at a scan rate of 200 mV s^{-1} for 10 000 cycles. The capacitance in the aqueous system was calculated by using Equation (4):[58]

$$C = \frac{\int_{U_0}^{U_{end}} \frac{I\mathrm{d}U}{v}}{m\Delta U} \quad (4)$$

where I is the current, v the scan rate, m the mass of the working electrode, and ΔU the potential window. The capacity of one electrode was measured according to Equation (5):[58]

$$C = \frac{\int_{U_0}^{U_{end}} \frac{I\mathrm{d}U}{v}}{m} \quad (5)$$

Electrochemical impedance spectroscopy was performed at 0 V in full cells for the CF500, PQ-max, and OLC-PQ-max systems in the frequency range from 100 kHz to 10 mHz with six points per decade and five repetitions per point. The excitation amplitude was 5 mV.

Acknowledgements

We acknowledge funding from the German Federal Ministry for Research and Education (BMBF) in support of the nanoEES^{3D} project (award number 03K3013) as part of the strategic funding initiative energy storage framework. We kindly acknowledge additional funding via the INM FOCUS project ELECTRIC and thank Prof. Eduard Arzt (INM) for his continuing support.

Keywords: binder-free electrodes · carbon · quinones · rate handling · supercapacitors

[1] F. Béguin, V. Presser, A. Balducci, E. Frackowiak, *Adv. Mater.* **2014**, *26*, 2219.
[2] Z. Yang, J. Zhang, M. C. Kintner-Meyer, X. Lu, D. Choi, J. P. Lemmon, J. Liu, *Chem. Rev.* **2011**, *111*, 3577.
[3] J. B. Goodenough, *Energy Environ. Sci.* **2014**, *7*, 14; J. N. Tiwari, R. N. Tiwari, K. S. Kim, *Prog. Mater. Sci.* **2012**, *57*, 724.
[4] N. S. Choi, Z. Chen, S. A. Freunberger, X. Ji, Y. K. Sun, K. Amine, G. Yushin, L. F. Nazar, J. Cho, P. G. Bruce, *Angew. Chem. Int. Ed.* **2012**, *51*, 9994; *Angew. Chem.* **2012**, *124*, 10134; C. Liu, F. Li, L. P. Ma, H. M. Cheng, *Adv. Mater.* **2010**, *22*, E28.
[5] P. Simon, Y. Gogotsi, B. Dunn, *Science* **2014**, *343*, 1210.
[6] H. Shi, *Electrochim. Acta* **1996**, *41*, 1633; D. Qu, H. Shi, *J. Power Sources* **1998**, *74*, 99.
[7] K. H. An, W. S. Kim, Y. S. Park, J.-M. Moon, D. J. Bae, S. C. Lim, Y. S. Lee, Y. H. Lee, *Adv. Funct. Mater.* **2001**, *11*, 387.
[8] L. L. Zhang, R. Zhou, X. Zhao, *J. Mater. Chem.* **2010**, *20*, 5983.
[9] V. Presser, L. Zhang, J. J. Niu, J. McDonough, C. Perez, H. Fong, Y. Gogotsi, *Adv. Energy Mater.* **2011**, *1*, 423.
[10] A. Fuertes, G. Lota, T. Centeno, E. Frackowiak, *Electrochim. Acta* **2005**, *50*, 2799.
[11] M. Toupin, D. Bélanger, I. R. Hill, D. Quinn, *J. Power Sources* **2005**, *140*, 203.
[12] Y. Gogotsi, V. Presser, *Carbon nanomaterials*, CRC Press, 2013; M. E. Plonska-Brzezinska, L. Echegoyen, *J. Mater. Chem. A* **2013**, *1*, 13703.
[13] H. W. Kroto, J. R. Heath, S. C. O'Brien, R. F. Curl, R. E. Smalley, *Nature* **1985**, *318*, 162; I. Suarez-Martinez, N. Grobert, C. P. Ewels, *Carbon* **2012**, *50*, 741.
[14] C. Portet, G. Yushin, Y. Gogotsi, *Carbon* **2007**, *45*, 2511.
[15] D. M. Anjos, J. K. McDonough, E. Perre, G. M. Brown, S. H. Overbury, Y. Gogotsi, V. Presser, *Nano Energy* **2013**, *2*, 702.
[16] D. Pech, M. Brunet, H. Durou, P. Huang, V. Mochalin, Y. Gogotsi, P.-L. Taberna, P. Simon, *Nat. Nanotechnol.* **2010**, *5*, 651.
[17] J. K. McDonough, A. I. Frolov, V. Presser, J. Niu, C. H. Miller, T. Ubieto, M. V. Fedorov, Y. Gogotsi, *Carbon* **2012**, *50*, 3298.
[18] P. Huang, M. Heon, D. Pech, M. Brunet, P.-L. Taberna, Y. Gogotsi, S. Lofland, J. D. Hettinger, P. Simon, *J. Power Sources* **2013**, *225*, 240.
[19] Y. V. Butenko, V. L. Kuznetsov, A. L. Chuvilin, V. N. Kolomiichuk, S. V. Stankus, R. A. Khairulin, B. Segall, *J. Appl. Phys.* **2000**, *88*, 4380; V. L. Kuznetsov, A. L. Chuvilin, Y. V. Butenko, I. Y. Mal'kov, V. M. Titov, *Chem. Phys.*

Lett. **1994**, *222*, 343; S. Tomita, A. Burian, J. C. Dore, D. LeBolloch, M. Fujii, S. Hayashi, *Carbon* **2002**, *40*, 1469.
[20] K. L. Van Aken, J. K. McDonough, S. Li, G. Feng, S. M. Chathoth, E. Mamontov, P. F. Fulvio, P. T. Cummings, S. Dai, Y. Gogotsi, *J. Phys. Condens. Matter* **2014**, *26*, 284104.
[21] R. Lin, P.-L. Taberna, S. Fantini, V. Presser, C. R. Pérez, F. Malbosc, N. L. Rupesinghe, K. B. Teo, Y. Gogotsi, P. Simon, *J. Phys. Chem. Lett.* **2011**, *2*, 2396.
[22] M. Zeiger, N. Jäckel, M. Aslan, D. Weingarth, V. Presser, *Carbon* **2015**, *84*, 584.
[23] W. Gu, G. Yushin, *WIREs Energy Environ.* **2014**, *3*, 424.
[24] J. R. Miller, A. F. Burke, *Electrochem. Soc. Interface* **2008**, *17*, 53.
[25] W. Gu, N. Peters, G. Yushin, *Carbon* **2013**, *53*, 292; Y. Gao, Y. S. Zhou, M. Qian, X. N. He, J. Redepenning, P. Goodman, H. M. Li, L. Jiang, Y. F. Lu, *Carbon* **2013**, *51*, 52.
[26] O. Barbieri, M. Hahn, A. Herzog, R. Kötz, *Carbon* **2005**, *43*, 1303.
[27] Y. Wang, S. F. Yu, C. Y. Sun, T. J. Zhu, H. Y. Yang, *J. Mater. Chem.* **2012**, *22*, 17584.
[28] M. V. K. Azhagan, M. V. Vaishampayan, M. V. Shelke, *J. Mater. Chem. A* **2014**, *2*, 2152.
[29] I. Kovalenko, D. G. Bucknall, G. Yushin, *Adv. Funct. Mater.* **2010**, *20*, 3979.
[30] E. Frackowiak, M. Meller, J. Menzel, D. Gastol, K. Fic, *Faraday Discuss.* **2014**, *172*, 179.
[31] E. Laviron, *J. Electroanal. Chem. Interfacial Electrochem.* **1984**, *164*, 213.
[32] S. Bailey, I. Ritchie, *Electrochim. Acta* **1985**, *30*, 3.
[33] S. Roldán, M. Granda, R. Menendez, R. Santamaria, C. Blanco, *The Journal of Physical Chemistry C* **2011**, *115*, 17606.
[34] J. Balach, M. M. Bruno, N. G. Cotella, D. F. Acevedo, C. A. Barbero, *J. Power Sources* **2012**, *199*, 386.
[35] K. Kalinathan, D. P. DesRoches, X. Liu, P. G. Pickup, *J. Power Sources* **2008**, *181*, 182.
[36] H. Wang, H. Wu, Y. Chang, Y. Chen, Z. Hu, *Chin. Sci. Bull.* **2011**, *56*, 2092.
[37] X. Chen, H. Wang, H. Yi, X. Wang, X. Yan, Z. Guo, *J. Phys. Chem. C* **2014**, *118*, 8262.
[38] V. Ruiz, C. Blanco, M. Granda, R. Menéndez, R. Santamaría, *J. Appl. Electrochem.* **2007**, *37*, 717.
[39] X. Wang, B. Ding, G. Sun, M. Wang, J. Yu, *Prog. Mater. Sci.* **2013**, *58*, 1173; Z.-M. Huang, Y.-Z. Zhang, M. Kotaki, S. Ramakrishna, *Compos. Sci. Technol.* **2003**, *63*, 2223.
[40] L. Zhang, A. Aboagye, A. Kelkar, C. Lai, H. Fong, *J. Mater. Sci.* **2014**, *49*, 463.
[41] T. Wang, S. Kumar, *J. Appl. Polym. Sci.* **2006**, *102*, 1023.
[42] M. S. A. Rahaman, A. F. Ismail, A. Mustafa, *Polym. Degrad. Stab.* **2007**, *92*, 1421.
[43] V. Kuznetsov, Y. V. Butenko, V. Zaikovskii, A. Chuvilin, *Carbon* **2004**, *42*, 1057.
[44] A. C. Ferrari, *Solid State Commun.* **2007**, *143*, 47.
[45] F. Tuinstra, *J. Chem. Phys.* **1970**, *53*, 1126; M. A. Pimenta, G. Dresselhaus, M. S. Dresselhaus, L. G. Cancado, A. Jorio, R. Saito, *Phys. Chem. Chem. Phys.* **2007**, *9*, 1276.
[46] N. Jäckel, D. Weingarth, M. Zeiger, M. Aslan, I. Grobelsek, V. Presser, *J. Power Sources* **2014**, *272*, 1122.
[47] D. Weingarth, M. Zeiger, N. Jäckel, M. Aslan, G. Feng, V. Presser, *Adv. Energy Mater.* **2014**, *4*, 1400316.
[48] H. Gerischer, R. McIntyre, D. Scherson, W. Storck, *J. Phys. Chem.* **1987**, *91*, 1930.
[49] A. Kornyshev, N. Luque, W. Schmickler, *J. Solid State Electrochem.* **2014**, *18*, 1345; P. Ruch, L. Hardwick, M. Hahn, A. Foelske, R. Kötz, A. Wokaun, *Carbon* **2009**, *47*, 38.
[50] D. M. Anjos, A. I. Kolesnikov, Z. Wu, Y. Cai, M. Neurock, G. M. Brown, S. H. Overbury, *Carbon* **2013**, *52*, 150.
[51] K. Kano, B. Uno, *Anal. Chem.* **1993**, *65*, 1088.
[52] F. M. Smits, *Bell Syst. Tech. J.* **1958**, *37*, 711.
[53] G. Y. Gor, M. Thommes, K. A. Cychosz, A. V. Neimark, *Carbon* **2012**, *50*, 1583; A. V. Neimark, Y. Lin, P. I. Ravikovitch, M. Thommes, *Carbon* **2009**, *47*, 1617.
[54] S. Brunauer, P. H. Emmett, E. Teller, *J. Am. Chem. Soc.* **1938**, *60*, 309.
[55] P. W. Ruch, D. Cericola, M. Hahn, R. Kötz, A. Wokaun, *J. Electroanal. Chem.* **2009**, *636*, 128.
[56] B. E. Conway, *Electrochemical Supercapacitors*, Springer, Berlin **1999**.
[57] a) M. D. Stoller, R. S. Ruoff, *Energy Environ. Sci.* **2010**, *3*, 1294; b) F. Beguin, E. Frackowiak, *Supercapacitors*, Wiley, Weinheim **2013**.
[58] S. Zhang, N. Pan, *Adv. Energy Mater.* **2015**, *5*.
[59] A. Le Comte, D. Chhin, A. Gagnon, R. Retoux, T. Brousse, D. Belanger, *J. Mater. Chem. A* **2015**, *3*, 6146.

Received: March 30, 2015
Published online on May 26, 2015

CHEMELECTROCHEM

Supporting Information

Quinone-Decorated Onion-Like Carbon/Carbon Fiber Hybrid Electrodes for High-Rate Supercapacitor Applications

Marco Zeiger,[a, b] Daniel Weingarth,[a] and Volker Presser*[a, b]

celc_201500130_sm_miscellaneous_information.pdf

Supporting Information

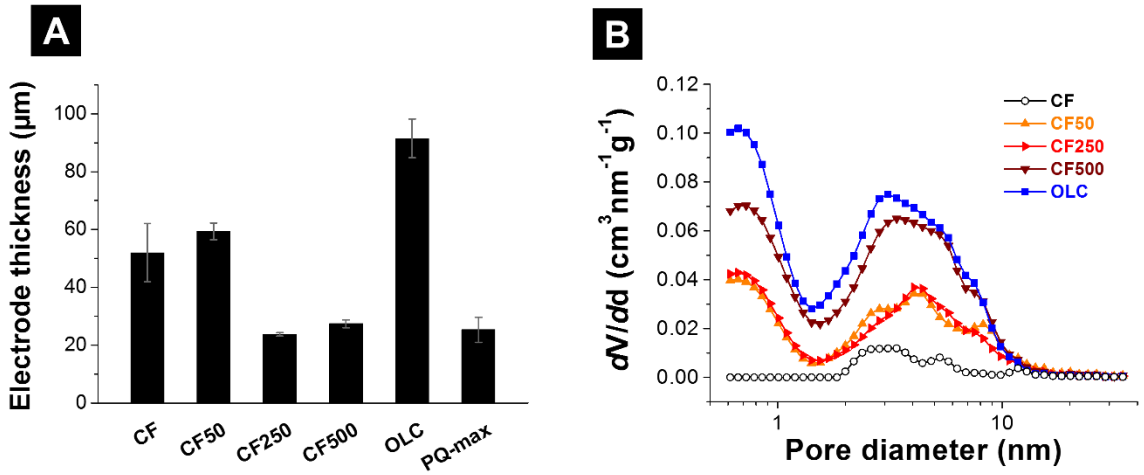

Figure S1. Electrode thickness measured with scanning electron microscopy on cross-sections (A) and pore size distributions from gas sorption analysis and DFT deconvolution (B).

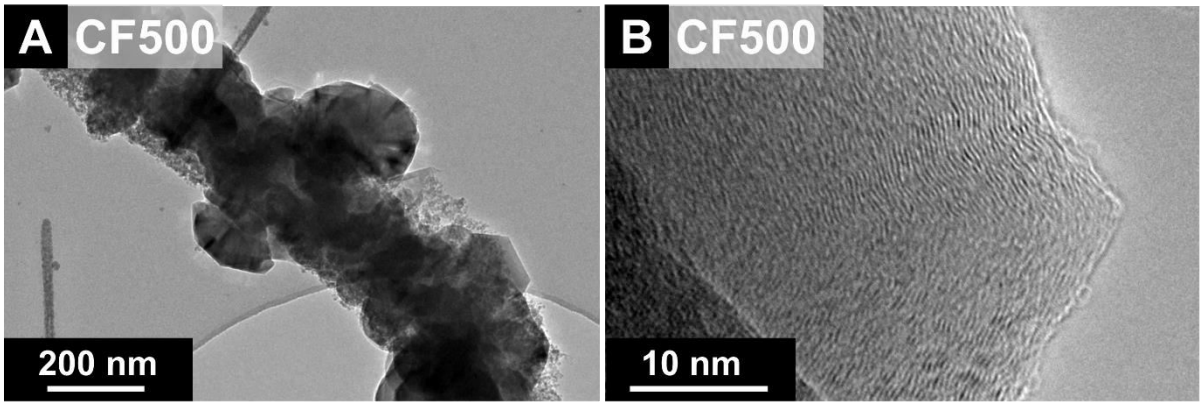

Figure S2. Transmission electron micrographs of the composite electrode CF500.

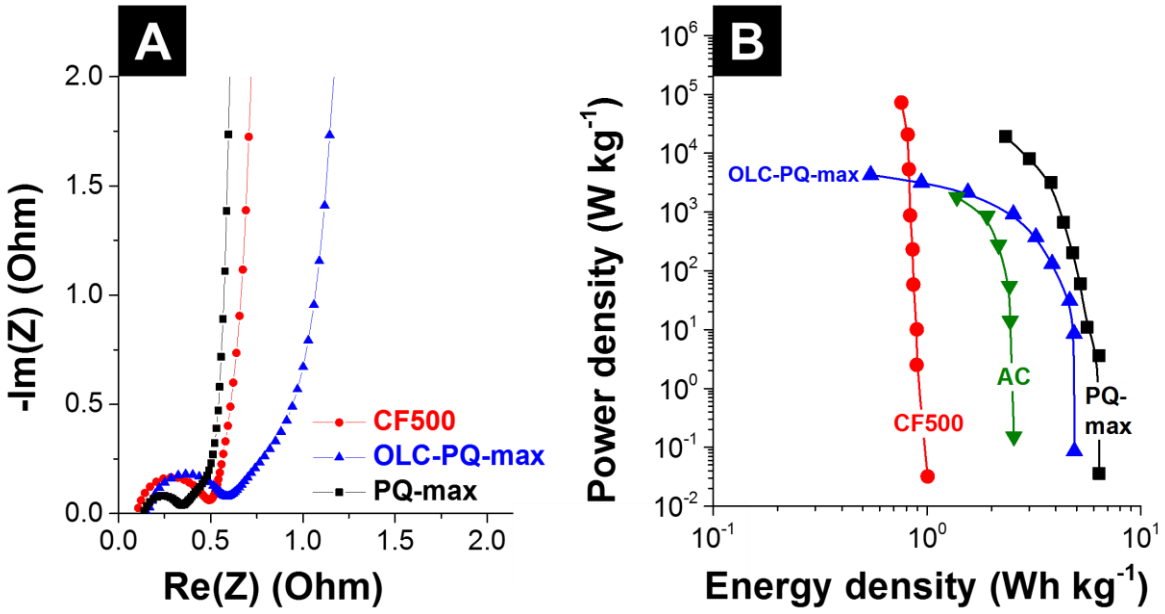

Figure S3. Electrochemical impedance spectroscopy (A) and Ragone plot (B) for CF-500, OLC-PQ-max, and PQ-max samples.

3.7 Vanadium pentoxide/carbide-derived carbon core shell hybrid particles for high performance electrochemical energy storage

Marco Zeiger,[1,2] Teguh Ariyanto,[3] Benjamin Krüner,[1,2] Nicolas J. Peter,[4] Simon Fleischmann,[2] Bastian J. M. Etzold,[3,5,*] and Volker Presser[1,2,*]

[1] *INM - Leibniz Institute for New Materials, 66123 Saarbrücken, Germany*
[2] *Department of Materials Science and Engineering, Saarland University, 66123 Saarbrücken, Germany*
[3] *Friedrich-Alexander Universität Erlangen-Nürnberg, Lehrstuhl für Chemische Reaktionstechnik, 91058 Erlangen, Germany*
[4] *Max-Planck Institut für Eisenforschung GmbH, 40237 Düsseldorf, Germany*
[5] *Technische Universität Darmstadt, Ernst-Berl-Institut für Technische und Makromolekulare Chemie, 64287 Darmstadt, Germany*

Citation:
Zeiger, M.; Ariyanto, T.; Krüner, B.; Peter, N. J.; Fleischmann, S.; Etzold, B. J. M.; Presser, V., Vanadium pentoxide/carbide-derived carbon core-shell hybrid particles for high performance electrochemical energy storage. *J. Mater. Chem. A* **2016,** 4, 18899-18909. (DOI: 10.1039/C6TA08900C)

Own contribution: Design, planning, writing, calcination of VC and CDC particles, Raman spectroscopy, transmission electron microscopy, thermogravimetric analysis, conductivity measurements, electrochemistry.

Abstract:

A novel, two step synthesis is presented combining the formation of carbide-derived carbon (CDC) and redox-active vanadium pentoxide (V_2O_5) in a core-shell manner using solely vanadium carbide (VC) as the precursor. In a first step, the outer part of VC particles is transformed to nanoporous CDC owing to the in situ formation of chlorine gas from $NiCl_2$ at 700 °C. In a second step, the remaining VC core is calcined in synthetic air to obtain V_2O_5/CDC core-shell particles. Materials characterization by means of electron microscopy, Raman spectroscopy, and X-ray diffraction clearly demonstrates the partial transformation from VC to CDC, as well as the successive oxidation to V_2O_5/CDC cor-shell particles. Electrochemical performance was tested in organic 1 M $LiClO_4$ in acetonitrile using half- and asymmetric full-cell configuration. High specific capacities of 420 mA h g^{-1} (normalized to V_2O_5) and 310 mA h g^{-1} (normalized to V_2O_5/CDC) were achieved. The unique nanotextured core-shell architecture enables high power retention with ultrafast charging and discharging, achieving more than 100 mA h g^{-1} at 5 A g^{-1} (rate of 12C). Asymmetric cell design with CDC on the positive polarization side leads to a high specific energy of up to 80 W h kg^{-1} with a superior retention of more than 80% over 10 000 cycles and an overall energy efficiency of up to 80% at low rates

Journal of Materials Chemistry A

PAPER

View Article Online
View Journal | View Issue

Cite this: J. Mater. Chem. A, 2016, 4, 18899

Vanadium pentoxide/carbide-derived carbon core–shell hybrid particles for high performance electrochemical energy storage†

Marco Zeiger,[ab] Teguh Ariyanto,[c] Benjamin Krüner,[ab] Nicolas J. Peter,[d] Simon Fleischmann,[b] Bastian J. M. Etzold*[ce] and Volker Presser*[ab]

Received 13th October 2016
Accepted 31st October 2016

DOI: 10.1039/c6ta08900c

www.rsc.org/MaterialsA

A novel, two step synthesis is presented combining the formation of carbide-derived carbon (CDC) and redox-active vanadium pentoxide (V_2O_5) in a core–shell manner using solely vanadium carbide (VC) as the precursor. In a first step, the outer part of VC particles is transformed to nanoporous CDC owing to the *in situ* formation of chlorine gas from $NiCl_2$ at 700 °C. In a second step, the remaining VC core is calcined in synthetic air to obtain V_2O_5/CDC core–shell particles. Materials characterization by means of electron microscopy, Raman spectroscopy, and X-ray diffraction clearly demonstrates the partial transformation from VC to CDC, as well as the successive oxidation to V_2O_5/CDC core–shell particles. Electrochemical performance was tested in organic 1 M $LiClO_4$ in acetonitrile using half- and asymmetric full-cell configuration. High specific capacities of 420 mA h g^{-1} (normalized to V_2O_5) and 310 mA h g^{-1} (normalized to V_2O_5/CDC) were achieved. The unique nanotextured core–shell architecture enables high power retention with ultrafast charging and discharging, achieving more than 100 mA h g^{-1} at 5 A g^{-1} (rate of 12C). Asymmetric cell design with CDC on the positive polarization side leads to a high specific energy of up to 80 W h kg^{-1} with a superior retention of more than 80% over 10 000 cycles and an overall energy efficiency of up to 80% at low rates.

1. Introduction

Supercapacitors are electrochemical energy storage devices, which present ultrafast charge–discharge rates leading to higher power compared to conventional batteries, but suffer from relatively low specific energies.[1–4] The high specific power of ~10 kW kg^{-1} benefits applications with charge- and discharge rates in the order of seconds and minutes, such as flashlights, high power machinery, or emergency doors in airplanes, to name just a few.[2,5] Depending on the energy storage mechanism, we can differentiate between two types of supercapacitors, namely electrical double-layer capacitors (EDLCs) that store energy by ion electrosorption, and pseudocapacitors that accomplish a capacitor-like charge-voltage behavior by fast redox reactions.[6] Today, most EDLCs employ activated carbon (AC) electrodes with surface areas between 1500 and 2000 m^2 g^{-1}, leading to typical capacitance values of 100–200 F g^{-1} and specific energies of up to *ca.* 20 W h kg^{-1}, depending on the electrolyte and the cell configuration.[6] By virtue of these values, the energy storage capacity of supercapacitors is significantly smaller than conventional batteries (*e.g.*, lithium ion batteries: >100 W h kg^{-1}).[6] A facile way to enhance the electrochemical performance is to increase the specific surface area of the electrode material and to optimize the pore size distribution.[7] This is particularly effective for a material with very high pore tunability, as presented in the case of carbide-derived carbons (CDCs).[8] However, this strategy is limited by the minimum pore size required for ion accessibility and the charge screening ability of carbon.[7,9,10] Further enhancements of the energy storage capacity can be accomplished by employing redox-active materials for faradaic charge transfer.[11,12] The latter can be either in the form of fast redox processes of surface groups, ion intercalation in the electrode material, or redox reactions of the electrolyte.[13,14] Depending on the charge-voltage profile of the involved faradaic reaction(s), one differentiates between capacitor-like (*i.e.*, pseudocapacitive) or battery-like behavior.[15] Pseudocapacitive materials, exhibiting a constant ratio of charge and voltage (*i.e.*, capacitance, unit: farad), are, for example, ruthenium oxide,[16] manganese oxide,[17] or MXene.[18] Battery-like systems, exhibiting distinct redox peaks

[a]INM – Leibniz Institute for New Materials, 66123 Saarbrücken, Germany. E-mail: volker.presser@leibniz-inm.de

[b]Department of Materials Science and Engineering, Saarland University, 66123 Saarbrücken, Germany

[c]Friedrich-Alexander Universität Erlangen-Nürnberg, Lehrstuhl für Chemische Reaktionstechnik, 91058 Erlangen, Germany

[d]Max-Planck Institut für Eisenforschung GmbH, 40237 Düsseldorf, Germany

[e]Technische Universität Darmstadt, Ernst-Berl-Institut für Technische und Makromolekulare Chemie, 64287 Darmstadt, Germany. E-mail: etzold@tc1.tu-darmstadt.de

† Electronic supplementary information (ESI) available. See DOI: 10.1039/c6ta08900c

in the cyclic voltammogram, are, for example, quinone surface groups[19,20] or many metal oxides working as cathodic lithium-intercalation hosts (such as $LiFePO_4$, $LiCoO_2$, $LiMn_2O_4$, and $LiFeSO_4F$; ref. 21).

A very promising electrochemical system employs the hybridization of carbon materials with vanadium pentoxide (V_2O_5).[22–26] By this way, the beneficial electrical conductivity and nanotextured surface of carbon is complemented by the high, battery-like charge storage capacity of vanadia with a theoretical capacity of 147 mA h g^{-1} for intercalation of 1 M of Li in the V_2O_5 structure.[27] Several studies have investigated vanadium pentoxide as a cathode material in lithium ion batteries, exhibiting high capacities between 350 and 750 mA h g^{-1}.[28–30] Furthermore, other types of vanadia in different oxidation states can be used in batteries, such as VO_2,[31] and also dissolved as an electrolyte in redox-flow batteries.[32] In a previous study, we used atomic layer deposition (ALD) for highly controllable decoration of carbon onions with V_2O_5, achieving defined thickness, morphology, and crystallinity of the metal oxide phase.[33] A high specific energy (38 W h kg^{-1}) was achieved for a full-cell using V_2O_5/carbon onion *vs.* activated carbon (asymmetric cell), which is *ca.* 2-times higher than that of standard activated carbon in organic electrolytes.[33] Even higher values for the specific energy were found for interpenetrating networks of CNTs and V_2O_5 nanowires (40 W h kg^{-1})[22] and vanadia-coated reduced graphene oxide sheets (76 W h kg^{-1}).[34] While promising, the practical adaptation of microfabrication and ALD remains limited and more facile synthesis routes for V_2O_5/carbon hybrid materials remain in high demand.

The combination of redox-active metal oxides with conductive and porous carbons in a hybrid device can be achieved by mechanical mixing (thus exhibiting strongly reduced conductivity), or the decoration of the carbon with metal oxides. For the latter, especially when using highly porous carbons, issues of pore clogging may arise, leading to a strong decrease in capacitance and specific energy. These complications are avoided by not coating the carbon with the metal oxide, but rather fabricating a metal oxide core with a porous carbon shell. Inspired by carbon only core–shell architectures, which can be obtained for CDCs,[35,36] we present a novel two-step synthesis for V_2O_5/CDC composites in a core–shell arrangement. Our approach requires only one precursor (vanadium carbide), which is first partially transformed to nanoporous CDC by chlorine treatment of carbide, and then partially calcined, yielding core–shell V_2O_5/CDC particles. The chlorination step was needed as it is an effective way to transform a metal carbide to carbon. The nanoporous carbon shell makes the vanadium pentoxide core accessible for ion intercalation and works as a conductive additive. This was accomplished by a high level of control over the synthesis steps, which prevented a completion of both the chlorination and the oxidation processes. Rigorous structural and electrochemical characterization was carried out to establish the high energy storage capacity of the material in organic electrolytes. The combination of carbon and vanadia is of mutual benefit: carbon contributes electrical conductivity (and, to a lesser extent, double-layer capacitance) and vanadia provides a large energy storage capacity. However, the design of the two phases and their nanoscopic arrangement are of high importance for the resulting electrochemical performance. As our data will show, the firm of transformed VC-derived V_2O_5 and VC-CDC enables attractive electrochemical performances.

2. Materials and methods

V_2O_5/porous carbon core–shell particles were synthesized using a two-step approach: (1) VC/CDC core–shell particles are produced by etching vanadium from the outside to the inside of VC particles with a remaining VC core. (2) The residual VC core inside the CDC matrix is calcined by oxidation in synthetic air, resulting in V_2O_5/CDC core–shell particles. These two steps are explained in detail in the next sections.

2.1 Synthesis of vanadium carbide/carbide-derived carbon core–shell particles

Vanadium carbide (VC)/CDC core–shell particles were synthesized by reactive extraction of vanadium using *in situ* generation of chlorine. 1 g VC powder (purity 99.9%, <2 μm, Sigma Aldrich) was thoroughly mixed with $NiCl_2 \cdot 6H_2O$ (purity 99.95%, Alfa Aesar) and filled into a graphite crucible placed in an isothermal zone of the reactor (Ø = 32 cm, length = 1 m). The reactor was evacuated to 0.01 mbar and then heated to 700 °C at a heating rate of 2.5 °C min^{-1}. After a holding period of 3 h at this temperature, the reactor was cooled to room temperature under a helium purge. The resulting product was then poured into 500 mL of 1 M HCl and the solution was vigorously stirred using a magnetic stir bar. After filtration, the acid washing was repeated with similar procedures to ensure the removal of nickel species. The product was finally washed using distilled water until neutral pH and then dried in an oven (60 °C) overnight.

To achieve incomplete carbide-to-CDC conversion, we used molar ratios of $NiCl_2 \cdot 6H_2O$-to-VC of 1.4, 1.8, and 2.7. It is assumed that chlorine (Cl_2) is released during vacuum decomposition of $NiCl_2$ and reacts with VC in a stoichiometric reaction to produce VCl_4 *via* eqn (1) and (2).

$$[NiCl_2 \cdot 6H_2O]^{solid} \rightarrow [Ni]^{solid} + [Cl_2]^{gas} + [6H_2O]^{gas} \quad (1)$$

$$[VC]^{solid} + [2Cl_2]^{gas} \rightarrow [C]^{solid} + [VCl_4]^{gas} \quad (2)$$

Based on these reactions and assuming that all chlorine reacts with carbide the theoretical conversion ($X_{theo.}$) can be derived from eqn (3) assuming full reaction of VC with Cl_2 release.

$$X_{theo.} = \frac{0.5 n_{Cl_2}}{n_{VC}} \times 100\% = \frac{0.5 n_{NiCl_2 \cdot 6H_2O}}{n_{VC}} \times 100\% \quad (3)$$

where n is in molar units. Ratios of 1.4 and 1.8 correspond to a theoretical value ($X_{theo.}$) of the conversion of 70% and 90%, respectively. A ratio of 2.7 provides a surplus of evolving chlorine to facilitate complete CDC formation, theoretically 100%. The resulting samples are labelled VC-X70, VC-X90, and VC-X100.

To produce a reference material through the "classical" and not *in situ* chlorine generation route, VC was exposed to chlorine gas diluted in helium at 700 °C for 5 h, as described elsewhere.[63] The resulting material is labelled VC-CDC.

2.2 Synthesis of V_2O_5/carbide-derived carbon core–shell particles

Calcination of the VC/CDC particles was performed at 450 °C for 30 min in a VG Scienta furnace using synthetic air. Additionally, VC particles without prior chlorine gas treatment were oxidized at different temperatures (450, 500, and 600 °C) for 4 h to produce V_2O_5 without an additional carbon shell.

2.3 Chemical and structural characterization

The chemical composition of all samples was measured by energy-dispersive X-ray analysis (EDX) using a X-Max-150 detector from Oxford Instruments in a JSM-7500F (JEOL) scanning electron microscope. Spectra were taken at ten different positions with an acceleration voltage of 10 kV.

Transmission electron microscopy (TEM) was carried out with a JEOL 2100F microscope using 200 kV acceleration voltage. Powders were dispersed in isopropanol, tip sonicated for 10 s and dropcast on a copper grid with a lacey carbon film (Gatan) support.

Chemical composition maps were acquired by energy filtered transmission electron microscopy (EF-TEM) using a FEI Titan Themis 60-300 at an acceleration voltage of 300 kV. Electron energy loss spectra (EELS) were recorded using a Gatan GIF Quantum ERS energy filter at an energy resolution of ~1.1 eV. From the acquired EELS the edge onsets of the carbon K-edge, the vanadium L-edge and the oxygen K-edge were determined and the three-window method applied to acquire the respective elemental maps. A slit width of 10 eV was utilized for the pre- and post-edge images. Since the vanadium and oxygen edges overlap, the exact same pre-edge windows were taken for both images. More information can be found in the ESI.†

Thermogravimetric analysis (TGA) was carried out with a TG 209 F1 Libra system (Netzsch). Samples were heated up to 900 °C in synthetic air with a rate of 20 °C min^{-1} as well as isothermally at 450 °C for 30 min. The sample mass ranged between 10 mg and 20 mg.

The nitrogen gas sorption analysis at −196 °C was carried out with a Quantachrome Autosorb iQ system and the calculations were performed with ASiQwin-software 3.0. The samples were degassed at 100 °C for 1 h and subsequently heated to 150 °C and kept at this temperature for up to 20 h at a relative pressure of 0.1 Pa to remove volatile molecules from the surface. The relative pressure with nitrogen was 5×10^{-7} to 1.0 in 76 steps. The specific surface area (SSA) was calculated using the Brunauer–Emmett–Teller equation (BET) in the linear regime of the measured isotherms, typically 3×10^{-2} to 2×10^{-1} (relative pressure), with a Quantachrome Autosorb 6B.[64]

Raman spectra were recorded with a Renishaw inVia Raman Microscope equipped with a Nd–YAG laser (532 nm). A 50× objective was used with a power of 0.02 mW at the surface of the sample. The spectra of CDC samples were recorded with 10 accumulations and 20 s acquisition time. Vanadium pentoxide and vanadium carbide spectra were recorded with 1 accumulation and 10 s acquisition as well as in two separate measurements for the full wavenumber range (0–4000 cm^{-1}). All spectra were normalized and background corrected by subtracting a linear baseline.

X-ray diffractograms were collected with a Bruker D8 Discover diffractometer using Cu-K_α radiation (0.154 nm) with a step size of 0.02° and a measurement time of 1 s per step. The system was calibrated with a corundum standard. The free-standing PTFE-bound electrodes were placed on a sapphire single crystal for the measurement.

2.4 Electrochemical characterization

For electrochemical characterization, free-standing, polymer-bound electrodes were used. The powder materials were dispersed in isopropanol and stirred in a mortar until most of the isopropanol was evaporated and a carbon slurry was obtained. For all samples, 10 mass% PTFE (60 mass% aqueous solution, Sigma Aldrich) was added and mixed in a mortar until a dough-like paste was formed. For the electrodes with pure V_2O_5 (VC-500) an additional conductive additive (see also the ESI, Table S1†), in this case 25 mass% VC-CDC was added to achieve the same amount of carbon as in the core–shell electrodes. Using a rolling machine (MTI HR01, MTI Corp.) electrodes with a thickness of 60 μm (±10 μm) were fabricated and dried overnight at 90 °C and 20 mbar.

Electrochemical characterization was carried out in 1 M $LiClO_4$ in acetonitrile (ACN) from BASF. For all measurements, a two- and three-electrode setup was used, corresponding to full- and half-cell configuration, respectively. The electrodes were punched out to obtain discs with a diameter of 6 mm (1–3 mg) and were separated by a glass-fiber disc with a diameter of 13 mm (type GF/A, GE Healthcare). The electrode/separator/electrode arrangement was compressed between two carbon-coated aluminum discs (diameter 12 mm, type Zflo 2653, Coveris Advanced Coatings) using spring-loaded titanium pistons, sealed by a polyether ether ketone (PEEK) body. The cells were dried at 90 °C and 20 mbar before they were put in an argon-filled glove box (MBraun Labmaster 130; O_2, H_2O <1 ppm). The cells were vacuum back-filled with a syringe containing the electrolyte. Full-cell measurements were carried out in an asymmetric configuration with a charge-balanced counter VC-CDC electrode by measuring the discharge capacity at 0.05 A g^{-1} in a half-cell setup for both, working and counter electrodes, and adjusting the mass of the VC-CDC electrode. In the half-cell setup, a *ca.* five times oversized AC counter electrode was used together with a reference electrode; the latter was PTFE-bound activated carbon YP-50F from Kuraray.

Electrochemical characterization was performed using a VSP300 and VMP300 potentiostat/galvanostat from Bio-Logic in cyclic voltammetry (CV) and galvanostatic mode with potential limitation (GCPL). In the half-cell configuration a potential window from −1.2 V to +1.2 V *vs.* carbon was used. For data obtained with cyclic voltammetry, a scan rate of 1 mV

s^{-1} was chosen to clearly identify the redox peaks. In galvanostatic mode with potential limitation (GCPL), specific currents up to 20 A g^{-1} were applied. All specific current values were normalized to the active mass of the working electrode (*i.e.*, without the binder). Every cycle was repeated 2 times, followed by a 10 s resting time. The specific capacity of the working electrode in the half-cell configuration was calculated according to eqn (4), using the data from GCPL.

$$\text{Specific capacity} = \int_{t_1}^{t_2} I\,\mathrm{d}t \Big/ m \tag{4}$$

with m the active mass of the working electrode (*i.e.*, without the binder), I the applied current, and t_1 and t_2 the start and end of discharging (from +1.2 V to −1.2 V *vs.* carbon), respectively. The charge efficiency was calculated by dividing the discharge by the charge capacity and is presented in percent.

The specific energy (E_{specific}) and specific power (P_{specific}) of the asymmetric full-cells (two electrodes) were calculated using eqn (5) and (6):

$$E_{\text{specific}} = \int_{t_1}^{t_2} U\,\mathrm{d}t \times I/M \tag{5}$$

$$P_{\text{specific}} = E_{\text{specific}}/(t_2 - t_1) \tag{6}$$

with M the active mass of both electrodes (*i.e.*, without the binder), I the applied current, U the applied cell voltage, t_1 and t_2 the start and end of charging or discharging. Charging is in this case defined as the potential step from 0 V to 2.5 V cell voltage.

Long-time stability was measured by galvanostatic cycling at 1 A g^{-1} from 0 V to 2.5 V cell voltage for 10 000 times. The energy efficiencies, as well as the energy retention, were calculated dividing the respective value from discharging by the value from the charging part of the curve and are presented in percent.

3. Results and discussion

3.1 Structure, chemical composition, and porosity

In this study, a novel two-step process is presented, which can be used for the synthesis of vanadium oxide combined with porous carbide-derived carbon hybrid structures in a core–shell arrangement: (1) VC/CDC core–shell particles are produced by etching vanadium from the outside to the inside of VC particles with a remaining VC core. (2) The residual VC core inside the CDC matrix is calcined by oxidation in synthetic air, resulting in V_2O_5/CDC core–shell particles. The resulting samples are labelled VC-X70, VC-X90, and VC-X100 for a theoretical conversion of 70%, 90%, and 100%. For additional calcination the samples were labelled VC-X70-air, VC-X90-air, and VC-X100-air. Complete transformation from VC to CDC (*i.e.*, VC-CDC) was achieved by conventional chlorine gas treatment at 700 °C, resulting in highly disordered carbon (Fig. 1A). Minor amounts of VC are still visible in VC-CDC (Fig. 1A) but not quantitatively significant according to the chemical analysis (Table 1). For the synthesis of VC/CDC core–shell particles with different ratios of VC to CDC, the amount of $NiCl_2$ was varied for *in situ* chlorine formation during thermal treatment. As expected from the stoichiometric calculation presented in eqn (3), VC-X70 had the largest amount of VC in the composite with 40.2 ± 5.3 mass%. Larger amounts of $NiCl_2$ led to lower VC contents of 29.0 ± 7.5 mass% and 6.9 ± 2.4 mass% for VC-X90 and VC-X100, respectively (Table 1). Although a stoichiometric surplus of chlorine in VC-X100 should result in complete transformation to CDC, TEM analysis still shows a small core region of residual VC. We explain this by a reduced vanadium etching rate because of the graphitic carbon layers wrapped around the carbide domains.[37]

A calcination temperature of 450 °C was chosen to completely transform residual VC to vanadium oxide after initial benchmarking of the samples *via* thermogravimetric analysis (see the ESI, Fig. S1†). After calcination, vanadium oxide cores inside the carbon shell are clearly visible (Fig. 1D, G and J). The smallest vanadia cores are measured for VC-X100-air (d_{50} = 150 ± 100 nm), similar to VC-X90-air (d_{50} = 160 ± 110 nm), much smaller than for VC-X70-air (d_{50} = 410 ± 190 nm) and the calcined VC particles (VC-500 °C) (d_{50} = 520 ± 200 nm). As seen in Table 1, EDX measurements are in qualitative agreement with TEM and show V_2O_5 contents of 98.1 ± 6.2 mass% for the precursor VC particles oxidized at 500 °C and lower amounts from 78.2 ± 2.3 mass% for VC-X70-air to 67.4 ± 4.1 mass% for VC-X100-air.

To show the structure and morphology in more detail, the two step synthesis process is illustrated in Fig. 2 using energy filtered TEM (EF-TEM) based chemical mapping. As exemplified for VC, VC-X90, and VC-X90-air, we first see how VC particles were successively transformed to CDC from the outside to the inside retaining a VC core. Calcination of VC inside the composite particles leads to V_2O_5 domains engulfed in nanoporous VC-CDC. EF-TEM chemical mapping confirms the distribution of carbon around the V_2O_5. During calcination, a partial cracking of the carbon shell is induced due to expansion of the core, as a result of the different skeletal densities of 3.36 g cm^{-3} for V_2O_5 and 5.48 g cm^{-3} for VC.[38,39]

By use of Raman spectroscopy, we can track the structural changes after CDC synthesis (Fig. 3A) and calcination (Fig. 3C). It is shown that the VC signal intensity at 269 cm^{-1} decreases with successive transformation from VC to CDC (see the inset in Fig. 3A).[40] In addition to the VC signal, the Raman spectra show incompletely graphitized carbon, with the D-mode at *ca.* 1340–1350 cm^{-1}, the G-mode at *ca.* 1580–1600 cm^{-1}, and a pronounced second order spectrum at 2200–3500 cm^{-1}. The degree of carbon ordering in VC/CDC core–shell particles is significantly higher than for the fully transformed CDC by chlorine treatment (VC-CDC). This is evidenced by the broader peak shapes and transition between D- and G-mode due to amorphous carbon at ~1520 cm^{-1}, as well as the less distinct second order spectrum for the VC-CDC sample (Fig. 3A).[41,42] However, the process stemming from $NiCl_2$ also leads to the local emergence of metallic Ni, which, in turn, catalyzes the formation of graphitic carbon arranged in onion-like shells (Fig. 1I and J).[43]

As seen from Fig. S1 (ESI†), precise control over the calcination process temperature and duration is required to avoid

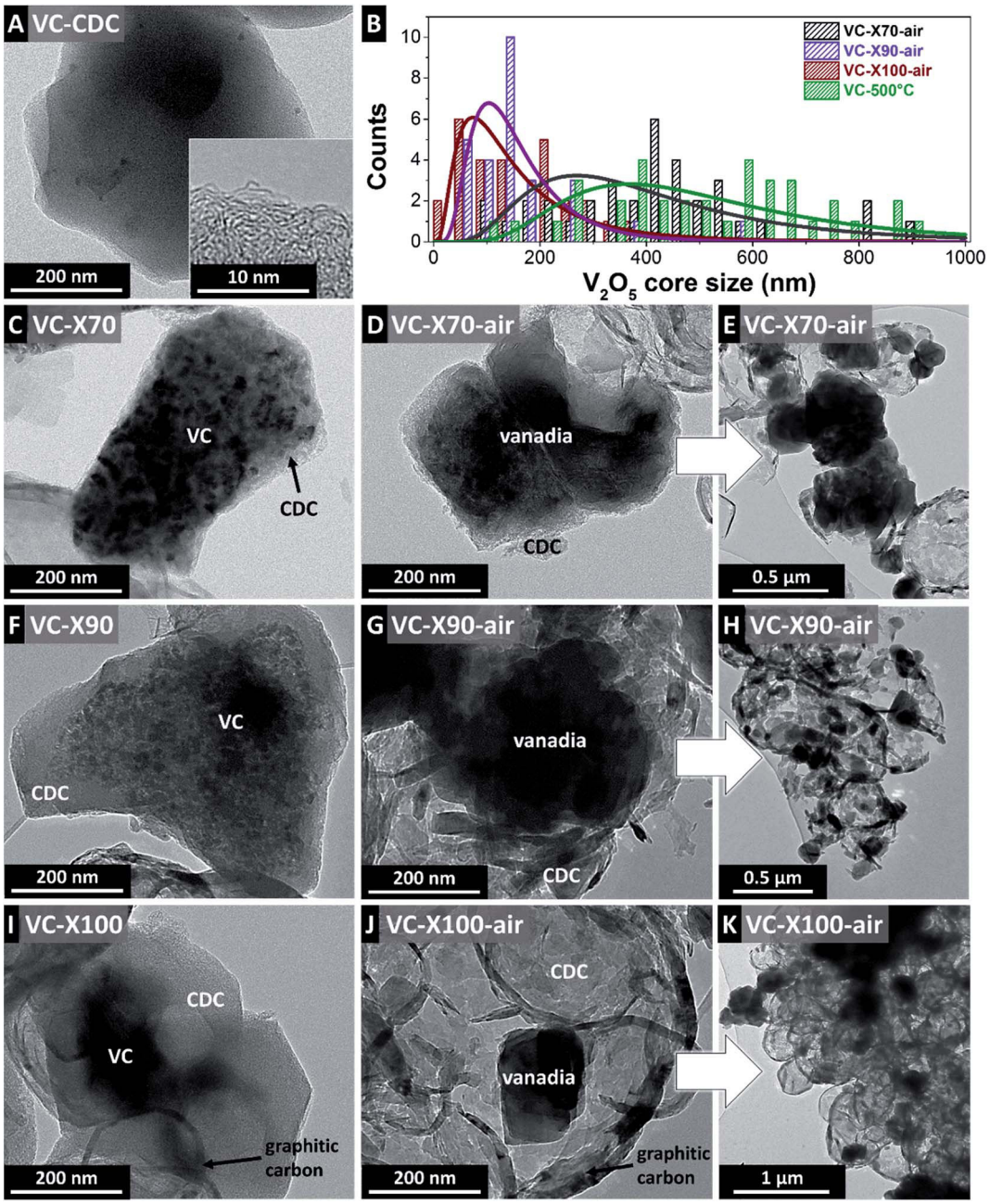

Fig. 1 Transmission electron micrographs of the transformation process from VC to V_2O_5/CDC core–shell particles with different transformational degrees. (A) VC-CDC, (C–E) VC-X70 and VC-X70-air, (F–H) VC-X90 and VC-X90-air, and (I–K) VC-X100 and VC-X100-air. (B) V_2O_5 core diameter distributions derived from TEM image analyses for all calcined samples.

either incomplete carbide oxidation or complete CDC burn-off. For this reason, we conducted first oxidation experiments only on the initial VC powder. The increase in mass of the initial VC particles, without prior $NiCl_2$ treatment, is ~40 mass% (ESI, Fig. S1†) for an annealing at 600 °C, leading to crystalline V_2O_5 (Fig. 3B). However, using this calcination temperature, more than 50 mass% of the CDC was burned-off. Therefore, the synthesis was repeated at a lower temperature of 450 °C for a duration of 30 min. With this annealing process, the same mass increase (~40 mass%) was achieved, expecting the same vanadia phase, and only ~20 mass% of the CDC material was removed. Synthesis at 450 °C for 30 min results in a mixture of V_2O_5,[44] amorphous V_2O_5,[45] and VO_2 (ref. 46) because of the large size of the precursor VC particles (~1 µm) (Fig. 3B). The particles with the VC/CDC core–shell arrangement present much smaller cores than the initial VC particles (Fig. 1B), which leads to the formation of V_2O_5 already at 450 °C applied for 30 min (Fig. 3C). These findings are supported by X-ray diffraction (XRD), shown in the ESI, Fig. S2.† Transformation from VC to VC/CDC is clearly evidenced by the emergence of the (002) graphite signal at 26.4° 2θ for VC-X70 and the continuous increase of its intensity up to the highest degree of

Table 1 Elemental composition measured with EDX. "n.d." denotes not detected

	C (mass%)	V (mass%)	O (mass%)	Cl (mass%)	Ni (mass%)	VC (mass%)	V_2O_5 (mass%)
VC	22.0 ± 0.5	77.6 ± 0.7	n.d.	n.d.	n.d.	95.9 ± 1.1	
VC-X70	60.6 ± 4.1	32.5 ± 4.7	6.3 ± 1.1	0.6 ± 0.1	n.d.	40.2 ± 5.3	
VC-X90	58.2 ± 9.5	23.5 ± 7.1	6.9 ± 2.1	0.5 ± 0.2	n.d.	29.0 ± 7.5	
VC-X100	74.8 ± 8.0	5.6 ± 2.3	4.5 ± 0.9	0.4 ± 0.1	n.d.	6.9 ± 2.4	
VC-CDC	97.8 ± 0.4	0.2 ± 0.1	1.8 ± 0.5	0.1 ± 0.1	n.d.	0.2 ± 0.1	
VC-500	1.9 ± 0.4	69.0 ± 3.2	29.1 ± 3.0	n.d.	n.d.		98.1 ± 6.2
VC-X70-air	20.0 ± 2.2	57.9 ± 1.1	22.1 ± 1.2	n.d.	n.d.		78.2 ± 2.3
VC-X90-air	23.3 ± 5.4	53.3 ± 4.2	22.8 ± 2.0	n.d.	0.6 ± 0.2		74.3 ± 6.2
VC-X100-air	30.7 ± 1.7	48.5 ± 2.4	20.7 ± 1.7	n.d.	n.d.		67.4 ± 4.1

transformation for VC-X100 (ESI, Fig. S2A†). The fully transformed VC-CDC presents a less distinct carbon signal, coming from nanocrystalline and amorphous carbon, in agreement with Raman spectroscopy. After calcination, only V_2O_5 is identified (ESI, Fig. S2B†).

Highly nanoporous materials with high specific surface areas typically result from chlorine treatment of VC (*i.e.*, VC-CDC).[38] The nitrogen gas sorption isotherm of VC-CDC shows a characteristic type I(b) shape related to microporous materials with pore sizes <2.5 nm (ESI, Fig. S3A†). Both micro- and mesopores are found for the partial transformation of VC with type I(b) isotherms, related to the internal microporosity, combined with type IV(b) isotherms related to mesopores with a small H4 hysteresis (Fig. S3B†).[47] The combination of micro- and mesopores has been reported in other studies on carbon core–shell structures.[36] The BET surface area increases from 120 $m^2 g^{-1}$ for VC-X70 to 577 $m^2 g^{-1}$ for VC-X100, and to 1466 $m^2 g^{-1}$ for VC-CDC (Table 2). Calcination of VC/CDC core–shell particles does not change the pore type (micro- and mesopores), but leads to oxidation of the high surface area carbon, with consequent decrease in surface area. For VC-X100-air and VC-X90-air, the surface area collapses to 61 $m^2 g^{-1}$ (−89%) and 124 $m^2 g^{-1}$ (−38%), respectively, due to oxidation of the CDC shell. The surface area of VC-X70-air is even larger than before calcination with 310 $m^2 g^{-1}$ (+158%; Table 2). The high content of VC in VC-X70 (40 mass%), which is turned into the lower density V_2O_5, has a stronger impact on the surface area than the CDC, compared to VC-X90 and VC-X100 with lower VC contents.

3.2 Electrochemical performance

As seen from the previous section, partial chlorination of VC to VC/CDC and successive calcination to V_2O_5/CDC in a facile two-step approach leads to highly crystalline V_2O_5 embedded graphitic and porous carbon. This combination is promising for electrochemical hybrid energy storage applications, which was benchmarked in our study in 1 M $LiClO_4$ in ACN as the electrolyte. Cyclic voltammetry of VC-CDC using the half-cell setup shows a nearly ideal double-layer capacitor behavior with a rectangular CV shape without any redox reactions. This behavior is expected from nanoporous carbons in general and CDC materials in specific.[6] VC-X70-air is characterized by double-layer capacitance on the positive side between +0.5 V and +1.2 V *vs.* carbon. In the negative range, a very broad redox peak emerges (Fig. 4B and ESI, Fig. S4B†). This broad peak correlates with the larger V_2O_5 core of VC-X70 compared to the nanotextured V_2O_5 particles in VC-X90-air and VC-X100-air. Due to longer ion pathways in the V_2O_5 crystal, the system presents slower redox reactions and broader redox peaks.

In stark contrast to the capacitor-like behavior of VC-CDC, the CVs of VC-X90-air and VC-X100-air are characterized by several, very sharp redox peaks from Li-ion intercalation.[30,48,49] The occurring electrochemical Li^+ insertion process for V_2O_5 can be expressed by eqn (7):[50]

$$V_2O_5 + xLi^+ + xe^- \leftrightarrow Li_xV_2O_5 \quad (7)$$

with x as the mole fraction of Li-ions.

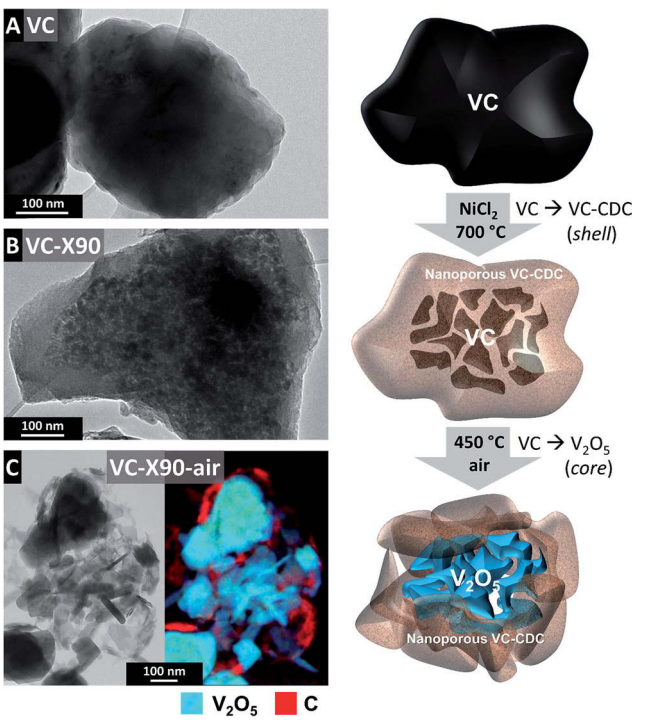

Fig. 2 Transmission electron micrographs and schematic illustration of the transformation process from VC to V_2O_5/CDC core–shell particles. (A) VC, (B) VC-X90, and (C) VC-X90-air. Panel (C) shows the TEM image (filtered ±5 eV around the zero loss peak) and the corresponding chemical EELS mapping.

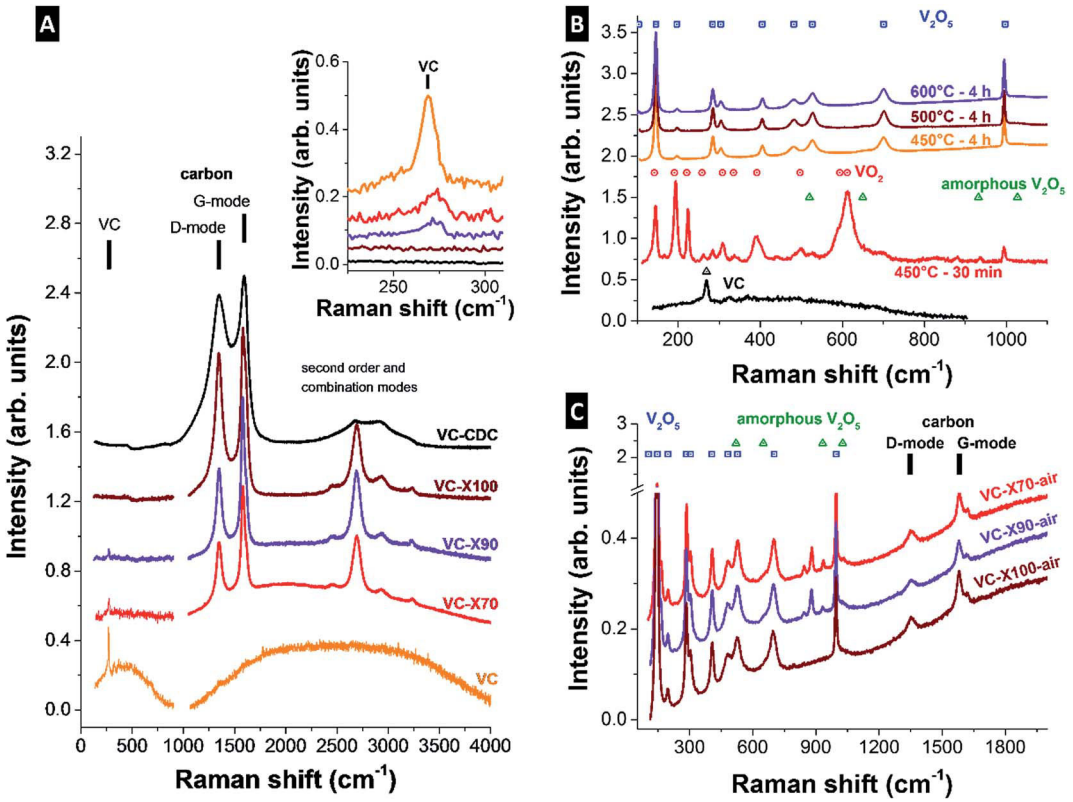

Fig. 3 Raman spectra of (A) VC and VC/CDC core–shell particles, (B) VC calcined at different temperatures, and (C) V_2O_5/CDC core–shell particles after calcination at 450 °C for 30 min. The reference Raman peaks are from VC,[40] VO_2,[46] V_2O_5,[44] and amorphous V_2O_5.[45]

Typically, a set of two peaks for inter- and deintercalation is observed between +2 and +4 V *vs.* Li/Li^+ or −1.2 V and +0.8 V *vs.* carbon.[48] The structural changes during Li^+ intercalation into V_2O_5 involve several phases like α, ε, δ, and γ for $x \leq 2$, with three voltage plateaus at 3.4, 3.2, and 2.3 V *vs.* Li/Li^+ (−0.7 V, 0 V, and +0.2 V *vs.* carbon) (Fig. 4B).[48] The plateaus seen from the galvanostatic curves (Fig. 4B) and the pairs of redox peaks in the CVs (Fig. 4A) belong to the two-phase regions α/ε, ε/δ, and δ/γ. Larger lithium contents ($x > 2$) for potentials below 2 V *vs.* Li/Li^+ (−1.2 V *vs.* carbon) would lead to irreversible reactions and the formation of the γ-phase.[48,51,52] A detailed discussion of the structural changes is already given in ref. 48 and 51–53. The first set of redox peaks emerges between −0.25 V and +0.8 V *vs.* carbon for inter- and deintercalation of the first Li-ion. A second lithiation step occurs between −1.2 V and 0 V *vs.* carbon (ESI, Fig. S4A†). For potentials above +0.8 V *vs.* carbon, only double-layer capacitance of the porous carbon is encountered. Calcined VC without the core–shell structure, but the same V_2O_5 phase, shows very broad sets of redox peaks in the CV compared to the core–shell structure. It is expected that longer ion intercalation paths of the larger size of V_2O_5 domains in VC-500 °C result in slower redox reactions of the electrode, similar to VC-X70-air. In contrast, the core–shell structures present much smaller V_2O_5 particles due to partial transformation into porous carbon.

Galvanostatic charge/discharge cycling (GCPL) in half-cells was further employed for assessing the power handling ability of the electrode materials. As seen from Fig. 4B, GCPL curves of VC-X100-air and VC-X90-air exhibited several voltage plateaus between −1.2 V and +1.2 V *vs.* carbon, in agreement with the redox peaks in the CVs. Nearly ideal double-layer behavior with triangular-shape GCPL curves was observed for VC-CDC. The Li^+ intercalation and deintercalation leads to phase transitions during cycling and is kinetically enhanced for nanoscopic materials because of better accessibility of intercalation pathways.[54] Therefore, smaller V_2O_5 core sizes of V_2O_5/CDC core–shell samples show superior rate handling compared to VC-500 with a more than 2-times larger V_2O_5 particle size (Fig. 4C). This is especially seen for VC-X100-air with more than 100 mA h g^{-1} capacity at 5 A g^{-1} (equivalent to a rate of *ca.* 28C).

The lower vanadium oxide content of VC-X100-air limits the maximum capacity at low rates. The highest value is achieved

Table 2 Porosity data from nitrogen gas sorption analysis

	BET SSA (m^2 g^{-1})	DFT SSA (m^2 g^{-1})	Pore volume (cm^3 g^{-1})
VC-X70	120	100	0.185
VC-X90	200	208	0.224
VC-X100	577	485	0.424
VC-CDC	1466	1535	0.673
VC-500	42	23	0.053
VC-X70-air	310	269	0.254
VC-X90-air	124	66	0.171
VC-X100-air	61	38	0.108

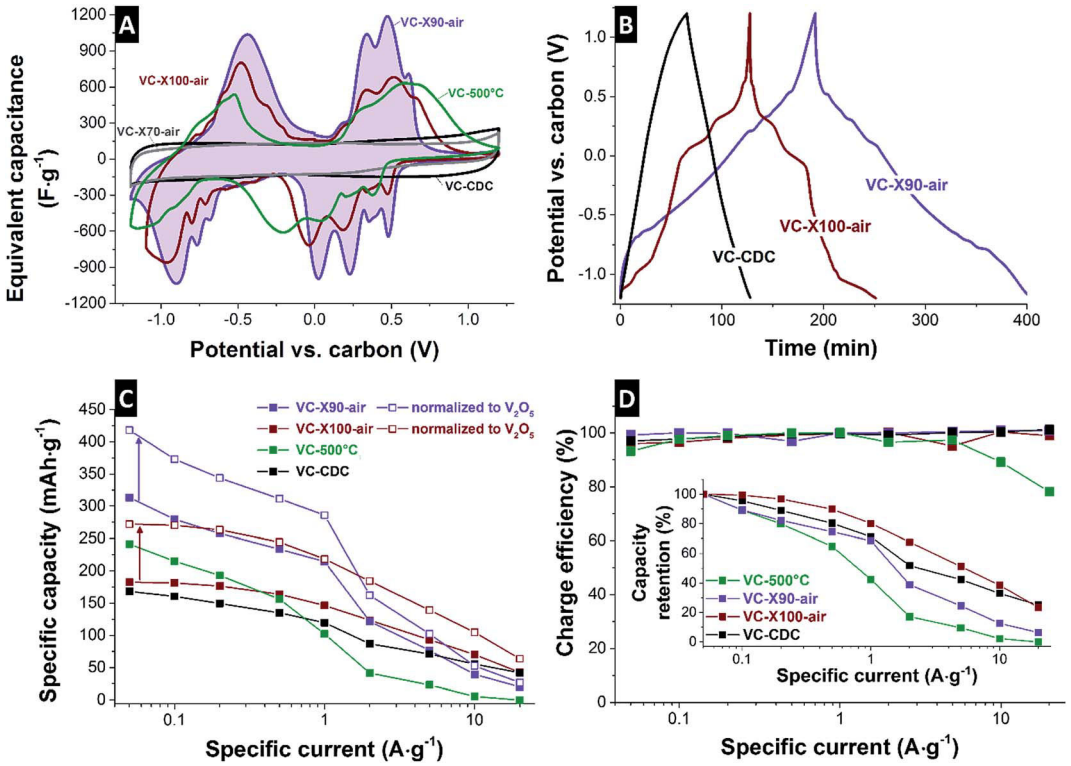

Fig. 4 (A) Cyclic voltammograms at 1 mV s^{-1}, (B) galvanostatic charge–discharge curves at 0.05 A g^{-1}, (C) capacity values dependent on the specific current, and (D) the charge efficiency and capacity retention. All measurements were performed in the half-cell configuration with activated carbon counter and reference electrodes from −1.2 V to +1.2 V *vs.* carbon.

for VC-X90-air with more than 300 mA h g^{-1}. Typically, in the literature capacity values are normalized to the active mass, in this case the mass of V_2O_5 in the composite electrode. Using this way of normalization, the highest capacity for VC-X90-air is 415 mA h g^{-1}. Even for higher specific currents of 5 A g^{-1} the specific capacity reaches more than 100 mA h g^{-1} (comparable to a C-rate of 12C). The normalized values are given as an inset in Fig. 4D for comparison. Cycling in the potential window of −1.2 V to +1.2 V *vs.* carbon is expected to be completely reversible,[48,51,52] and this behavior was confirmed for all V_2O_5/CDC core–shell particles with a coulombic efficiency of *ca.* 100% (Fig. 4D). The VC particles calcined at 500 °C with much larger particle sizes (Fig. 1B) and without CDC shells, present a lower charge efficiency of less than 80% at 20 A g^{-1}. This might be the result of V_2O_5 degeneration due to kinetic limitations.[30]

Electrochemical properties on a device level were measured using an asymmetric full-cell setup with nanoporous VC-CDC as the counter electrode. Typically, symmetric setups for electrode

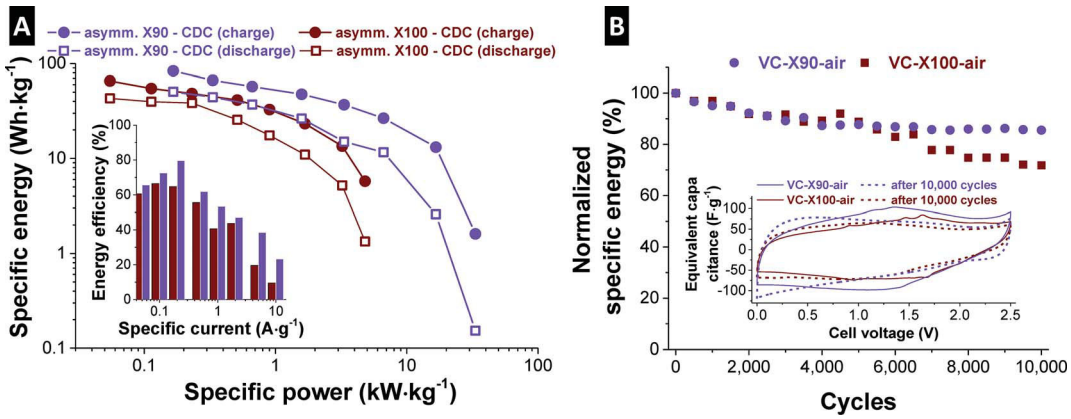

Fig. 5 (A) Ragone plot with energy efficiency values and (B) specific energy retention for 10 000 galvanostatic cycles at 1 A g^{-1} (rate of *ca.* 2.4C) with cyclic voltammograms recorded before and after stability testing. All measurements were performed in the full-cell configuration with a charge-balanced VC-CDC working electrode and V_2O_5/CDC composite electrode with a cell voltage of 2.5 V.

Table 3 Literature values for full-cell measurements (two-electrodes) in symmetric and asymmetric fabrication. OLC: onion-like carbon; CNT: carbon nanotube; NW: nanowire; rGO: reduced graphene oxide; ACC: activated carbon fabric; NS: nanosheet; PPy: polypyrrole; sym.: symmetric; asym.: asymmetric; ACN: acetonitrile; PC: propylene carbonate; LiTFSI: lithium bis(trifluoromethylsulphonyl)imide; WE: working electrode; CE: counter electrode

Material (WE)	Setup	CE	Electrolyte	Specific energy W h kg^{-1}	Specific power W kg^{-1}	Ref.
V_2O_5/CDC core–shell	asym.	CDC	1 M $LiClO_4$ in ACN	84 (51)	166	This study
				27 (12)	6653	
V_2O_5/OLC	asym.	AC	1 M $LiClO_4$ in ACN	38	57	33
				10	2004	
V_2O_5/CNTs	asym.	AC	1 M $LiClO_4$ in PC	40	200	22
				7	6300	
V_2O_5 nanowires	asym.	AC fabric	0.1 M LiTFSI in ACN	46	662	59
				6	5260	
Li^+ exchanged V_2O_5 NWs	asym.	AC fabric	0.1 M LiTFSI in ACN	66	720	59
				7	8320	
V_2O_5 NWs/rGO	asym.	MnO_2/rGO	1 M LiTFSI in ACN	15	437	60
V_2O_5/Pin/ACC	asym.	rGO/ACC	$LiNO_3$/PVA gel	39	900	65
				33	18 000	
V_2O_5/rGO NS	asym.	rGO	1 M KCl	76	900	34
				25	30 000	
$V_2O_5 \cdot 0.6H_2O$	asym.	AC	0.5 M K_2SO_4	29	70	58
				20	2000	
Layered V_2O_5 aerogel	asym.	AC	1 M Na_2SO_4	11	280	66
				5	2200	
V_2O_5/MWCNTs	sym.	WE	1 M Na_2SO_4	87	250	56
V_2O_5 nanofibers	sym.	WE	1 M $LiClO_4$ in PC	78	1800	55
				15	1500	
			2 M KCl	5	1700	55
				3	1800	
V_2O_5/PPy core–shell	sym.	WE	$LiNO_3$/PVA gel	10	5000	67
V_2O_5/graphene	sym.	WE	1 M Na_2SO_4	68	250	57

materials with battery-like behavior (*e.g.*, intercalation/deintercalation) are disadvantageous due to their polarization dependent redox-reactions. Yet, several studies used different types of V_2O_5 or V_2O_5/carbon composites, such as electrospun V_2O_5 nanofibers,[55] V_2O_5/MWCNT core–shell aerogels,[56] and V_2O_5/graphene aerogels[57] with the symmetrical full-cell setup. However, in some of these studies, negative and positive polarization in the full-cell arrangement was used (*e.g.* −1 V to +1 V in an aqueous electrolyte), instead of 0 V to 1 V. In these cases the capacitance and specific energies are much larger reaching misleading high values of 87 W h kg^{-1} in aqueous 1 M Na_2SO_4 (ref. 56) and 78 W h kg^{-1} in organic 1 M $LiClO_4$ in PC.[55]

Enhanced electrochemical performance can be obtained by use of an asymmetric two-electrode setup (Fig. 5). Studies so far have shown, for aqueous systems, the highest specific energy of 29 W h kg^{-1} (Table 3) for hydrothermally prepared $V_2O_5 \cdot 0.6H_2O$ with activated carbon as the counter electrode.[58] Due to the improved voltage stability of organic electrolytes, much higher energies can be achieved, ranging from 15 to 76 W h kg^{-1} with MnO_2/rGO, AC fabric, or rGO as the counter electrode in an asymmetric arrangement.[34,59,60] In this study, an asymmetric full-cell setup with V_2O_5/CDC on the negative polarization side and charge-balanced VC-CDC on the positive polarization side was used. VC-X90-air as a negative electrode material presents superior performance with a specific energy in excess of 80 W h kg^{-1} for charging and more than 50 W h kg^{-1} for discharging (Fig. 5A). Even at higher rates, with a specific power of ~6.7 kW kg^{-1}, the specific energy is 27 W h kg^{-1} (12 W h kg^{-1} for discharging). In agreement with half-cell measurements, VC-X100-air shows a lower specific energy of 66 W h kg^{-1} with comparable power handling because of the lower V_2O_5 content. The energy and power performance of this core–shell system is highly competitive with current literature values and is, to the best of our knowledge, the only core–shell system reaching 50–80 W h kg^{-1} specific energy when using asymmetric full-cell measurements and proper application of the cell voltage.[61]

The high attractiveness of this material for electrochemical energy storage is underlined by the high cycling stability with an energy retention of more than 80% and 70% over 10 000 galvanostatic cycles for VC-X90-air and VC-X100-air, respectively, measured at 1 A g^{-1} (Fig. 5B). The nearly ideal charge efficiency of the half-cell measurements (100%) translates to a still attractive energy efficiency of the asymmetric devices between 60 and 80% for low rates. For comparison, standard double-layer capacitors using activated carbon electrodes only reach slightly higher values of 80–95% dependent on the electrode.[62]

4. Conclusions

This study, for the first time, demonstrates a two-step *in situ* synthesis of hybrid particles consisting of porous carbon and redox-active V_2O_5 by solely using VC as the precursor. The

particles present a V_2O_5/CDC core–shell structure with nanoscopic V_2O_5 cores, completely accessible to electrolyte ions and interconnected by highly conductive carbon. High specific energies of 50 and 80 W h kg^{-1} for discharging and charging, respectively, were measured in a facile asymmetric full-cell setup, while simultaneously retaining ultrafast cycling. The asymmetric cell design with CDC on the positive polarization side leads to superior stability over 10 000 cycles and comparably high energy efficiency of 60–80% at low rates. The novel synthesis procedure can easily be scaled up by means of larger precursor mass and may also be very attractive for other redox-active compounds.

Acknowledgements

M. Z., B. K., and V. P. gratefully acknowledge funding from the German Federal Ministry for Research and Education (BMBF) in support of the nanoEES^{3D} project (award number 03EK3013) as part of the strategic funding initiative energy storage framework and Prof. Eduard Arzt (INM) for his continuing support. T. A., and B. E. gratefully acknowledge the funding of the German Federal Ministry of Education and Research (BMBF) under the project AktivCAPs (award number 02E2-ESP077) and the German Research Council (DFG), which, within the framework of its "Excellence Initiative", supports the Cluster of Excellence "Engineering of Advanced Materials" (http://www.eam.uni-erlangen.de) at the University of Erlangen-Nuremberg. T. A. gratefully acknowledges the Indonesian Directorate General of Higher Education (DIKTI) for a PhD scholarship. Dr Mesut Aslan is thanked for vanadium carbide chlorination.

References

1 P. Simon, Y. Gogotsi and B. Dunn, *Science*, 2014, **343**, 1210–1211.
2 P. Simon and Y. Gogotsi, *Nat. Mater.*, 2008, **7**, 845–854.
3 J. B. Goodenough, *Energy Environ. Sci.*, 2014, **7**, 14–18.
4 Z. Yang, J. Zhang, M. C. Kintner-Meyer, X. Lu, D. Choi, J. P. Lemmon and J. Liu, *Chem. Rev.*, 2011, **111**, 3577–3613.
5 J. R. Miller, *J. Power Sources*, 2016, **326**, 726–735.
6 F. Béguin, V. Presser, A. Balducci and E. Frackowiak, *Adv. Mater.*, 2014, **26**, 2219–2251.
7 N. Jäckel, M. Rodner, A. Schreiber, J. Jeongwook, M. Zeiger, M. Aslan, D. Weingarth and V. Presser, *J. Power Sources*, 2016, **326**, 660–671.
8 V. Presser, M. Heon and Y. Gogotsi, *Adv. Funct. Mater.*, 2011, **21**, 810–833.
9 O. Barbieri, M. Hahn, A. Herzog and R. Kötz, *Carbon*, 2005, **43**, 1303–1310.
10 J. Chmiola, G. Yushin, Y. Gogotsi, C. Portet, P. Simon and P. L. Taberna, *Science*, 2006, **313**, 1760–1763.
11 E. Frackowiak, K. Fic, M. Meller and G. Lota, *ChemSusChem*, 2012, **5**, 1181–1185.
12 B. E. Conway, V. Birss and J. Wojtowicz, *J. Power Sources*, 1997, **66**, 1–14.
13 M. Salanne, B. Rotenberg, K. Naoi, K. Kaneko, P.-L. Taberna, C. Grey, B. Dunn and P. Simon, *Nat. Energy*, 2016, **1**, 16070.
14 J. Lee, B. Krüner, A. Tolosa, S. Sethuraman, D. Kim, S. Choudhury, K. H. Seo and V. Presser, *Energy Environ. Sci.*, 2016, **9**, 3392–3398.
15 T. Brousse, D. Bélanger and J. W. Long, *J. Electrochem. Soc.*, 2015, **162**, A5185–A5189.
16 J. Zheng, P. Cygan and T. Jow, *J. Electrochem. Soc.*, 1995, **142**, 2699–2703.
17 C. Xu, F. Kang, B. Li and H. Du, *J. Mater. Res.*, 2010, **25**, 1421–1432.
18 M. Ghidiu, M. R. Lukatskaya, M.-Q. Zhao, Y. Gogotsi and M. W. Barsoum, *Nature*, 2014, **516**, 78–81.
19 S. Roldán, C. Blanco, M. Granda, R. Menéndez and R. Santamaría, *Angew. Chem., Int. Ed.*, 2011, **50**, 1699–1701.
20 M. Zeiger, D. Weingarth and V. Presser, *ChemElectroChem*, 2015, **2**, 1117–1127.
21 N. Nitta, F. Wu, J. T. Lee and G. Yushin, *Mater. Today*, 2015, **18**, 252–264.
22 Z. Chen, V. Augustyn, J. Wen, Y. Zhang, M. Shen, B. Dunn and Y. Lu, *Adv. Mater.*, 2011, **23**, 791–795.
23 J. S. Daubert, N. P. Lewis, H. N. Gotsch, J. Z. Mundy, D. N. Monroe, E. C. Dickey, M. D. Losego and G. N. Parsons, *Chem. Mater.*, 2015, **27**, 6524–6534.
24 L.-M. Chen, Q.-Y. Lai, Y.-J. Hao, Y. Zhao and X.-Y. Ji, *J. Alloys Compd.*, 2009, **467**, 465–471.
25 T. Kudo, Y. Ikeda, T. Watanabe, M. Hibino, M. Miyayama, H. Abe and K. Kajita, *Solid State Ionics*, 2002, **152–153**, 833–841.
26 D. Chao, X. Xia, J. Liu, Z. Fan, C. F. Ng, J. Lin, H. Zhang, Z. X. Shen and H. J. Fan, *Adv. Mater.*, 2014, **26**, 5794–5800.
27 Y. L. Cheah, V. Aravindan and S. Madhavi, *ACS Appl. Mater. Interfaces*, 2013, **5**, 3475–3480.
28 D. Zhu, H. Liu, L. Lv, Y. D. Yao and W. Z. Yang, *Scr. Mater.*, 2008, **59**, 642–645.
29 M. Sathiya, A. S. Prakash, K. Ramesha, J. M. Tarascon and A. K. Shukla, *J. Am. Chem. Soc.*, 2011, **133**, 16291–16299.
30 Y. Liu, M. Clark, Q. Zhang, D. Yu, D. Liu, J. Liu and G. Cao, *Adv. Energy Mater.*, 2011, **1**, 194–202.
31 M.-S. Balogun, Y. Luo, F. Lyu, F. Wang, H. Yang, H. Li, C. Liang, M. Huang, Y. Huang and Y. Tong, *ACS Appl. Mater. Interfaces*, 2016, **8**, 9733–9744.
32 Q. Xu and T. Zhao, *Prog. Energy Combust. Sci.*, 2015, **49**, 40–58.
33 S. Fleischmann, N. Jäckel, M. Zeiger, B. Krüner, I. Grobelsek, P. Formanek, S. Choudhury, D. Weingarth and V. Presser, *Chem. Mater.*, 2016, **28**, 2082–2813.
34 D. H. Nagaraju, Q. Wang, P. Beaujuge and H. N. Alshareef, *J. Mater. Chem. A*, 2014, **2**, 17146–17152.
35 M. Schmirler, F. Glenk and B. J. Etzold, *Carbon*, 2011, **49**, 3679–3686.
36 T. Ariyanto, B. Dyatkin, G.-R. Zhang, A. Kern, Y. Gogotsi and B. J. Etzold, *Microporous Mesoporous Mater.*, 2015, **218**, 130–136.
37 C. R. Pérez, S. H. Yeon, J. Ségalini, V. Presser, P. L. Taberna, P. Simon and Y. Gogotsi, *Adv. Funct. Mater.*, 2013, **23**, 1081–1089.
38 A. Jänes, T. Thomberg and E. Lust, *Carbon*, 2007, **45**, 2717–2722.

39 J. G. Speight, *Lange's Handbook of Chemistry*, McGraw-Hill, New York, 16 edn, 2005.
40 T. Huang, S. Mao, G. Zhou, Z. Wen, X. Huang, S. Ci and J. Chen, *Nanoscale*, 2014, **6**, 9608–9613.
41 A. Ferrari and J. Robertson, *Phys. Rev. B: Condens. Matter Mater. Phys.*, 2000, **61**, 14095.
42 A. C. Ferrari and J. Robertson, *Phys. Rev. B*, 2001, **64**, 075414.
43 Z. Huang, D. Wang, J. Wen, M. Sennett, H. Gibson and Z. Ren, *Appl. Phys. A: Mater. Sci. Process.*, 2002, **74**, 387–391.
44 R. Baddour-Hadjean, J. P. Pereira-Ramos, C. Navone and M. Smirnov, *Chem. Mater.*, 2008, **20**, 1916–1923.
45 S.-H. Lee, H. M. Cheong, M. J. Seong, P. Liu, C. E. Tracy, A. Mascarenhas, J. R. Pitts and S. K. Deb, *Solid State Ionics*, 2003, **165**, 111–116.
46 G. Petrov, V. Yakovlev and J. Squier, *Appl. Phys. Lett.*, 2002, **81**, 1023–1025.
47 M. Thommes, K. Kaneko, A. V. Neimark, J. P. Olivier, F. Rodriguez-Reinoso, J. Rouquerol and K. S. Sing, *Pure Appl. Chem.*, 2015, **87**, 1051–1069.
48 C. Leger, S. Bach, P. Soudan and J.-P. Pereira-Ramos, *J. Electrochem. Soc.*, 2005, **152**, A236–A241.
49 M. Koltypin, V. Pol, A. Gedanken and D. Aurbach, *J. Electrochem. Soc.*, 2007, **154**, A605–A613.
50 J. Livage, *Chem. Mater.*, 1991, **3**, 578–593.
51 C. Delmas, H. Cognac-Auradou, J. Cocciantelli, M. Menetrier and J. Doumerc, *Solid State Ionics*, 1994, **69**, 257–264.
52 C. Delmas, S. Brethes and M. Menetrier, *J. Power Sources*, 1991, **34**, 113–118.
53 M. S. Whittingham, *Chem. Rev.*, 2004, **104**, 4271–4302.
54 V. Augustyn, P. Simon and B. Dunn, *Energy Environ. Sci.*, 2014, **7**, 1597–1614.
55 G. Wee, H. Z. Soh, Y. L. Cheah, S. G. Mhaisalkar and M. Srinivasan, *J. Mater. Chem.*, 2010, **20**, 6720–6725.
56 Y. Wu, G. Gao, H. Yang, W. Bi, X. Liang, Y. Zhang, G. Zhang and G. Wu, *J. Mater. Chem. A*, 2015, **3**, 15692–15699.
57 Y. Wu, G. Gao and G. Wu, *J. Mater. Chem. A*, 2015, **3**, 1828–1832.
58 Q. T. Qu, Y. Shi, L. L. Li, W. L. Guo, Y. P. Wu, H. P. Zhang, S. Y. Guan and R. Holze, *Electrochem. Commun.*, 2009, **11**, 1325–1328.
59 S. D. Perera, B. Patel, N. Nijem, K. Roodenko, O. Seitz, J. P. Ferraris, Y. J. Chabal and K. J. Balkus, *Adv. Energy Mater.*, 2011, **1**, 936–945.
60 S. D. Perera, M. Rudolph, R. G. Mariano, N. Nijem, J. P. Ferraris, Y. J. Chabal and K. J. Balkus Jr, *Nano Energy*, 2013, **2**, 966–975.
61 M. D. Stoller and R. S. Ruoff, *Energy Environ. Sci.*, 2010, **3**, 1294–1301.
62 A. Laheäär, P. Przygocki, Q. Abbas and F. Béguin, *Electrochem. Commun.*, 2015, **60**, 21–25.
63 T. Ariyanto, A. M. Laziz, J. Gläsel, G.-R. Zhang, J. Garbes and B. J. Etzold, *Chem. Eng. J.*, 2016, **283**, 676–681.
64 S. Brunauer, P. H. Emmett and E. Teller, *J. Am. Chem. Soc.*, 1938, **60**, 11.
65 X. Zhou, Q. Chen, A. Wang, J. Xu, S. Wu and J. Shen, *ACS Appl. Mater. Interfaces*, 2016, **8**, 3776–3783.
66 C. X. Guo, G. Yilmaz, S. Chen, S. Chen and X. Lu, *Nano Energy*, 2015, **12**, 76–87.
67 T. Qian, N. Xu, J. Zhou, T. Yang, X. Liu, X. Shen, J. Liang and C. Yan, *J. Mater. Chem. A*, 2015, **3**, 488–493.

Electronic Supplementary Material (ESI) for Journal of Materials Chemistry A.

Supporting Information

VANADIUM PENTOXIDE / CARBIDE-DERIVED CARBON CORE-SHELL HYBRID PARTICLES FOR HIGH PERFORMANCE ELECTROCHEMICAL ENERGY STORAGE

Marco Zeiger,[1,2] Teguh Ariyanto,[3] Benjamin Krüner,[1,2] Nicolas J. Peter,[4] Simon Fleischmann,[2]

Bastian J. M. Etzold,[3,5,] and Volker Presser[1,2,*]*

[1] *INM - Leibniz Institute for New Materials, 66123 Saarbrücken, Germany*

[2] *Department of Materials Science and Engineering, Saarland University, 66123 Saarbrücken, Germany*

[3] *Friedrich-Alexander Universität Erlangen-Nürnberg, Lehrstuhl für Chemische Reaktionstechnik, 91058 Erlangen, Germany*

[4] *Max-Planck Institut für Eisenforschung GmbH, 40237 Düsseldorf, Germany*

[5] *Technische Universität Darmstadt, Ernst-Berl-Institut für Technische und Makromolekulare Chemie, 64287 Darmstadt, Germany*

* *Corresponding authors. Bastian Etzold:* etzold@tc1.tu-darmstadt.de. *Volker Presser:* volker.presser@leibniz-inm.de

Elemental mapping with EF-TEM

The vanadium post-edge window ranged from 523-533 eV, while the oxygen post-edge window ranged from 534-544 eV. Thereby, both the major white lines of the vanadium and the two peaks of the oxygen K-edge were captured separately. Each image of an energy-filtered map was taken with an exposure time of 40 s in case of carbon and 60 s of vanadium and oxygen. The background was fitted from the two pre-edge images with a power law function. The two pre-edge and one post-edge image were automatically taken in Digital Micrograph (Gatan) to form one elemental map. Cross-correlation was applied to account for sample drift between the images acquired in a three-window series. In addition, the three separately obtained elemental maps of carbon, vanadium and oxygen were aligned using a cross-correlation to ensure a proper spatial superposition of the individual RGB channels. Oxygen is shown in green, vanadium in blue and carbon in red to finally form the multi-component elemental distribution map. The reference TEM image of the exact same area of the elemental distribution map was acquired using mainly the elastically scattered electrons by centering an energy selecting slit with a width of 10 eV around the zero loss peak to increase the contrast in the image. The corresponding thickness map, for which an additional unfiltered image without slit was captured, revealed relative thicknesses t/λ (in units of λ, the material-dependent mean free path for inelastic scattering) ranging from 0.1 to about 1.5.

Thermogravimetric analysis

In **Figure S1** the results of the annealing process in synthetic air of all VC/CDC samples as well as the VC precursor are shown. The calcination of VC to V_2O_5 starts at ~375 °C. At ~600 °C the transformation is complete with a mass gain of ~40 mass%. As expected the same procedures completely burns off the CDC. A suitable temperature between 375 °C and 600 °C is 450 °C which was used for the synthesis of V_2O_5/CDC. At 450 °C for 30 min the VC reaches a mass gain of ~40 mass% similar to the annealing procedure with a maximum temperature of 600 °C accompanied by a phase transformation from VC to V_2O_5. The pure carbon sample VC-CDC loses around 20 mass%. Partially etched VC samples with porous carbon shell and VC core presents slightly smaller mass loss due to the remaining carbon shell.

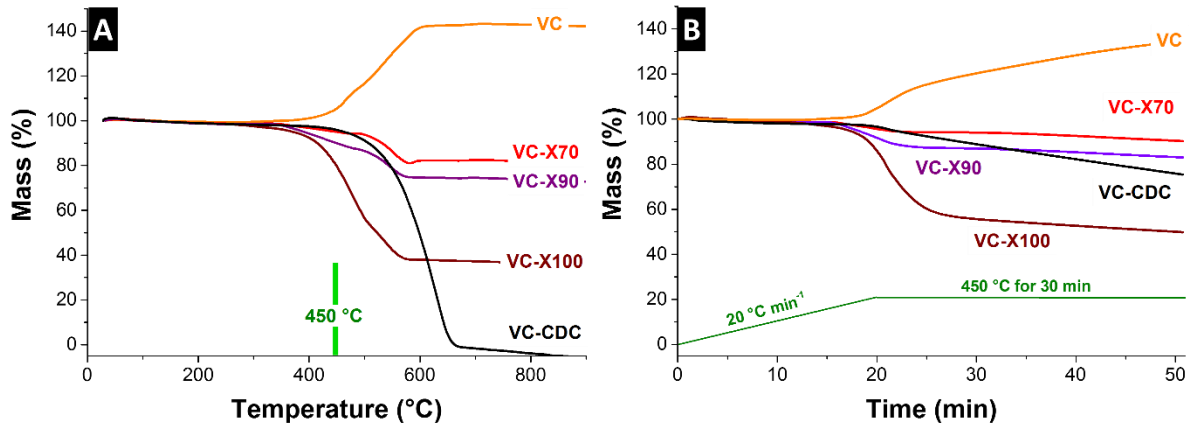

Figure S1: Thermogravimetric analysis in synthetic air with a heating rate of 20 °C·min^{-1} (A) until 900 °C and (B) until 450 °C and holding for 30 min.

X-ray diffraction

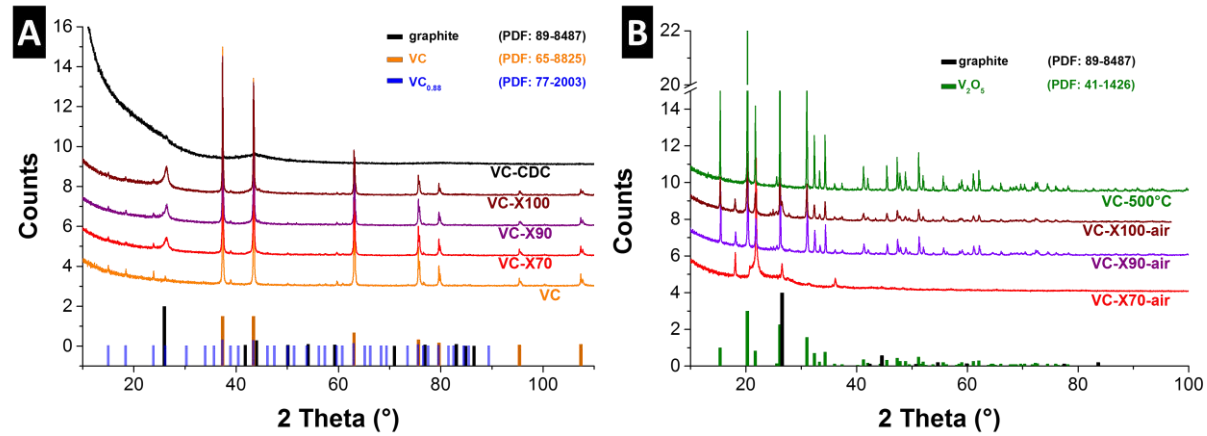

Figure S2: X-ray diffractogramms of VC/CDC composites (A) and V_2O_5/CDC composites (B).

Nitrogen gas sorption analysis

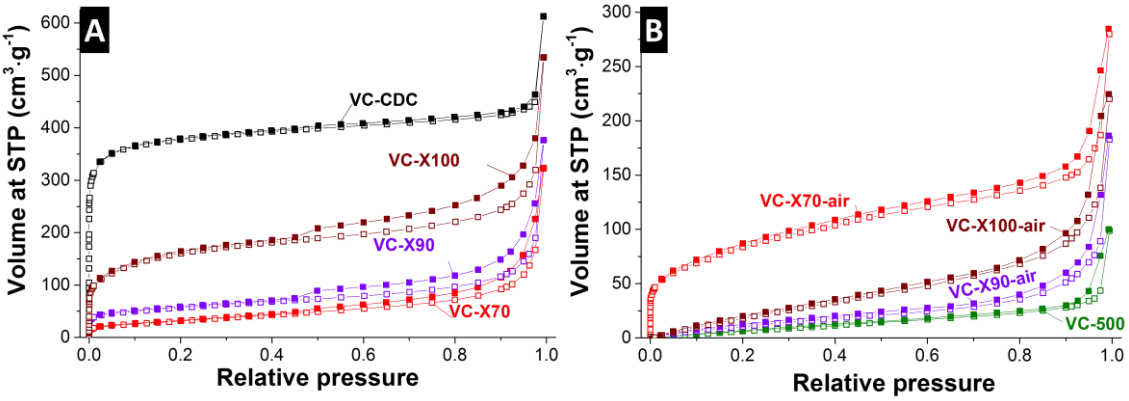

Figure S3: Nitrogen sorption isotherms of VC/CDC composites (A) and V_2O_5/CDC composites (B).

Electrochemical measurements

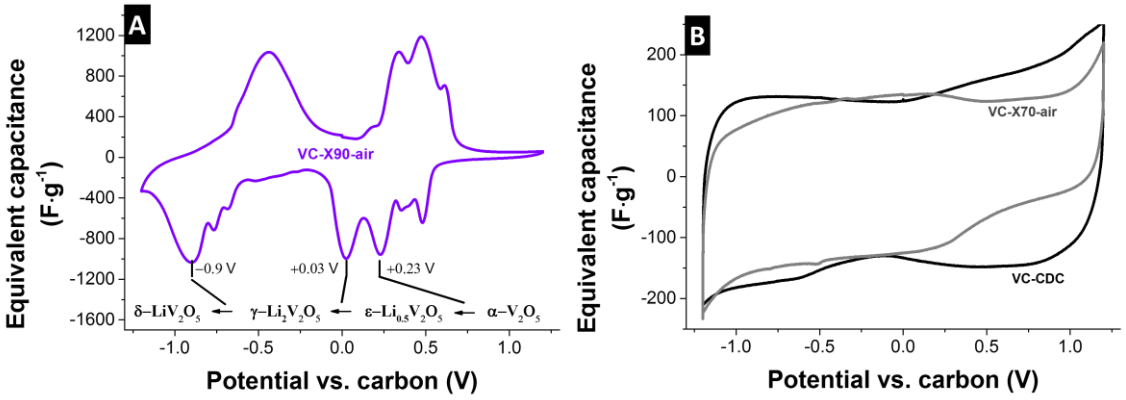

Figure S4: Cyclic voltammograms of VC-X90-air (A) and VC-X70-air and VC-CDC (B) at 1 $mV \cdot s^{-1}$ in half cell configuration.

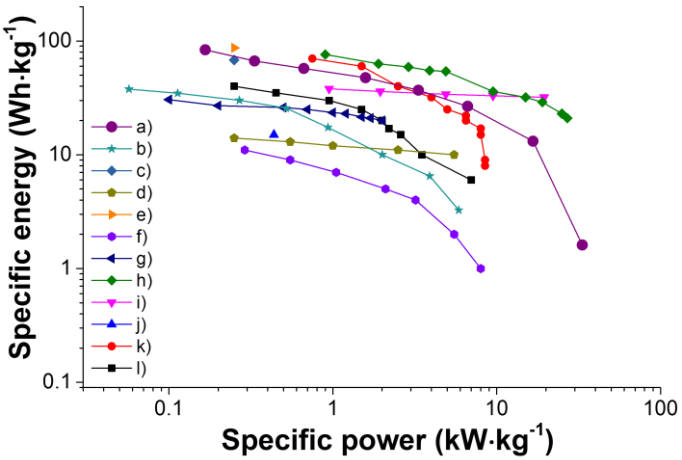

Figure S5: Ragone plot. a) this study, b)[1], c)[2], d)[3] e)[4], f)[5], g)[6], h)[7], i)[8], j)[9], k)[10].

Scanning electron micrographs

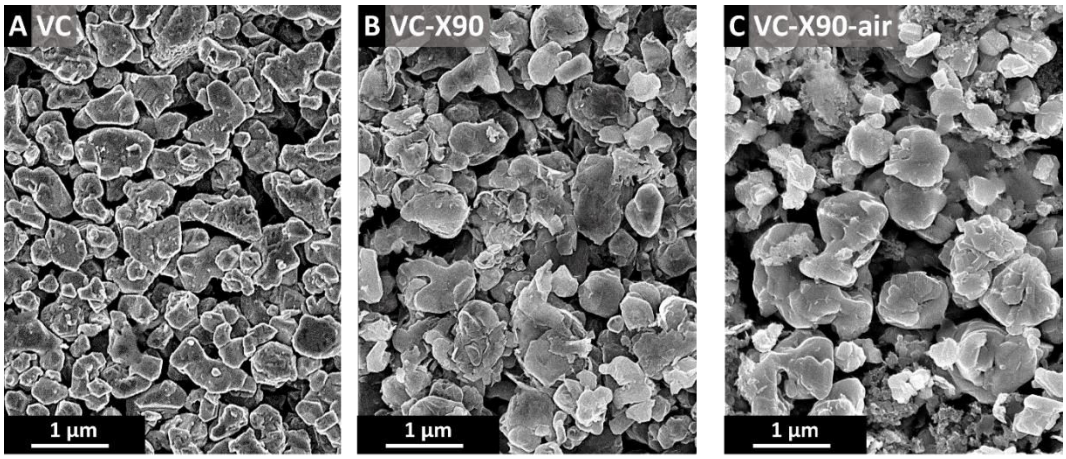

Figure S6: Scanning electron micrographs of (A) VC, (B) VC-X90, and (C) VC-X90-air.

Electrode conductivity measured using 4-point probe

Table S1: Electrode conductivity measured using 4-point probe. "n.d." means not detectable and related to values which are below the detection limit of the system.

	Electrode conductivity $S \cdot cm^{-1}$
VC-CDC	0.54±0.02
VC-X70-air	0.12±0.03
VC-X90-air	0.14±0.05
VC-X100-air	0.13±0.03
VC-500 pure	n.d.
VC-500 (25mass% VC-CDC)	0.05±0.01

Supporting references

1. S. Fleischmann, N. Jäckel, M. Zeiger, B. Krüner, I. Grobelsek, P. Formanek, S. Choudhury, D. Weingarth and V. Presser, *Chemistry of Materials*, 2016, **28**, 2802-2813..
2. Y. Wu, G. Gao and G. Wu, *Journal of Materials Chemistry A*, 2015, **3**, 1828-1832.
3. T. Qian, N. Xu, J. Zhou, T. Yang, X. Liu, X. Shen, J. Liang and C. Yan, *Journal of Materials Chemistry A*, 2015, **3**, 488-493.
4. Y. Wu, G. Gao, H. Yang, W. Bi, X. Liang, Y. Zhang, G. Zhang and G. Wu, *Journal of Materials Chemistry A*, 2015, **3**, 15692-15699.
5. C. X. Guo, G. Yilmaz, S. Chen, S. Chen and X. Lu, *Nano Energy*, 2015, **12**, 76-87.
6. Q. T. Qu, Y. Shi, L. L. Li, W. L. Guo, Y. P. Wu, H. P. Zhang, S. Y. Guan and R. Holze, *Electrochemistry Communications*, 2009, **11**, 1325-1328.
7. D. H. Nagaraju, Q. Wang, P. Beaujuge and H. N. Alshareef, *Journal of Materials Chemistry A*, 2014, **2**, 17146-17152.
8. X. Zhou, Q. Chen, A. Wang, J. Xu, S. Wu and J. Shen, *ACS Applied Materials & Interfaces*, 2016, **8**, 3776-3783.
9. S. D. Perera, M. Rudolph, R. G. Mariano, N. Nijem, J. P. Ferraris, Y. J. Chabal and K. J. Balkus Jr, *Nano Energy*, 2013, **2**, 966-975.
10. S. D. Perera, B. Patel, N. Nijem, K. Roodenko, O. Seitz, J. P. Ferraris, Y. J. Chabal and K. J. Balkus, *Advanced Energy Materials*, 2011, **1**, 936-945.

4. CONCLUSIONS AND OUTLOOK

In this PhD thesis, several strategies and material architectures were employed to synergistically combine the high rate capability of carbon materials with the high energy storage capacity of redox-active compounds. A special focus was set on the optimization of porosity, surface area, and the structure of the carbon support. Since microporous carbons, which are commonly used in EDLCs, present some disadvantages as substrate for pseudocapacitive and battery materials, carbon nanomaterials were investigated and compared. For this purpose, nanodiamond-derived carbon onions were used, because their surface area, structure, degree of carbon ordering, and chemical composition can be precisely tuned. Several key findings were extracted to synthesize carbon onions with optimal properties to support redox-active materials:

- The surface area of nanodiamond-derived carbon onions can be increased by higher synthesis temperatures to ~160%, due to the decrease in density and the volume expansion of the particles.
- High synthesis temperatures of 1700 °C lead to sintering and carbon redistribution processes, which limit the surface area increase.
- Nanodiamond-derived carbon onions demonstrate predominantly mesopores and only a small pore volume fraction is in the micropore range. The pores are located between the particles, which makes them easily accessible for decoration with redox-active species.
- Annealing of nanodiamonds in argon flow induces the formation of few-layer graphene between the carbon onions. Its high degree of carbon ordering and high conductivity are responsible for the better rate handling compared to vacuum-annealed carbon onions.

Different types of carbon onions and microporous carbons were hybridized with redox-active species and electrochemically benchmarked. The hybridization strategies range from surface functionalization using quinones, wet-chemical coatings with manganese oxide, sulfur nanoparticle deposits, to vanadium oxide/microporous carbon core-shell architectures. Especially the influence of the carbon substrate was investigated by

comparing exohedral carbon onions with endohedral microporous carbons. The main conclusions are listed and explained below:

- Free-standing and binder-free carbon onion/carbon fiber composite mats demonstrate a superior conductivity and rate capability (>60% capacitance retention at 100 A/g) in organic electrolyte. The exohedral and easily accessible surface area makes it to an ideal substrate for redox-active quinones, with high capacitance of 288 F/g and short charge/discharge times.
- High temperature carbon onions as support for pseudocapacitive manganese oxide demonstrate a higher specific capacitance of ~150 F/g compared to low temperature carbon onions and microporous AC. A high graphitization is necessary to enable high rate applications of the non-conductive manganese oxide. Additionally, the use of microporous AC leads to pore blocking issues during the coating process, resulting in a large decrease of surface area of ~90 % for a manganese oxide loading of 60 mass%.
- A combination of double-layer capacitance and redox-activity can be achieved using microporous carbon as conductive shell and Faradaic material as core. This was exemplarily shown for vanadium pentoxide/CDC core-shell particles with supercapacitor-like specific power and battery-like specific energy, exceeding 80 Wh/kg in asymmetric full cell set up.
- Carbon onions were also shown to be suitable as substrate for redox-active sulfur in lithium-sulfur batteries. An *in situ* generation of sulfur nanoparticles on carbon onions followed by annealing led to a homogeneous coating and high mass loadings with sulfur, which was easily accessible for the electrolyte ions. Combined with the high carbon conductivity, a high capacity of 800 mAh/g and a long life time, showing 400 mAh/g after 500 cycles, could be achieved.

These studies demonstrate the importance of the carbon substrate in pseudocapacitor and battery hybrids. Dependent on the material architecture, a microporous carbon with inner surface area presents a perfect support, for example, as conductive shell, when the battery material is in the core. In this case, pore blocking issues can be avoided, which typically happen when the carbon surface is coated. Alternatively, exohedral carbons with exclusively outer surface area are the materials of choice for on-top coating procedures.

The mesoporous external surface area is only slightly decreased by adding redox-active species. Electrolyte ions can easily access the Faradaic coating and – in combination with the very high conductivity - an improved electrochemical performance is achieved, compared to microporous substrates or just adding carbon as a conductive additive to the Faradaic material.

Further improvements of the energy storage properties of hybrid devices are expected by means of tuning the interface between carbon and the redox-active material, the material architecture, and the synthesis process. Metal oxide/microporous carbon core-shell particles were shown to be very suitable for high power and high energy devices. Their synthesis procedure includes several chlorination, oxidation, and washing steps, which is time-consuming and costly. However, the synthesis byproducts, in this case nickel, could be oxidized to form nickel oxide. This would avoid an additional washing step and a second redox-active material can contribute to the energy storing capacity. Additionally, owing to the open porous carbon shell, the metal oxide core is accessible for further synthesis steps. For example, a sulfidation could form a metal sulfide or different mixtures of metal oxide and metal sulfide with interesting electrochemical properties.

Apart from core-shell architectures, endohedral carbons with a mesoporous structure in the pore size range of ~10-20 nm are also promising as substrate, since their intraparticle pores can be coated, yielding high loadings, and at the same time, pore blocking can be avoided to a certain degree. The very large interface between the Faradaic coating and the electrolyte is expected to show high specific power due to the fast kinetics.

The development of full-cell devices, typically composed of the hybrid electrode and a microporous carbon counter electrode, leads to distinct charge balancing issues. Due to the high capacity of the Faradaic material in the hybrid, the counter electrode needs to compensate the charge by adjusting its electrode mass. Since the carbon electrode presents a low capacity, the full-cell specific energy is significantly reduced. To overcome this issue, adequate combinations have to be found to avoid pure carbon electrodes. Possible materials, which are well-known in the battery community, are lithium titanium oxide (LTO) as anode and lithium manganese oxide (LMO) as cathode. These materials could be synthesized as hybrid electrodes with carbon and used in full-cell arrangements.

REFERENCES

1. Karl, T.R. and K.E. Trenberth, *Modern global climate change.* science, 2003. **302**(5651): p. 1719-1723.
2. Arunachalam, V. and E. Fleischer, *The global energy landscape and materials innovation.* Mrs Bull, 2008. **33**: p. 264-276.
3. Herzog, A.V., et al., *Renewable energy: a viable choice.* Environment: Science and Policy for Sustainable Development, 2001. **43**(10): p. 8-20.
4. Yang, Z., et al., *Electrochemical energy storage for green grid.* Chemical reviews, 2011. **111**(5): p. 3577-3613.
5. Bosomworth, D., *Mobile marketing statistics 2015.* Leeds: Smart Insights (Marketing Intelligence) Ltd, 2015.
6. Ragone, D.V., *Review of battery systems for electrically powered vehicles*. 1968, SAE Technical Paper.
7. Denholm, P., et al., *The role of energy storage with renewable electricity generation.* National Renewable Energy Laboratory, 2010.
8. Hadjipaschalis, I., A. Poullikkas, and V. Efthimiou, *Overview of current and future energy storage technologies for electric power applications.* Renewable and Sustainable Energy Reviews, 2009. **13**(6-7): p. 1513-1522.
9. Bueno, C. and J.A. Carta, *Wind powered pumped hydro storage systems, a means of increasing the penetration of renewable energy in the Canary Islands.* Renewable and Sustainable Energy Reviews, 2006. **10**(4): p. 312-340.
10. Xue, X., K. Cheng, and D. Sutanto, *A study of the status and future of superconducting magnetic energy storage in power systems.* Superconductor Science and Technology, 2006. **19**(6): p. R31.
11. Whittingham, M.S., *History, evolution, and future status of energy storage.* Proceedings of the IEEE, 2012. **100**(Special Centennial Issue): p. 1518-1534.
12. Goodenough, J.B., *Electrochemical energy storage in a sustainable modern society.* Energy & Environmental Science, 2014. **7**(1): p. 14-18.
13. Simon, P. and Y. Gogotsi, *Materials for electrochemical capacitors.* Nature Materials, 2008. **7**(11): p. 845-854.
14. Béguin, F., et al., *Carbons and Electrolytes for Advanced Supercapacitors.* Advanced Materials, 2014. **26**(14): p. 2219-2251.
15. Scrosati, B., *Lithium rocking chair batteries: An old concept?* Journal of The Electrochemical Society, 1992. **139**(10): p. 2776-2781.
16. Nitta, N., et al., *Li-ion battery materials: present and future.* Materials Today, 2015. **18**(5): p. 252-264.
17. Whittingham, M.S., *Lithium batteries and cathode materials.* Chemical reviews, 2004. **104**(10): p. 4271-4302.
18. Speirs, J., et al., *The future of lithium availability for electric vehicle batteries.* Renewable and Sustainable Energy Reviews, 2014. **35**: p. 183-193.
19. Manthiram, A., et al., *Rechargeable lithium–sulfur batteries.* Chemical reviews, 2014. **114**(23): p. 11751-11787.
20. Borchardt, L., M. Oschatz, and S. Kaskel, *Carbon Materials for Lithium Sulfur Batteries - Ten Critical Questions.* Chemistry - A European Journal, 2016. **22**(22): p. 7324-7351.

21. Manthiram, A., S.H. Chung, and C. Zu, *Lithium–Sulfur Batteries: Progress and Prospects.* Advanced Materials, 2015. **27**(12): p. 1980-2006.
22. Manthiram, A., Y. Fu, and Y.-S. Su, *Challenges and prospects of lithium–sulfur batteries.* Accounts of chemical research, 2012. **46**(5): p. 1125-1134.
23. Frackowiak, E. and F. Beguin, *Carbon materials for the electrochemical storage of energy in capacitors.* Carbon, 2001. **39**(6): p. 937-950.
24. Augustyn, V., P. Simon, and B. Dunn, *Pseudocapacitive oxide materials for high-rate electrochemical energy storage.* Energy & Environmental Science, 2014. **7**(5): p. 1597-1614.
25. Dubal, D., et al., *Hybrid energy storage: the merging of battery and supercapacitor chemistries.* Chemical Society Reviews, 2015. **44**(7): p. 1777-1790.
26. Nishino, A., *Capacitors: operating principles, current market and technical trends.* Journal of power sources, 1996. **60**(2): p. 137-147.
27. Zhang, S. and N. Pan, *Supercapacitors performance evaluation.* Advanced Energy Materials, 2015. **5**(6).
28. Miller, J.R. and A.F. Burke, *Electrochemical capacitors: challenges and opportunities for real-world applications.* The Electrochemical Society Interface, 2008. **17**(1): p. 53.
29. Miller, J.M., *Ultracapacitor applications*. 2011: The Institution of Engineering and Technology.
30. Qu, D. and H. Shi, *Studies of activated carbons used in double-layer capacitors.* Journal of Power Sources, 1998. **74**(1): p. 99-107.
31. Shi, H., *Activated carbons and double layer capacitance.* Electrochimica Acta, 1996. **41**(10): p. 1633-1639.
32. Barbieri, O., et al., *Capacitance limits of high surface area activated carbons for double layer capacitors.* Carbon, 2005. **43**(6): p. 1303-1310.
33. Chmiola, J., et al., *Anomalous increase in carbon capacitance at pore sizes less than 1 nanometer.* Science, 2006. **313**(5794): p. 1760-3.
34. Lozano-Castello, D., et al., *Influence of pore structure and surface chemistry on electric double layer capacitance in non-aqueous electrolyte.* Carbon, 2003. **41**(9): p. 1765-1775.
35. Stoller, M.D., et al., *Interfacial capacitance of single layer graphene.* Energy & Environmental Science, 2011. **4**(11): p. 4685-4689.
36. Endo, M., et al., *Poly (vinylidene chloride)-based carbon as an electrode material for high power capacitors with an aqueous electrolyte.* Journal of the Electrochemical Society, 2001. **148**(10): p. A1135-A1140.
37. Shiraishi, S., H. Kurihara, and A. Oya, *Preparation and electric double layer capacitance of mesoporous carbon.* Carbon letters, 2001. **1**(3_4): p. 133-137.
38. Stoeckli, F. and T.A. Centeno, *Pore size distribution and capacitance in microporous carbons.* Physical Chemistry Chemical Physics, 2012. **14**(33): p. 11589-11591.
39. Centeno, T.A., O. Sereda, and F. Stoeckli, *Capacitance in carbon pores of 0.7 to 15 nm: a regular pattern.* Physical Chemistry Chemical Physics, 2011. **13**(27): p. 12403-12406.
40. Jäckel, N., et al., *Anomalous or regular capacitance? The influence of pore size dispersity on double-layer formation.* Journal of Power Sources, 2016.
41. Brunauer, S., P.H. Emmett, and E. Teller, *Adsorption of gases in multimolecular layers.* Journal of the American Chemical Society, 1938. **60**(2): p. 309-319.
42. Neimark, A.V., et al., *Quenched solid density functional theory and pore size analysis of micro-mesoporous carbons.* Carbon, 2009. **47**(7): p. 1617-1628.

43. Gor, G.Y., et al., *Quenched solid density functional theory method for characterization of mesoporous carbons by nitrogen adsorption.* Carbon, 2012. **50**(4): p. 1583-1590.
44. Jäckel, N., et al., *Increase in capacitance by subnanometer pores in carbon.* ACS Energy Letters, 2016. **1**(6): p. 1262-1265.
45. Gerischer, H., et al., *Density of the electronic states of graphite: derivation from differential capacitance measurements.* Journal of Physical Chemistry, 1987. **91**(7): p. 1930-1935.
46. Ruch, P., R. Kötz, and A. Wokaun, *Electrochemical characterization of single-walled carbon nanotubes for electrochemical double layer capacitors using non-aqueous electrolyte.* Electrochimica Acta, 2009. **54**(19): p. 4451-4458.
47. Weingarth, D., et al., *Graphitization as a Universal Tool to Tailor the Potential-Dependent Capacitance of Carbon Supercapacitors.* Advanced Energy Materials, 2014. **4**(13).
48. Moon, J.S., et al., *Increasing capacitance of zeolite-templated carbons in electric double layer capacitors.* Journal of The Electrochemical Society, 2015. **162**(5): p. A5070-A5076.
49. Yamada, Y., et al., *Electrochemical behavior of metallic and semiconducting single-wall carbon nanotubes for electric double-layer capacitor.* Carbon, 2012. **50**(3): p. 1422-1424.
50. Rand, B., et al., *Introduction to carbon science.* Butterworths, London, 1989: p. 75-92.
51. Kroto, H.W., et al., *C60: Buckminsterfullerene.* Nature, 1985. **318**(6042): p. 162-163.
52. Iijima, S., *Helical microtubules of graphitic carbon.* Nature, 1991. **354**(6348): p. 56-58.
53. Gogotsi, Y. and V. Presser, *Carbon nanomaterials*. 2013: CRC Press.
54. Brookes, C. and E. Brookes, *Diamond in perspective: a review of mechanical properties of natural diamond.* Diamond and related materials, 1991. **1**(1): p. 13-17.
55. Gu, W. and G. Yushin, *Review of nanostructured carbon materials for electrochemical capacitor applications: advantages and limitations of activated carbon, carbide-derived carbon, zeolite-templated carbon, carbon aerogels, carbon nanotubes, onion-like carbon, and graphene.* Wiley Interdisciplinary Reviews: Energy and Environment, 2014. **3**(5): p. 424-473.
56. Stoeckli, H.F., *Microporous carbons and their characterization: The present state of the art.* Carbon, 1990. **28**(1): p. 1-6.
57. Laine, J. and S. Yunes, *Effect of the preparation method on the pore size distribution of activated carbon from coconut shell.* Carbon, 1992. **30**(4): p. 601-604.
58. Krüner, B., et al., *Sub-micrometer novolac-derived carbon beads for high performance supercapacitors and redox electrolyte energy storage.* ACS applied materials & interfaces, 2016. **8**(14): p. 9104-9115.
59. Borchardt, L., M. Oschatz, and S. Kaskel, *Tailoring porosity in carbon materials for supercapacitor applications.* Materials Horizons, 2014. **1**(2): p. 157-168.
60. Lee, J., J. Kim, and T. Hyeon, *Recent progress in the synthesis of porous carbon materials.* Advanced Materials, 2006. **18**(16): p. 2073-2094.
61. Thommes, M., et al., *Physisorption of gases, with special reference to the evaluation of surface area and pore size distribution (IUPAC Technical Report).* Pure and Applied Chemistry, 2015. **87**(9-10): p. 1051-1069.
62. Zeiger, M., D. Weingarth, and V. Presser, *Quinone-Decorated Onion-Like Carbon/Carbon Fiber Hybrid Electrodes for High-Rate Supercapacitor Applications.* ChemElectroChem, 2015. **2**(8): p. 1117-1127.

63. Sutasinpromprae, J., et al., *Preparation and characterization of ultrafine electrospun polyacrylonitrile fibers and their subsequent pyrolysis to carbon fibers.* Polymer International, 2006. **55**(8): p. 825-833.
64. Presser, V., M. Heon, and Y. Gogotsi, *Carbide-Derived Carbons–From Porous Networks to Nanotubes and Graphene.* Advanced Functional Materials, 2011. **21**(5): p. 810-833.
65. Huang, J., et al., *Curvature effects in carbon nanomaterials: Exohedral versus endohedral supercapacitors.* Journal of Materials Research, 2011. **25**(08): p. 1525-1531.
66. Donnet, J.-B., *Carbon black: science and technology*. 1993: CRC Press.
67. Dominko, R., et al., *Influence of carbon black distribution on performance of oxide cathodes for Li ion batteries.* Electrochimica Acta, 2003. **48**(24): p. 3709-3716.
68. Jäckel, N., et al., *Comparison of carbon onions and carbon blacks as conductive additives for carbon supercapacitors in organic electrolytes.* Journal of Power Sources, 2014. **272**(0): p. 1122-1133.
69. Jäckel, N., et al., *Performance evaluation of conductive additives for activated carbon supercapacitors in organic electrolyte.* Electrochimica Acta, 2016. **191**: p. 284-298.
70. Zeiger, M., et al., *Review: carbon onions for electrochemical energy storage.* Journal of Materials Chemistry A, 2016. **4**(9): p. 3172-3196.
71. Zeiger, M., et al., *Influence of carbon substrate on the electrochemical performance of carbon/manganese oxide hybrids in aqueous and organic electrolytes.* RSC Advances, 2016. **6**(109): p. 107163-107179.
72. Simon, P., Y. Gogotsi, and B. Dunn, *Where Do Batteries End and Supercapacitors Begin?* Science, 2014. **343**(6176): p. 1210-1211.
73. Wang, G., L. Zhang, and J. Zhang, *A review of electrode materials for electrochemical supercapacitors.* Chemical Society Reviews, 2012. **41**(2): p. 797-828.
74. Lee, J., et al., *Tin/vanadium redox electrolyte for battery-like energy storage capacity combined with supercapacitor-like power handling.* Energy & Environmental Science, 2016. **9**(11): p. 3392-3398.
75. Chathoth, S.M., et al., *Dynamics of phenanthrenequinone on carbon nano-onion surfaces probed by quasielastic neutron scattering.* The Journal of Physical Chemistry B, 2012. **116**(24): p. 7291-7295.
76. Anjos, D.M., et al., *Pseudocapacitance and performance stability of quinone-coated carbon onions.* Nano Energy, 2013. **2**(5): p. 702-712.
77. Trasatti, S. and G. Buzzanca, *Ruthenium dioxide: A new interesting electrode material. Solid state structure and electrochemical behaviour.* Journal of Electroanalytical Chemistry and Interfacial Electrochemistry, 1971. **29**(2): p. A1-A5.
78. Wei, W., et al., *Manganese oxide-based materials as electrochemical supercapacitor electrodes.* Chemical Society Reviews, 2011. **40**(3): p. 1697-1721.
79. Fleischmann, S., et al., *Tuning pseudocapacitive and battery-like lithium intercalation in vanadium dioxide/carbon onion hybrids for asymmetric supercapacitor anodes.* Journal of Materials Chemistry A, 2017: p. accepted.
80. Kim, J.W., V. Augustyn, and B. Dunn, *The effect of crystallinity on the rapid pseudocapacitive response of Nb_2O_5.* Advanced Energy Materials, 2012. **2**(1): p. 141-148.
81. Sathiya, M., et al., *V_2O_5-anchored carbon nanotubes for enhanced electrochemical energy storage.* Journal of the American Chemical Society, 2011. **133**(40): p. 16291-16299.

82. Augustyn, V., et al., *High-rate electrochemical energy storage through Li^+ intercalation pseudocapacitance.* Nature materials, 2013. **12**(6): p. 518-522.
83. Anasori, B., M.R. Lukatskaya, and Y. Gogotsi, *2D metal carbides and nitrides (MXenes) for energy storage.* Nature Reviews Materials, 2017. **2**: p. 16098.
84. Li, H. and H. Zhou, *Enhancing the performances of Li-ion batteries by carbon-coating: present and future.* Chemical Communications, 2012. **48**(9): p. 1201-1217.
85. Spahr, M.E., et al., *Development of carbon conductive additives for advanced lithium ion batteries.* Journal of Power Sources, 2011. **196**(7): p. 3404-3413.
86. Chen, Y.-H., et al., *Selection of conductive additives in li-ion battery cathodes a numerical study.* Journal of the Electrochemical Society, 2007. **154**(10): p. A978-A986.
87. Vilatela, J.J. and D. Eder, *Nanocarbon composites and hybrids in sustainability: a review.* ChemSusChem, 2012. **5**(3): p. 456-478.
88. Kickelbick, G., *Hybrid materials: synthesis, characterization, and applications*. 2007: John Wiley & Sons.
89. Fleischmann, S., et al., *Enhanced Electrochemical Energy Storage by Nanoscopic Decoration of Endohedral and Exohedral Carbon with Vanadium Oxide via Atomic Layer Deposition.* Chemistry of Materials, 2016. **28**(8): p. 2802-2813.
90. Upare, D.P., S. Yoon, and C.W. Lee, *Nano-structured porous carbon materials for catalysis and energy storage.* Korean Journal of Chemical Engineering, 2011. **28**(3): p. 731-743.
91. Frackowiak, E., et al., *Supercapacitor electrodes from multiwalled carbon nanotubes.* Applied Physics Letters, 2000. **77**(15): p. 2421-2423.
92. Makgopa, K., et al., *A high-rate aqueous symmetric pseudocapacitor based on highly graphitized onion-like carbon/birnessite-type manganese oxide nanohybrids.* Journal of Materials Chemistry A, 2015. **3**(7): p. 3480-3490.
93. Choudhury, S., et al., *Carbon onion-sulfur hybrid cathodes for lithium-sulfur batteries.* Sustainable Energy & Fuels, 2017. **1**(1): p. 84-94.
94. Fleischmann, S., et al., *Vanadia-titania multilayer nanodecoration of carbon onions via atomic layer deposition for high performance electrochemical energy storage.* Journal of Materials Chemistry A, 2016. **5**(6): p. 2792-2801.
95. Boukhalfa, S., K. Evanoff, and G. Yushin, *Atomic layer deposition of vanadium oxide on carbon nanotubes for high-power supercapacitor electrodes.* Energy & Environmental Science, 2012. **5**(5): p. 6872-6879.
96. Özer, N., *Electrochemical properties of sol-gel deposited vanadium pentoxide films.* Thin Solid Films, 1997. **305**(1–2): p. 80-87.
97. Long, J.W., et al., *Spectroelectrochemical investigations of cation-insertion reactions at sol-gel-derived nanostructured, mesoporous thin films of manganese oxide.* The Journal of Physical Chemistry B, 2001. **105**(37): p. 8712-8717.
98. Zeiger, M., et al., *Vanadium pentoxide/carbide-derived carbon core-shell hybrid particles for high performance electrochemical energy storage.* Journal of Materials Chemistry A, 2016. **4**(48): p. 18899-18909.
99. Zeiger, M., et al., *Understanding structure and porosity of nanodiamond-derived carbon onions.* Carbon, 2015. **84**(0): p. 584-598.
100. Zeiger, M., et al., *Vacuum or flowing argon: What is the best synthesis atmosphere for nanodiamond-derived carbon onions for supercapacitor electrodes?* Carbon, 2015. **94**: p. 507-517.
101. Zhang, L.L., et al., *Manganese oxide–carbon composite as supercapacitor electrode materials.* Microporous and Mesoporous Materials, 2009. **123**(1): p. 260-267.

102. Xu, C., et al., *Recent progress on manganese dioxide based supercapacitors.* Journal of materials research, 2010. **25**(08): p. 1421-1432.
103. Lee, S.W., et al., *Carbon nanotube/manganese oxide ultrathin film electrodes for electrochemical capacitors.* Acs Nano, 2010. **4**(7): p. 3889-3896.
104. Toupin, M., T. Brousse, and D. Bélanger, *Influence of Microstucture on the Charge Storage Properties of Chemically Synthesized Manganese Dioxide.* Chemistry of Materials, 2002. **14**(9): p. 3946-3952.

CURRICULUM VITAE

MARCO ZEIGER, M.SC.

- ***Deputy Group Leader***
  Energy Materials Group at
  INM - Leibniz Institute for New Materials
- ***PhD Student***
  Saarland University &
  INM - Leibniz Institute for New Materials
- ***Master of Science***
  Microfabrication and Nanostructures
  Department of Physics and Mechatronics,
  Saarland University

- Date of birth: February 13th, 1988
- Nationality: German
- Family status: unmarried

- Saarland University & INM - Leibniz Institute for New Materials (Program Division Energy Materials, Prof. Presser)
- Campus D2 2, 66123, Saarbrücken, Germany
  www.leibniz-inm.de

- www.marco-zeiger.com

- marco.zeiger@leibniz-inm.de
- +49 (681) 9300-218 +49 (176) 969 00 904

EDUCATION

- **Master of Science** in Microfabrication and Nanostructures, 06/2014
  - Saarland University & INM - Leibniz Institute for New Materials (Energy Materials Group)
  - ***Title*: Synthesis and properties of onion-like carbons and their use in supercapacitors**
    (grade: 1.0 - 1 peer-review paper)

- **Bachelor of Science** in Microfabrication and Nanostructures, 10/2012
  - Saarland University & INM - Leibniz Institute for New Materials (Metallic Microstructures Group)
  - ***Title*: Optimization of the antibacterial effect of copper using microfabrication methods**
    (grade: 1.0 - 1 Patent - 1 peer-review paper - 1 best talk award)

- **German High School Diploma (Abitur)**, 06/2007
  - Gymnasium am Steinwald, Neunkirchen, Germany
  - Mathematics, Biology, Politics, English

PROFESSIONAL EXPERIENCE

INM - Leibniz Institute for New Materials

- Deputy Group Leader - Energy Materials Group, since 06/2016
- PhD Student - Energy Materials Group, since 08/2014
- Master Student - Energy Materials Group, 05/2013 - 07/2014
- Student Intern - Metallic Microstructures Group, 10/2012 - 05/2013
- Bachelor Student - Metallic Microstructures Group, 04/2012 - 10/2012
- Student Intern - Metallic Microstructures Group, 01/2011 - 04/2012

Saarland University

- Student Intern - Institute of Production Engineering, 09/2009 - 03/2011
- Student Intern - Laboratory for Measurement Technology, 01/2010 - 04/2010

SCIENTIFIC QUALIFICATIONS AND EXPERTISE

- Synthesis of carbon nanomaterials using chemical and physical approaches
- Electrospinning
- Electrode preparation for batteries and supercapacitors
- Electrochemical characterization using potentiostats/galvanostats

- Transmission electron microscopy
- Scanning electron microscopy
- Raman spectroscopy
- X-ray diffraction
- Helium gas pycnometry
- Thermogravimetric analysis
- Gas sorption analysis

AWARDS & HONORS

- **DAAD travel grant**, Carbon conference, Melbourne (Australia), July 23rd - 28th, 2017.
- **Nominated for the 66th Lindau Nobel Laureate Meeting by the Leibniz association and the Lindau Nobel Laureate committee,** Lindau (Germany), June 26th - July 1st, 2016.
- **Best poster award** "ELECTROCHEMICAL ENERGY STORAGE WITH CARBON ONIONS" 3rd PhD Student Day of Saarland University, Saarbrücken (Germany), November 11th, 2015.
- **Best poster award** "CARBON ONION / NANOFIBER COMPOSITES FOR ELECTRICAL ENERGY STORAGE", 2nd International INM/UdS Poster Symposium, Saarbrücken (Germany), August 14th, 2014.
- **Best talk award** "BIOCIDAL SURFACES", INASCON, London (England) August 19th-22nd, 2013.

TEACHING

2013-2017 (summer term)	Lecture: **Introduction to Thermodynamics**
2013-2017 (summer term)	Exercises: **Introduction to Thermodynamics**
2013-2017 (summer term)	Lecture: **Smart Materials**
2015 (summer term)	Practical training: **Energy Materials**
2012 (summer term)	Lecture: **NanoBiomaterials**
2010-2013 (winter term)	Exercises**: Introduction to Materials science**
2011 (winter term)	Lecture+Exercises: **Maths for social pedadogy**

SUPERVISION

2017 **Master thesis** (Synthesis, properties and application of carbon nanodots for energy storage; Alexander Ridder)

2016 **Master thesis** (Heteroatom-doped carbon onions and their use in supercapacitors; Javier Diez Sierra)

PATENT

- A. Schneider, M. Zeiger, Christian A. Frontzek (2013). ANTIMIKROBIELL AUSGERÜSTETES POLYMER MIT EINGEBUNDENEN PARTIKELN UND DESINFEKTIONSELEMENT AUF BASIS DES POLYMERS.
  13002999.4-1356 (European patent)

PUBLICATIONS

33 peer-review publications (**7** x first author)
h-index: **12**

(Nano)materials Synthesis and Characterization

J-1 **Zeiger, M.**, Jäckel, N., Aslan, M., Weingarth, D., Presser, V. UNDERSTANDING STRUCTURE AND POROSITY OF NANODIAMOND-DERIVED CARBON ONIONS. Carbon. 2015;84:584-98.

J-2 Golshadi, M., Maita, J., Lanza, D., **Zeiger, M.**, Presser, V., Schrlau, M.G. EFFECTS OF SYNTHESIS PARAMETERS ON CARBON NANOTUBES MANUFACTURED BY TEMPLATE-BASED CHEMICAL VAPOR DEPOSITION. *Carbon*. 2014;80:28-39.

J-3 Souza, N., **Zeiger, M.**, Presser, V., Mücklich, F. IN SITU TRACKING OF DEFECT HEALING AND PURIFICATION OF SINGLE-WALL CARBON NANOTUBES WITH LASER RADIATION BY TIME-RESOLVED RAMAN SPECTROSCOPY. *RSC Adv.* 2015;5(76):62149-59.

J-4 Atchison, J.S., **Zeiger, M.**, Tolosa, A., Funke, L.M., Jäckel, N., Presser, V. ELECTROSPINNING OF ULTRAFINE METAL OXIDE/CARBON AND METAL CARBIDE/CARBON NANOCOMPOSITE FIBERS. *RSC Adv.* 2015;5(45):35683-92.

J-5 Forse, A.C., Merlet, C., Allan, P.K., Humphreys, E.K., Griffin, J.M., Aslan, M., **Zeiger, M.** et al. NEW INSIGHTS INTO THE STRUCTURE OF NANOPOROUS CARBONS FROM NMR, RAMAN, AND PAIR DISTRIBUTION FUNCTION ANALYSIS. *Chem. Mater.* 2015, 27, 6848-6857.

J-6 Reinert, L., **Zeiger, M.**, Suarez, S., Presser, V., Mücklich, F. DISPERSION ANALYSIS OF CARBON NANOTUBES, CARBON ONIONS, AND NANODIAMONDS FOR THEIR APPLICATION AS REINFORCEMENT PHASE IN NICKEL METAL MATRIX COMPOSITES. *RSC Adv*. 2015, 5, 95149-95159.

J-7 Souza, N., Lasserre, F., Blickley, A., **Zeiger, M.**, Suarez, S., Duarte, M., Presser, V., Mücklich, F. UPCYCLING SPENT PETROLEUM CRACKING CATALYST: PULSED LASER DEPOSITION OF SINGLE-WALL CARBON NANOTUBES AND SILICA NANOWIRES. *RSC Adv.* 2016, 6 (76), 72596-72606.

Energy Storage

J-8 **Zeiger, M.**, Weingarth, D., Presser, V. QUINONE-DECORATED ONION-LIKE CARBON/CARBON FIBER HYBRID ELECTRODES FOR HIGH-RATE SUPERCAPACITOR APPLICATIONS. *ChemElectroChem*. 2015, 2, 1117-1127.

J-9 **Zeiger, M.**, Jäckel, N., Weingarth, D., Presser, V. VACUUM OR FLOWING ARGON: WHAT IS THE BEST SYNTHESIS ATMOSPHERE FOR NANODIAMOND-DERIVED CARBON ONIONS FOR SUPERCAPACITOR ELECTRODES? *Carbon*. 2015; 94:507-17.

J-10 Weingarth, D., **Zeiger, M.**, Jäckel, N., Aslan, M., Feng, G., Presser, V. GRAPHITIZATION AS A UNIVERSAL TOOL TO TAILOR THE POTENTIAL-DEPENDENT CAPACITANCE OF CARBON SUPERCAPACITORS. *Adv. Energy Mater.* 2014, 4.

J-11 Makgopa, K., Ejikeme, P.M., Jafta, C.J., Raju, K., **Zeiger, M.**, Presser, V., et al. A HIGH-RATE AQUEOUS SYMMETRIC PSEUDOCAPACITOR BASED ON HIGHLY GRAPHITIZED ONION-LIKE CARBON/BIRNESSITE-TYPE MANGANESE OXIDE NANOHYBRIDS. *J. Mater. Chem. A*. 2015; 3(7):3480-90.

J-12 Jäckel, N., Weingarth, D., **Zeiger, M.**, Aslan, M., Grobelsek, I., Presser, V. COMPARISON OF CARBON ONIONS AND CARBON BLACKS AS CONDUCTIVE ADDITIVES FOR CARBON SUPERCAPACITORS IN ORGANIC ELECTROLYTES. *J. Power Sources*. 2014; 272:1122-33.

J-13 Oschatz, M., **Zeiger, M.**, Jäckel, N., Strubel, P., Borchardt, L., Reinhold, R., et al. EMULSION SOFT TEMPLATING OF CARBIDE-DERIVED CARBON NANOSPHERES WITH CONTROLLABLE POROSITY FOR CAPACITIVE ELECTROCHEMICAL ENERGY STORAGE. *J. Mater. Chem. A*. 2015;3(35):17983-90.

J-14 Ewert, J.K., Weingarth, D., Denner, C., Friedrich, M., **Zeiger M.**, Schreiber A., et al. ENHANCED CAPACITANCE OF NITROGEN-DOPED HIERARCHICALLY POROUS CARBIDE-DERIVED CARBON IN MATCHED IONIC LIQUIDS. *J. Mater. Chem. A*. 2015;3(37):18906-12

J-15 **Zeiger, M.**, Jäckel, N., Mochalin, V.N., Presser V. REVIEW: CARBON ONIONS FOR ELECTROCHEMICAL ENERGY STORAGE. *J. Mater. Chem. A*. 2016, 4, 3172-3196

J-16 Jäckel, N., Weingarth, D., Schreiber, A., Krüner, B., **Zeiger, M.**, Tolosa, A., et al. PERFORMANCE EVALUATION OF CONDUCTIVE ADDITIVES FOR ACTIVATED CARBON SUPERCAPACITORS IN ORGANIC ELECTROLYTE. *Electroch. Acta*. 2016, 191, 284–298

J-17 Fleischmann, S., Jäckel, N., **Zeiger, M.**, Krüner, B., Grobelsek, I., Formanek, P., Choudhury, S., Weingarth, D., Presser, V. ENHANCED ELECTROCHEMICAL ENERGY STORAGE BY NANOSCOPIC DECORATION OF ENDOHEDRAL AND EXOHEDRAL CARBON WITH VANADIUM OXIDE VIA ATOMIC LAYER DEPOSITION. *Chem. Mater.* 2016, 28, 2802-2813.

J-18 Jäckel, N., Rodner, M., Schreiber, A., Jeongwook, J., **Zeiger, M.**, Aslan, M., Weingarth, D., Presser, V. ANOMALOUS OR REGULAR CAPACITANCE? THE INFLUENCE OF PORE SIZE DISPERSITY ON DOUBLE-LAYER FORMATION. *J. Power Sources* 2016, 326, 660-671.

J-19 Tolosa, A., Krüner, B., Fleischmann, S., Jäckel, N., **Zeiger, M.**, Aslan, M., Grobelsek, I., Presser, V.. NIOBIUM CARBIDE NANOFIBERS AS A VERSATILE PRECURSOR FOR HIGH POWER SUPERCAPACITOR AND HIGH ENERGY BATTERY ELECTRODES. *J. Mater. Chem. A* 2016, 4, 16003-16016.

J-20 **Zeiger, M.**, Ariyanto, T., Krüner, B., Fleischmann, S., Peter, N. J., Etzold, B. J. M., Presser, V. VANADIUM PENTOXIDE / CARBIDE-DERIVED CARBON CORE-SHELL HYBRID PARTICLES FOR HIGH PERFORMANCE ELECTROCHEMICAL ENERGY STORAGE. *J. Mater. Chem. A* 2016, 4 (48), 18899-18909.

J-21 **Zeiger, M.**, Fleischmann, S., Krüner, B., Tolosa, A., Bechtel, S., Baltes, M., Schreiber, A., Moroni, R., Vierrath, S., Thiele, S., Presser, V. INFLUENCE OF CARBON SUBSTRATE ON THE ELECTROCHEMICAL PERFORMANCE OF CARBON/MANGANESE OXIDE HYBRIDS IN AQUEOUS AND ORGANIC ELECTROLYTES. *RSC Adv.* 2016, 6(109), 107163-107179.

J-22 Lee, J., Jäckel, N., Kim, D., Widmaier, M., Sathyamoorthi, S., Pattarachai, S., Kim, C., Fleischmann, S., **Zeiger, M.**, Presser, V. FEASIBILITY OF POROUS CARBON AS A QUASI-REFERENCE ELECTRODE IN AQUEOUS ELECTROLYTES. *Electroch. Acta*. 2016, 222, 1800-1805

J-23 Fleischmann, S., Tolosa, A., **Zeiger, M.**, Krüner, B., Peter, N. J., Grobelsek, I., Quade, A., Kruth, A., Presser, V. VANADIA-TITANIA MULTILAYER NANODECORATION OF CARBON ONIONS VIA ATOMIC LAYER DEPOSITION FOR HIGH PERFORMANCE ELECTROCHEMICAL ENERGY STORAGE. *J. Mater. Chem. A* 2016, 5 (6), 2792-2801.

J-24 Choudhury, S., **Zeiger, M.**, Massuti-Ballester, P., Fleischmann, S., Formanek, P., Borchardt, L., Presser, V. CARBON ONION - SULFUR HYBRID CATHODES FOR LITHIUM-SULFUR BATTERIES. *Sustainable Energy & Fuels* 2017, 1**,** 84-94.

J-25 Lee, J., Tolosa, A., Krüner, B., Jäckel, N., Fleischmann, S., **Zeiger, M.**, Kim, D., Presser, V. ASYMMETRIC TIN-VANADIUM REDOX ELECTROLYTE FOR HYBRID ENERGY STORAGE WITH NANOPOROUS CARBON ELECTRODES. *Sustainable Energy & Fuels* 2017, **1**, 299-307.

J-26 Fleischmann, S., **Zeiger, M**., Jäckel, N., Krüner, B., Lemkova, V., Widmaier, M., Presser, V. TUNING PSEUDOCAPACITIVE AND BATTERY-LIKE LITHIUM INTERCALATION IN VANADIUM DIOXIDE/CARBON ONION HYBRIDS FOR ASYMMETRIC SUPERCAPACITOR ANODES. *J. Mater. Chem. A* 2017.

J-27 Lee, J., Srimuk, P., Fleischmann, S., Ridder, A., **Zeiger, M.**, Presser, V. NANOCONFINEMENT OF REDOX REACTIONS ENABLES RAPID ZINC IODIDE ENERGY STORAGE WITH HIGH EFFICIENCY. *J. Mater. Chem.* A 2017, 5 (24), 12520-1527.

Water treatment

J-28 Aslan, M., **Zeiger, M.**, Jäckel, N., Grobelsek, I., Weingarth, D., Presser, V. IMPROVED CAPACITIVE DEIONIZATION PERFORMANCE OF MIXED HYDROPHOBIC/HYDROPHILIC ACTIVATED CARBON ELECTRODES. *J. Phys.: Condens. Matter* 2016, 28, 114003.

J-29 Srimuk, P., Ries, L., **Zeiger, M.**, Fleischmann, S., Jäckel, N., Tolosa, A., Krüner, B., Aslan, M., Presser, V. HIGH PERFORMANCE STABILITY OF TITANIA DECORATED CARBON FOR DESALINATION WITH CAPACITIVE DEIONIZATION IN OXYGENATED WATER. *RSC Adv.* 2016, 6 (108), 106081-106089.

J-30 Srimuk, P., **Zeiger, M.**, Jäckel, N., Tolosa, A., Krüner, B., Fleischmann, S., Grobelsek, I., Aslan, M., Shvartsev, B., Suss, M. E., Presser, V. ENHANCED PERFORMANCE STABILITY OF CARBON/TITANIA HYBRID ELECTRODES DURING CAPACITIVE DEIONIZATION OF OXYGEN SATURATED SALINE WATER. *Electroch. Acta* 2017, 224, 314-328.

J-31 Krüner, B., Srimuk, P., Fleischmann, S., **Zeiger, M.**, Schreiber, A., Aslan, M., Quade, A., Presser, V. HYDROGEN-TREATED, SUB-MICROMETER CARBON BEADS FOR FAST CAPACITIVE DEIONIZATION WITH HIGH PERFORMANCE STABILITY. *Carbon 2017*, 117, 46-54.

Biointerfaces and Biomaterials

J-32 **Zeiger, M.**, Solioz, M., Edongué, H., Arzt, E., Schneider, A.S. SURFACE STRUCTURE INFLUENCES CONTACT KILLING OF BACTERIA BY COPPER. *MicrobiologyOpen*. 2014; 3(3):327-32.

J-33 Lemloh, M-L., Pohl, A., Weber, E., **Zeiger, M.**, Bauer, P., Weiss, I.M., et al. STRUCTURE-PROPERTY RELATIONSHIPS IN MECHANICALLY STIMULATED SORGHUM BICOLOR STALKS. *Bioinspired Materials.* 2014, 1, 1-11.

TALKS

T-1 **Zeiger, M.**, Arzt, E., Schneider A.S. OPTIMIERUNG ANTIBAKTERIELLER KUPFERFOLIEN MITTELS MIKROSTRUKTURIERUNG. WÜMEK. Würzburg (Germany). May 13th-14th.

T-2 **Zeiger, M.,** Arzt, E., Schneider A.S. BIOCIDAL SURFACES. INASCON. London (England). August 19th-22nd. 2013. (***Best talk award***)

T-3 **Zeiger, M.**, Presser, V. RAMAN SPECTROSCOPY OF CARBON NANOMATERIALS FOR ENERGY APPLICATIONS. Renishaw's Inside Raman Seminar. Pliezhausen (Germany). September 25th-26th. 2014 (***Invited Talk***).

T-4 Jäckel, N., Weingarth, D., **Zeiger, M.**, Aslan, M., Grobelsek, I., Presser, V. COMPARISON OF CARBON ONIONS AND CARBON BLACKS AS CONDUCTIVE ADDITIVES FOR CARBON SUPERCAPACITORS IN ORGANIC ELECTROLYTES. 65th Annual Meeting of the International Society of Electrochemistry (ISE). Lausanne (Switzerland). August 31st-September 5th. 2014.

T-5 **Zeiger, M.**, Jäckel, N., Aslan, M., Weingarth, D., Presser, V. TUNING STRUCTURE AND POROSITY OF ONION-LIKE CARBON SYNTHESIZED VIA THERMAL ANNEALING OF NANODIAMOND. 9th Torunian Carbon Symposium. Torun (Poland). September 14th-18th. 2014.

T-6 **Zeiger, M.**, Jäckel, N., Weingarth, D., and Presser, V. HIGHLY CONDUCTIVE CARBON ONION / NANOFIBER COMPOSITE SUPERCAPACITOR ELECTRODES. COST Winter Seminar Latest Developments in Electrochemical Capacitors. Poznan (Poland). January 29th-31st. 2015.

T-7 **Zeiger, M.**, Jäckel, N., Aslan, M., Weingarth, D., Presser, V. TUNING STRUCTURE AND POROSITY OF ONION-LIKE CARBON SYNTHESIZED VIA THERMAL ANNEALING OF NANODIAMOND. Carbon 2015. Dresden (Germany). July 12th-17th. 2015. .

T-8 Jäckel, N., Weingarth, D., **M. Zeiger**, Aslan, M., Presser, V. ELECTRICAL CONDUCTIVITY OF CARBON SUPERCAPACITOR ELECTRODES AND ITS BEARING ON ELECTROCHEMICAL PERFORMANCE. Carbon 2015. Dresden (Germany). July 12th-17th. 2015.

T-9 **Zeiger, M.**, Presser, V. SPICY ENERGY STORAGE WITH CARBON ONIONS. BMBF Junior Investigation Workshop Energy Research. Saarbrücken INM (Germany). September 28th-29th. 2015.

T-10 **Zeiger, M.**, Weingarth, D., Presser, V. CARBON ONIONS FOR SUPERCAPACITOR AND PSEUDOCAPACITOR ELECTRODES. 6th International Conference Carbon for Energy Storage/conversion and Environment Protection (CESEP). Poznan (Poland), October 18th-22nd. 2015.

T-11 **Zeiger, M.**, Jäckel, N., Fleischmann, S., Presser, V. CARBON ONIONS FOR ELECTROCHEMICAL ENERGY STORAGE. Workshop Future Capacitive Technologies. University of Tartu. Tartu (Estonia). December 11th-14th. 2015.

T-12 **Zeiger, M.**, Jäckel, N., Presser, V. SPICY ENERGY STORAGE: ELECTROCHEMICAL APPLICATIONS OF NANODIAMOND-DERIVED CARBON ONIONS. MRS Spring Meeting & Exhibit. Phoenix. Arizona (USA). March 28th-April 1st. 2016. (***Invited talk***)

T-13 **Zeiger, M.**, Fleischmann, S., Presser, V. NANOCARBONS AND REDOX-ACTIVE METAL OXIDES FOR SUPERCAPACITORS, PSEUDOCAPACITORS, AND BATTERY-HYBRIDS. IMRC. Cancun (Mexico). August 14th-August 19st. 2016. (***Invited talk***)

T-14 **Zeiger, M.**, Presser, V. CAPACITIVE AND BATTERY-LIKE ENERGY STORAGE WITH REDOX-ENABLED NANOCARBONS. 3rd BMBF meeting. Dresden (Germany). November 22th-November 24th. 2016.

T-15 **Zeiger, M.**, Fleischmann, S., Etzold, B.J.M., Presser, V. DESIGNING THE CARBON/VANADIA INTERFACE FOR HYBRID ELECTROCHEMICAL ENERGY STORAGE. Carbon conference, Melbourne (Australia). July 23rd- July 28th. 2017.

T-16 **Zeiger, M.**, Etzold, B.J.M., Presser, V. TAILORING THE PROPERTIES OF NANOCARBON/METAL OXIDE HYBRIDS FOR PSEUDOCAPACITIVE AND BATTERY-LIKE ELECTROCHEMICAL ENERGY STORAGE. 254th American Chemical Society National Meeting, Washington DC (USA). August 20th-August 24th. 2017.

POSTERS

P-1 Fleischmann, S., Jäckel, N., **Zeiger, M.**, Weingarth, D., Presser, V. ATOMIC LAYER DEPOSITION OF VANADIUM OXIDE ON CARBON ONIONS FOR HYBRID ENERGY STORAGE. 9th International Nanoscience Student Conference (INASCON). Basel (Switzerland). August 11th-14th. 2015.

P-2 **Zeiger, M.**, Weingarth, D., Aslan, M., Atchison, J.S., Presser, V. CARBON ONION / NANOFIBER COMPOSITES FOR ELECTRICAL ENERGY STORAGE. 2nd PhD Student Day of Saarland University. Saarbrücken (Germany). November 12th. 2014.

P-3 Jäckel, N., Weingarth, D., **Zeiger, M.**, Aslan, M., Presser, V. GRAPHITIZATION AS A UNIVERSAL TOOL TO IMPROVE THE ENERGY DENSITY OF SUPERCAPACITORS. 2nd International INM/UdS Poster Symposium. Saarbrücken (Germany). August 14th. 2014.

P-4 **Zeiger, M.**, Weingarth, D., M. Aslan, Atchison, J.S., Presser, V. CARBON ONION / NANOFIBER COMPOSITES FOR ELECTRICAL ENERGY STORAGE. 2nd International

INM/UdS Poster Symposium. Saarbrücken (Germany). August 14th. 2014. ***(1st place for best PhD student poster)***

P-5 **Zeiger, M.**, Jäckel, N., Fleischmann, S., Presser, V. ELECTROCHEMICAL ENERGY STORAGE WITH CARBON ONIONS. 3rd PhD Student Day of Saarland University. Saarbrücken (Germany). November 11th. 2015. (***Best poster award***)

P-6 Quilitz, M., **Zeiger, M.**, Kraus, T., Moh, K., Presser, V., Arzt, E. INNOVATIVE ENERGIEFORSCHUNG AM INM. AG LIESA congress. Congress hall. Saarbrücken (Germany). October 26th. 2016.

P-7 **Zeiger, M.**, Jäckel, N., Fleischmann, S., Presser, V. CAPACITIVE AND BATTERY-LIKE ENERGY STORAGE WITH REDOX-ENABLED NANOCARBONS. 4th PhD Student Day of Saarland University. Saarbrücken (Germany). November 9th. 2016.

P-8 **Zeiger, M.**, Ariyanto T., Krüner, B., Peter, N.J., Fleischmann, S., Etzold, B.J.M., Presser, V. VANADIUM PENTOXIDE / CARBIDE-DERIVED CARBON CORE-SHELL PARTICLES FOR HIGH PERFORMANCE ELECTROCHEMICAL ENERGY STORAGE. International Conference on Multifunctional Hybrid and Nanomaterials. Lissabon (Portugal). March 6th-10th.

INM/UdS Poster Symposium. Saarbrücken (Germany). August 14th. 2014. ***(1st place for best PhD student poster)***

P-5 **Zeiger, M.**, Jäckel, N., Fleischmann, S., Presser, V. ELECTROCHEMICAL ENERGY STORAGE WITH CARBON ONIONS. 3rd PhD Student Day of Saarland University. Saarbrücken (Germany). November 11th. 2015. (***Best poster award***)

P-6 Quilitz, M., **Zeiger, M.**, Kraus, T., Moh, K., Presser, V., Arzt, E. INNOVATIVE ENERGIEFORSCHUNG AM INM. AG LIESA congress. Congress hall. Saarbrücken (Germany). October 26th. 2016.

P-7 **Zeiger, M.**, Jäckel, N., Fleischmann, S., Presser, V. CAPACITIVE AND BATTERY-LIKE ENERGY STORAGE WITH REDOX-ENABLED NANOCARBONS. 4th PhD Student Day of Saarland University. Saarbrücken (Germany). November 9th. 2016.

P-8 **Zeiger, M.**, Ariyanto T., Krüner, B., Peter, N.J., Fleischmann, S., Etzold, B.J.M., Presser, V. VANADIUM PENTOXIDE / CARBIDE-DERIVED CARBON CORE-SHELL PARTICLES FOR HIGH PERFORMANCE ELECTROCHEMICAL ENERGY STORAGE. International Conference on Multifunctional Hybrid and Nanomaterials. Lissabon (Portugal). March 6th-10th.